Alma Mater Studiorum – Università di Bologna

DOTTORATO DI RICERCA IN

Ingegneria Civile, Ambientale e dei Materiali

Ciclo XXVII

Settore Concorsuale di afferenza: 04/A3

Settore Scientifico disciplinare: GEO/05

Lateral spreading and associated slope processes in fractured rock slabs

Presentata da: Margherita Cecilia Spreafico

Coordinatore Dottorato   Relatore

Prof. Alberto Lamberti   Prof.ssa Lisa Borgatti

Esame finale anno 2015

TABLE OF CONTENTS

Lateral spreading and associated slope processes

in fractured rock slabs

ABSTRACT

Landslides of the lateral spreading type, involving brittle geological units overlying ductile terrains, are a common occurrence in the sandstone and limestone plateaux of the northern Apennines of Italy. These instability phenomena can become particularly risky, when historical towns and cultural heritage sites built on the top of them are endangered. Nevertheless, the mechanisms controlling the developing of related instabilities, i.e. toppling and rock falls, at the edges of rock plateaux are not fully understood yet. In addition, the groundwater flow paths developing at the contact between the more permeable units, i.e. the jointed rock slab, and the relatively impermeable clay-rich units have not been already studied in details, even if they may play a role in this kind of instability processes, acting as eventual predisposing and/or triggering factors. Field survey, Terrestrial Laser Scanner and Close Range Photogrammetry techniques, laboratory tests on the involved materials, hydrogeological monitoring and modelling, displacements evaluation and stability analysis through continuum and discontinuum numerical codes have been performed on the San Leo case study, with the aim to bring further insights for the understanding and the assessment of the slope processes taking place in this geological context.

The current research permitted to relate the aquifer behaviour of the rocky plateau to slope instability processes. The aquifer hosted in the fractured slab leads to the development of perennial and ephemeral springs at the contact between the two units. The related piping erosion phenomena, together with slope processes in the clay-shales led to the progressive undermining of the slab. The cliff becomes progressively unstable due to undermining and undergoes large-scale landslides due to fall or topple.

FOREWORD

The present research was focused on particular geological context, namely brittle fractured rock plateaux lying on a ductile clay-rich substratum. These settings can be recognized in several areas in the Apennines and, more generally, in all Europe, and give rise to typical hydrogeological and slope instability processes. The research, focused on slope processes associated to lateral spreading in the Valmarecchia area was started by Prof. Lisa Borgatti, following the suggestions of Prof. Maurizio Pellegrini.

All the work here presented was conducted under her supervision and thanks to her advices.

The San Leo plateau was chosen as case study, due to the numerous landslides that threatened this outstanding cultural heritage site since centuries. The 2014 landslide, occurred during the last year of research, allowed to test the hypotheses elaborated in the previous years, back-analysing the failure.

The current research was carried out by means of a multidisciplinary approach, including different techniques. Several experts were involved and gave their contribution to the present work.

STB Romagna and Enser srl provided useful data regarding the study area and about the investigation conducted before the beginning and during the research project.

The Geological model of the area was developed under the guidance of Prof. Alberto Landuzzi.

Terrestrial Laser Scanner surveys were conducted thanks to the cooperation with the Laboratory of Land Surveying and Geomatics - LARIG, and in particular with Prof. Gabriele Bitelli.

The Close Range Photogrammetry surveys were performed together with the Earth Sciences Department, University of Torino, which also provided the Coltop software.

The laboratory tests on the rock samples were conducted in the Laboratory of Geoengineering and Natural Resources – LAGIRN, (Prof. Paolo Berry).

The hydrogeological characterization, including field survey, monitoring and numerical modelling, was conducted in collaboration with Dr. Federico Cervi (University of Bologna).

The Permanent Scatterers Satellite Aperture Radar Interferometry (PS-InSAR) were analysed together with Eng. Francesca Franci (University of Bologna).

Finally, the research included two periods abroad. The first one, financed by the DAAD (German Academic Exchange Service) scholarship, was conducted in the laboratory of the Chair of Foundation Engineering, Soil and Rock Mechanics of the Ruhr Universität Bochum. Under the supervision of Prof. Tom Schanz, several laboratory tests were conducted to analyse the behaviour of the clay-shales outcropping in the study area. The second one, financed by the Marco Polo program issued by DICAM, was spent in the Engineering Geology and Resource Geotechnics research group at Simon Fraser University (SFU), Vancouver, BC, Canada. During these months the research work was carried out under the supervision of Prof. Doug Stead and was mainly focused on the numerical modelling of complex landslide mechanisms using 2D/3D continuum and discontinuum codes.

INTRODUCTION

Deep Seated Gravitational Slope Deformations (DSGSDs) are gravity-induced processes which affect entire slopes, evolving over long time intervals (Goudie 2004). These phenomena have been discussed by numerous Authors (Malgot 1977; Dramis & Sorriso-Valvo 1994; Varnes 1978; Crosta & Clague 2006; Martinotti et al. 2011). They represent the most exceptional and interesting phenomena among all the landslides, due to their dimensions, to the complexity of the acting processes, often driven by several factors, and the associated secondary slope instability phenomena.

Referring to the Varnes landslides classification (1978), two main types of DSGSD are recognizable, namely *sackungen* and *lateral spreading phenomena*. The first can be described as a sagging of a high and steep slope, made up of homogeneous, jointed or stratified rock masses, due to viscoplastic deformations taking place at depth (Zischinsky 1969; Bisci et al. 1996). The latter are defined as lateral expansion of rock masses occurring along shear or tensile discontinuities (Soldati 2013). Among them Pasuto and Soldati (2013) differentiated between the type of materials involved: (a) brittle formations overlying ductile terrains, generally the instability is caused by the deformation of the latter; (b) homogeneous rock masses, in this case the basal surface is not well defined and the morphological pieces of evidences are not easily recognizable, and (c) spreading involving soils, mainly recognized in presence of terrains prone to liquefaction, e.g. quick clays, varved clays or fine sands (Rauch et al. 1997). In the present work the attention will be focused on the first type, i.e. brittle geological units overlying ductile terrains.

Cruden and Varnes (1996) described the movements which involve a thick layer of rock overlying softer materials as *block spreads*. Hungr et al. (2014), in a recent update of the Varnes classification, used the term *rock slope spreading* to indicate the quasi-horizontal stretching of a mass of coherent blocks of rock (cap rock), resulting from the deformation of the underlying weak material or by multiple retrogressive sliding. The observed mechanism depends on both the local geological and structural setting and on the geodynamical evolution of the area (Bozzano et al. 2013). Anyway, due to the different factors influencing the slope phenomena, both in the hydrogeological and in the slope stability frameworks, an exhaustive description and explanation of the predisposing and triggering factors is not straightforward.

The process is often driven by deformation within the underlying weaker material and generally induces horizontal spreading and progressive break-up of the cap-rock mass. As the rate of movement is usually very low, the effects are most evident at the edges of a plateau, where rock falls and topples may occur. In fact, lateral spreading is usually coupled with secondary slope instability processes. This variety of mechanisms, strictly related to the DSGSD evolution, can produce a high level of risk for the settlements located both at the top and at the toe of the rocky plateau. The stiffer slab can fracture or progressively

separate along pre-existing discontinuities or newly-formed fractures. In some cases, the spreading can evolve into the complete fragmentation of the slab (Figure 1, Conti & Tosatti 1996). The softer material can be squeezed out from beneath the rock slab either into the discontinuities between the overlying stiffer blocks or at the border of the plateau (Benko 1997). An advanced evolution of these processes can be seen at *Cinque Torri*, in the Eastern Alps (Viero et al. 2010).
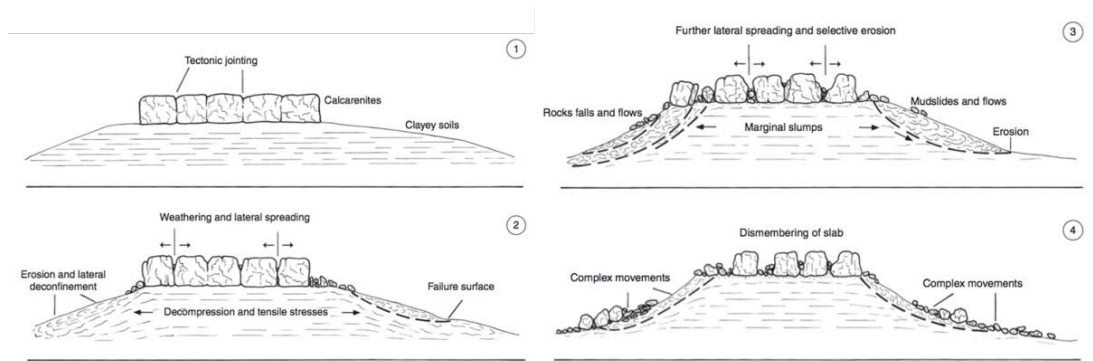

Figure 1. Rock spreading evolution (Conti & Tosatti 1996)

Several examples have been widely accounted for (Pašek & Pulinowa 1975; Cecere & Lembo-Fazio 1986; Canuti et al. 1990; Rohn et al. 2004; Bozzano et al. 2008). In Europe, slope instabilities associated to lateral spreading phenomena can become particularly risky when historical towns and cultural heritage sites built on the top of them are endangered. Slope instability phenomena threatening the towns of Orvieto, Civita di Bagnoregio and Pitigliano (Central Italy) have been recognized and investigated (Cencetti et al. 2005; Delmonaco et al. 2009; Tapete et al. 2013). Both touristic and historical sites are affected by similar phenomena in the Maltese archipelago (Gigli et al. 2012; Devoto 2013). The differential movement of the cliff faces caused by lateral spread is the main cause of the processes endangering the *Spis* castle in Slovakia (Vlcko 2004).

Several hypotheses were made on the factors influencing these phenomena; among the others, Casagli (1994) and D'Ambra et al. (2004) used numerical models to show how the deformability contrast between the brittle and the ductile units leads to the development of a complex stress state within the rock slab. This stress can cause the gradual opening of the fractures striking parallel to the cliffs. Pasuto & Soldati (2013) indicated the overburden weight of the slab as a common cause for long-term deformations in softer terrains. Lateral erosion and removal of the clayey substratum, e.g. caused by erosion, were also suggested as a triggering factor. Bozzano et al. (2008) investigated the geological evolution of the *Orvieto* slab using a stress-strain analysis. The numerical simulations demonstrated that the deformation was driven by stress reduction in the tuff plate. Moreover, the evolution of the phenomenon can be also accelerated by the presence of a well-developed system of fractures within the rock mass (Pasuto & Soldati 2013).

Despite lateral spreading landslides are very common in the northern Apennines, where brittle limestone and sandstone slabs overlie a softer clay-rich substratum, detailed investigations on this topic are not so frequent or adequately documented in the scientific literature (Pasuto & Soldati 2013).

Furthermore, the groundwater flow path developing at the contact between the more permeable units, i.e. the jointed rock slab, and the relatively impermeable clay-rich units may play a role in this kind of instability processes and they have not been already studied in details, as eventual predisposing and/or triggering factors.

The present work has been focused on the investigation of the factors driving lateral spread in fractured slabs laying on clayey units. Particular attention has been given to the interaction between hydrogeological processes and slope instability phenomena developing within the slabs and in their vicinity.

Among the others, due to the threatened cultural heritage site and to the spectacular location, the slope instability phenomena affecting the San Leo slab (Valmarecchia, northern Apennines) are of great interest. The slab has been prone to failures since centuries: during the first half of 1600 the old access to the village and an entire neighbourhood were destroyed and between 1700 and 1800 a large number of landslides occurred in the whole region (Benedetti et al. 2013). In the last decades two main landslide events were registered, involving a total of 350,000 m^3 of rock. Countermeasures were adopted since the 1970s but none of them seems to have been effective in controlling the phenomena (Borgatti et al. 2015). Anyway the performed investigations provided a number of data regarding the site and the ongoing slope instability phenomena. The San Leo case study can bring further insights for the understanding and the assessment of the slope processes taking place in this geological context. Field surveys, terrestrial remote sensing techniques, laboratory tests, monitoring data, hydrogeological and stability numerical modelling have been combined to describe and interpret the phenomena.

The most recent landslide, which occurred on the 27th of February 2014, provided additional data and permitted to back-analyse some of the hypothesised slope instability mechanisms. Due to this recent landslide, the medieval town built on the top of the calcarenite slab, was seriously threatened by the retrogression of the main scarp.

A brief introduction about the case study, together with the description of a simplified geological model of the area, is given in Chapter 1.

In order to analyse the discontinuity affecting the San Leo rock slab, a complete terrestrial laser scanner survey all around the San Leo cliff was performed. Moreover, close-range photogrammetric surveys and traditional geomechanical surveys have been carried out. On two selected areas the same were performed using the three above-mentioned methods, allowing the comparison of the results (Chapter 2).

The geological materials have been analysed by means of laboratory tests. Due to the relevant role played in the slope instability phenomena by the clay-shale substratum and to its interaction with the groundwater flow, a particular attention was paid on its swelling/shrinking behaviour and on the geotechnical properties of these soils in saturated and unsaturated conditions (Chapter 3).

Starting from these data an hydrogeological model has been built. The results confirmed the presence of an aquifer within the plateau. Spring discharge and groundwater table monitoring data has been

analysed with classic and statistic tools to better understand the groundwater behaviour and to estimate its response to rainfall regime (Chapter 4).

Displacements monitoring data are usually missing or lacking in similar contexts. Thus, an attempt to reach an overview of the movements using the Permanent Scatterers Satellite Aperture Radar Interferometry (PS-InSAR) technique and combining analysis on the PS velocity, on the direction of the movement and statistical consideration on the trend of the time series, has been tested in Chapter 5.

Finally, the slope instability phenomena were investigated through geomechanical modelling (Chapter 6). The model of the whole slab was performed with the Flac3D (Itasca^{TM} 2014) explicit continuum code. The analyses were focused on the comprehension of the general behaviour of the slab. The deformability contrast between the two units (the rock slab and the clay-shale substratum) and the subsequent stress development in the slab were investigated. Stability analyses were conducted coupling Terrestrial Laser Scanning (TLS) and Distinct Element Methods (DEMs) through a 3D back analysis of the 2014 landslide, performed with the 3DEC code (Itasca^{TM} 2014). Furthermore, the role of the softened clayey layer and of the undermining at the base of the rock slab, due to water circulation, has been investigated, performing a back analysis of the 2014 landslide with the finite element program Phase2 (Rocscience Inc. 2013).

The current research permitted to relate the aquifer behaviour of the rocky slabs to softening and erosional processes occurring in the clay-rich substratum and to the related undermining of the rock cliffs, which in turn are proven to act as a predisposing factors for the rockfalls and topples affecting the edge of the slabs.

THE SAN LEO CASE STUDY

1.1 Cultural heritage

The town of San Leo is well-known for its historical and cultural relevance. The first settlement dates back to the III century B.C. when the Ancient Romans constructed the Jupiter temple and a fortification in the highest part of the slab. Between 962 and 964 A.D. it became the last capital of the Italic Longobardic Empire of Berengario II, after his defeat in Pavia. Several intellectual and religious historical figures lived within the town, such as Dante Alighieri, S. Francesco d'Assisi and San Leone; the latter gave his name to the town. The medieval castle, situated on the south-eastern side of the slab, overlooks the Valmarecchia Valley and during the Renaissance period was the location of important battles. Later, under the Papal States, San Leo became the location of a prison, where the Count of Cagliostro, a famous occultist, and Felice Orsini, an Italian revolutionary who tried to assassinate Napoleon III, were imprisoned. Other noteworthy buildings are located in the historical centre of San Leo including the parish church, the cathedral and the bell tower.

The San Leo cliffs have been affected by several slope instability phenomena over the centuries predominantly related to the occurrence of lateral spreading and related secondary slope instability processes. The access to the town has been moved several times after being destroyed by rock falls (Figure 2).

Figure 2. Ancient access to the San Leo town, abandoned after being affected by landslides

1.2 **Geographical, geological and geomorphological setting**

The northern Apennines of Italy are a fold-and-thrust belt which is composed by several sedimentary units building up an accretionary wedge (Kligfield 1979; Molli 2008). They are mainly represented by the Ligurian units. The latter are composed by clayey, silty and marly materials which were deposited, between the Cretaceous and Middle Eocene, in a deep marine environment and then translated up to their current position (i.e. allochthonous units).

During the migration process, they overthrusted the autochthonos Umbro-Marchean-Romagnan units which are composed by turbiditic sandstones and conglomerates interlayered with hemipelagic marls. The accompanying translation mechanisms are still debated; several hypotheses were made to explain it: purely tectonic (Conti & Tosatti 1996), or mixed tectonic and gravitational processes (Ricci Lucchi 1987). In all the cases, the processes led to the high deformation of the Ligurian deposits which is clearly visible even at the microscopic scale (scaly-scale fabric; Vannucchi et al. 2003). It consists of a complex network of closed-spaced discontinuities crossing the overconsolidated clayey materials which can be clustered in three or more sets as a result of the varying direction of tectonic stress during the migration (Bettelli et al. 1989a; Bettelli et al. 1989b).

The resulting highly fissured and overconsolidated clays can be considered as formed by relatively hard scales weakly bound together (Ribacchi & Tommasi 1988) and are defined as clay-shales. Lithic bodies, mostly whitish marly limestones belonging to the *Alberese* formation and completely disarranged by tectonic movements, can be found within the clayey matrix. An example of one of the largest of these bodies is the *Sella dei Quattro Venti*, in the San Leo area. While the Ligurian units were translated, from the Middle-Late Eocene to the Late Messinian, minor sedimentary piggy-back basins developed and were filled up by sedimentary successions (Epiligurian units), which overlay unconformably the deformed clay-shales basement. Usually, these successions are composed of marls, sandstones and limestones (Figure 3).
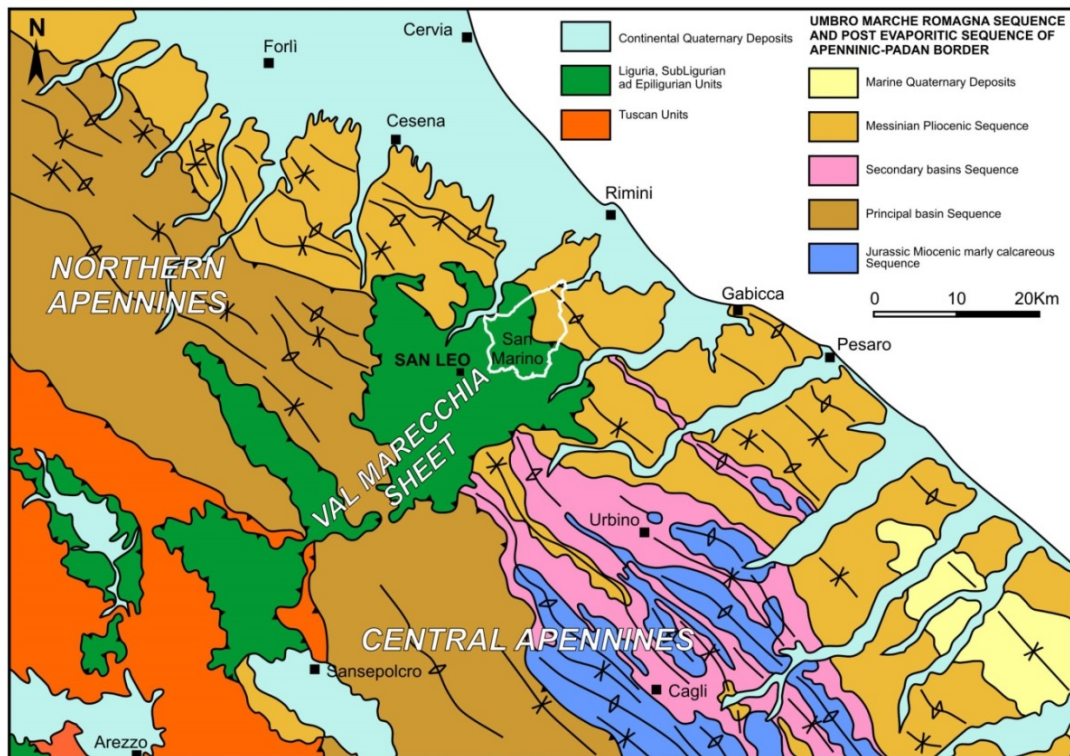
Figure 3. Geological sketch of the area

Due to the lithological characteristics, the Ligurian and Epiligurian units have been affected differently by the weathering processes. This results in the Val Marecchia typical landscape (Figure 5), with gentle clayey slopes spotted by rock slabs. The Epiligurian slabs, on the base of their shape, can be subdivided in arcuate, tabular and small slabs (Conti 1992). The arcuate slabs are usually characterized by a convex shape, with the most elevated edge oriented towards E-NE. They are usually located in the frontal area of the Valmarecchia thrust sheet. The tabular slabs, showing top edges located at the same altitude, can be find in the most internal parts of the thrust sheet.

In the Valmarecchia area several of the main historical towns and citadels were built on the top of these rock slabs, to control the valley, which was a major communication route. Among them the towns of San Leo, Verucchio, Torriana, Pennabilli, Maiolo and the confining San Marino. The valley name comes from the Marecchia river, which flows through its territory, from the central Apennines to the Adriatic sea (Figure 4).

Figure 4. The Valmarecchia territory

The San Leo slab is located 43°53'47.87"N and 12°20'35.61"E, at about 590 m a.s.l., it can be considered a typical example of rock plate belonging to the *Valmarecchia* Epiligurian Basal Complex (Conti & Tosatti 1996). In the study area, the Ligurian units are composed by the so-called *Argille Varicolori*, varicoloured clay-shales, presenting a strongly disrupted structure as a result of the intense tectonization (APAT, 267 San Marino). The Epiligurian units forming the San Leo slab belong to the *San Marino* limestone and to the upper *Monte Fumaiolo* sandstone (APAT, 267 San Marino).

Figure 5. The San Leo rock slab, East cliff

The slab is about 600 m long EW and 500 NS. It has a general North-Westward inclination and is bordered by subvertical and overhanging cliffs, up to 100 m high (Figure 3). The rock mass is crossed by several discontinuities. Sub-horizontal boreholes drilled in the slab have highlighted that discontinuities

are present for the whole investigated thickness (25 metres; D'Ambra et al. 2004). The slab is surrounded by two catchments, departing from *Sella dei Quattro Venti*, situated near the South-Eastern corner of the plateau. The Seripa ditch runs along the southern side of the slab, while the Campone ditch flanks the western and then the northern side of the same. The latter has a more developed catchment area and a rugged morphology, influenced by badland erosion (Ribacchi & Tommasi 1988). The erosive activity of the two ditches influenced the morphology of the area and is considered as a predisposing and triggering factor of slope instability in the surrounding areas.
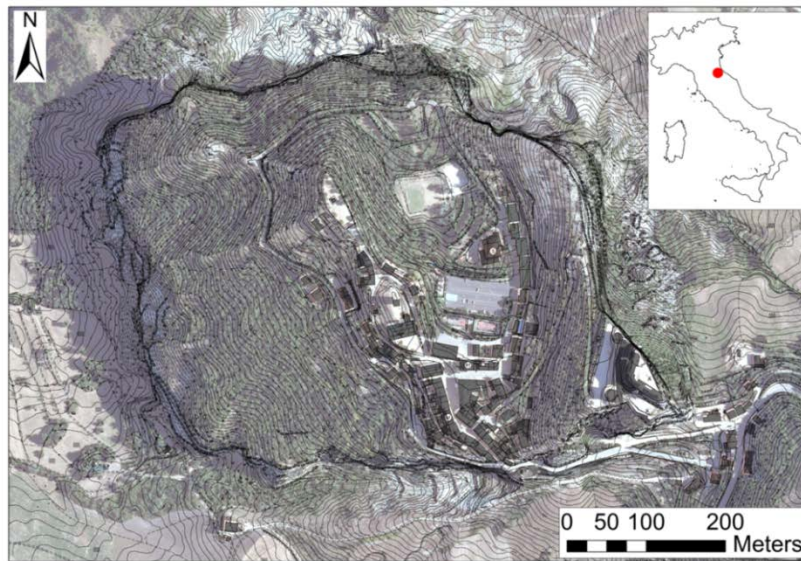
Figure 6. San Leo slab, orthophoto (2007)

1.3   **Climatic and hydrogeological settings**

The mean annual rainfall in the area ranges from 369 mm to 1,258 mm (2002-2011; San Marino raingauge). The main precipitation peak is in autumn (October–November) while a secondary one can be recognized in spring (April). The snow cover is variable, it is usually registered, according to the ARPA dataset (http://www.arpa.emr.it/sim/?telerilevamento/innevamento), between December and March. In the last years the cumulative snow cover varies from 7 (2009) to 307 (2012) cm. The mean annual temperatures are between 11.7 and 14.5 °C, with maximum in July and August (27.6°C) and minimum (0.4°C) in January. The mean annual effective rainfall was estimated in 223 mm and could be supplied to the soil between October and May.

As far as the hydrogeological setting is concerned, the clay-shales from the Northern Apennines of Italy are always characterized by low conductivity values, due to their high clay content (10^{-8}-10^{-11} m/s, Civita 2005). The permeability of the rock slab is mostly of secondary type. Due to the different degree of fracturing, permeability can range between 10^{-2} m/s (jointed or weathered rock mass) and 10^{-10} m/s (undeformed rock) (Gonzalez de Vallejo et al. 2011). The storativity values are in the order of 1-2% (Cervi et al., 2014).

1.4 **Typical slope instability phenomena**

Slope instability processes affect both the rocky slab and the surrounding clay-shale units. The overall slope deformation can be described as a lateral spread involving the brittle rock slab overlying a more ductile terrain. Deep Seated Gravitational Slope Deformations (DSGSDs) generally involve large portions of slopes (Dramis 1985; Soldati 2004). However, the overall movements are generally slow and the main risk is due to secondary instability phenomena (Agliardi et al. 2001; Imiriland Project 2004). Focusing on lateral rock spreads phenomena, the associated instabilities are usually located at the edges of the brittle plateaux. Pasuto & Soldati (2013) listed some typical geomorphological features of this kind of lateral spreading i.e., trenches, gullies, graben and karst-like depressions in the brittle rocks, while bulges were recognized in the ductile material.

The San Leo slab is affected by rock falls and topples, occurring at its perimeter, and involving a volume of rock variable from a few m^3 to several thousand of m^3. In particular, detachment of rock wedges along pre-existent discontinuities occurred frequently in the cliff underneath the castle and at the entrance of the town. An example can be found in the rockfall (volume equal to about 6 m^3) which, in the night between the 29th and the 30th of November 2008, affected the cliff overlooking the only access road to the town, blocking the transit for several days. Major slope instabilities involved the collapse of whole slices of rocks, often undermined by the removal of the underlying clayey layers. These kind of phenomena are typical especially in the northern cliffs, e.g. the 2006 and 2014 landslides, which will be described in the next sections.

The clay-shale substratum is involved in slower slope movements, including earth slides and earth flows. The poor mechanical properties of the involved materials, the water infiltration and other external causes can trigger these relatively shallow movements in the clayey slope, also causing the material removal in the area where the contact between the slab and the substratum is located. Moreover, subsequently to a rock detachment from the cliffs, also the undrained loading on the substratum can bring about the reactivation of slope instability phenomena in the clayey units.

The study area was affected by slope instability phenomena since centuries. These appear in ancient drawings, writings and photographs, covering the last 4 centuries. In the work carried out by Benedetti et al. (2013) all these documents were analysed to describe the past instability events, comparing them with the present-day situation. The first documented phase occurred in the first half of the XVII century. During this period the Porta di Sotto entrance to the town was completely destroyed by a series of subsequent rockfalls. A second instability phase was recognized between the end of 1700 and the first decades of 1800, during a period in which all the Montefeltro region was affected by diffuse landslide events. A secondary entrance to the city centre, located in the northern area and an entire neighbourhood were destroyed by a landslide in 1634 (D'Ambra at al. 2004). The results of the documents comparison show how the slope instability phenomena occurred in the past are very similar to the ones observed during the recent years. In the same work the presence and conformation of the slope deposits surrounding the slab were explained considering past landslide events. In particular, the

presence of huge rock blocks at distances of few kilometres from the source areas was ascribed to the relatively shallow landslides developing in the clay-shale substratum, which transported the rock falls deposit. The southern cliff was affected in the last centuries by a number of rockfall, mostly in the area underneath the castle and the entrance to the town. Between 1930 and 1940 a rock fall involved the southern perimetral massive wall of the castle, while in the February of 1949 a detachment affected the access road. A considerable wedge rockfall was registered between 1949 and 1962. During 1954 a viaduct was built to distance the only entrance road from the cliff, threatened by rockfalls. Other minor detachments occurred from 1962 to the present days (Lembo-Fazio et al. 1998; Tommasi 1997).

In the last decade two important slope failures occurred. The first, on the 11th May 2006, affected the northern side of the slab (Benedetti et al. 2013), while the most recent landslide occurred on the 27th February 2014 and is described in detail by Borgatti et al. (2015).

Several authors investigated on the causes of this instability, both at a large scale, considering the lateral spread, and at a more detailed scale, focusing on the secondary phenomena developing at the edge of the plateaux.

Ribacchi and Tommasi (1988) ascribed the evolution of the clay-shales slope mainly to the mudflows occupying the two valleys surrounding the slab. The collapse of vertical slices of rocks was attributed to the undermining of their toe, produced by the same mudflows, which progressively remove the clayey materials. Cecere & Lembo Fazio (1986) hypothesized that the deformation of the clay at the base of the cliffs induces an intense stress concentration, producing vertical fractures parallel to the rock faces and, at times, the subsidence of marginal blocks. Casagli (1994) analysed similar rock slabs in the northern Apennines, namely Sasso Simone and Simoncello, La Verna and Monte Fumaiolo. As the main causes of the slope instability phenomena, he recognized, the contrast in the mechanical properties of the involved units, the high value of the tectonically-induced horizontal in-situ stress, the existence of pre-existing well developed discontinuity system and the periglacial paleo-climatic conditions during the Pleistocene. The results of the 2D numerical analysis carried out in his work highlighted the role of the strength contrast between the slab and the underlying clay-shales, capable to generate in the rock mass a tensile stress of the same order of magnitude its tensile strength. D'Ambra et al. (2004) performed numerical analyses (Finite Difference Methods FEMs and Distinct Element Methods DEMs) on a 2D section located on the rock face under the castle. They confirmed that the stress state which characterizes the toe of the slab is due to the interaction between the rigid rock mass and the deformable substratum. Moreover, comparing the DEM results with field observation they recognized a progressive opening of the rock joints striking parallel to the cliff, subjected to tensile and shear stresses. Pasuto and Soldati (2013), describing the lateral spreading phenomena occurring in stiff plateau ling on a softer material, ascribed the overburden of the rock slabs among the causes of the deformation affecting the substratum, resulting in the squeezing out and bulging of clayey material.

Bozzano et al. (2008) modelled the geological evolution of *Orvieto* and *Radicofani* cliff slopes, taking into account the changes in deformability parameters due to the changing in the geological conditions. They

concluded that a stiff sub-horizontal plate resting on a ductile substrate undergoes horizontal stress unloading. This process was retained responsible for the generation of tensile stresses at the plateau borders and tension cracks along the cliffs, in turn responsible for local landsliding. Lateral stress release, i.e. due to valley incision, was indicated as a triggering condition by Bozzano et al. (2013) (Figure 7).
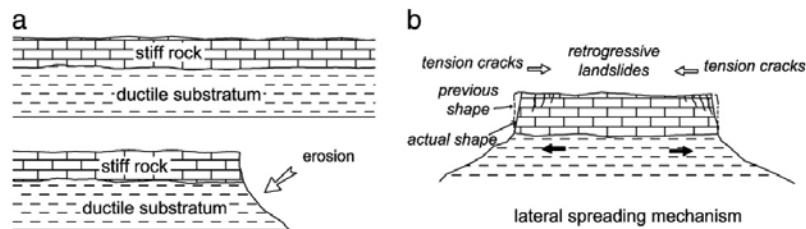

Figure 7. a) Conditions necessary for a gravitational induced lateral spreading: lithological overlapping of a stiff lithology on a more ductile one; b) the horizontal deformation of the ductile substratum cause the jointing of external and not confined portion of the stiff lithology (Bozzano et al. 2013).

Moreover, following Pasuto and Soldati (2013), the water percolation through fractures and the subsequent softening of the weaker material can accelerate the process.

Summarizing the previous works, the recognized slope instability causes are:

- the deformability contrast between the stiffer rock slab and the softer substratum;
- the overload of the rock slab;
- the water percolating through fractures in the rock mass;
- the lateral erosion and material removal which causes confining stress relief in the slab;
- the discontinuities in the rock mass.

In the present work the above-mentioned factors were examined and an attempt to determine their role in the overall and local slope phenomena was carried out. Moreover, due to the high degree of fracturing of the rock slab, and so to its relatively higher permeability, if compared with the clayey substratum, the presence of a piezometric surface inside the slab was hypothesized. The aquifer hosted in the slab can assume an important role in the developing of slope instability processes, i.e. increasing locally the pore-water pressure, influencing the stresses acting in the slab and in the underlying clays. Moreover, the springs located at the contact with the almost impermeable substratum, can promote, through chemical alteration and physical weathering, the softening of the basal ductile terrains and the erosional processes.

1.5 The 2006 landslide

During one of the most recent landslide event, occurred on 11th May 2006, a rock fall affected the northern side of the slab, suddenly detaching from the vertical cliff (Figure 8). The landslide volume was estimated in the order of 50.000 m^3 of material (Benedetti et al. 2013). An high degree of undermining at the base of the cliff was recognized prior to the failure. A calcite coating was also found in the rock

discontinuities with an orientation parallel to the cliff face, indicating water circulation and thus the pre-existence of the latters (Gibertoni 2007).
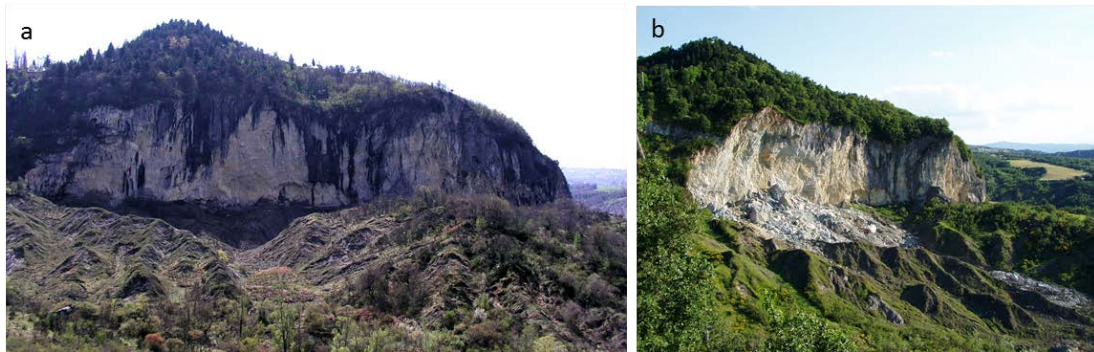

Figure 8. 2006 landslide: a) pre- and b) post-failure.

Some inhabitants living down the slope perceived the event as an earthquake shake, followed by wind and dust. The retrogression of the scarp, due to the 2006 landslide was estimated in the order of 10 meters (Benedetti et al. 2013). A public secondary road, located at the top of the cliff was closed, as a precautionary measure. The undrained loading at the top of the clay-shale slope triggered an earthflow, which reached velocities in the order of 4.2 cm/h (moderate velocity following Cruden & Varnes 1996). The earthflow reached an accumulation area of a dormant earth slide, nearby the Rio Maggio stream, reactivating the gravitational movement. After the field investigations, monitoring and laboratory tests have been carried out, to characterize the phenomena. Three main stratigraphic units with different geomechanical behaviour were individuated in the substratum, namely (a) the landslide body, formed by silty-clayey materials including calcarenitic blocks, (b) a softened and (c) a stiffer clay-shale layers. Their mechanical properties were analysed by means of oedometric, triaxial and shear tests. Furthermore, countermeasures were built to avoid the repetition of similar events in this area. In particular, retaining walls founded on piles, drainage trenches and superficial ditches were constructed and the landslide body was reshaped.

1.6   **The 2014 landslide**

The 2014 landslide took place at 16:56':37'' (UTC) of the 27th February 2014 on the North-Eastern side of the slab, in an area strongly affected by the erosion and undermining at the slope toe, as clearly shown in photographs taken before the event (Figure 9b). The cliff showed a retrogression of about 40 m. The volume of the landslide has been estimated at about 300,000 m[3].
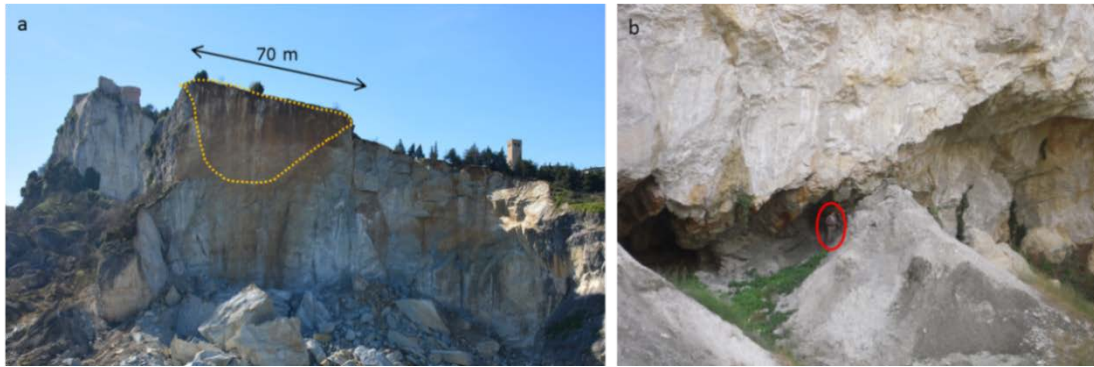
Figure 9. View of the 2014 landslide area: a) the dashed yellow line highlights the discontinuities named SL3.1; b) pre-failure photograph showing the undermining at the base of the cliff, in the red circle a person for scale (Photo courtesy STB Romagna).

Inhabitants reported to have heard noises coming from the cliff since the night before the landslide, and a loud rumble during the collapse. The produced ground shaking was recorded by a strong-motion seismic station belonging to the National Institute of Geophysics and Volcanology (INGV). The seismic records, reported in Figure 10, showed minor cracks propagation around 30 s before the first event and between the two registered signal peaks.
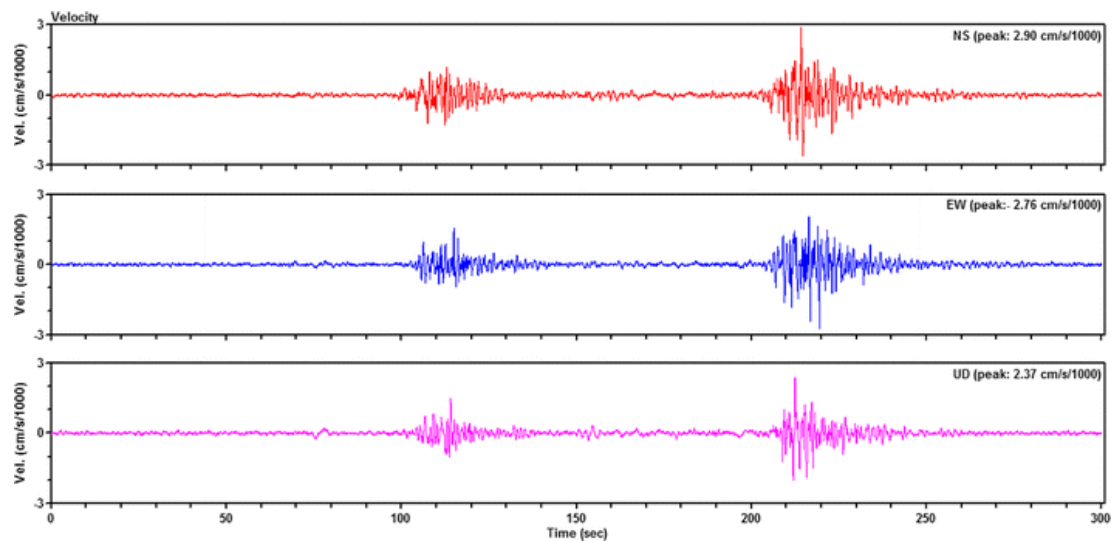
Figure 10. Ground shaking due to the landslide event, recorded by the seismic station of Mount Carpegna, 11 km far from San Leo. Time axis starts at 16:55':00" UTC (Borgatti et al. 2015).

The description of the event is reported in Borgatti et al. (2015), who also gave a first temporal interpretation (Figure 11), based on these seismic records and on eyewitnesses descriptions:

- Progressive detachment of the cliff;
- Toppling of the whole block;
- Collapse and total disaggregation;
- Evolution in rock-debris avalanche.
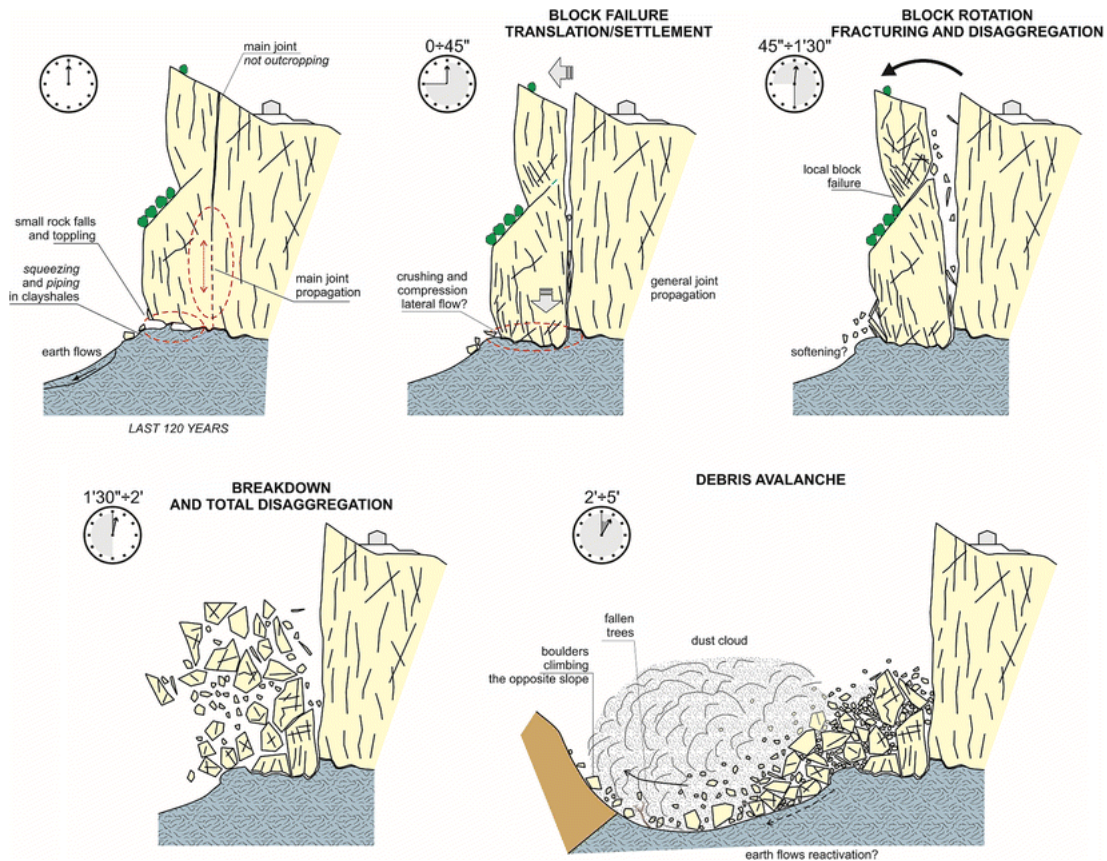
Figure 11. Tentative reconstruction of the time evolution of the landslide event (Borgatti et al. 2015).

The landslide debris were spread on an area of about 70,000 m³ (Figure 14), reaching the opposite side of the valley up to 30 m above the valley bottom. In the following days the undrained load provoked an earth flow in the clay-shales substratum (speed up to 30 cm/day), as happened after the 2006 landslide. Minor rock falls affected the area until the evening of the 28th February and also afterwards. The retreat of the cliff scarp endangered a road, several private buildings, a police station and a public school (Figure 12).

Figure 12. Views of the 2014 landslide, from the top views the closeness between the landslide crown and the buildings is evident

After the event, a clear discontinuity surface, about 70 m long and 40 m wide, was recognized in the upper part of the landslide scarp. This fracture, referred to as SL3.1 (Figure 9a), was recognized as the plane along which part of the initial movement took place. Considering the degree of oxidation of its surface, due to water circulation, it is suggested that the discontinuity was pre-existing. Several field surveys conducted after the landslide allowed discontinuities with similar orientation to be mapped on the top of the slab, in the area behind the north-eastern cliff: they showed a mean spacing of about 20-22 m (Enser srl 2014). In the lower area of the scarp, the failure seemed to propagate along smaller joints and through the breaking of intact rock bridges, showing a backward propagation (Figure 13).
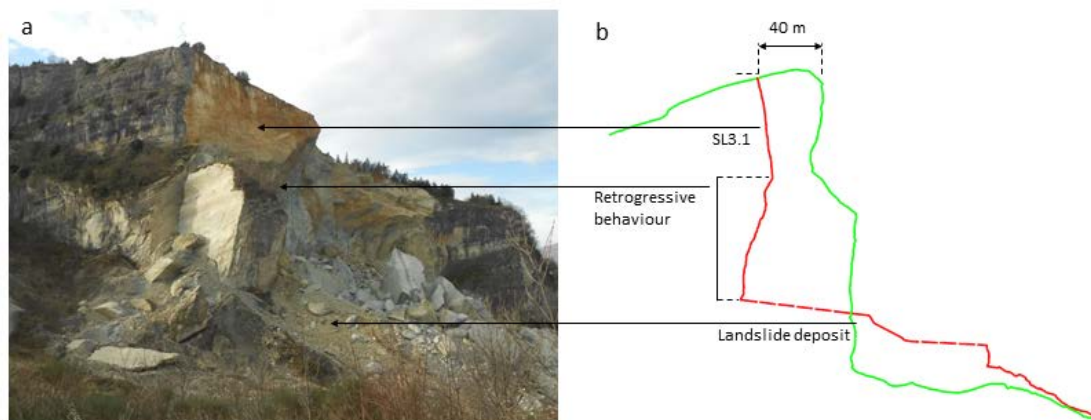
Figure 13. a)View of the 2014 landslide; b) Cross section extracted from the Terrestrial Laser Scanner point cloud, illustrating the pre-existing discontinuity SL3.1 and its retrogressive propagation in the lower portion of the scarp

As anticipated, surveys conducted before the failure highlighted the presence of undermining in the same area: caverns extending about 20 m under the slab were individuated. Anyway, the quantification of the undermining extent is not easy, due to the rough topography and to the hazard of the area.

Figure 14. San Leo rock slab, in red the 2014 landslide. On the Northern side of the slab also the deposit area of the 2006 landslide is visible.

1.7 Geological model

As previously illustrated the San Leo town was built on one of the slab spotting the Valmarecchia valley. The slab has an area of about 280,000 m², and is constituted, from the bottom to the top, by limestone of the *San Marino* Fm., mainly outcropping in the northern and eastern cliffs, and sandstone of the *Monte Fumaiolo* Fm., more visible in the southern and western slopes. The limestone appears to be more massive at the toe of the slab, becoming more stratified and progressively richer of sandy fraction towards the top. The sandstone is mainly characterized by thick flat-parallel layers composed of thinner cross-bedded sets (Figure 15).

– *San Marino* formation

    a. Biocalcirudites with a micritic cement, relatively hard and competent;

    b. Well cemented calcarenites;

    c. More or less cemented calcarenites containing serpentine and glauconite grains;

– *Monte Fumaiolo* formation

    a. Coarse and poorly cemented greenish calcarenites, with thick siltstone layers;

    b. Alternations of arenaceous-pelitic layers (sandstone/mudstone ratio 4:1).

Figure 15. Geological description of the San Leo area

The Geological maps (1:50,000) and the description of the units outcropping in the study area can be found in APAT (http://www.isprambiente.gov.it/Media/carg/267_SAN_MARINO/Foglio.html). A brief summary of the main characteristics of these units is here reported:

Argille Varicolori clay-shales
Allochthonous formation, mainly constituted by varicoloured clays, deposited in deep marine environments. Their colour can vary from red to green to dark grey or ochre. The structure is highly disrupted, due to the shear deformations that affected the units during their migration. The hard scales composing these units are weakly bounded together (Ribacchi & Tommasi 1988). Towards the ground surface the scales become smaller and flatter, due to weathering processes.

San Marino limestones
Constituted by grey organogenic limestone and white-greyish calcarenites. They show a concave-convex first-order stratification, composed of cross-bedded second-order sets, e.g. megaripples, indicating a shallow marine deposit environment.

Monte Fumaiolo sandstones
Hybrid grey-yellowish sandstones, with thickening-upward first-order layers, composed of cross-bedded second-order sets, e.g. megaripples. They were deposited in a shallow marine environment. They are usually separated from the *San Marino* formation by a glauconitic horizon.

The detailed description of the emplacements mechanisms of the outcropping units is still debated and goes beyond the scope of this thesis.

The San Leo slab is generally highly fractured and crossed by faults and discontinuities. The south-eastern edge of the plateau, on which rises the castle, is disarranged by one of the main faults, showing a high degree of fracturing (Figure 18a, Figure 18).

A central SSE-NNW depression, named *Valsanto* and covered by debris, divides the plateau into two zones (Figure 17), the eastern and most elevated one and the western area, more extended and showing a rectangular shape. A lower area is visible in the western side of the south cliff (Figure 16), where the sandstones are intensely pervaded by fractures and normal faults, related to an early stage of gravity-driven collapse. The south-western sector appears almost undeformed, with respect to the other parts of the slab (Figure 18b).
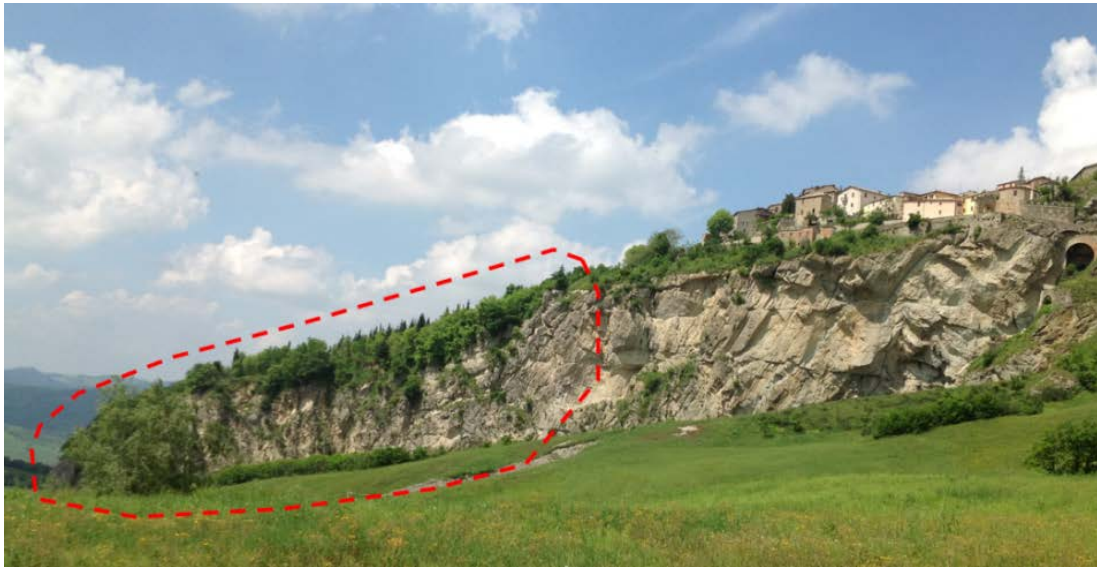
Figure 16. Fractures and normal faults in the sandstones of the southern cliff.

An highly fractured zone was individuated in correspondence of the division between the Western collapsed area and the Eastern side of the cliff. It is probably correlated by a NNW-SSE fault to another disrupted zone outcropping in the Northern cliff. In the Western part of the slab the presence of a WSW-ENE structural lineament was supposed, separating the competent South-Western edge to the more fractured Northern side of the cliff (Figure 18).
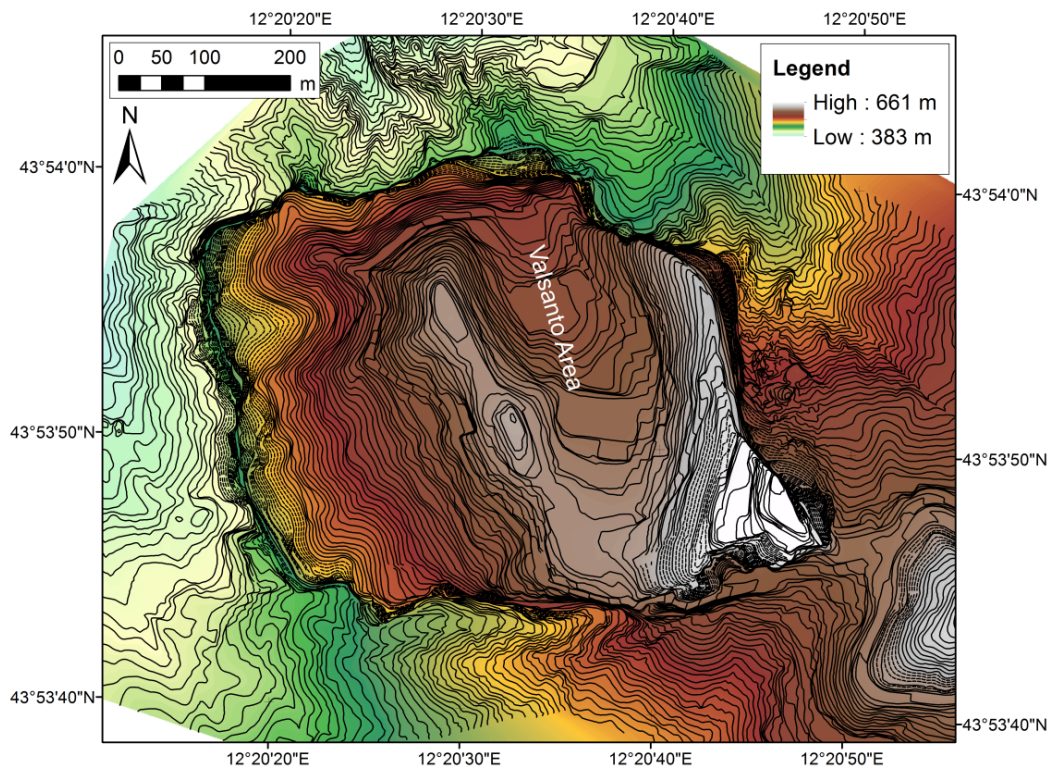
Figure 17. Digital Elevation Model of the San Leo area

All around the slab, and mostly in the Northern and Eastern sides, landslide deposits were mapped. They mainly consists of ancient shallow earthflows in the clay-shale unit and in rock blocks detached from the cliffs. Usually these rock boulders were transported away from the slab by the triggering/reactivation of movements in the clayey materials.

Apart from the 2006 and 2014 landslide deposits, previously described, a concentration of these blocks can be recognized below the Eastern cliff and the Western part of the North cliff (Figure 18c).

Figure 18. Views of the cliff: a) south-eastern edge of the plateau showing a high degree of fracturing; b) south-western sector, less deformed in respect to the other parts of the slab; c) landslide deposit in the western part of the northern cliff
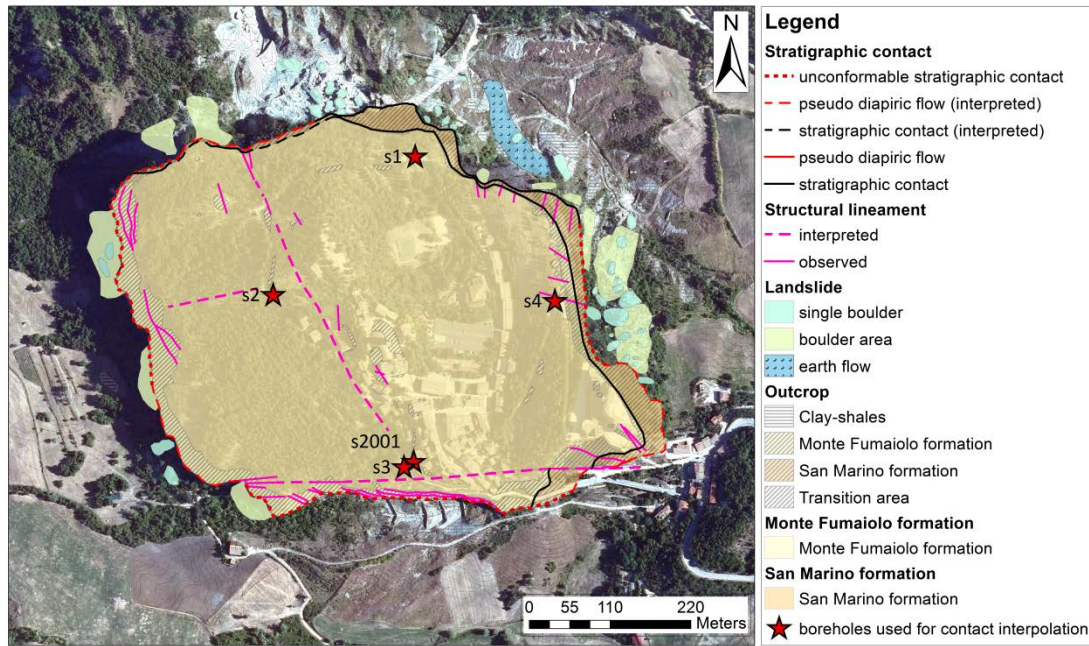
Figure 19. Geological and structural map of the slab, the red stars indicates the boreholes drilled in 1972. The 2001 borehole is located in South part of the slab, close to the 1972 one (modified from Badioli 2012).

The contact between the rock slab and the clay-shales unit is clearly visible in the northern side of the slab. The structural data originate from several geognostic and geological surveys were used to interpolate the contact surface over the whole area. More in detail, five boreholes were drilled in 1972 and 2001 near the borders of the slab, three of them entirely crossed the calcarenites from the top up to the substratum.

The 1:2000 Scale geological survey carried out by Badioli (2012) was used to map the contact between the slab and the clay-shales along the border of the cliffs. Results showed a general north-westward dipping of the contact. A EW section of the interpolated contact is showed in Figure 20.
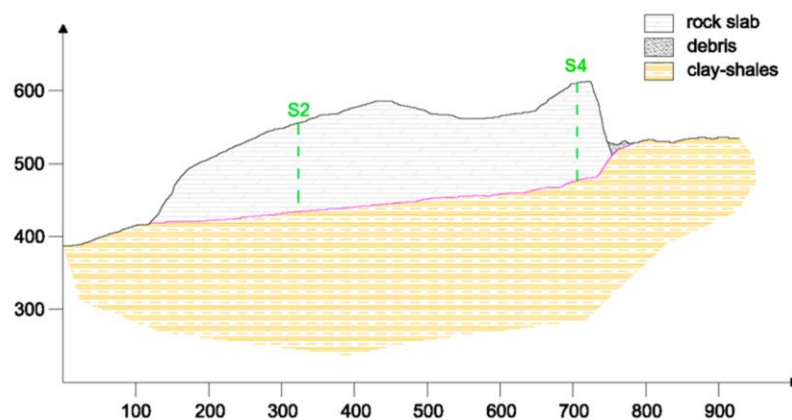
Figure 20. EW section showing the interpolated contact between the clay-shales and the rock slab (magenta) and the boreholes (green)

Table 1. Boreholes used for thegeological contact interpolation

Borehole	Date	Maximum depth	Depth of the clay-shale unit
s1	21st Sept. 1972	103.8	102.3
s2	21st Sept. 1972	109.34	-
s3	21st Sept. 1972	122.3	105.9
s4	21st Sept. 1972	134.1	-
s2001	2nd April 2001	104	97.1

APPROACH AND METHODS OF THE RESEARCH

Slope instability processes can be promoted by a number of factors, e.g. the rise in groundwater level or pore pressure development, earthquakes, weakening of the involved materials, erosion at the toe of the slope; these factors can act alone or together. Comprehensive investigations about possible predisposing or triggering factors should be performed in order to recognize the most influencing ones and to evaluate the evolution in time of the phenomena. This becomes particularly important in case of complex processes, e.g. involving different materials or being the combination of different type of movements.

In the presented research, relatively new technologies and standardized procedures have been combined with a multidisciplinary approach in order to reach a complete description of the slope processes occurring in fractured plateaux lying on a more deformable clay-rich substratum. Slope processes comprises both hydrogeological and stability aspects, in this work, they are both taken into account and carefully analysed. Based on these investigations different hypotheses regarding the acting slope processes have been made and tested by means of numerical models.

A schematization of the workflow is reported in *Figure 21*.
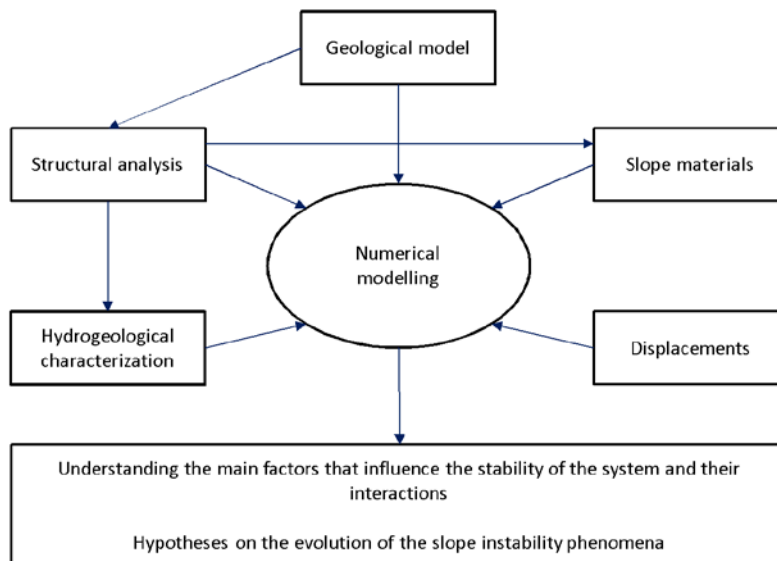
Figure 21. Research workflow

In particular, the geological model described in the previous chapter was adopted as a starting point for the successive hypotheses and interpretations. The knowledge about the structural behaviour of the rock plateau was enhanced analysing Terrestrial Laser Scanner (TLS) and Close Range Photogrammetry (CRP) data, which allowed the study of inaccessible areas, coupled with field investigations and engineering geological surveys. The mapped discontinuities were inserted both in the hydrogeological and in the stability models. In the first one, the results of the structural characterization permitted to

estimate a mean equivalent hydraulic conductivity for the rocky plateau and to characterize the different areas of the slab from an hydrogeological point of view. In the stability analyses, the mapped discontinuities were inserted both directly and indirectly (e.g. through GSI), by the evaluation of the whole rock mass properties. Moreover the parameters collected during the field surveys allowed a first estimation of the mechanical properties of these discontinuities. The rock mass strength was further investigated through laboratory tests. Also the clay-shales behaviour was tested, with a particular focus on their interactions with groundwater. The mechanical parameters estimated from these laboratory tests were inserted in the stability models. Moreover the hydrogeological characterization and modelling of the slab permitted to derive a mean piezometric surface. Although a reliable monitoring of superficial and deep displacements was not available, the main movement trends were estimated thanks to the PSinSAR technology. As anticipated, all these pieces of information, besides their importance in the definition of the numerical models, constituted the basis on which several hypotheses, regarding the instability mechanisms, were formulated. The modelling phase was adopted to tests and refine these interpretations, reaching a deeper understanding about the most influencing factors, about the relationship between hydrogeological and stability processes in these particular contexts, and about the evolution of the slope processes.

STRUCTURAL ANALYSIS

2.1 **Introduction**

As stated by Pasuto and Soldati (2013) for similar contexts, the presence of a well-developed system of discontinuities can be considered as a controlling factor for the evolution of lateral spreading and related slope instability phenomena. The orientation, termination, roughness, aperture, spacing and persistence of the discontinuity network influence the stability of the area and the mechanism of failure. The evaluation of these characteristics is fundamental also in the definition of the jointed rock mass strength parameters, e.g. using the RMR or GSI classifications. Moreover, besides the structural setting of the slab, the discontinuity network plays a primary role also in the groundwater flow paths, allowing the flow inside the rocky slab and driving its direction and velocity, as will be illustrated in Chapter 4. Thus, the description and understanding of the rock mass structure, of the discontinuity pattern and characteristics are a crucial issue also for hydrogeological studies (Lee & Farmer 1993; Singhal & Gupta 2010). Discontinuities can include different types of features, e.g. joints, faults, bedding planes and fractures along other directions of weakness (ISRM 1978; Priest 1993). Usually, the analyses of the geological structures are performed by traditional field surveys. These can be challenging, due to the difficulty to access steep, high and dangerous rock faces or due to the large dimensions of the area to be surveyed. Terrestrial remote sensing techniques, including both Terrestrial Laser Scanning (TLS) and digital photogrammetry, represent a useful complement to conventional field mapping and rock mass discontinuity characterization (Bistacchi et al. 2011). TLS is getting measurements that make the process of interpretation of geological structures easier (De Souza et al. 2013); on the other hand, Close Range Photogrammetry (CRP) procedures can be convenient in relatively small areas. Both these techniques were proven to be useful in the study of rock slopes by several Authors (Abellán et al. 2006; Sturzenegger & D. Stead 2009; Humair et al. 2013; Wolter 2014).

In order to analyse the discontinuity characteristics affecting the San Leo plateau, a complete TLS survey all around the San Leo cliff was performed. Moreover, CRP surveys and traditional structural surveys have been carried out. The 3D geometry was extracted and structural analyses were conducted for all the cliff faces. On two selected areas the same were performed using the three above-mentioned methods, allowing the comparison of the results.

The 3D point clouds derived from the TLS survey were used to build a 3D model of the slab. Francioni et al. (2014) highlight the advantages of using geometrical models obtained from terrestrial remote sensing instead that the ones based on topographic maps, in the framework of slope stability modelling. This applies particularly in case of overhanging cliffs.

Furthermore, a comparison of the multi-temporal scans acquired in the area involved in the 2014 landslide permitted to calculate the volume of the dethatched material and to obtain the pre- and post-

failure geometries. Measurements of the block sizes in the deposit area were used to infer an effective equivalent spacing for the three recognized main joint sets.

2.2 **Discontinuity geometric characteristics – definitions and basic concepts**

− *Orientation*

The orientation or attitude of the discontinuity plane can be defined through the measure of three angles (Figure 22):

- dip, which is the angle between the feature and the horizontal plane, expressed in degrees (0-90°);

- dip direction, representing the direction towards which the plane is inclined. It is defined by the angle (0-360°) between the direction of the dip, projected to the horizontal and the North, and it is measured clockwise from the true North;

- strike, the azimuth of the line representing the intersection of the feature with a horizontal plane (0-360°).

The strike can be calculated by adding 90° to the dip direction angle, so only two of them are necessary to determine the plane orientation. The orientation is usually measured in the field using a compass.

By means of terrestrial remote sensing data, the orientation of a plane can be measured automatically, e.g. by software performing a recognition of planar or quasi-planar regions (Brideau et al. 2011; Viero et al. 2010; Derron & Jaboyedoff 2010), or manually, fitting the recognized discontinuities with planes or circles (Sturzenegger & D Stead 2009; De Souza et al. 2013).
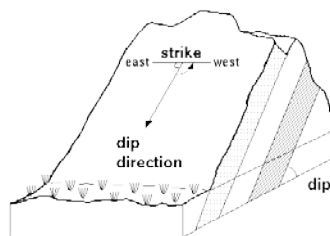
Figure 22. Orientation of a plane in the space

− *Frequency*

Discontinuity frequency is the number of fractures for a unit of space. It can be expressed in term of spacing, density or intensity. The spacing is defined as the mean space between discontinuities intersecting a scanline. The scanline direction can introduce an orientation bias in the measure of the apparent spacing (s_a), when it is not perpendicular to the discontinuities. The real spacing (s) can be found applying the following equation (Terzaghi 1965; Priest 1993):

$$s_a = s \, sen\gamma$$

where γ is the angle between the rock face normal and average orientation plane of the discontinuity set.

When the acute angle between the discontinuity and the scanline is small it results in an overestimation of the spacing (Priest 1993). To avoid this bias, scanline with different orientations should be used. The terminology used in this work refers to the one developed within the Discrete Fracture Network (DFN) code Fracman (Dershowitz et al. 1998; Golder Associates 2009a) and showed in Figure 23. Fracture spacing influence rock mass permeability and controls the block size (Singhal & Gupta 2010).

Dimension of sampling region		Dimension of feature				
		Number of fractures	Fracture trace length	Fracture area	Fracture volume	
		0	1	2	3	
Point	0	P_{00} [-] Number of fracture samples per point sample of rock mass				Point measures
Line	1	P_{10} [1/m] Number of fracture per unit length of scanline *(frequency or linear density)*	P_{11} [-] Total fracture aperture per unit length of scanline *(linear porosity)*			Linear Masures
Area	2	P_{20} [1/m²] Number of trace centers per unit area of sampling surface *(areal density or trace intensity)*	P_{21} [1/m] Length of fracture traces per unit area of sampling surface *(areal intensity or trace intensity)*	P_{22} [-] Area of fractures per unit area of sampling plane *(areal porosity)*		Areal measures
Volume	3	P_{30} [1/m³] Number of fracture centers per unit volume of rock mass *(volumetric density)*		P_{32} [1/m] Area of fractures per unit volume of rock mass *(volumetric intensity)*	P_{33} [-] Volume of fractures per unit volume of rock mass *(volumetric porosity)*	Volumetric measures
		Density		**Intensity**	**Porosity**	

Figure 23. Graphical illustration of Fracman fracture quantification parameters. Modified from slide n.20 in http://fracman.golder.com/Gallery/guidtour.asp

   – *Persistence*

Persistence is defined as the discontinuity trace length observed in an exposure. It is supposed to give an indication about the areal extent of a discontinuity (ISRM 1978). Usually discontinuities appear in outcrops as traces or exposed surfaces, but their entire surface is not visible. It can be hidden in the rock mass or eroded (censoring bias). Moreover a truncation bias can occur, when is not possible to recognize discontinuity traces shorter than a certain threshold (Zhang & Einstein 1998). For example, as pointed out by Sturzenegger & Stead (2009), applying remote sensing techniques, fractures smaller than the image resolution cannot be detected. For all these reasons it is often not possible to obtain a real estimation of the discontinuities areal extension. A method to estimate the true trace length distribution and avoid length bias and censoring using circular windows of finite size was proposed by Mauldon (1998) and Zhang & Einstein (1998). Mauldon et al. (2001) developed a further method to estimate trace density, intensity and true mean trace length. It is based on the number of joint

endpoints inside or intersecting a circular window. Sturzenegger et al. (2011b) adapt the proposed method for terrestrial remote sensing techniques, introducing the concept of topographical windows.

− *Roughness*

The deviation of a discontinuity surface from planarity is called roughness. It can be measured at different scales (Sturzenegger & Stead 2009). (Priest 1993) defines the curvature as surface irregularities with a wavelength greater than 100 mm. The ISRM (1978) proposed several methods to measure the surface roughness. It is usually quantified using the Joint Roughness Coefficient (JRC), by taking the discontinuity profile in the field, using the Barton comb, and comparing it with standard ones, presented in charts (Barton et al. 1974; Barton & Choubey 1977). Roughness has recently been investigated using both TLS and CRP in some works by Fardin et al. (2004) Haneberg (2007) and Poropat (2009). M Sturzenegger & D Stead (2009) suggested two methods, adapted from the ISRM (1978). The first consists in the fitting of an average plane on discontinuity. The derived error map, displaying the orthogonal distance between the real surface and the fitted plane can describe the roughness. In the second method numerous orientation measurement are achieved at different locations on the same discontinuity and then plotted on a stereonet.

The JRC can be used, joined with the Joint Compression Strength (JCS) to describe the shear strength behaviour of discontinuities (Barton & Choubey 1977).

− *Aperture*

The aperture is the perpendicular distance between adjacent rock walls of a discontinuity. The space between the walls can be air- or water-filled. The discontinuity aperture assumes a primary role from the hydrogeological point of view, influencing the rate of groundwater flowing within the fracture and thus controlling the secondary permeability of the rock mass. Dissolution, erosion, tensile stress can lead to an increasing in the aperture, while depth due to lithostatic load and normal stress can reduce it (Singhal & Gupta 2010). Usually callipers or gauges can be used to measure the mechanical aperture, then classified according to the size (Table 2). Asperities can affect the aperture size and its measurements.

Table 2. Classification of the discontinuity aperture following Barton (1973)

Aperture (mm)	Classification
< 0.10	Very tight
0.10 – 0.25	Tight
0.25 – 0.50	Partly open
0.50 – 2.50	Open
2.50 – 10.00	Moderately wide
> 10.00	Wide

− *Termination*

Barton & Choubey (1977)classified fractures into different categories: abutting, crossing and blind. (Davis et al. 1996) defined the termination as Y, X or T intersections. Fracture terminations influence their connectivity and hence the groundwater flow. Moreover the nature of termination can provide an idea of the rock-bridge amount (Priest 1993).

– *Block dimension and shape*

Block size and shape are related to the number of discontinuity sets and to their spacing, orientation and persistence. Block shape can be described using the Block Shape Characterization Method (BSCM) proposed by Kalenchuck et al. (2006). It relies on two parameters, α and β, representing the flatness and the elongation of a block (Figure 24).
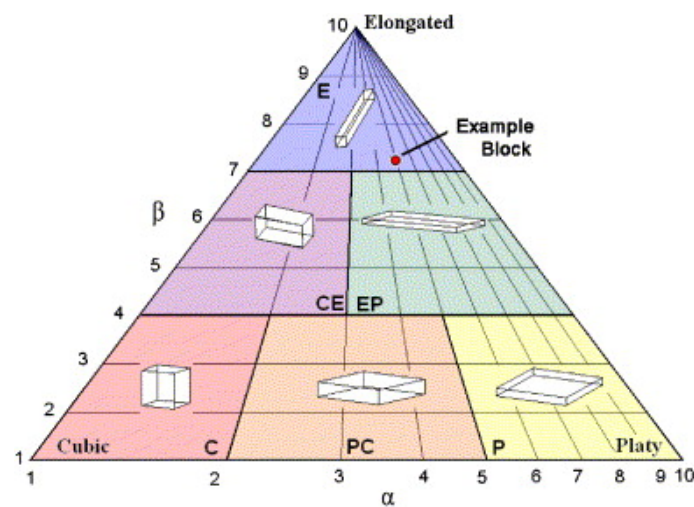
Figure 24. Block Shape Diagram (Kalenchuk et al. 2006)

Block size can be sometimes measured directly in the field or it can be calculated using mean spacing and orientation of discontinuities (Palmstrøm 1996). The size distribution is usually described trough cumulative graphs, borrowed from soil analysis (Kalenchuk et al. 2006). Sturzenegger et al. (2011a) used the DFN code Fracman (Golder Associates 2009a) to visualize in 3D the blocks defined by intersecting discontinuities. Shugar and Clague (2011) analysed the rock avalanche deposits on glaciers, measuring their dimensions using a digital photo-sieving method on large-scale orthophotographs with commercial GIS software.

- *Discrete Fracture Networks*

In the last years new approaches developed from the need to represent more realistically the discontinuities within the rock mass, including all the previously mentioned characteristics (Figure 25). Discrete Fracture Networks (DFN) are 3D stochastical model of fracture networks based on qualitative and quantitative data collected at a specific site location (Elmo 2006). The basis of conceptual DFN can

be found in Dershowitz & Einstein (1988), Staub et al. (2002), Jing (2003) and Dershowitz et al. (1998). An example of the DFN generation workflow is fully described in Elmo (2006). DFNs have been employed both in stability analyses (Grenon et al. 2014; Hamdi et al. 2014; Zhang et al. 2015) and in hydrogeology characterization (Selroos et al. 2002; Svensson 2001; Pan et al. 2010; Hartley & Joyce 2013; Antonellini et al. 2014). The quality of the DFN is strictly related to the quality of the field data and to their interpretation. In the last years it has been pointed out by several Authors (Cvetkovic & Frampton 2010; Francioni et al. 2014) that coupling these stochastic DFN model with the deterministic definition of the main structural features can lead to a more efficient approach for the discontinuities definition in numerical models.
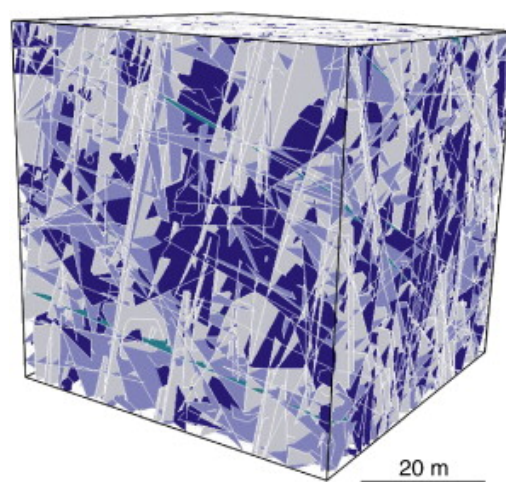

Figure 25. Example of Discrete fracture network (DFN) model generated using FracMan (Golder Associates 2009b) *based on the Mount Seymour remote sensing data* (Sturzenegger et al. 2011)*.*

2.3   **Discontinuity mapping techniques**

To date, different investigation methods are available to collect data about the discontinuities. The rock mass can be investigated directly on site, through scanline or observation windows, or terrestrial remote sensing techniques can be used to acquire the raw outcrop geometry, and then discontinuity characteristics can be determined examining the resulting point cloud or 3D model. Moreover some pieces of information can be derived from oriented boreholes.

2.3.1   Engineering geological survey

Traditionally, structural surveys are performed along scanlines or through observation windows, directly on the discontinuities. Suggested methodology are reported in ISRM (1978). Fracture planes or traces intersecting the scanline or within the window are measured. The discontinuity position, orientation, spacing, termination, aperture and frequency can be registered. Moreover the infilling material can be examined and some basic parameters, as the JRC and the JCS can be measured, to derive the strength properties of the discontinuities (Barton & Choubey 1977). A summary of the possible sampling bias, i.e.

censoring, truncation, length and f-bias, with proposed corrections is reported in Zhang and Einstein (1998; 2000).

2.3.2   Close Range Photogrammetry (CRP)

Analytical photogrammetry is based on the concepts of stereoscopic parallax and collinearity. The first is the observed displacement of an object caused by a change in the point of observation. Thanks to this we own the perception of depth. This principle is employed in photogrammetry by taking photographs of the same object from different points of observation. The principle of collinearity states that an object point, the perspective centre and an image point on the focal plane of the camera are aligned in a straight line (Wolf & Dewitt 2000). According to these principles the 3D position of an object can be measured from 2 overlapping images taken from different points of view (intersection; Atkinson 1996). Inversely, knowing the coordinates of at least 7 points on the images is possible to apply the resection process (Inus Technology 2012) and find the cameras position. The interior geometry of the camera during exposure must be known. Theory of photogrammetry can be found in Slama et al. (1980) and Atkinson (1996).

2.3.3   Terrestrial Laser Scanner (TLS)

A LASER (Light Amplification by Stimulated Emission of Radiation) emits a beam of highly collimated, directional, coherent and in-phase electromagnetic radiation. The sensor sends out this pulse, the signal is back scattered by ground surface or others objects and then recorded. It automatically collects 3D coordinates of an object surface in a systematic pattern, using laser light (Boehler & Marbs 2004). The result is a very dense 3D point cloud. According to the principle of the distance measurement system different categories can be individuated:

- systems based on the optical triangulation principle, in which the point is surveyed as the intersection of two lines. These tools are suitable for small or medium size objects, i.e. statues. The point cloud is very dense and accuracies down to some micrometres can be achieved;

- system based on the Time Of Flight (TOF) principle. The travel time required to the laser beam to reach the surface and come back is measured. Knowing its velocity, the distance can be calculated. These instruments allow the measurements of distances up to several hundred of meters;

- system based on the phase comparison method, in which the distance is calculated by using the phase difference between the transmitted and received laser waves. They are more accurate but suffer from a limited range.

Principles and fundamentals of Laser Scanning techniques can be found in Shan & Toth (2008). In the present work, systems based on the TOF method have been used. Using a ground-based device, usually the resolution ranges between centimetres and millimetres (Shan & Toth 2008), depending from the point spacing and from the laser beam width.

3D coordinates (X, Y, Z) plus the intensity information, e.g. the power of the backscattered component of the laser pulse, are registered for each acquired point. Moreover, coupling the instrument with a photocamera it is possible to obtain also the RGB values of the acquired point cloud. The resulting data have to be georeferenced, firstly aligning the scans together and then globally, i.e. using a set of Ground Control Points (GCP). The alignment procedure usually consists of a preliminary rough registration, using homologous points and in a subsequent refinement, obtained using the Iterative Closest Point (ICP) procedure (Besl & McKay 1992; Chen & Medioni 1991). Depending from the final purpose, registration can be required in an absolute or in a relative coordinate system (oriented with respect to North). Different approaches can be adopted, pros and cons are described in (Sturzenegger & Stead 2009) depending on the required accuracy, time, effort and cost constraints. For the global georeferentiation a GPS and/or a total station is required.

2.3.4   CRP and TLS for slope stability

Applications of CRP to slope stability analysis can be found in the field of rock mass characterisation (Sturzenegger & Stead 2009; Firpo et al. 2011; Curtaz et al. 2014) and in slope stability monitoring (Mora et al. 2003; Stumpf et al. 2014; Laribi et al. 2015). Potential of TLS techniques has been demonstrated by several Authors: Matasci et al. (2012), Prokop & Panholzer (2009) and the SafeLand deliverable 4.1 (2010) give a general overview of the different applications that both aerial and ground-based LiDAR techniques can have in the landslide investigations framework. In the field of slope stability analysis Sturzenegger & Stead (2012) combined terrestrial and airborne laser scanner for the structural characterization of large landslides; Matasci et al. (2012) performed a structural analysis on the West face of the Drus (Mont Blanc massif) while Brideau et al. (2011) used discontinuity data obtained from TLS surveys to assess the failure mechanism of the Chenalis lake landslide (BC, Canada).

Numerous software, developed in the last years, allow to use this data in a rock mechanics framework, especially for discontinuity automatic extraction, although this automatism should be used with care, comparing the obtained results with traditional surveys and an expert knowledge. Among them Jaboyedoff et al. (2007) create a software which displays the orientation of each vertex of the point cloud using an Intensity-Hue-Saturation coding in a stereographic projection; Kemeny & Post (2003) and Kemeny & Turner (2008) described a tool (Split-FX) for the automatic delineation of fracture surfaces in a point cloud and the determination of their orientation, area, and roughness; Umili et al. (2013) developed an automatic approach based on trace mapping and sampling on a DSM; Assali et al. (2014) proposed and tested a semi-automated 3D point cloud process for rock mass characterization.

Sturzenegger and Stead (2009) and Sturzenegger et al. (2011b) gave some important advices for rock mass characterization analysing the results of TLS and Close-Range terrestrial digital photogrammetry applications on rock outcrops. To date location, orientation, frequency, persistence, roughness of the discontinuities, plus block size and shape, can be extracted from photogrammetric models and TLS point clouds, even if some biases have to be accounted for.

The data gathered using the presented devices were widely used also for monitoring purposes. In fact, if traditional monitoring techniques are based on single-points measurements, the complete field of displacements can be obtained using TLS (Jaboyedoff et al. 2010). As an example, Oppikofer et al. (2009) monitored displacements of more than 70 cm/day, while Bitelli et al. (2004) and Teza et al. (2007), and Mueller & Loew (2009) computed volume differences using surface comparison for different acquisition epochs.

Moreover, from the 3D point cloud, it is possible to extract the geometry of the examined area, creating an accurate Digital Elevation Model (DEM) which can be used for numerical models. This is particularly useful when examining vertical or overhanging cliffs, which are not well described in classic topographical map or Airborne Laser Scanner-derived DEM.

Main advantages of remote sensing techniques, including both CRP and TLS, have been found in the gathering of real 3D information, in the relatively fast data acquisition, in the possibility to create a permanent record of the slope at a certain time and in the ability to survey large outcrops and inaccessible areas (Sturzenegger & D. Stead 2009; Jaboyedoff et al. 2010). The limitations of these techniques are manly related to the presence of occlusions, due to the acquisition geometry and to the time-consuming post-processing workflow.

2.4   **Materials and methods**

Traditional surveys, CRP and TLS were integrated to provide a description of the discontinuity affecting the San Leo rock mass. A comparison of the three techniques, in the rock mass characterization framework, was carried out on two selected areas. Moreover, applications regarding the construction of a 3D model of the slab and the 2014 landslide multi-temporal analysis are presented.

2.4.1   Engineering geological survey

Traditional geomechanical surveys were used to statistically define the discontinuity orientations and to assess the mechanical properties of each set. Furthermore, they were used to validate the TLS results. The survey were undertaken in the areas indicated in Figure 26.
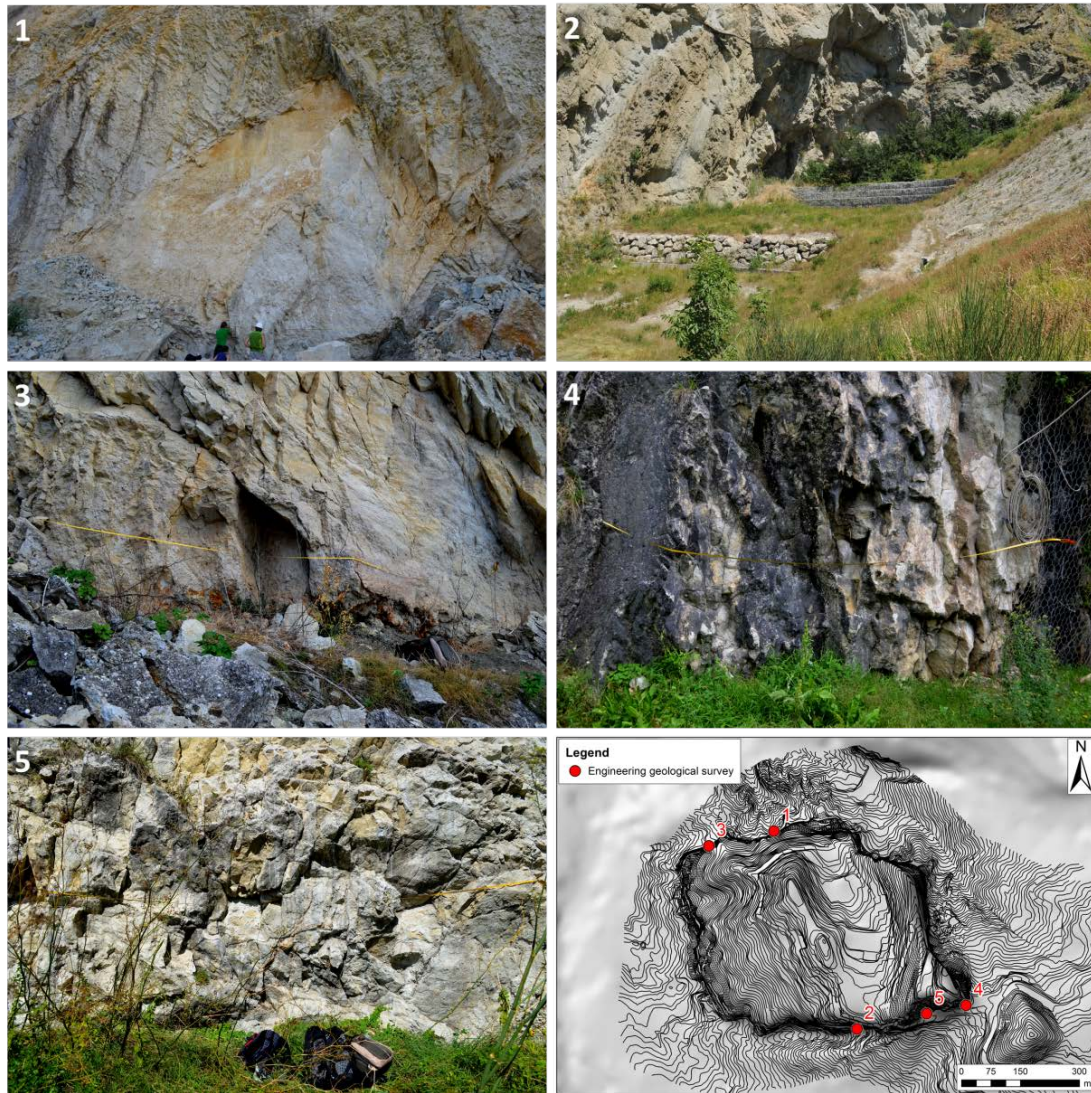
Figure 26. Views and locations of the areas surveyed along scanlines

According to the International Society for Rock Mechanics (ISRM 1978; ISRM 1985), several parameters such as orientation, spacing, roughness, aperture and infilling of the discontinuities were collected using scan-line methods,. The Joint Roughness Coefficient (JRC; Barton & Choubey 1977) and the Joint Compression Strength (JCS; Deere & Miller 1966) were also measured.

2.4.2   Close Range Photogrammetry

The photogrammetric survey was carried out in two selected areas (Figure 28). A Nikon D300 camera was used with Structure for Motion (SfM) technique. SfM is a recent photogrammetric approach derived from Computer Vision where the 3D model structure can be resolved from a series of overlapping images acquired from different points of view, without the strict requirements on the geometry followed in conventional photogrammetry (Westoby et al. 2012). The three-dimensional scene, camera positions and orientation are reconstructed automatically using a highly redundant, iterative bundle adjustment procedure, without necessarily disposing of ground control points (GCPs) with known 3D

coordinates. This technique does not require a-priori camera calibration parameters and the knowledge of the camera position, when results are provided in a local reference system.

The resulting 3D models are generated in a relative 'image-space' coordinate system, which must be aligned to a real world, 'object-space' coordinate system. The transformation of SfM image-space coordinates to an absolute coordinate system can be achieved using a small number of known GCPs with known object-space coordinates. Such GCPs can be derived identifying features clearly visible in both the resulting point clouds and in the field and obtaining their coordinates by ground survey (i.e., by GNSS) or from other georeferenced images/maps/models.

The general scheme followed in the image acquisition of the cliff, largely due to the logistic constraints, is shown in Figure 27. In the Northern cliff, three camera positions were chosen with a 10 m interspace and a distance of about 60 meters from the cliff. For the Southern area it was possible to place the camera less than 25 m far from the cliff and the distance between the positions was about 9.3 m.

For each position five acquisitions were made, with different angles between the line of sight of the camera and the perpendicular to the cliff (0°/-5°/-10°/+5°/+10°) in order to have the maximum redundancy of images. The commercial software Agisoft Photoscan Pro (Agisoft 2014) has been used. The 3D models were georeferenced using GNSS differential acquisition and with TLS point cloud as reference. The final root mean square total error referred to the point cloud georeferentiation was about 0.20 m. The Nord cliff point cloud is composed by about 4.6 millions of points, while the South cliff one consist of 3 million of points. The mean spacing between the points is around 6 cm.

The 3D models were exported as point clouds, the georeferentiation was refined applying the dedicated procedure in the CloudCompare (Girardeau-Montaut 2014) software.
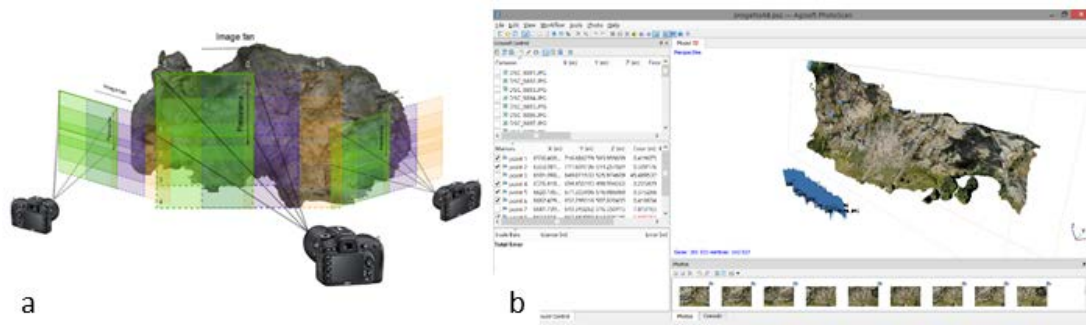
Figure 27. a) SfM survey configuration example; b) SfM software: camera positions, textured point cloud and GCPs, in a sector of the North cliff

2.4.3 Terrestrial Laser Scanner

TLS surveys were undertaken using a Riegl VZ400 system (Table 3) coupled with a calibrated digital camera. Due to the topography of the area, to the lack of intervisibility between survey positions and to the difficulties to access to certain areas, a careful planning of the survey was essential.

Table 3. Riegl VZ400 characteristics

Range	Precision	Accuracy	Measurement rate	Field of view

Up to 600 m (laser class 1)	3 mm	5 mm	122000 measurements/sec in High speed mode 42000 measurements/sec in Long range mode	Up to 100 x 360 degrees

A series of TLS scans were taken between 2008 and 2011 with a Riegl420i system under the STB Romagna guidance. The survey covered both the Northern and Eastern cliffs. The scanning of the remaining cliffs was completed in 2013 using a Riegl VZ400 system coupled with a calibrated digital camera (Figure 28).
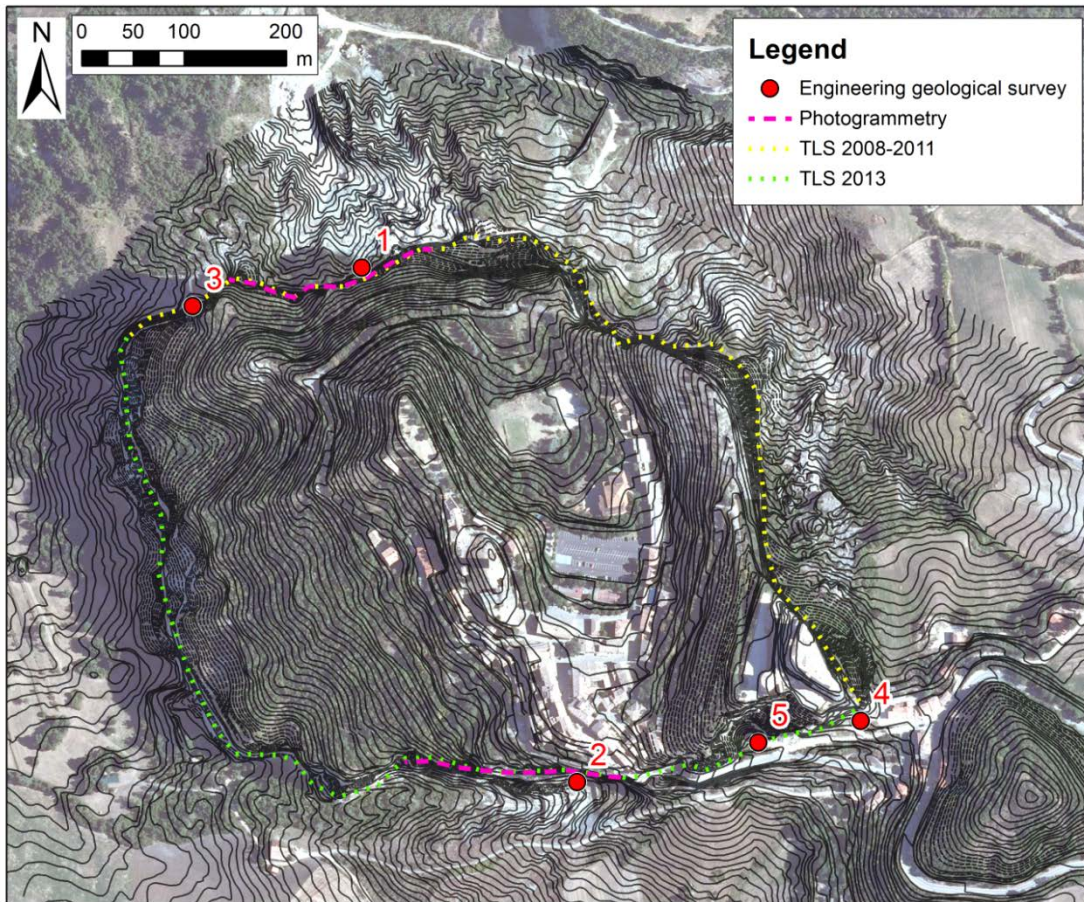
Figure 28. Localization of the engineering geological surveys

The South and West cliff were scanned from 14 positions around the slab (Figure 29), with a mean sampling step of about 20 mm on the rock surface (Figure 30). Due to the topography of the area to be surveyed, it was not always possible to perform a close-range survey, therefore the long-range mode was used. High-resolution images were also collected during the surveys with the calibrated digital camera and then used to texture the point clouds. A point cloud composed by about 900 millions of RGB coloured points was obtained (Figure 30a).

Figure 29. Localization of the TLS acquisition points

Clouds alignment and georeferentiation were performed using natural and artificial targets (purpose-built polystyrene spheres with 30 cm diameter or retro reflective target tape). The latters were surveyed through a three dimensional network measured by integrated topographical and GNSS techniques, to obtain the absolute ETRF2000 (2008.0 epoch) position of total station stand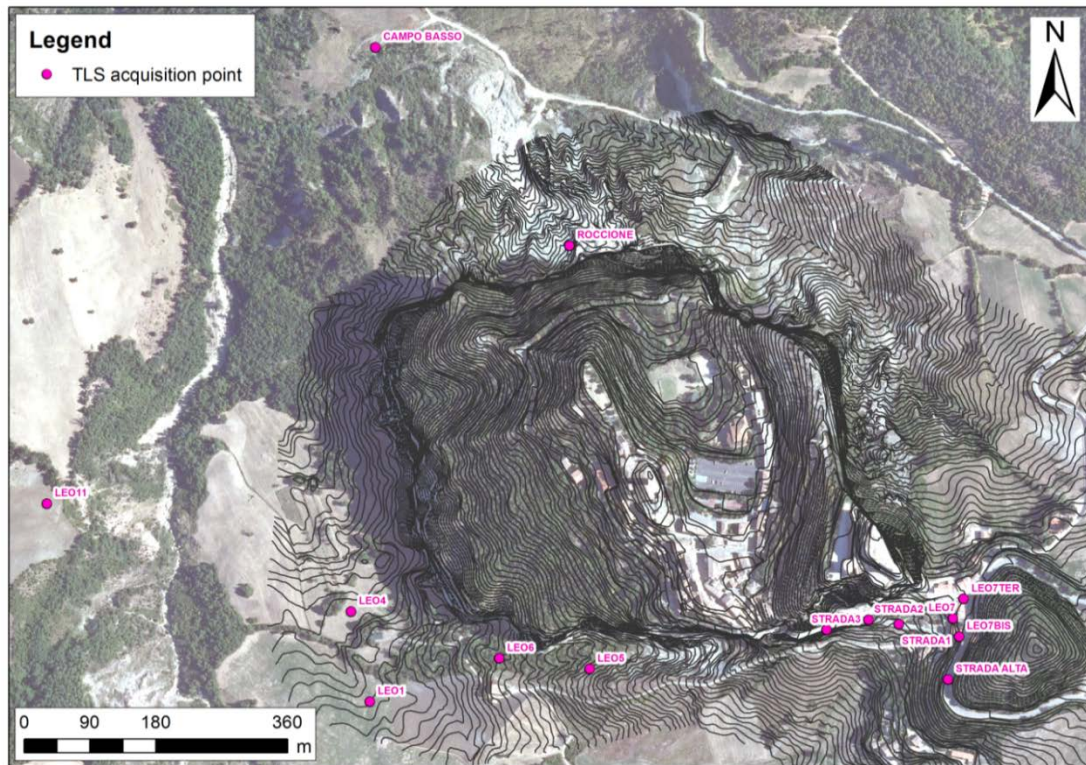points. In order to obtain the 3D position of the centre of the spheres in the WGS84 reference system a GNSS fast static survey was conducted. Therefore, after the scanning operation, each sphere was replaced with the GNSS antenna. Knowing the mutual difference in height between the centre of the sphere and the GPS antenna, it was possible to obtain the WGS84 coordinates of each sphere centre. In the global georeferentiation process, a GNSS station, situated on the street below the castle, was used as master station to frame the TLS survey to a global reference system. Its coordinates were derived using the permanent GNSS stations of Firenze, San Marino, Perugia and Medicina. The 3D geocentric positions were finally projected in the cartographic system UTM-WGS84 (zone 33); the ellipsoidal heights were converted in the orthometric ones by means of a model provided by Emilia-Romagna Region.

The scans of the 2013 surveys were joined with the ones derived from the previous surveys (2008-2011), permitting a complete model of the cliffs to be obtained. Due to the complexity of putting together point clouds of different surveys, it is difficult to attribute an overall quality index to the whole model; however, a centimetre accuracy can be considered.

After the 27th February 2014 landslide, the TLS survey was repeated in the area affected by the failure using the Riegl VZ400 equipment. In particular, this survey was conducted the 6th March 2014 from two scan positions, acquiring the detachment surface with a resolution of about 5 cm.

47

The point clouds registration was performed using tie points in the form of 6 polystyrene spheres. During the laser scanning survey, the spheres were sampled using very high density point cloud.

The 3D WGS84 positions were then projected in the cartographic system UTM-WGS84 (zone 33). After the GNSS and laser scanner data post processing, the overall accuracy of the point cloud is sub-centimetre in terms of relative positioning and at the centimetre level in terms of absolute orientation. The coloured point cloud (RGB information obtained from the calibrated digital camera set up on the laser scanner) comprises more than 53 million points oriented in the UTM-WGS84 cartographic system.
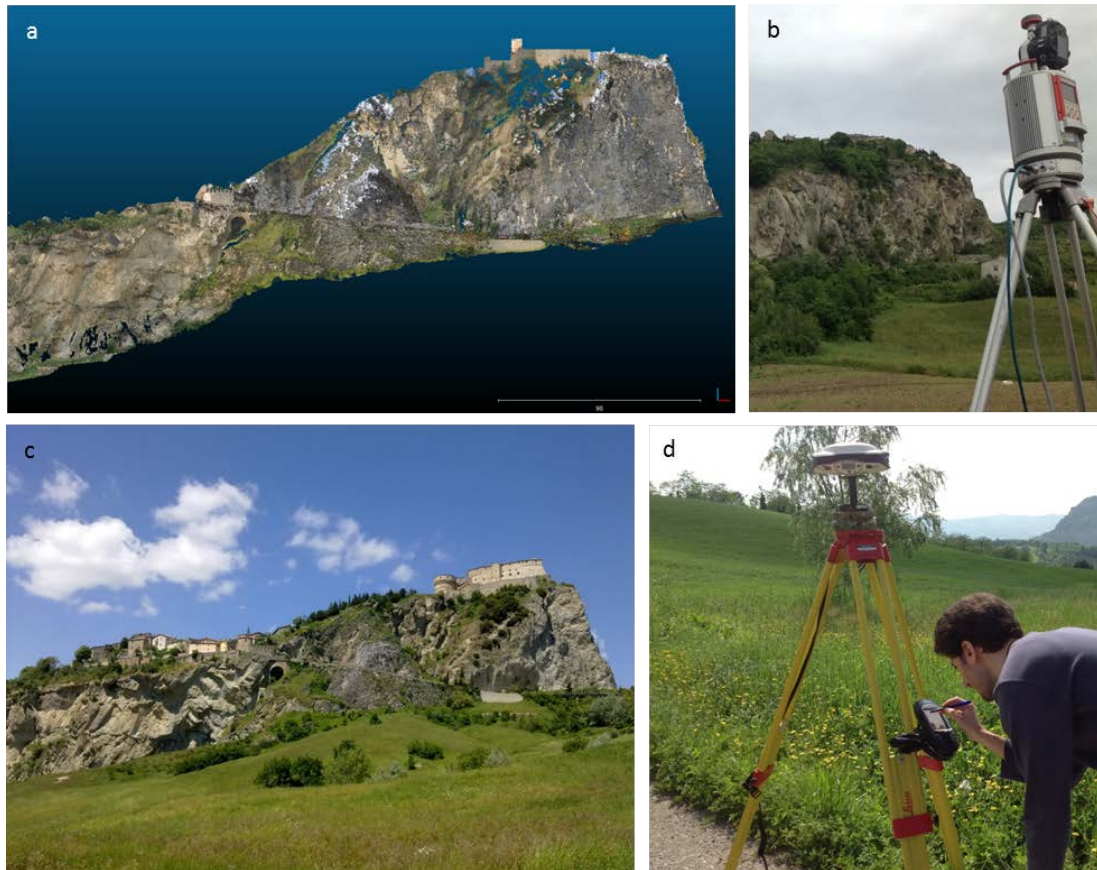
Figure 30. a) TLS point cloud of the South cliff; b) TLS survey; c) view of the South cliff; d) GPS acquisition

2.4.4   Discontinuity mapping

Due to the extensive area of the outcrop, the danger for the operators and the difficulties encountered accessing the majority of the slab perimeter, only small sectors at the base of the cliffs could be surveyed using traditional methods. The extraction of the main discontinuities was therefore performed directly on the 3D point clouds (both from TLS and Photogrammetry), using two different software programs, COLTOP 3D (Jaboyedoff et al. 2007) and Polyworks (Innovmetric Software 2014). The first displays the orientation of each vertex of the point cloud using an Intensity-Hue-Saturation coding in a stereographic projection; the result is a coloured shaded relief map combining both terrain slope angle and slope aspect (direction of slope) in a unique representation, which can assist in the characterization of potentially unstable slopes. In the Polyworks software, a manual method was used, fitting the recognized discontinuities both with planes and circles; the best-fit algorithm that performs a pure least-

squares approach on all selected element points was used. This planar regression method is shown to be effective in calculating the orientation of planes from selected points of a point-cloud (De Souza et al. 2013). Dip and dip direction were calculated from the plane's equation coefficients or from the direction cosines of the normals to the circles representing the discontinuities. When discontinuity window mapping was undertaken, the procedure suggested by Sturzenegger et al. (2011b) was followed: several circular windows with a radius equal to 20 m were selected for each part of the point cloud. Mauldon et al. (2001) noted that the use of circular windows can eliminate the sampling bias along mapped surfaces. The windows were located on exposures with different orientations, to reduce the orientation bias occurring in the third dimension. During the window mapping procedure fractures were assumed to be planar and circular. The survey results were validated by comparison with the results of the geomechanical surveys. Moreover, by averaging the diameters of the mapped discontinuities a Mean Trace Length (MTL) value was obtained for each joint set (Sturzenegger & D. Stead 2009). The joint persistence was estimated as the length of fracture traces per unit area of sampling surfaces (P_{21}, as defined in Dershowitz et al. 1998). Moreover, both the true mean trace length (μ) and the fracture intensity (I) were estimated following the method suggested by Mauldon et al. (2001) and modified by Sturzenegger et al. (2011b).

In particular, considering a circular window with radius r, the intensity I is given by:

$$I = \frac{n}{4r}$$

Where n is the number of joint intersection with the perimeter of the window.

Following the same procedure, the true mean trace length (μ) was calculated as:

$$\mu = \frac{\pi r}{2} \frac{n}{m}$$

Where m is the number of joint endpoints within the circular window. A summary of the methods applied to calculate the mean trace length and the intensity/P_{21} is given Figure 31.

The window size should be selected in order to respect the criteria suggested by Zhang and Einstein (1998): all the joints have not to be contained within the window and at the same time all the joints have not to be censored at both ends. Moreover, Rohrbaugh et al. (2002) suggested that, using the procedure illustrated by Mauldon et al. (2001), the windows should be larger than the mean block size and recommended to have a value of m (number of discontinuity ends within the selected window) greater than 30. Sturzenegger and Stead (2011a) suggested to use multiple windows of the same size at different locations.
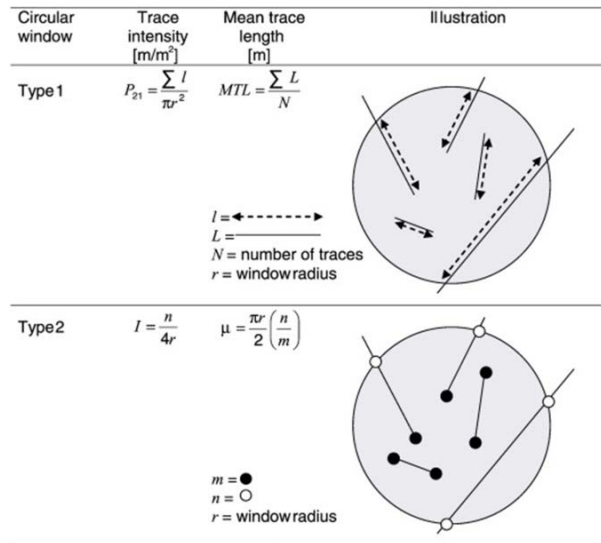
Figure 31. Different methods proposed for trace intensity and mean trace length estimation, modified from Sturzenegger et al. (2011a)

2.4.5 Comparison of TLS, CRP and engineering geological survey in the structural characterization framework

Structural surveys have been carried out by means of the three techniques in two selected areas of the cliff, in order to compare the geo-structural features extraction capabilities of all these techniques. The comparison among the raw data obtained from TLS and CRP, e.g. the point clouds precision, goes beyond the purposes of the present work. The mapped discontinuities were plotted on stereonets and grouped into sets, and the differences evaluation was made directly on the recognized joint sets. Moreover, sections extracted from the TLS and CRP point clouds were analysed.

2.4.6 3D model of the slab

The TLS scans acquired on all the sides of the slab permitted to reconstruct a full 3D model. The first alignment process was performed through the TLS software, Riscan Pro 2.0 (Riegl 2014), using the target point coordinates obtained by the auxiliary survey and applying a rototraslation to the scans.

The useless points, like vegetation, were removed from the clouds both manually and using the Full Wave Form technology, implemented in the Riegl VZ400 TLS. The data were exported to Rapidform XOR3 (Inus Technology 2012) software for the alignment refinement. The Iterative Closest Point (ICP) algorithm, which iteratively recomputes the transformation needed to minimize the distance between the points of two raw scans, was used. Then the scans of the 2013 surveys were joined with the ones of the previous survey, permitting to obtain a complete model of the cliffs.

2.4.7 Block size distribution

Block size dimensions were estimated by inspecting the TLS point cloud of the deposit area. The main purpose of the analysis was the evaluation of the effective mean spacing between discontinuities bordering the blocks. The procedures illustrated by Shugar and Clague (2011) for aerial photogrammetry

mapping was adapted to calculate the block dimensions from the TLS point cloud. For each block, the visible surfaces were fitted by rectangles. The length and width of the rectangles were subsequently measured. Often, it was not possible to measure all the block surfaces. Indeed, depending on the TLS position during data acquisition, some blocks were not visible in the TLS line of sight, while others were partially obscured by debris. For all the inspected blocks, at least one surface was measured (2 dimensions). Where possible, the third dimension was also collected. In the remaining cases, the third dimension was estimated as the average value of the other two. The volume and the average side length of the blocks were finally calculated.

2.4.8   Multi-temporal analysis

A comparison between multi-temporal TLS data has been demonstrated to be useful for monitoring slope displacements and deformation (Abellan et al. 2009), to delineate their extent, to estimate the involved volume (Kuhn & Prüfer 2014) and to provide a general description of the on-going processes (Pesci et al. 2007).

As stated before, two point clouds of the 2014 landslide area were available, before and after the event. First 2D change detection was performed by comparing sections extracted directly from the point clouds. With the aim to perform a 3D comparison and to delineate the landslide extent, a polygonal model was generated from the point clouds. The deviation of the pre-landslide surface from the post-landslide surface was measured along the North direction, almost perpendicular to the cliff face, using a specific tool available in the Polyworks IMsurvey module (Innovmetric Software 2014). The difference between the two surfaces was then calculated and projected onto the post-failure surface.

2.5   **Results**

2.5.1   Discontinuity mapping

The rock mass characterization was performed for each sector of the cliff. In the following sections the results of the engineering geological, photogrammetric and TLS surveys are subdivided by location, to permit a better comprehension of the structural features of the slab.

2.5.1.1   *North Cliff*

The North cliff was affected by the most recent relevant landslides, namely the one occurred in 2006 and the latter occurred in 2014. Results of the discontinuity mapping performed on this cliff were thus further subdivided, to individuate the discontinuities involved in the detachments. Moreover, in the Western area of this cliff a highly fractured zone can be detected, also observing the weathering due to water circulation on the rock surfaces (Figure 32), thus suggesting the presence of pre-existing open fractures.

Figure 32. *Highly fractured area in the Northern cliff. An higher degree of fracturing is indicated also by the presence of a higher amount of water circulation* (highlighted by darker secondary deposits)

2.5.1.1.1   2006 landslide area

− *Engineering Geological Survey*

Results of the field surveys, which are shown in Table 4 and Figure 33, were statistically grouped into 3 discontinuity sets plus several vertical discontinuities. All the sets showed similar values of JRC and JCS. It is noticeable that the joint set SL2 has a mean spacing almost 4 times greater than the SL1 and SL3.

Table 4. *Joint properties derived from engineering geological surveys 1. In the set name the first letter indicates the technique (Traditional survey), the second one the area (North).The set named TNV groups all the identified vertical discontinuities*

Joint set ID	Dip [°]	Dip direction [°]	Mean JRC	Mean JCS	Mean aperture [mm]	Infilling	Mean Spacing [m]
TN1	65	272	8.6	40.3	1.9	yes	0.5
TN3	75	025	9.0	38.3	0.01	no	1.9
TN4	67	067	10.0	39.7	0.6	yes	0.6
TNV	90	-	7	26.3	0.6	yes	1.25

− *CRP survey*

Mapping the point cloud resulting from the CRP survey, discontinuities belonging to six sets were individuated, the bedding plane was also measured. Results are showed in Table 5 and Figure 33.

Table 5. *Results of the discontinuity mapping on CRP point clouds in the 2006 landslide area. In the set name the first letter indicates the technique (close range Photogrammetry), the last one the area (North)*

ID Set – NORTH CLIFF	Dip	Dip direction

PN1	67°	227°
PN2	73°	295°
PN3	84°	11°
PN4	59°	38°
PN5	65°	104°
PN6 - bedding plane	26°	149°
PN7	83°	165°

– *TLS survey*

Using the TLS point clouds, in the area affected by the 2006 landslide, six main discontinuity sets were identified. The bedding attitude was detected. Dip and dip direction of these sets are reported in Table 6 and Figure 33.

Table 6. Results of the discontinuity mapping on TLS point clouds. In the set name the first letter indicates the technique (terrestrial Laser scanner), the last one the area (North)

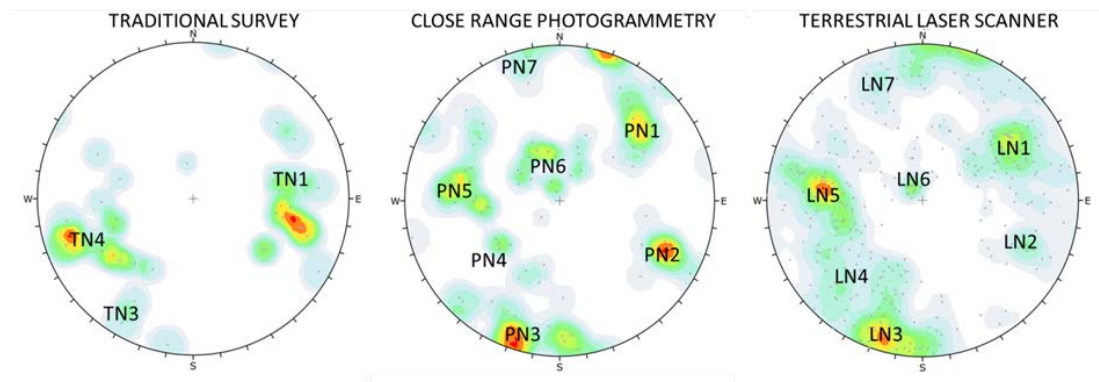| ID Set – NORTH CLIFF	Dip	Dip direction
LN1	62°	240°
LN2	72°	293°
LN3	83°	10°
LN4	63°	42°
LN5	64°	95°
LN6 - bedding plane	11°	144°
LN7	79°	160°

Figure 33. Discontinuities mapped in the 2006 landslide area with the different techniques

The subsets obtained by processing the TLS point clouds have been used together with the structural field surveys to perform kinematic analyses. The latter were carried out by using the Markland test procedure implemented in the Dips Software (Rocscience Inc. 2014a). The method allows to depict which mechanisms among sliding, toppling and wedging are driving the slope instability processes affecting the cliffs. More in detail, results were able to evidence the joint sets promoting the 2006 landslide in the Northern side of the slab (Figure 34). Discontinuities grouped in LN7 set could induce toppling phenomena as the poles cluster is included in the failure area. Set LN3 can both cause toppling

or sliding. This dual behaviour depends on the almost vertical orientation; anyway, most of the discontinuities belonging to this subset are potential sliding surfaces.
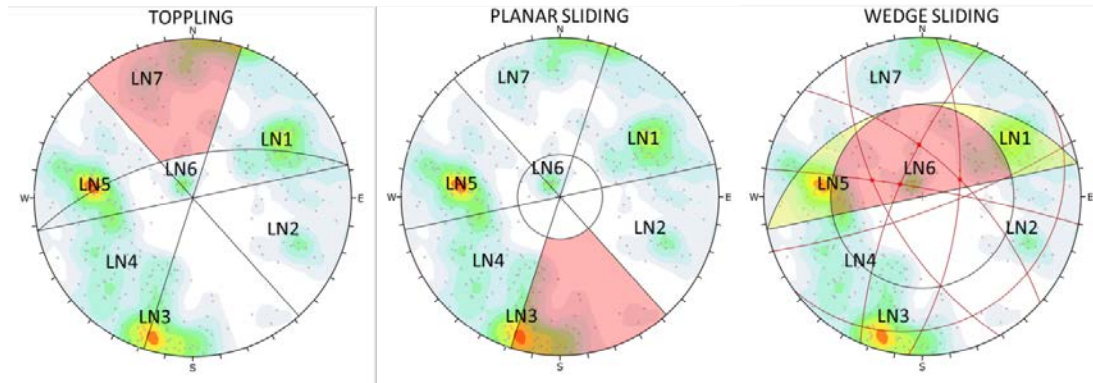

Figure 34. Kinematic analysis (area of the 2006 landslide)

Observing the point clouds, set LN5 and LN1 seem to behave as lateral release surfaces. Wedge sliding can occur due to the intersection of several subset, namely LN1, LN2, LN3 (subvertical), LN4 and LN5. To date, they allowed the development of several wedges at the base of 2006 failure cliff, which are recognizable at different scales (Figure 35). Examining the point cloud, it is clear that most of the existing wedges are formed by the intersection of two about 60° dip - subsets (LN5 and LN1) and the contemporary presence of the subvertical set LN3 which allows the releasing of the block.
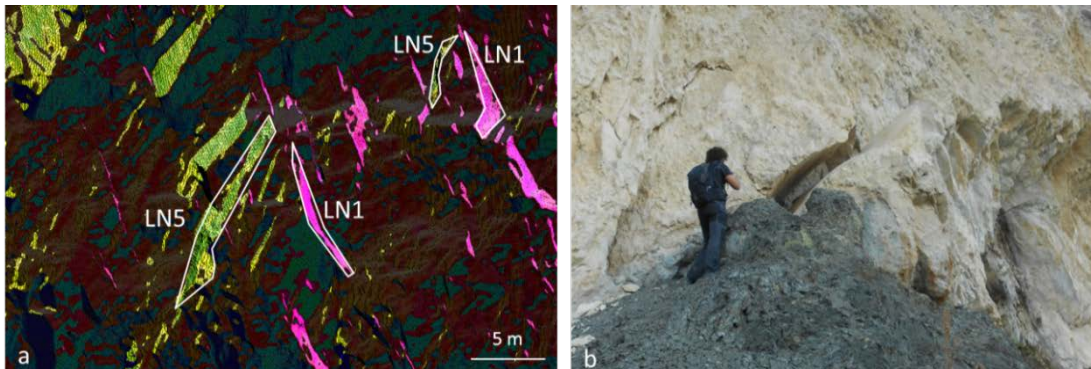

Figure 35. Examples of wedges: a) recognized in the point cloud using the Coltop software (Jaboyedoff et al. 2007) and b) in the field

2.5.1.1.2   2014 landslide

The results of the fracture mapping from TLS are shown in Table 9 and in Figure 38. The main joint sets are identified in addition to the bedding planes which have an average orientation of $25^o/230^o$.

The windows mapping technique was used, in particular three circular windows were chosen for each scan, i.e. pre- and post-landslide. Initially two different dimension for the windows radius was tested, namely 10 and 20 m. The 20m radius windows were chosen, as they respect the recommendations by Zhang and Einstein (2000), Rohrbaugh (2002) and Sturzenegger et al. (2011a). The discontinuity intensity, calculated as the length of fracture traces per unit area of sampling surfaces (P_{21}, as defined in

Dershowitz et al. 1998) and following the method suggested by Mauldon et al. (2001) and modified by Sturzenegger et al. (2011a) is showed in Table 7 and Figure 36.

Table 7. P21 and Intensity (I) calculated for the three main sets affecting the 2014 landslide area

	Pre-Landslide		**Post-Landslide**	
Joint set ID	Intensity (I)	P21	Intensity (I)	P21
LN1	0.14	0.10	0.11	0.14
LN3	0.14	0.08	0.07	0.09
LN4	0.08	0.11	0.09	0.11
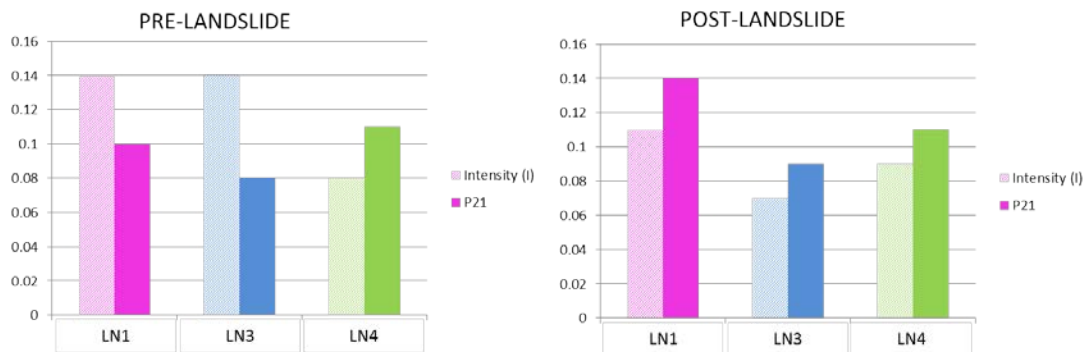
Figure 36. Histograms representing the P21 and the Intensity (I) calculated for the three main sets affecting the 2014 landslide area

The mapped trace length were reported in the frequency histograms in Figure 37. Trace length measurements seems to follow a lognormal distribution but, as showed in Sturzenegger et al. (2011a) it mainly depends from the truncation cut-off; in other words, it is not possible to map discontinuities smaller than a certain dimension due to the point cloud resolution. The recommended distribution is a negative exponential, which takes into account the cut-off bias (Sturzenegger et al. 2011).

Figure 37. Mean Trace Length (MTL) frequency histograms of the main joint sets individuated in the area of the 2014 landslide (LN1, LN2, LN3) pre- (le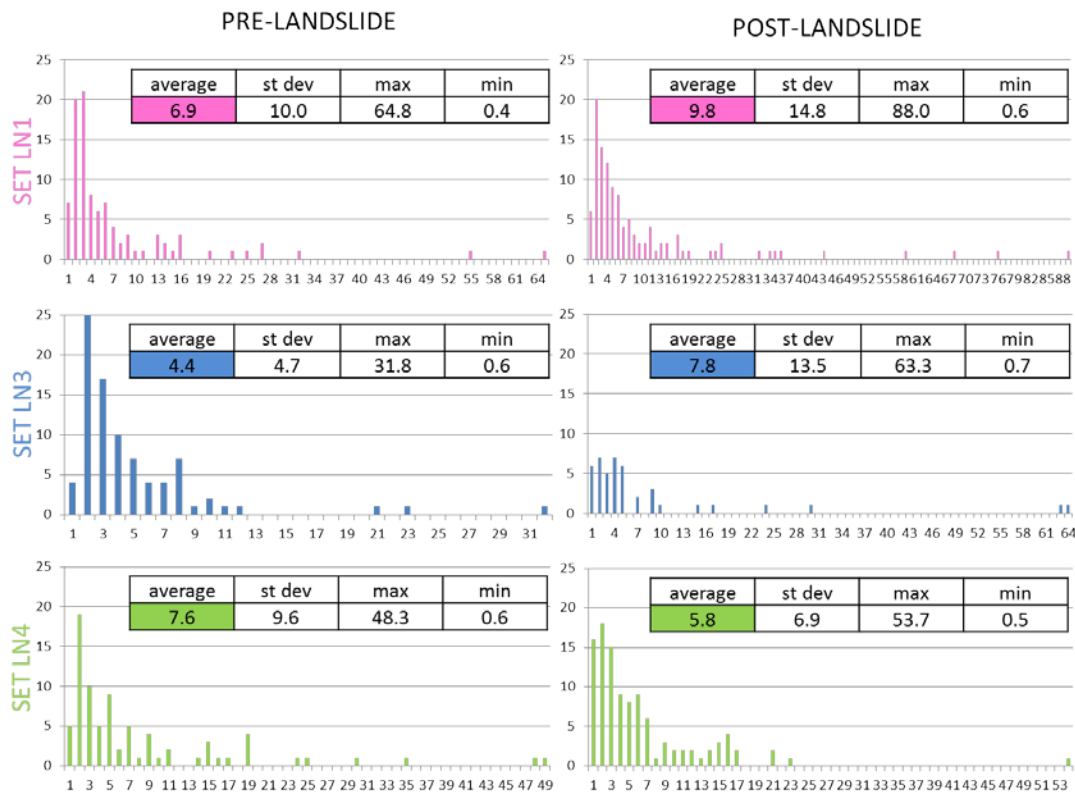ft column) and post-landslide (right column). Trace length (m) on the x-axis, frequency on the y-axis. All dimensions are in meters

The true mean trace length (μ), calculated also using the method proposed by (Mauldon et al. 2001) and modified by (Sturzenegger et al. 2011) is showed in Table 8.

Table 8. MTL calculated following the method illustrated in (Mauldon et al. 2001) and modified by (Sturzenegger et al. 2011)

Joint set ID	true mean trace length (μ) pre-landslide	true mean trace length (μ) post-landslide
LN1	7.4	4.9
LN3	6.2	5.9
LN4	4.2	4

The two adopted methods shows slightly different results, both for the mean trace length estimation and for the trace intensity. This can be due to the intrinsic uncertainty of the measurements and to the natural variability in the joint properties. Sturzenegger et al. (2011a) tested the same methodologies on outcrops, registering an average difference of 15% when planar windows were used and concluding that the estimated trace length derived with the method proposed by (Mauldon et al. 2001) should be critically evaluated, as it involve a statistical approach. Moreover, comparing the data before and after the landslide the P_{21} shows an increase in the joint intensity after the failure while a decrease appears in

56

the intensity *I* (Figure 36 and Table 9). The behaviour registered using the P_{21} seems to be more close to the field evidence.

Thus, taking into account the results of previous studies and trying to better interpret the field observations, P_{21} results obtained from the methodology defined in Dershowitz et al. (1998) and MTL were chosen to be representative of the rock mass behaviour. Data chosen and used for further analysis are reported in Table 9, together with the calculated joint sets orientation.

Discontinuity orientation was compared with the results of field survey mapping performed by a climber directly on the cliff face (Enser srl 2014), reported in Table 10.

Table 9. Joint properties derived from the TLS point clouds. P21 is defined in Dershowitz et al. (1998).
MTL refers to the joint Mean Trace Length

Joint set ID	Dip [°]	Dip direction [°]	P21 pre landslide	P21 post landslide	MTL pre landslide [m]	MTL post landslide [m]
LN1	79	239	0.10	0.14	6.9	9.8
LN2	84	023	0.08	0.09	4.4	7.8
LN3	59	043	0.11	0.11	7.6	5.8

Table 10. Results of field survey mapping performed by a climber directly on the cliff face (Enser srl 2014)

Joint set ID	Dip [°]	Dip direction [°]
Ks - bedding	25	230
K1	80	240
K2	75	225
K3	75	025
K4	55	060

For the kinematic slope stability analysis (Figure 38), two values of cliff orientation were used; one related to the lower part (Figure 38a, b, c) and the other to the upper part (Figure 38d, e, f) of the slope. The results, shown in Figure 38, indicate the possibility of planar sliding along the LN3 and LN2 in the upper part and along LN2 in the lower part. A toppling mechanism is indicated along LN1 in the upper part of the slope. The higher probability of wedge failure is indicated for the rock wedge involving joint set intersections between sets LN1 and LN2.
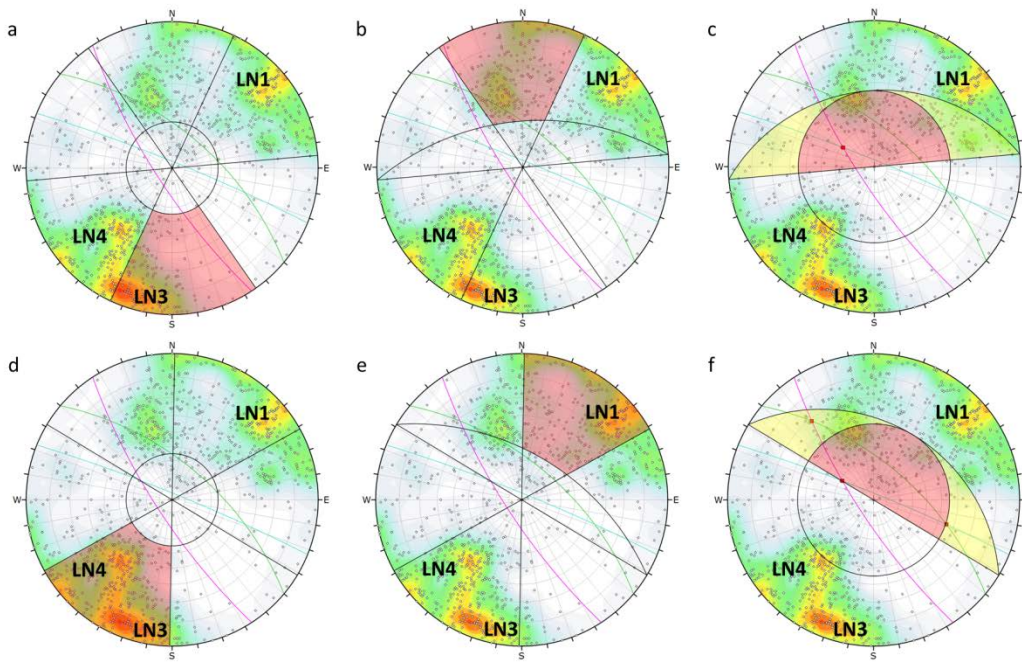
Figure 38. Kinematic analysis assuming the joint sets derived from the TLS point clouds: a) planar sliding on the lower part of the cliff, b) toppling on the lower part of the cliff, c) wedge sliding on the lower part of the cliff, d) planar sliding on the upper part of the cliff

It should be noted that a fourth set (around 165°/56°) is visible in Figure 38. The measurements related to this set were obtained mainly in the lower parts of the cliff, where the slope face has a similar dip direction. Due to this, the measurements associated with this discontinuity set were interpreted as part of the slope faces and not as discontinuities. Moreover, this set was not recognized during the engineering geological surveys. For these reasons it was decided not to consider it in the kinematic and numerical analyses.

2.5.1.1.3   North Western edge

Discontinuities affecting the North Western wedge were mapped by means of engineering geological surveys and TLS.

    ‒ *Engineering Geological Survey*

Results of the engineering geological survey are illustrated in Figure 39 (traditional survey 3) and reported in Table 11.

Table 11. Joint properties derived from engineering geological surveys 3. In the set name the first letter indicates the technique (Traditional survey), the second one the area (North)

Joint set ID	Dip [°]	Dip direction [°]	Mean JRC	Mean JCS	Mean aperture [mm]	Infilling	Mean Spacing [m]
TN1	66	257	13	23.5	4	yes/no	0.4
TN3	68	350	15	35	4.1	yes/no	0.8

TN4	59	081	13	12	1.5	yes	1.1

– *TLS Survey*

Results of the survey are reported in Figure 39 (window N4 and N5). Mapping windows with a 15 m radius were used in the structural analyses. Windows N1, N2 and N3 refers to the 2006 landslide area and are reported for comparison, together with the stereographic projection summarizing the orientation of all the discontinuities mapped on the North cliff on the TLS point cloud. The orientation of the 6 main joint sets derived from the TLS survey are reported in Table 12. A view of the North cliff with a superimposed Coltop (Jaboyedoff et al. 2007) visualization is reported in Figure 40: the orientation of each vertex of the point cloud is represented using an Intensity-Hue-Saturation coding in a stereographic projection. The black dotted circles represent the circular windows adopted in the discontinuity mapping procedure.

Table 12. Results of the discontinuity mapping on TLS point clouds. In the set name the first letter indicates the technique (terrestrial Laser scanner), the last one the area (North)

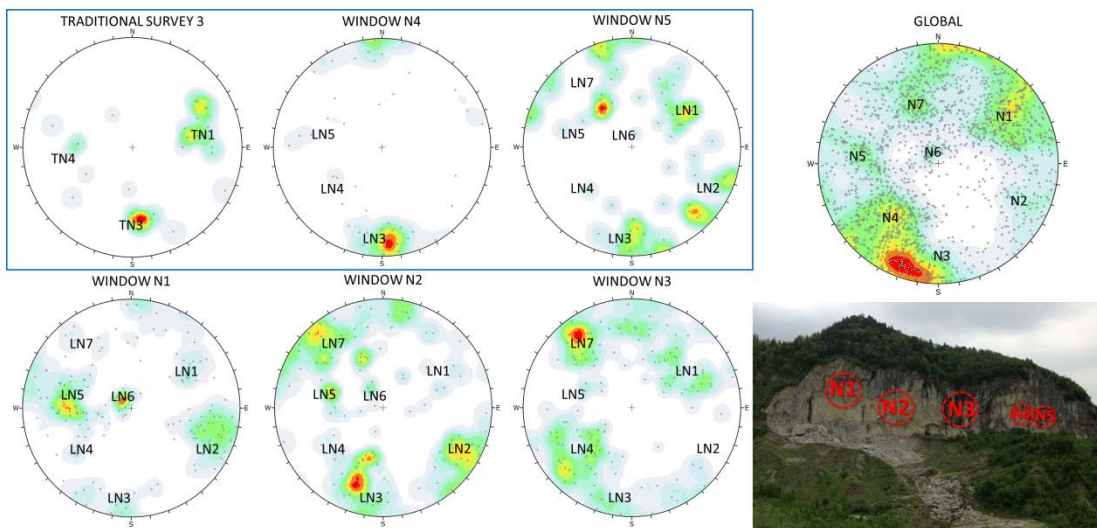| ID Set – NORTH WESTERN EDGE	Dip	Dip direction
LN1	56°	230°
LN2	82°	303°
LN3	83°	357°
LN4	55°	46°
LN5	72°	98°
LN7	51°	137°

Figure 39. Discontinuities mapped in the North-Western edge (blue rectangle) by means of traditional survey and TLS (window mapping) and location of the employed circular windows. Windows N1, N2 and N3 refers to the 2006 landslide area and are reported for comparison
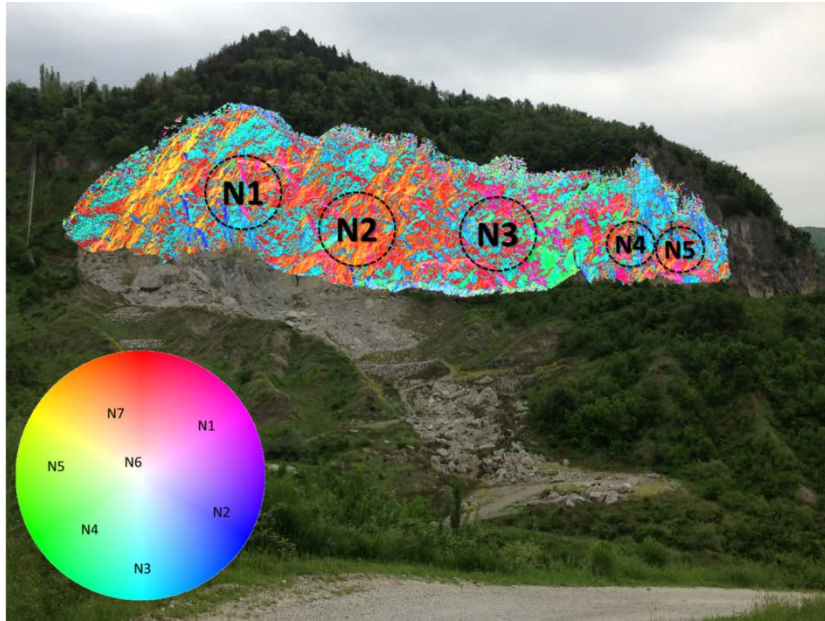
Figure 40.View of the North cliff with a superimposed Coltop visualization: the orientation of each vertex of the point cloud is represented using an Intensity-Hue-Saturation coding in a stereographic projection. The black dotted circles represent the circular windows adopted in the discontinuity mapping procedure

2.5.1.2   East Cliff

The East cliff was analysed only by means of TLS, due to its inaccessibility. Several circular mapping windows, with a radius equal to 20m were used (Figure 42). The circular window 4 was chosen to have a radius of 15m, due to its position, which do not permit a larger dimension without the inclusion of vegetation or soil. In Figure 41, the coloured 3D map of the Eastern cliff, obtained thank to the software COLTOP (Jaboyedoff et al. 2007), was superimposed to a photograph of the same cliff. The mapped discontinuity sets are reported on the Intensity-Hue-Saturation coded stereographic projection.
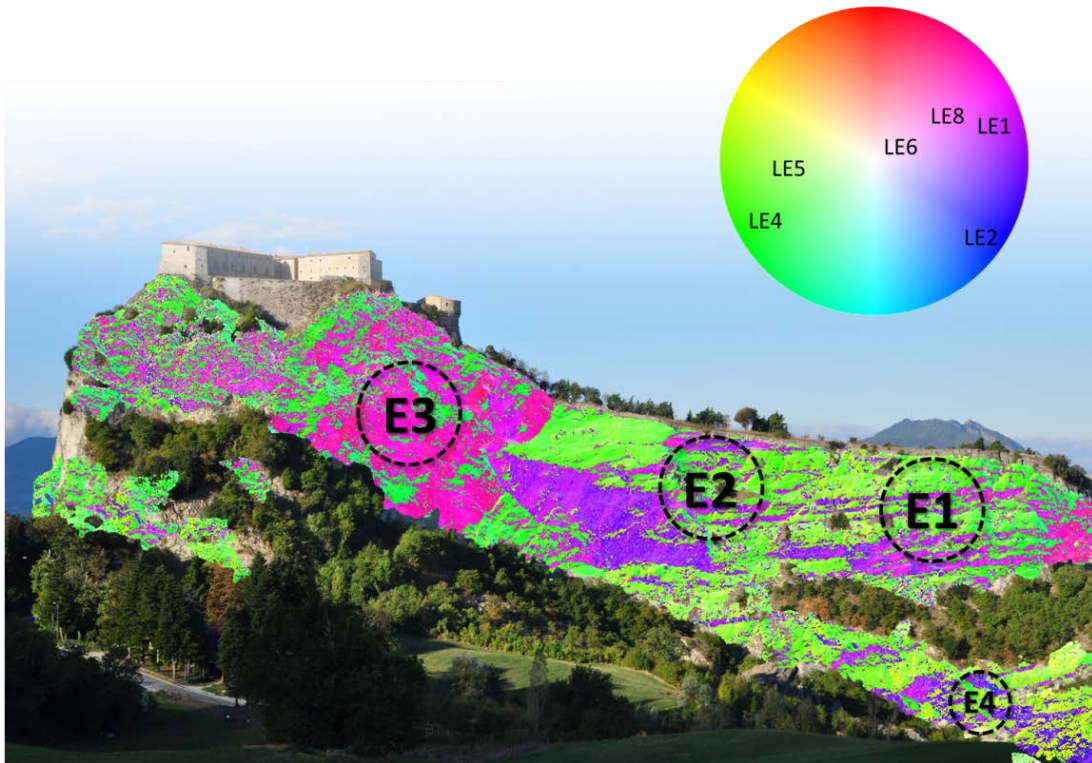
Figure 41. View of the East cliff with a superimposed Coltop (Jaboyedoff et al. 2007) visualization: the orientation of each vertex of the point cloud is represented using an Intensity-Hue-Saturation coding in a stereographic projection. The black dotted circles represent the circular windows adopted in the discontinuity mapping procedure

Four main joint sets plus the bedding plane (LE8) and the foreset planes (LE6) were recognized (Figure 42 and Table 13). Due to the slightly different orientation of the cliff face, different sets appears to be more visible in an area rather in the other one. The use of several windows permitted to reduce the orientation bias.

Table 13. Results of the discontinuity mapping on TLS point clouds. In the set name the first letter indicates the technique (terrestrial Laser scanner), the last one the area (East)

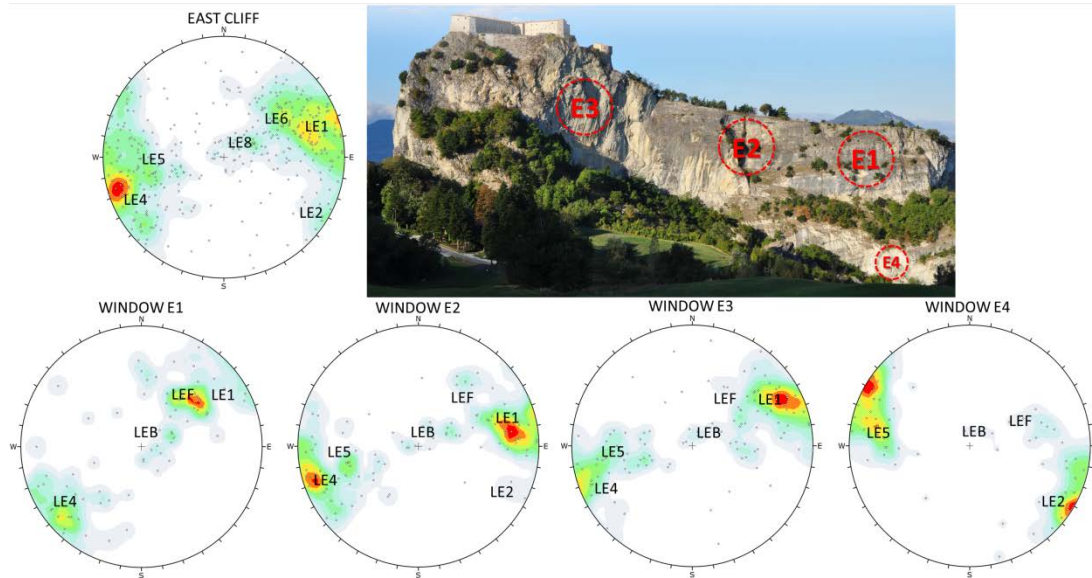| ID Set – NORTH CLIFF	Dip	Dip direction
LE1	68°	246°
LE2	88°	298°
LE4	75°	63°
LE5	73°	82°
LE6 - bedding plane	18°	241°
LE8 – foreset plane	60°	235°

Figure 42. Discontinuities mapped in the East cliff and location of the employed circular windows

2.5.1.3   West Cliff

The Southern part of the West cliff has a lower fracturing degree. Discontinuities are widespread and only the bedding plane is clearly recognizable. The Northern part is more fractured and shows a discontinuity orientation similar to the ones mapped in the Western area of the North cliff (windows N5). Results of the TLS fracture mapping are reported in Table 14 and Figure 43. The two areas seem to be divided by a structural lineaments, i.e. a fault.

Table 14. Results of the discontinuity mapping on TLS point clouds. In the set name the first letter indicates the technique (terrestrial Laser scanner), the last one the area (West)

ID Set – NORTH WESTERN EDGE	Dip	Dip direction
LW1	67°	243°
LW2	76°	294°
LW3	68°	357°
LW4	58°	47°
LW5	62°	103°
LW6- bedding	38°	237°
LW7	83°	151°
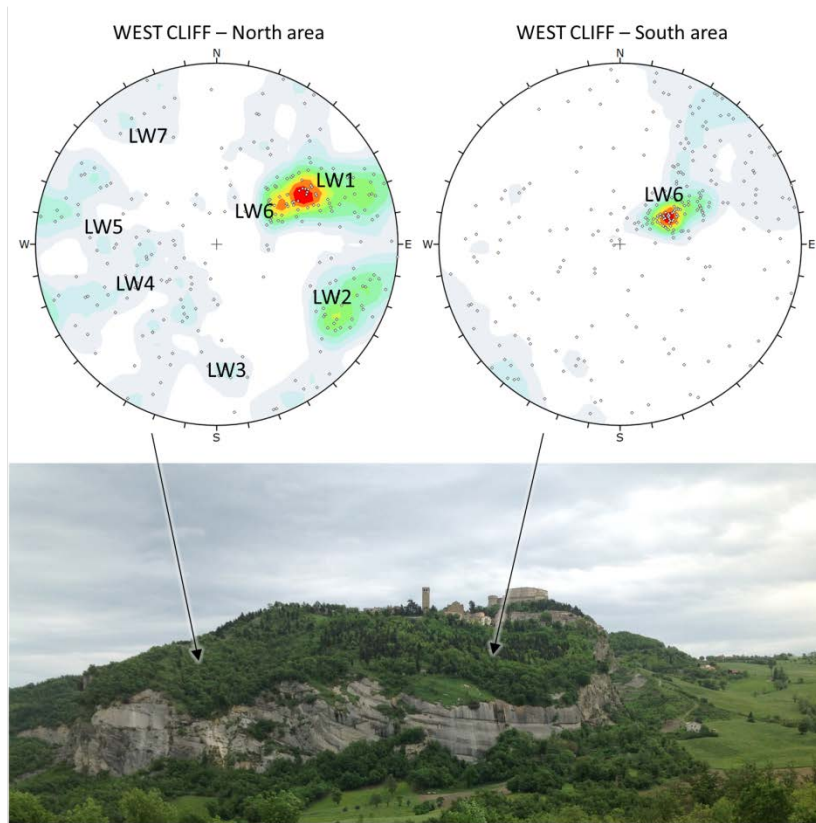
Figure 43. Discontinuities mapped in the Western cliff, by means TLS

2.5.1.4   South Cliff

The Southern cliff is affected by two highly fractured areas, indicating the presence of faults or others structural lineaments. The first is located in the Eastern section of the cliff, involving the cliff below the San Leo castle, while the second is situated towards West (Figure 44). These areas were considered separately.

Figure 44. Highly fractured areas on the South cliff

− *Engineering Geological Survey*

63

Results of the field surveys, which are shown in Table 15 and Figure 45, were statistically grouped into 3 discontinuity sets plus several vertical discontinuities. All the sets showed similar values of JRC and JCS.

Table 15. Joint properties derived from engineering geological surveys 2. In the set name the first letter indicates the technique (Traditional survey), the second one the area (South).The set named TSV groups all the identified vertical discontinuities

Joint set ID	Dip [°]	Dip direction [°]	Mean JRC	Mean JCS	Mean aperture [mm]	Infilling	Mean Spacing [m]
TS2	62	234	15	24.5	0.01	no	2.3
TS6	53	334	10	23.2	0.01	no	2.3
TS5	48	48	11	37.4	0.01	yes	1.4
TSV	90	100	13	33.7	0.36	no	0.5

− *CRP survey*

Mapping the point cloud resulting from the CRP survey, discontinuities belonging to six sets were individuated, the bedding plane was also measured. Results are showed in Table 16.

Table 16. Results of the discontinuity mapping on CRP point clouds in the South cliff. In the set name the first letter indicates the technique (close range Photogrammetry), the last one the area (South)

ID Set – SOUTH CLIFF	Dip	Dip direction
PS1	85	177
PS2	82°	214°
PS3	73°	236°
PS4 - bedding plane	10°	25°
PS5	55°	31°
PS6	66°	320°

− *TLS survey*

Using the TLS point clouds, in the Northern area six main discontinuity sets were identified. The bedding attitude was detected. Dip and dip direction of these sets are reported in Table 17.

Table 17. Results of the discontinuity mapping on TLS point clouds. In the set name the first letter indicates the technique (terrestrial Laser scanner), the last one the area (South).

ID Set – SOUTH CLIFF	Dip	Dip direction
LS1	74°	179°
LS2	76°	219°
LS3	64°	256°
LS4- bedding plane	25°	25°
LS5	56°	43°
LS6	65°	298°

Stereonets representing the discontinuities mapped using the different techniques are reported in Figure 45.
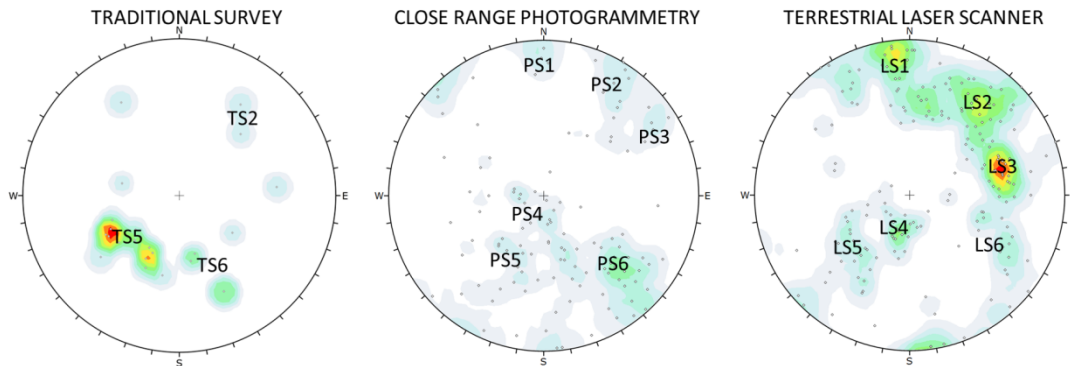

Figure 45. Comparison between traditional survey, CRP and TLS in fracture mapping, for the South cliff.

2.5.1.4.1 South Eastern edge

The fracturing degree in this area is higher, due to the presence of a EW fault. Data collected in the proximity of this fault were thus considered separately.

Two traditional field surveys were conducted. Results are reported in Table 18 and Table 19 and illustrated in Figure 46. Even if the discontinuities in this area appear even more scattered than in the rest of the slab, they were grouped in 6 sets.

Table 18. Joint properties derived from engineering geological surveys 4. In the set name the first letter indicates the technique (Traditional survey), the second one the area (South)

Joint set ID	Dip [°]	Dip direction [°]	Mean JRC	Mean JCS	Mean aperture [mm]	Infilling	Mean Spacing [m]
TS1/5	78	171	9	38	1.3	yes/no	1.7
TS2/6	78	212	12	35	2.5	no	1.3
TS3/1	71	257	13	46	3.4	yes/no	0.34
TS5/3	69	21	7	37	1.5	yes/no	0.6
TS6/2	45	324	10	47	2.2	yes/no	0.4
TS7/4	64	93	6	52.5	0.6	yes/no	0.4

Table 19. Joint properties derived from engineering geological surveys 4. In the set name the first letter indicates the technique (Traditional survey), the second one the area (South)

Joint set ID	Dip [°]	Dip direction [°]	Mean JRC	Mean JCS	Mean aperture [mm]	Infilling	Mean Spacing [m]
TS1/1	74	168	4	50	1.8	yes/no	0.9
TS2/2	80	221	16	35	1.3	yes/no	1.2
TS3/3	71	272	-	31	0.9	yes/no	0.5

TS5/5	73	46	14	38	0.6	yes/no	0.3
TS6/4	60	323	16	25	1	yes/no	0.5
TS7/6	80	116	14	41	0.9	yes/no	0.5

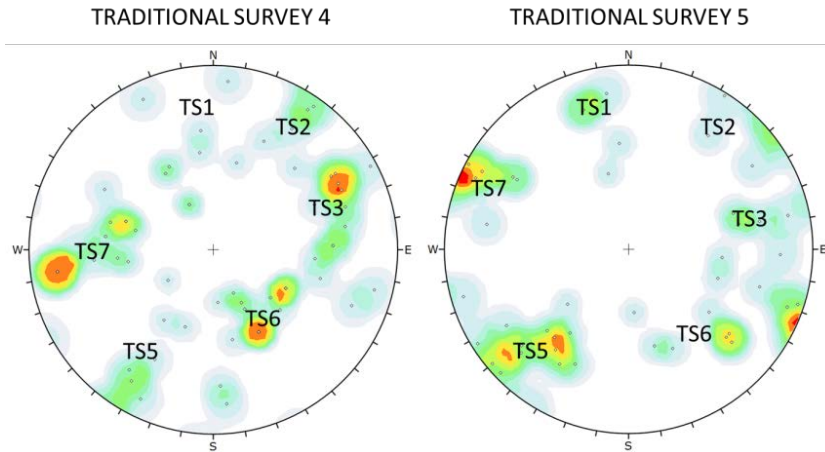TRADITIONAL SURVEY 4   TRADITIONAL SURVEY 5

Figure 46. Discontinuities mapped in the South-Eastern edge by means of traditional survey.

The results were compared with previous ones from surveys taken by others Authors approximately in the same area (D'Ambra et al. 2004; Enser srl 2006). In particular, in Figure 47 are reported the discontinuities mapped at the top and at the base of the cliff.
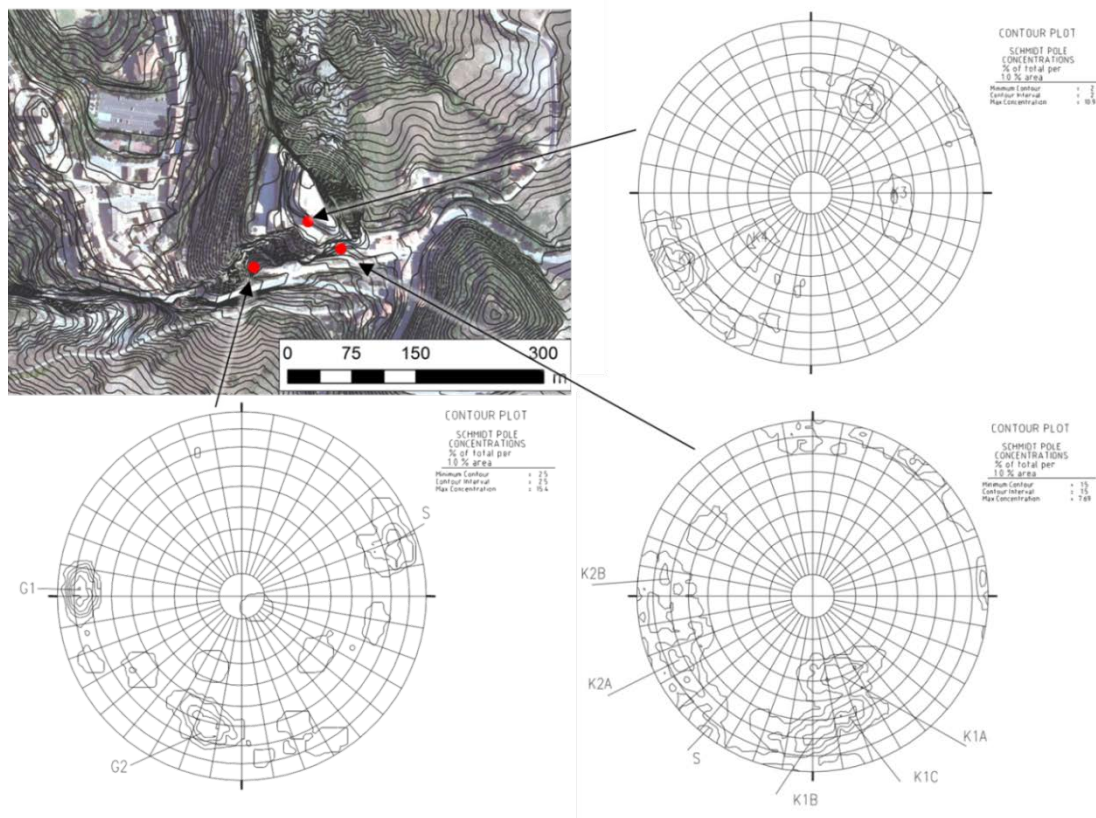

Figure 47. Previous surveys taken by others authors in the South-Eastern edge of the slab with their locations (red points) modified from D'Ambra et al. (2004) and Enser (2006).

2.5.1.4.2   South cliff – Western highly fractured area

This area (Figure 48) was investigated by means of TLS. Discontinuities orientation appears quite scattered (Figure 49), five sets were recognized (Table 20).
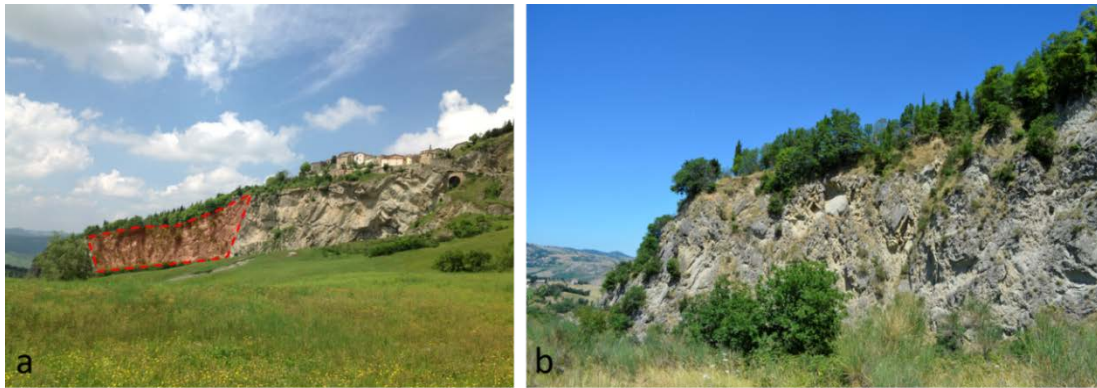

Figure 48. a) South cliff, the red shaded area indicates the more fractured Western part of the cliff, b) particular of the South-Western cliff

Table 20. Results of the discontinuity mapping on TLS point clouds. In the set name the first letter indicates the technique (terrestrial Laser scanner), the last one the area (South cliff – Western area).

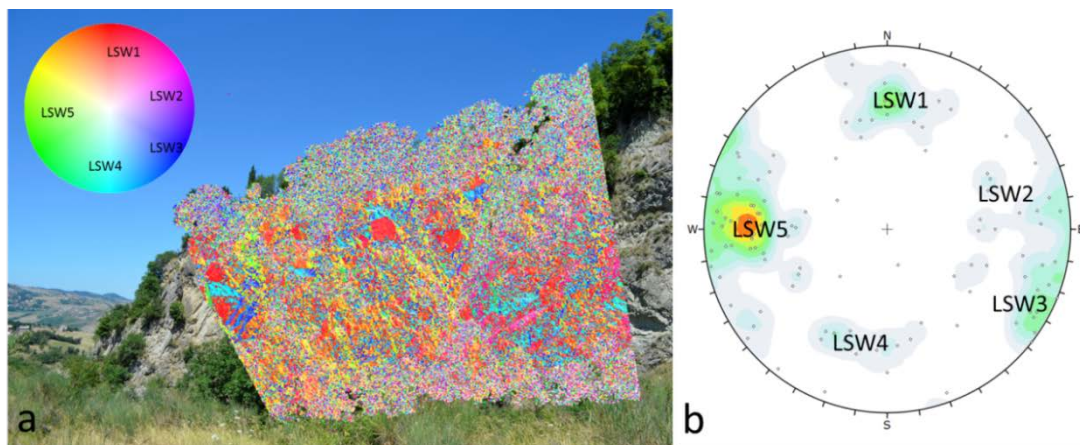| ID Set – SOUTH WEST AREA	Dip	Dip direction
LSW1	68°	182°
LSW 2	70°	256°
LSW 3	77°	295°
LSW 4	65°	10°
LSW 5	76°	90°

Figure 49. a) View of the South-Western highly fractured area with a superimposed Coltop [36] visualization: the orientation of each vertex of the point cloud is represented using an Intensity-Hue-Saturation coding in a stereographic projection and b) Discontinuities mapped in the same area by means of TLS

2.5.2   Comparison of TLS, CRP and engineering geological survey in the structural characterization framework

The three methods, namely TLS, CRP and engineering geological survey were applied together in two areas: North cliff – area of the 2006 landslide and South cliff. The obtained joint sets were compared to assess advantages and limitations of the different survey techniques. Firstly, it is clear how certain characteristics can be obtained only from some survey techniques, e.g. the JCS can be measured only through traditional surveys, while the 3D model of the cliffs can be made available only using the remote sensing techniques.

Regarding the orientation of the discontinuities, some of the sets are recognized with all the techniques (sets 2, 5 and 6 for the South cliff; sets 1, 4, and 3 for the North cliff, Fig. 6), and not all of them were detected using the traditional technique.

This is probably due to the reduced extension of the area which can be investigated with traditional scanlines. As an example, the bedding plane was not identified by traditional surveys, probably because it is clearly visible only in inaccessible areas, at the top of the cliff. Instead, the traditional survey can be more effective in recognizing the fractures in which the plane is not clearly visible from the remote sensing surveys, e.g. when the fractures appear as traces and don't have an adequate relief (Sturzenegger and Stead, 2009a) or the visible plane is too small compared to the point spacing of the cloud. Results from the TLS and CRP are similar. A comparison between sections extracted from the two point clouds is presented in Figure 50. The TLS section (in red) is rougher, well describing the real asperity of the rock cliff, while the one from the photogrammetry (in blue) is smoother, approximating the real cliff face. The accuracy of two methods is pretty different due to methodology, in particular in the edge zones SfM method tends to smooth the landforms, mainly because of the interpolation process. The result is a less accurate surface if compared to the one produced by the TLS.
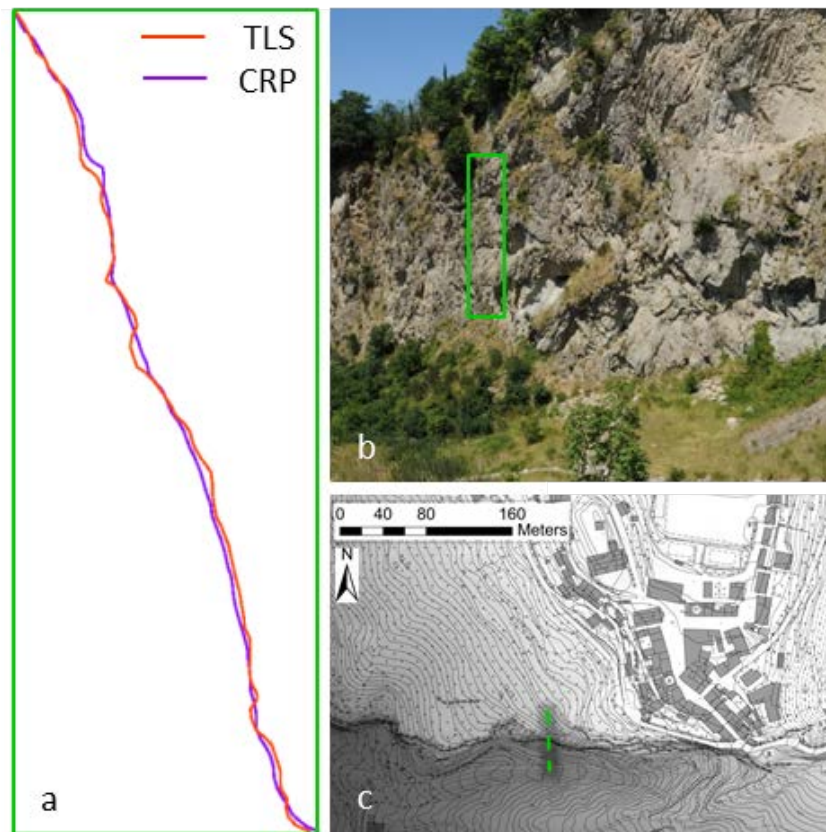
*Figure 50. a)Example of sections extracted from the CRP (purple) and TLS (red) point clouds; b,c)
photograph and DTM of the area with the section localization*

2.5.3   3D model of the slab

Using the above-illustrated procedures, the 3D model of the San Leo slab was obtained. An attempt to attribute an overall quality index to the whole model was made, although it was not straightforward, due to the complexity of the process and to the extension of the surveyed geometry. For the area acquired between 2013 and 2014 (South and West cliffs) a maximum error in the order of some centimeters can be considered. In the previous survey (North and East cliffs) the error could be higher, due to the instrumentation characteristics and the additional operations needed to import the scans originally acquired in the Gauss Boaga reference system into the WGS84 reference system. The whole model is composed of 618,084,619 points. The obtained point cloud was subdivided in subsets, depending on the cliff orientation, to allow a more convenient use (Figure 51). The 3D model of the cliff allows to perform direct measurements, to extract sections and prospects, making the rock slope analysis easier.
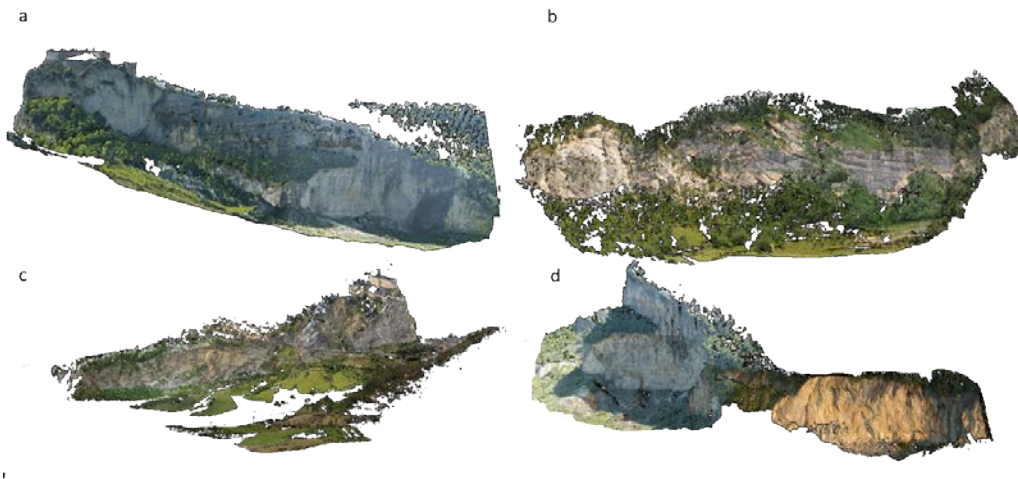
Figure 51. Views of the TLS point cloud of the rock slab: a) East cliff; b) West cliff; c) South cliff; d) North cliff

2.5.4   Block size distribution

The digitization of the blocks in the 2014 landslide deposit area allowed an evaluation of the block size distribution. More than 300 blocks were mapped, corresponding to almost the 37% of the estimated deposit volume. The majority of larger blocks have been broken only on impact with the ground (Figure 52).

Figure 52. Blocks in the deposit area, which appear to have been broken on impact with the ground

A block volume distribution diagram was used to summarize the results (Figure 53). The graph in Figure 54 is related to the measured length of the block sides. An average length was calculated from the three measures extracted for each block. From this analysis, 48% of the blocks have an average side longer than 4 m and the 33% longer than 5 m. In the neighboring areas a mean spacing of about 0.5, 1.9 and 0.6 m was recognized, respectively for the joint sets TN1, TN3 and TN4 (Table 4). Considering the possible rock fragmentation of the blocks during the free fall phase, a minimum joint spacing to be inserted in the numerical model was assumed to be equal to 5 m for the discontinuities belonging to the

set TN1 and TN3. The joint set TN2 shows, in the geomechanical field-surveys results, an average spacing greater than the SL1 and SL3. To maintain the same proportion (about 4x) a spacing of 20 m was assumed for the joints belonging to this set. This is in accordance with the geomechanical survey conducted on the top of the slab after the 2014 event, which showed a mean spacing of 20-22 m between the discontinuities belonging to the N3 set (Enser 2014).
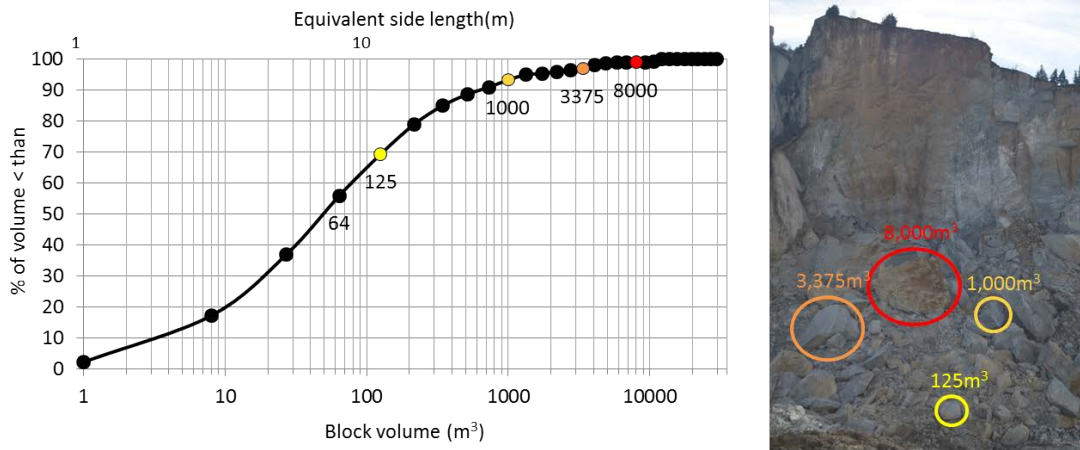
Figure 53. Block size distribution with examples of the block dimensions in the deposit area
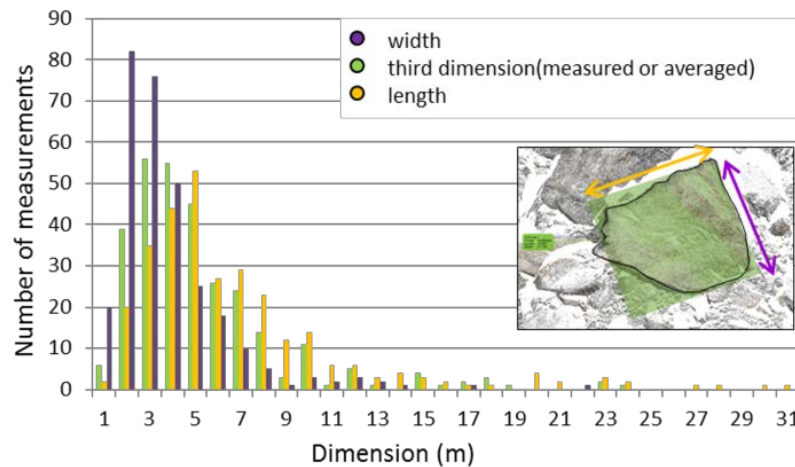
Figure 54. Distribution of the block dimensions

2.5.5   Multi-temporal analysis

The comparison of multi-temporal TLS scans (Figure 55) allows delineation of the area affected by the 2014 failure.

The differences are measured on a 50 m scale. As shown in Figure 56, the maximum difference between the two surfaces (purple area) is located in the lower Eastern part of the area, close to the section 3. The accumulation area can be seen in the lower part, showing positive values. Examining section 3, the discontinuity belonging to the set LN3 is clearly recognizable at the top.

Figure 55. TLS point clouds, pre- (a) and post-failure (b)

Figure 56. a) Difference between the 2 surfaces, projected on the post-failure surface, in blue and purple the areas influenced by the movement, in red and yellow the accumulation areas; b) sections from the pre- (green) and post-failure (red) TLS point clouds

2.6   **Discussion**
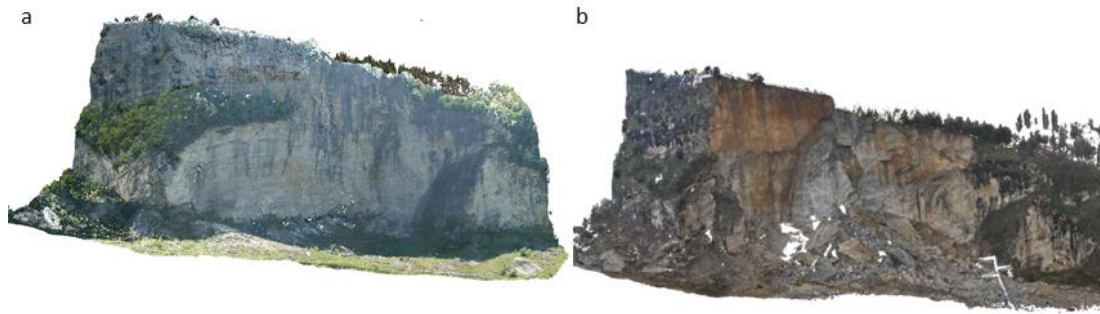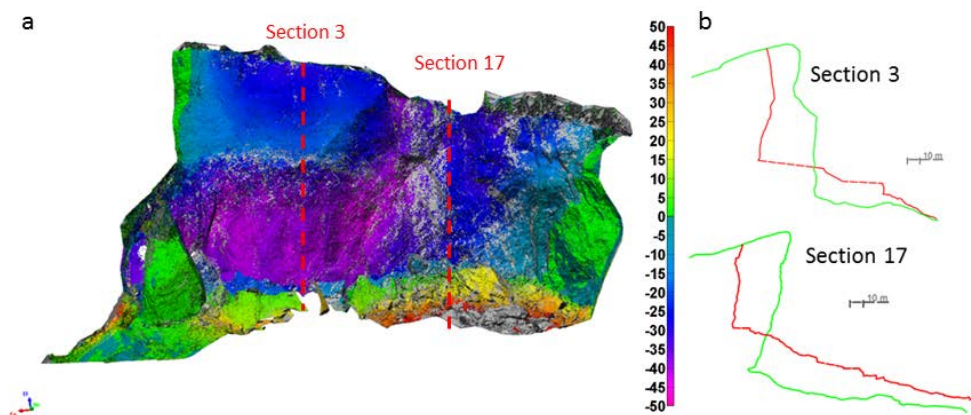
The dataset provided by the Remote Sensing Techniques (RST) measurements allowed an improved understanding of the slope failure mechanism affecting the San Leo rock slab. The RST contribution was critical in discontinuity mapping, due to the difficulties related to the traditional investigations of sub-vertical unstable rock cliffs. In fact, as discussed beforehand, because of the limited extension of the accessible areas, data from traditional engineering geological surveys are often scarce. This limitation can assume a particular importance in case of irregularly jointed rock masses, where discontinuities measured in a small areas cannot be representative of the whole rock mass (Sturzenegger & Stead 2009). Moreover, some structural features, such as the bedding planes, were not recognized using traditional methods alone.

The discontinuities mapped using the three different techniques were grouped in joint sets. From their spatial distributions some considerations can be done. Firstly some areas were recognized as highly fractured in respect to the rest of the rock slab. These zones are closely related to the recognized structural lineaments. In particular the South-Eastern edge can be linked to the presence of a EW fault.

The two highly fractured area recognized in the South and in the North cliffs can be related to the NNW-SSE fault mapped in the field. Finally, in the Western part of the slab, the different degree of fracturing between the Northern and the Southern area can suggest the presence of a WSW-ENE structural lineament. The South-Western part of the slab was instead recognized as less fractured: only scattered discontinuities and the bedding plane orientation were mapped.

In Figure 57 a summary of the discontinuities mapped by means of TLS and CRP is reported. Surveys performed in the same cliff were grouped together, to offer a more general perspective. The high number of discontinuities reported for the North cliff is mostly due to the number of surveys conducted on this area (location of the last two mean landslide events). Generally 5 or 6 joint sets plus the bedding plane were measured in all the areas, except for more massive the South-Western sector. In the North cliff the large part of the mapped discontinuities dip towards NNE or SSW. In the East cliff fractures are mainly dipping ENE or WSW. In the Southern cliff fracture poles are mainly located in the NE sector of the stereographic projection. Thus, have a large percentage of discontinuities dipping parallel to the cliff face seems to be a quite general behaviour in almost all the sectors. It is worth to mention that, as previously discussed, some planes can be not clearly visible from the remote sensing surveys, e.g. when the fractures appear as traces (normal vector of the discontinuity plane parallel to the cliff face) and don't have an adequate relief. So, this high percentage of discontinuities dipping parallel to the cliff face can be due both to the characteristics of the adopted terrestrial remote sensing techniques and to the presence of subvertical discontinuities due to unloading at the borders of the slab, which in the end increases the percentage of other structural features with a similar orientation, depending from the cliff face orientation.

For example, the sets LN3 and LS1, subvertical and parallel to the cliff orientation, can be interpreted as unloading joints.

Certain sets appear to change their orientation along the cliff surface, presenting curve surfaces and thus being difficult to fit with planes. To date the mapping and processing of these data is not usually included in structural analysis or DFN construction, since both the manual and automatic fracture mapping procedures allow only the recognition of plane features.
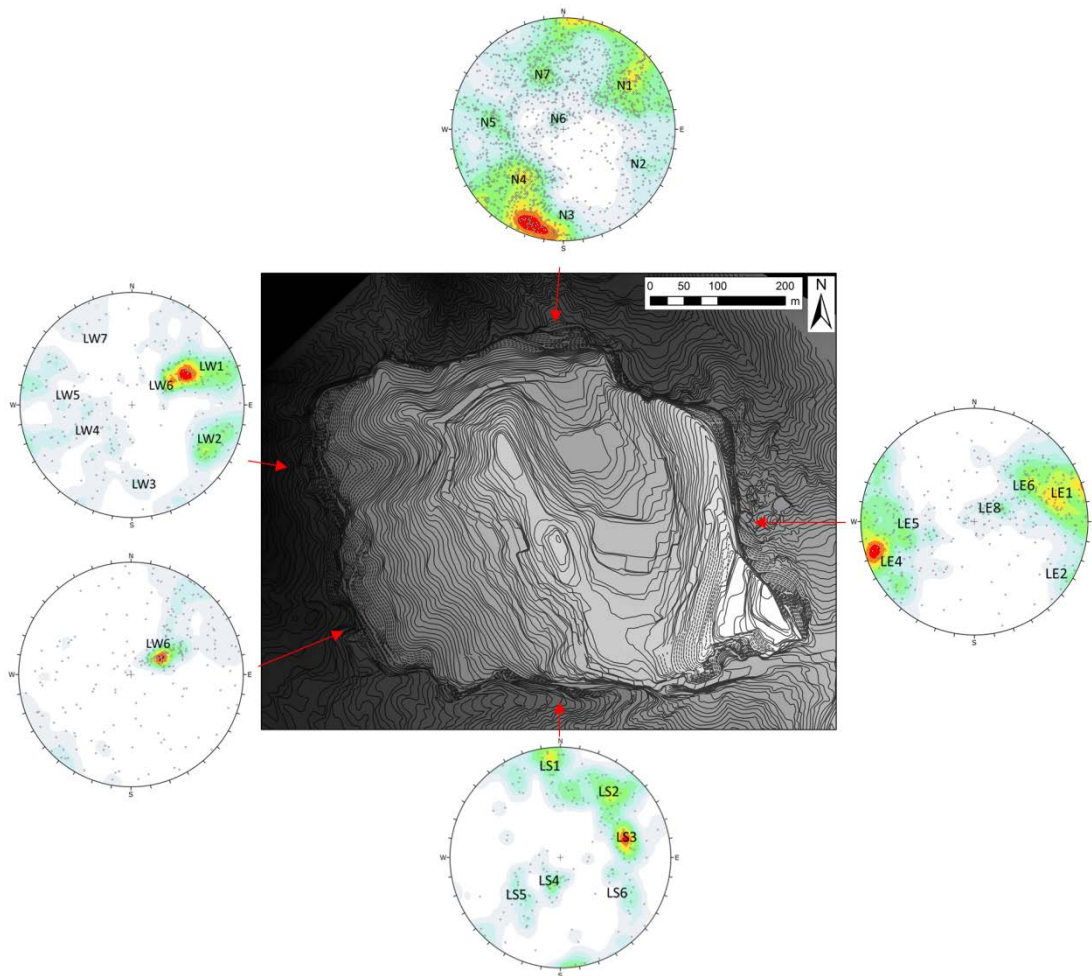
Figure 57. Summary of the fracture mapping for each side of the slab. The high number of discontinuities reported for the North cliff is mostly due to the number of surveys conducted on this area (location of the last two mean landslide events).

The analysis conducted in this study highlights the importance of the integration of different survey techniques to obtain a full representation of the 3D geometry and a characterization of the geological discontinuities. The comparison of the results allows the main strength and limitations of each procedure to be recognized. The TLS and CRP surveys permitted to obtain, at different scales, the 3D geometry of the cliff, which is of course not possible to determine with the traditional methods. Comparing the traditional surveys with the most extensive TLS and CRP data, some discontinuities characteristics, e.g. the aperture, can be inferred also for areas in which direct measures are not feasible.

Concerning the remote sensing techniques, altought TLS data should be considered more precise regarding the rock mass characterization, CRP results have shown to have a good correspondence with the TLS ones. The results are in agreement with previous works by other Authors (Ravanel & Curtaz 2011; Assali et al. 2014). Regarding the feasibility of the surveys, it is worthy to mention the flexibility

and the handiness of the CRP with respect to the larger amount of equipment needed for a TLS survey. Transporting the latter on an impervious terrain can be difficult, while for the CRP only a camera and the GNSS stations are required. A summary of the main strength and limitations regarding the three surveying methods is reported in Table 21.

Table 21. Summary of techniques comparison

	Traditional survey	Terrestrial Laser Scanner	Close Range photogrammetry (SfM)
Costs (HW and SW)	TBD*	HIGH	LOW
Difficulty	MEDIUM	HIGH	MEDIUM
Quality	MEDIUM	HIGH	MEDIUM

*To Be Decided: low to high, depending on the extension of the representative survey area and the related risks

The scale difference between the methods allows fractures with different persistence to be recognized. As a suggestion for future works, in Figure 58 is shown an indication of the scale at which the use of the different techniques is considered to be convenient. Both technical and economic issues are qualitatively considered. The traditional survey techniques are more indicated at the outcrop scale. As indicated also by Sturzenegger & Stead (2009), dealing with smaller areas, a larger amount of measures can be provided from the traditional methods, whereas data acquired along virtual scanlines are limited by the resolution of the point cloud.
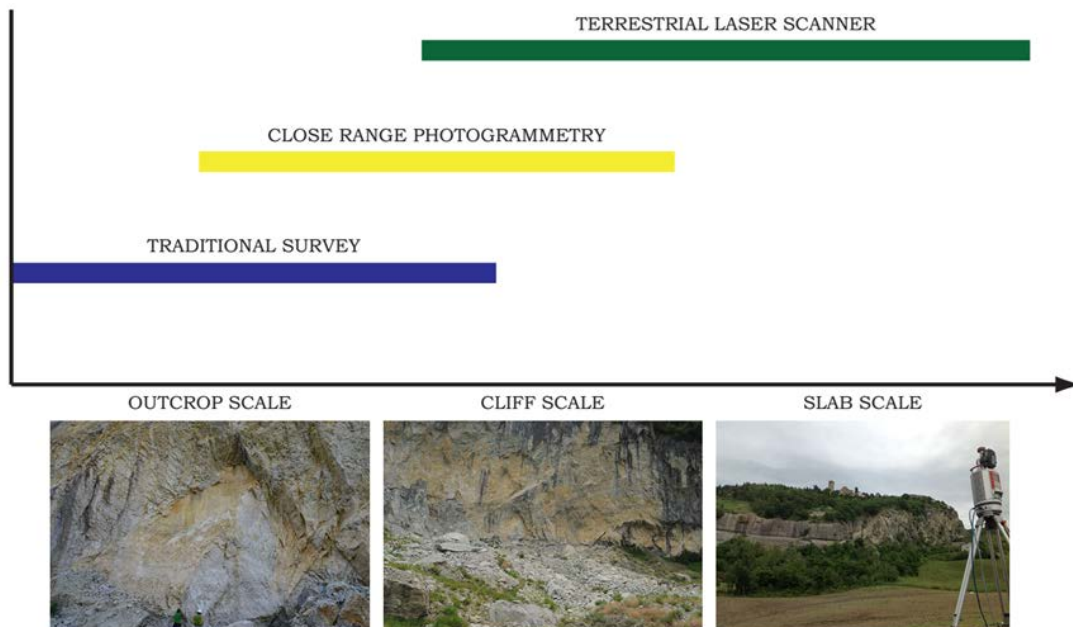

Figure 58. Suggested use of the three techniques at different scales

In order to be effective, remote sensing techniques have to cover a larger portion of the cliff. CRP is indicated for large outcrops or at the cliff scale, due to the flexibility of the acquisition and to the

obtained precision, almost comparable with the TLS one in the field of the geological discontinuities characterization. When dealing with a large cliff or with an entire rock slab, the TLS technique is preferred, allowing to collect a large number of measurements in a relative smaller amount of time, maintaining a sufficient precision also from long distances (about some hundreds of metres, depending from the acquisition range of the instrument). These general indications can help in the choice of the convenient method, but each different case has to be carefully evaluated, considering all the variables which can influence the final decision. Among them, the topography and the accessibility of the area, the purpose of the survey and the required characteristics of the final products should be taken into account for the survey planning.

The structural data from the TLS point cloud have been used for kinematic analysis in the area of the 2006 landslide. The use of these stereographic techniques is only the first step in the slope stability analysis of the cliff. The dataset acquired using traditional and remote sensing surveys provide a good description of the joint properties, which can be used to carry out more complex analyses. As an example, information about the discontinuities aperture, gained from the traditional survey and extended to the whole rock mass thanks to the TLS dataset, can be used to estimate an initial value for the equivalent permeability. In fact, these data were used, together with the geometry of the slab and the discontinuities mean orientation, as input for a 3D hydrogeological model (Chapter 4). Moreover, to build up a more complex slope stability model, the strength properties of the discontinuities are required. These can be estimated using the joints roughness and compression strength. The first can be estimated both in the field and extracting discontinuities profiles from remote sensing point cloud, although it can be difficult to estimate the small-scale roughness (Wolter 2014). The JCS can be easily obtained during traditional survey for each discontinuity, and then the averaged value can be associated to the specific joint set. The traditional field surveys allowed estimation of the geomechanical properties of the rock mass. Starting from these data it was possible to evaluate the cohesion and the friction angle for each joint set by fitting the non-linear Barton-Bandis strength envelope to the Mohr Coulomb envelope. The results, together with the properties obtained from laboratory tests for the intact rock were used in the continuum and discontinuum model described in Chapter 6.

Finally, another main advantage of the remote sensing techniques consisted in the possibility to observe and analyse the point clouds whenever measurements or comparisons with other datasets were needed. Previous acquisitions can be compared with new scans, making the monitoring of the cliff possible along with the estimation of the volume of the landslide. Regarding the 2014 landslide, pre- and post-failure surfaces were derived and compared to estimate the detachment area. Measurements of the block sizes in the deposit area were used to infer an effective equivalent spacing for the three recognized joint sets. In geological problems fractures can be frequently observed at different scales, but not all discontinuities can or should be practically considered in the modelling phase (Dershowitz, 2014). Moreover, when complex or extended geometries are used for numerical modelling, an increase in the joint spacing is required, to allow practical simulation times (Viero 2011; Francioni et al. 2014).

The procedure described was tested in the 3D back analysis of the 2014 landslide, and can be applied in similar cases to allow an assessment of a meaningful joint spacing.

SLOPE MATERIALS

3.1   Introduction

Slope instability is influenced by a variety of factors. The knowledge of the material properties can help in the prediction of the location, types, and volumes of potential failures (McColl 2014). Moreover reliable estimates of the strength and deformation characteristics of materials are necessary for any form of stability analysis.

The slope instability phenomena developing in the San Leo area appear to be mostly driven by the behaviour of the clay-shale substratum. The latter is composed by clay-rich units that are the product of a complex geological history. As anticipated in Chapter 1, they were deposited in a deep-marine environment and they underwent to a translational processes that modified their fabric and mechanical properties. As a result of the tectonic stresses, they appear sheared and highly fissured, the cracks surfaces are often polished and slickensided. As suggested by Picarelli et al. (2006), the available peak strength can be close to the residual one, along these closely spaced discontinuities. The marked heterogeneity of the clay-shales can influence their mechanical behaviour even at laboratory scale (Ribacchi & Tommasi 1988; Picarelli et al. 2000).

Furthermore, other different mechanisms, can provoke a loss in the shear strength. Among them, weathering, softening, cycles of wetting-drying or of freezing-thawing and cyclic loading. Almost all these mechanisms act on the superficial soil layers, and are related to water infiltration, facilitated by the presence of shrinkage-induced cracks in the soil.

In particular, regarding the varicoloured clay units, the presence of a superficial softened layer, in the order of some meters depth, was recognized in several areas of the Apennines (Picarelli et al. 2006; Di Maio et al. 2013). The same situation was detected also in the San Leo area. More in detail, the mechanical characteristics of the first meters of the San Leo substratum were analysed by means of in situ and laboratory tests: the results are reported in Gibertoni (2007), in which lower values of cohesion and friction angles were found for the softened layer.

Furthermore, in the San Leo area the water supply is not only limited to the direct rainfall, but also to the ephemeral and perennial springs outflowing at the contact between the plateau and the clayey units. They are fed by the groundwater hosted within the slab, and can cause the physical weathering and chemical alteration of the clayey soils at the contact between the two geological units. As a result, shallow landslides and erosion in the clay-rich substratum can promote the progressive undermining of the foot of the slab, and thus the stress development and the consequent failures in the rock cliffs. Thus, due to their importance in the developing slope instability processes, the analyses were focused on the clay-rich substratum. The behaviour of the clay-shales was analysed by means of classics soil

characterization tests (grain size distribution, Atterberg limits, natural water content, specific density, porosity and void ratio determination) and more specific analyses, with the aim to define the interactions between soil and water, e.g. the soil behaviour in unsaturated conditions and its swelling/shrinkage potential.

Beyond of the role of the clay-rich substratum, also the poor condition of the overlying rock mass, promotes the developing of the instability. More in detail, the discontinuities are supposed to control its mechanical behaviour and the different kinds of instability phenomena developing at the edge of the plateau. Generally the whole system can be treated as an equivalent continuous medium or by describing separately the intact rock and the discontinuities properties. The structural analysis, described in Chapter 2 and carried out by means of field surveys, TLS and CRP, permitted to identify and characterize the discontinuities within the rock mass. Besides the position, orientation, frequency and persistence data, also the roughness and the compression strength were collected in several outcrops. This parameters were used to derive the strength properties of the discontinuities (Barton & Choubey 1977). The rock matrix behaviour was investigated through laboratory tests, namely compression and Brazilian tests, performed on samples extracted from boreholes drilled in the neighbourhood of the study area. Even if the number and location of the analysed rock samples is not sufficient for an accurate and reliable evaluation of the mechanical properties, this approach allowed to derive the basic average parameters necessary for the stability analyses.

3.2   Interactions between water and clay-rich soils

The hydraulic and mechanical behaviours of soils are influenced by their water content (Wieczorek 1996; Van Asch et al. 1999). In particular, the interactions between soil particles and pore fluid are most relevant for soils with a large specific area, e.g. silts and clays. Volume and strength parameters of clayey soils are subject to change due to water absorption. As anticipated, different processes can act together, leading to the degradation of the soil mechanical properties. Both chemical alterations, e.g. due to the variation of the pore-water chemistry, and physical weathering, e.g. erosion, have been identified in the clay-rich terrains outcropping in the Italian Apennines.

Meisina et al. (2006) recognized In the northern Apennines (i.e., Oltrepo Pavese) the swelling and shrinkage behaviour of clayey units as a predisposing factor for landslide phenomena. More in detail, Picarelli et al. (2006) recognized two different mechanisms of soil weakening, acting on the tectonized and highly plastic clay-shales outcropping in the Bisaccia area (southern Apennines): a) the reduction of effective shear strength parameters due to exposure to fresh water, associated to the progressive change of the chemical composition of pore liquid, and b) the decrease of suction, for unsaturated soils, which leads to a reduction of the associated cohesion.

The interactions between the solid particles and pore fluid produce volume changes in clays, especially in the ones showing an high content of expansive minerals, e.g. smectites. Softening, i.e. decreasing in the peak strength, of these soils can be associated with the volumetric strains induced by swelling. The fully-softened strength could become very close to the critical value (Morgenstern 1985). In particular,

several Authors (Calabresi & Scarpelli 1985; Rampello 1992), based on laboratory tests on clay-shales from Italy, concluded that the swelling produced a decrease in the cohesion. This was associated to an increase in the water content. These soils usually shows low values of permeability but the network of cracks, formed at the soil surface during the drought season, can constitute a preferential flowpath for water infiltration and evaporation (Vogel et al. 2005), accelerating the related processes. The influence of mineral composition, pore fluid composition and stress state on these volume change behaviour is deeply investigated in Di Maio et al. (2004). During the swelling process, if the external fluid has a different chemical composition (e.g. rain water) in respect to the mineralized pore water, a progressive change in the pore liquid chemistry can occur. In the last decades, several Authors described consistent variations in the shear strength of clay-rich terrains, due to the different pore fluid chemistry. In particular, highly fissured plastic clay-shales have been shown decreases in the shear strength caused by their exposure to fresh water and by the consequent chemical-physical processes (Di Maio et al. 2013). According to Picarelli et al. (2006), these phenomena can be retained responsible of softening, i.e. time-depending processes of shear strength decrease, and are more frequent in highly plastic clayey soils of marine origin, whose susceptibility to exposure to fresh water is higher.

Furthermore, mechanisms and dynamics of shallow landslides can be influenced by their unsaturated behaviour (Lu & Godt 2008; Bittelli et al. 2012). Soils near the ground surface are seldom saturated (Freeze and Cherry 1979), thus having three phases: solid, water and air (Fredlund & Rahardjo 1993). The development of negative pore water pressures, or suction, influences the controlling stress regime, so materials in this condition can be difficult to describe within the framework of classical soil mechanics (Al-Badran 2011). In case of unsaturated soils, the suction plays an important role in defining these characteristic, e.g. abundant rainfalls can cause a decrease in suction and thus in the associated cohesion (Picarelli et al. 2006). In saturated soils the effective stress is defined as the difference between the total stress and the pore pressure. When dealing with unsaturated soils, both the pore water and pore air pressure has to be taken into account. Bishop (1959) modified the Terzaghi classical approach suggesting an equation for unsaturated soils. Biot (1941), Coleman (1962) and Freudlund & Morgenstern (1977) suggested the use of two independent variables to describe the stress state in unsaturated soils. The common point between these theories is the use of the soil suction, or a modified version of it, as the second stress variable (Nuth & Laloui 2008). The total soil suction was defined by Aitchison (1965) as the total free energy of the soil water, related to the ratio of the partial pressure of the pore water vapor to the saturation vapor pressure of the water vapor in equilibrium with free pure water. It is formed by two components, namely matric and osmotic suction. The matric suction arises from the difference between pore-air pressure and pore-water pressure and is thus associated with the capillarity phenomenon, occurring at the air-water interface (Arifin & Schanz 2009). The osmotic component derives from the dissolved solutes contained in the soil water. The soil suction can be measured in-situ or varying the volumetric water content. The obtained curve is called Soil Water Characteristic Curve (SWCC). It is used to estimate the hydraulic conductivity and the shear strength of

the soil, so to estimate the unsaturated soil behaviour. The SWCC depends from the soil characteristics, e.g. well graded soils show a flatter curve, and from the soil suction history.

3.3   **Clay-shales**

A schematic representation of the effects of the complex geological history experienced by these soils is showed in Figure 59. In the sub-marine sedimentation stages, the clay-shales were normally consolidated, during time some interparticle bonding developed, due to ageing and precipitation of cementing agents, as carbonates. During the tectonic evolution these materials undergone to a series of stress and displacements. The resulting tectonized, fissured or scaly clay-rich structure, is visible in some areas (Figure 60a). Finally, the softened upper layer is the product of relatively recent processes, as unloading, swelling and weathering. The description of the whole process can be found in Picarelli et al. (2000).
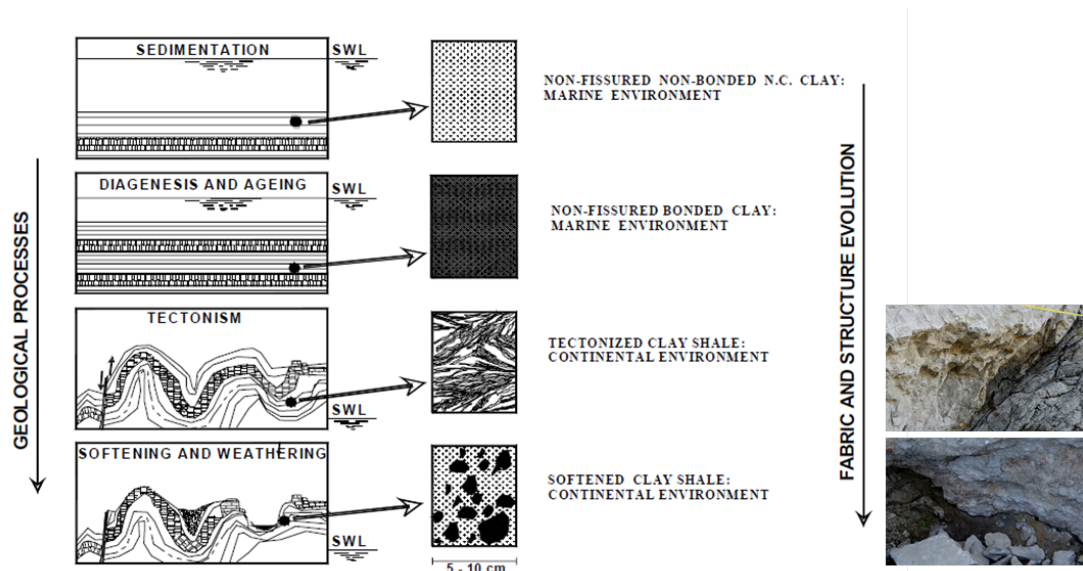

Figure 59. Approximate representation of the geological history of the Apennines chain and associated fabric of clay shales (modified from Picarelli et al., 1998)

In the zones affected by water circulation, a softened layer can be individuated (Figure 60b). The dry soil presents a well-defined network of shrinkage-induced cracks (Figure 60c), which can be individuated also in partially saturated area (Figure 60d). At the contact between this unit and the rock slab, the effects of mechanical and chemical weathering processes are recognizable. The first is proved by the undermining at the foot of the cliffs, while the second can be identified from the presence of sulphites and manganese and iron oxides precipitation (Figure 60a, b and d).

Regarding the available data, several in-situ and laboratory tests were performed by Enser srl after the 2006 landslide. The results, as published in Gibertoni (2007), were compared with the ones obtained in the present work.

Figure 60. Clay-shales: a, b and d) at the contact with the rock slab; c) during the sampling in the northern area of the slab.

3.3.1 Materials and methods

A series of laboratory tests was performed on the clay-shale substratum, in order to obtain their physical and mechanical characteristics. A particular attention was paid on its geotechnical properties in saturated and unsaturated conditions. Several samples were collected in the Northern area of the slab (Figure 60c and Figure 61) and analysed in the laboratory of the Chair of Foundation Engineering, Soil and Rock Mechanics of the Ruhr Universität Bochum (Prof. T. Schanz).
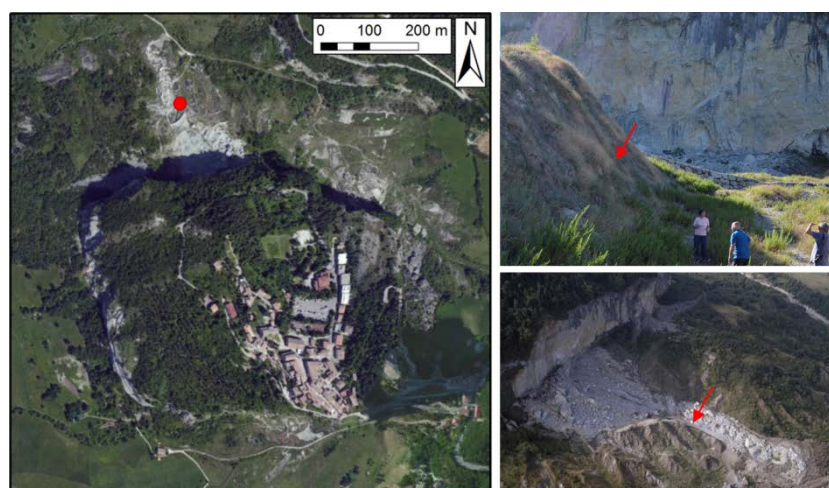

Figure 61. Clay-shales sampling position (red point and arrows)

Apart from the classical soil characterization analyses, more specific tests were performed to describe the behaviour of the materials in unsaturated conditions.

Standard direct shear tests to obtain peak shear strength parameters have been executed on three specimens. Other shear tests, focused on the residual strength and on the unsaturated (at in-situ suction) behaviour of the soil are still in progress. Oedometer tests were conducted on specimens both saturated and with natural water content. More tests, performed with a high stress device are in progress. Single oedometer collapse test permitted to analyse the soil behaviour (swelling/collapse) due to induced wetting of the samples. In-situ suction was derived, while the construction of the SWCC are in progress. Moreover the hydraulic conductivity, saturated and at varying suction, will be determined by means of triaxial and multipurpose cells.

  − *Grain size distribution*

The grain size distribution is usually performed by sieving (for the coarse material) and by sedimentation (for the finer particles), following the ASTM-Standard-D422 (2002).

The specimen was firstly put in the oven (105°) to be desiccated. All the material from the San Leo sample passed by the 0.125 mm sieve. The specimen was then prepared for the sedimentation test: it was mixed with water and anti-flocculant liquid with a stirring apparatus. Then it was put in a sedimentation cylinder (Figure 62). A controlled temperature and specific gravity must be maintained throughout the analysis. The temperature and the density were measured at predetermined time interval (30 sec, 1 min, 90 sec, 5 min, 15 min, 45 min, 2 hr, 6 hr, 1 day, 2 days). The hydrometer and thermometer measurements were interpreted following the Stokes' law, which relates the sedimentation velocity of a particle to the particle diameter and to the mixture density.

Figure 62. Sedimentation cylinder used for the grain size distribution determination

  − *Natural water content*

The in-situ water content was determined on 3 undisturbed samples following the ASTM-Standard-D2216 (2010). Undisturbed samples were weighted before and after the desiccation in the oven (105°C); the loss of mass due to drying is directly related to the water content.

  − *Atterberg limits*

The interaction between water and particles influences the behaviour and consistency of fine-grained soils. Conventional criteria have been established to individuate the water content necessary to pass from a state to another (solid, semi-solid, plastic and liquid). The limits between the different states, namely shrinkage, plastic and liquid limit, can be individuated trough standardized laboratory tests (ASTM-Standard-D4318 2010).

The Liquid Limit (LL) is defined as the water content (%) at which the soil begins to behave like a liquid material. In the laboratory it was determined using the Casagrande cup: the wet specimen was placed in the cup and a straight groove was cut in the middle of the cup (Figure 63). Then the cup was dropped by a standard mechanical device until the two halves of the soil pat come into contact at the bottom of the groove along a distance of 13 mm. The number of drops and the water content were measured and plotted on a graph, the value found on the best-fitting line, corresponding to 25 drops, is defined as the LL.
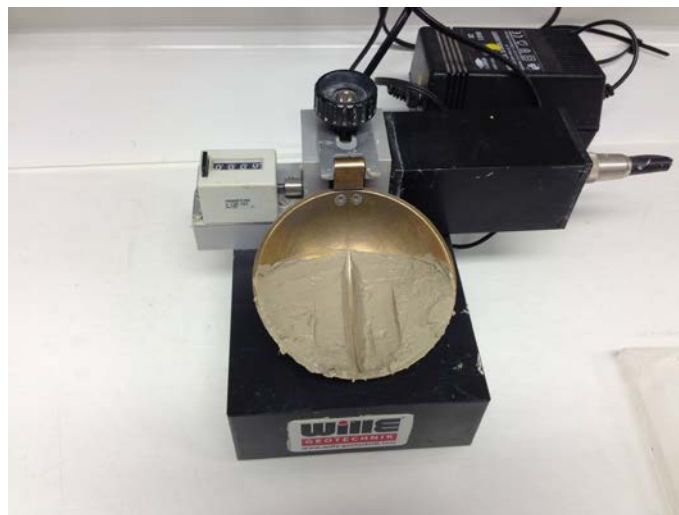

Figure 63. Casagrande cup with a straight groove cut in the middle of the sample

The Plastic Limit (PL) has been determined rolling the sample between the palm of the hand and a glass plate and forming 3.2 mm-diameter cylinder. The procedure was repeated until the soil crumbles. The corresponding the water content was measured and defined as PL.

The LL test was repeated for 5 samples, while three specimen were tested for the PL.

The values determined through the Atterberg tests were used to define the state of activity of the soil (A):

$$A = \frac{Ip}{\% < 2\mu m}$$

where

Ip = LL-LP (measure of the plasticity of a soil)

$\% < 2\mu m$ = percent of clay-sized particles (less than 2 μm) present in the soil.

The terrain can thus be classified as:

A<0.75   inactive soil

0.75<A<1.25   normally active soil

A>1.25   active soil

The activity can be correlated to the dominant clay type present in a soil and describes some of the related behaviour, e.g. highly active soils are more reactive chemically. Moreover large change in volume when the soil is wetted and large shrinkage when is dried usually correspond to high values of A. Finally, the soil consistency can be measured through a specific index Ic:

$$Ic = \frac{LL - w}{Ip}$$

where w is the natural water content of the soil.

- *Specific gravity*

Specific gravity of soil is defined as the ratio of the total mass of the soil particles to their volume. It was determined following the ASTM-standard-D854 (2014), using a pycnometer, on 3 samples, previously desiccated in the oven. The soil size were reduced with a mortar, until they passed through a 0.2 mm sieve. About 20 g of soil were put in the pycnometer and the weight was measured. Then 1 cm of water covering the soil was added and the pycnometer was shacked to mix soil and water. In one case it was not possible to mix them and the sample was discarded. To remove the entrapped air, the pycnometer was placed in a desiccator and vacuum was applied. More water was added and the weight was measured again, while the temperature was kept constant (20°C). The volume of the soil was determined by measuring the fluid displacement. Knowing the weight of the empty pycnometer, of the soil and of the water, the soil density was estimated.

Figure 64. Measure of the specific density: a) pycnometer weighting and b) desiccator

- *Porosity and void ratio*

A soil is constituted by solid particles and void, that can be filled with fluids, usually water and air (Figure 65).
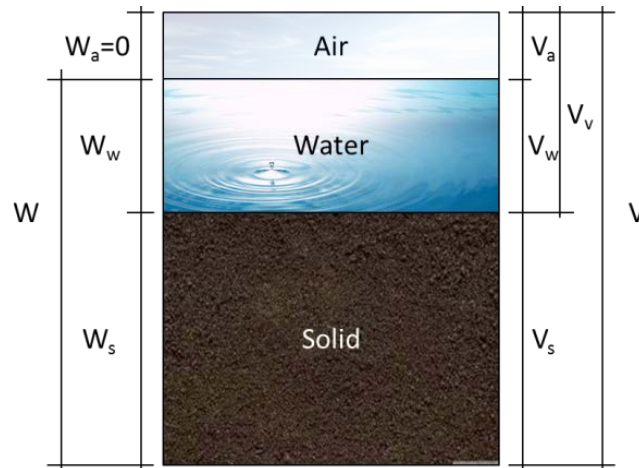
Figure 65. Phase diagram of a soil (scheme of total weight composition: air, water and soil to the left; scheme of total Volume to the right)

The solid volume is indicated as Vs, the water volume as Vw and the air one by Va. Porosity can be defined as the ratio between the voids volume Vv (Va+Vw) on the total volume V and is usually expressed as a percentage. By dividing the Vv by the Vs the void ratio e can be calculated. Measuring the density of the three samples of which the particle density was known, e.g. the ones used for the pycnometer analysis, it was possible to calculate the porosity and void ratio of the soil.

   − *Direct shear test*

The standard shear box test permit to obtain the soil shear strength parameters, namely the cohesion and friction angles as defined in the Mohr-Coulomb formulation.

Three disturbed samples, having a mean 60 mm-side square section and a height of about 20 mm, reconstructed with the same density of the undisturbed ones were tested (Figure 66). Saturated conditions were applied. The samples were introduced in a metallic shear box, divided in two parts and submerged by water. Firstly a confining vertical pressure, namely 112, 72 and 41 N/cm^2, was applied to the sample for at least 24 hours and kept for all the test duration. Then a pre-determined horizontal velocity of about 0.024 mm/min was applied to the lower part of the shear box. The velocity should be low, to avoid the developing of pore pressure.

Figure 66. Views of the direct shear test apparatus

During the shear phase the applied load and the induced strain were recorded at frequent intervals. The results are plotted on a σ-τ graph. The best-fitting curve represent the Mohr-Coulomb criterion: the y-intercept is the cohesion, while the slope of the line is the friction angle.

− *Oedometer test - standard procedure*

the soil stress-strain behaviour during one-dimensional compression was evaluated by means of fixed-ring oedometer tests. The tests were conducted on dry (undisturbed sample with in-situ water content) and wet (undisturbed sample, saturated before loading) samples, to test the soil response under different conditions. The difference between the compression curves should be equal to the deformation which would occur when the soil get saturated and can be measured for any investigated stress condition (Jennings & Knight 1975). The cylindrical samples are laterally confined by a metallic ring to prevent lateral displacements. To allow the drainage in the vertical direction, porous stones are located on the top and bottom of the sample. The samples were loaded vertically following incremental steps (5, 12.5, 25, 50, 100, 200, 50, 12.5, 25, 50, 100, 200, 400, 800, 1000 kPa). Each step was maintained until the sample reached the end of the primary consolidation. After the reaching of the complete consolidation at the last loading stage, the sample has been unloaded (250, 50, 12.5 kPa). The height variation of the sample was measured through time. The results were plotted in a semilogaritmic stress-void ratio (or stress-thickness variation of the sample) graph. The Swelling Index (Cs), Compression Index (Cc) and the soil stiffness E_s were calculated for dry and wet tests. Cc and Cs were determined from the void ratio-log σ'_v curve. They are usually correlate with the plasticity of the clay (Lambe & Whitman 1969).

− *Single oedometer collapse test*

Natural soils wetted under a load can collapse or swell. Soils containing a large amount of expansive clays usually are expected to exhibit swelling behaviour if wetted. This method is used, in alternative with the double ring oedometer test previously described, to measure one-dimensional wetting-induced swell or collapse.

A specimen was loaded to a total vertical stress equal to 150 kPa following incremental steps (9.37, 18.75, 37.5, 75, 150 kPa) and then inundated. The collapse strain was measured. The loading was continued after inundation (150, 300, 600, 800, 200, 50 kPa). The test was repeated on 2 samples.

− *In-situ suction*

Different devices can be used to measure suction, directly or indirectly (Ridley & Wray 1996). The in-situ suction was measured on 3 specimen, showing different water content, using the chilled mirror technique. The first sample was undisturbed, the second undergone to a shear test and the third was air-dried. The chilled mirror technique measures the relative humidity of the air space, over the soil sample. The specimen is placed in a closed chamber of the device (water activity meter, model series 3TE, Decagon Devices, Inc.) where one sensor measured the relative humidity at a given temperature. Applying the Kelvin's equation, the total suction can be derived:

$$s_t = -\frac{RT}{M_w\left(\frac{1}{\rho_w}\right)}\ln(RH)$$

where RH is the relative humidity measured by the instrument, s_t is total suction (kPa), R is the universal gas constant (8.31432 J/mol K), T is absolute temperature (Kelvin), M_w is the molecular weight of water (18.016 kg/kmol), ρ_w is the unit weight of water (kg/m) as a function of temperature.

The results were compared with the ones obtained for illite, calcigel and kaolinite (Baille 2014).

  – *Soil Water Characteristic Curve (SWCC): sample preparation and preliminary tests*

Four specimen were prepared for the SWCC determination. The samples were placed in plastic rings. A paper disc was attached at the bottom of the specimen. Then they were weighted and covered by a glass disc to maintain humidity (Figure 67).
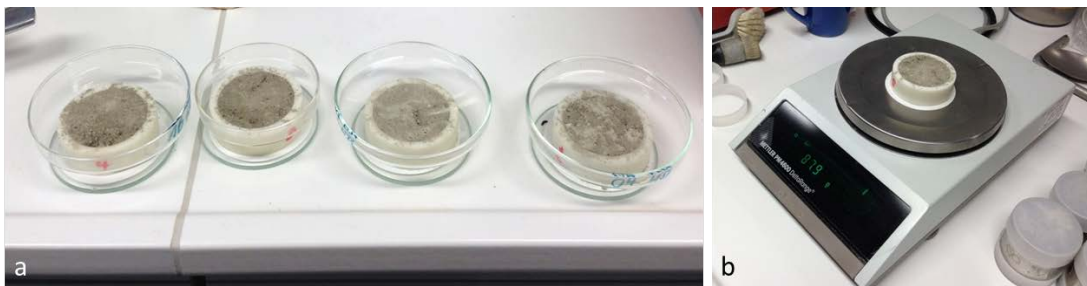

Figure 67. SWCC samples preparation: a) the four tested samples and b) weighting of one of the specimens

The paper disc was put in contact with a porous medium submerged by in water. The specimens were weighted at regular intervals, until they will reach a constant weight and can thus be considered saturated.

Two techniques were used to control the suction of specimen, namely the Axis Translation Technique (ATT) and the Vapor Equilibrium Technique (VET). The ATT controls the matric suction: increasing the pore-air pressure while the pore water pressure is kept at positive or zero values a negative pore water pressure is induced (Richards 1941). The VET is commonly used for higher suction range (Agus & Schanz 2005). This techniques is based on the relation between the total suction and the relative humidity of the vapour space, following the Kelvin's law. A total of 4 samples, 2 with the ATT and 2 with the VET techniques, are being tested at different suction values.

3.3.2   Results

  – *Grain size distribution*

Grain size distribution curve is reported in Figure 68. The 44% of the soil can be defined as clay (diameter<0.002 mm) and the 66% as silt (0.002mm<diameter<0.063), according to the (ISO 14688).
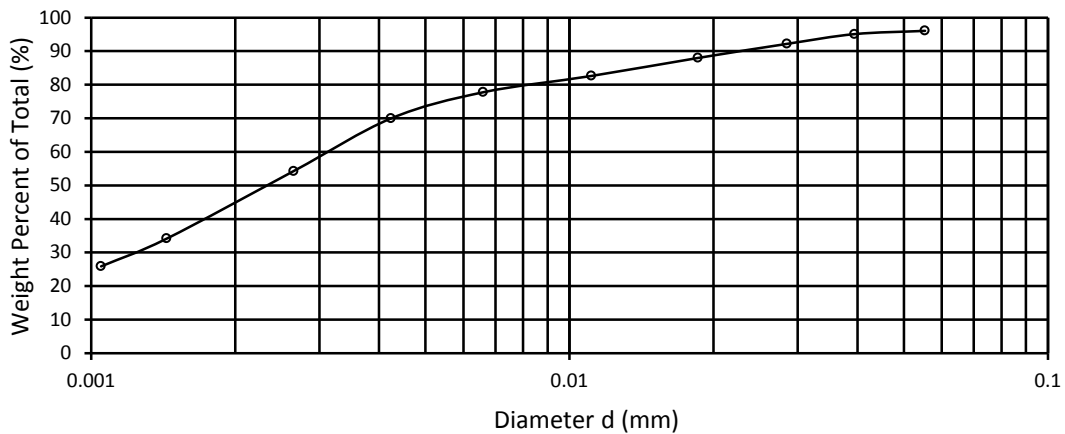
Figure 68. Grain size distribution

Results were compared with similar tests conducted after the 2006 landslide and summarized in Gibertoni (2007): the 25-35% of the soil was classified as clay, the 30-65% as silt, the 7.5-17.5% as sand. The presence of larger particles is probably due to the origin of the samples, taken at different depth in the proximity of the landslide body and thus containing also coarser material coming from old landslides. In fact, as stated by the Author, at depth the finer component becomes predominant.

  − *Natural water content*

Results of the test are reported in Table 22. The mean natural water content results equal to 7.5%.

Table 22. Measured water content

sample	1	2	3	4
water content (%)	9.1	6.8	7.9	6.3

  − *Atterberg limits*

Results of the LL determination are reported in Table 23. The number of drops and the corresponding water content values were plotted on a graph and the best fit straight line was interpolated (Figure 69).
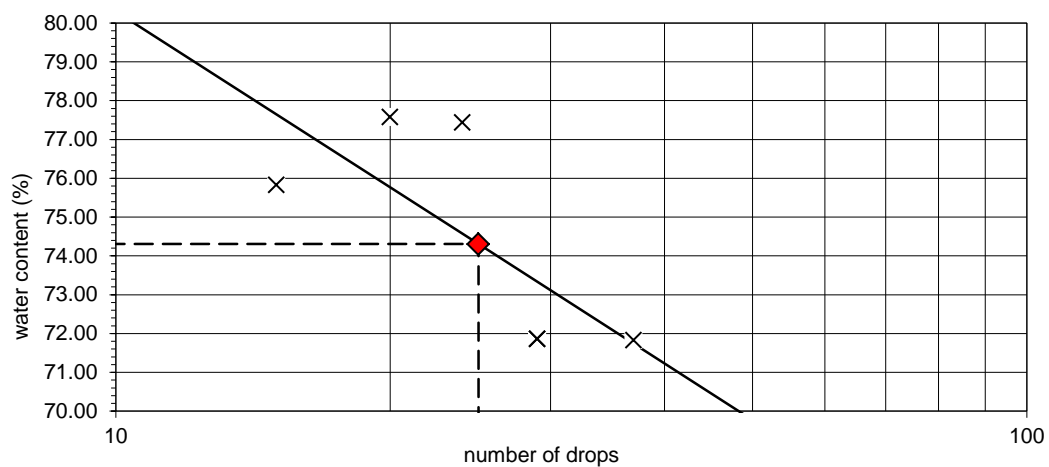

Figure 69. Liquid Limit determination

Table 23. Results of the LL determination

Sample	1	2	3	4	5
Number of drops	15	20	24	37	29
Water content (%)	75.8	77.6	77.4	71.8	71.9

The water content corresponding to 25 drops has been estimated in 74.3%.

Results of the PL tests indicated a mean value of 17.1% for the water content (Table 24).

Table 24. Results of the PL determination

Sample	1	2	3
Water content (%)	19.0	15.2	17.2

The most important indexes are summarized in Table 25 and Figure 70. In Figure 71 the sample values are reported on the Casagrande plasticity chart for the USCS classification. The tested material can be classified among the inorganic clays of high plasticity (Figure 71 and Table 26). In fact, the calculated plasticity index (%<2μm = 44%) falls in the range of the values associated to active soils.

Table 25. Characterization indexes

w (%) natural water content	7.5
LL (%) Liquid Limit	74.3
PL (%) Plastic Limit	17.1
Ip (%) Plasticity Index	57.2
Ic Consistency Index	1.17
A Active soil	1.3
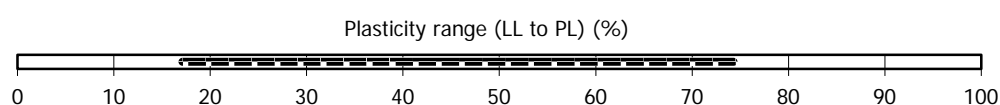
Figure 70. Plasticity range
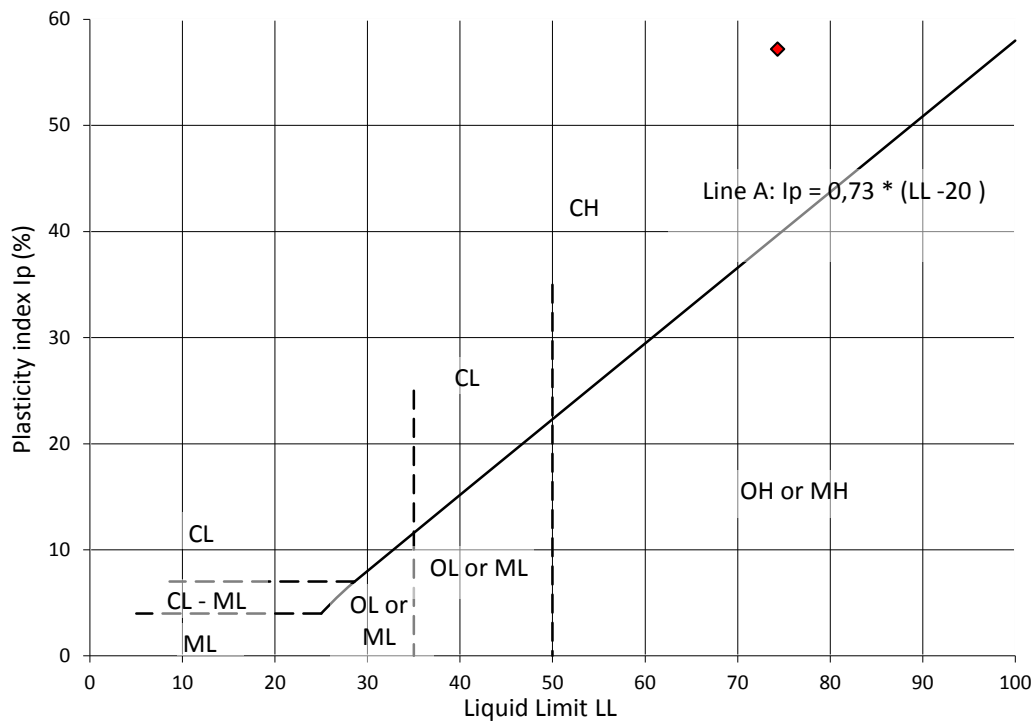
Figure 71. Plasticity chart

Table 26. Plasticity classes

ML	Inorganic silts and very fine sands, rock flour, silty or clayey fine sands with slight plasticity
CL	Inorganic clays of low to medium plasticity, gravel clays, sandy clays, silty clays, lean clays.
OL	Organic silts and organic silt-clays of low plasticity
MH	Inorganic silts, micaceous or diatomaceous fine sandy or silty soils, elastic silts
CH	Inorganic clays of high plasticity, fat clays
OH	Organic clays of medium to high plasticity

These values are quite in agreement with the ones found during the laboratory tests performed by Enser srl after the 2006 landslides and described in Gibertoni (2007). In particular, analysing several samples taken at different depth from the 2006 landslide area, they found a LL varying between 50 and 100%, a PL ranging from 30 to 70% and a Ip equal to 0.8-1.2. In Italian tectonized clay-shales the plasticity index is generally high or very high, in presence of smectite (Bilotta et al. 1985).

- *Specific gravity*

Results of the tests are reported in Table 27. The mean value of the soil specific density is equal to 2.490 g/cm3.

Table 27. Pycnometer results

Pycnometer n°	22	2
ρ(g/cm3)	2.4752	2.5040

− *Porosity and void ratio*

Porosity and void ratio were determined for 3 samples, results are reported in Table 28.

Table 28. Porosity and void ratio results

sample n°	ring box mass mB [g]	ring box V [cm³]	mB + m wet soil mf [g]	mf [g]	wet bulk density [g/cm³]	dry bulk density [g/cm³]	particle density pycnometer [g/cm³]	e (void ratio)	porosity
6	96,34	100,14	284,17	187,83	1,88	1,74	2,49	0,43	0,30
14	96,36	100,14	279,03	182,67	1,82	1,71	2,49	0,46	0,31
15	96	100,14	282,98	186,98	1,87	1,76	2,49	0,42	0,29

− *Shear strength*

Results for the three samples are reported in Figure 72 and Figure 73.

The R^2 of the fitting procedure is equal to 0.71. The estimated cohesion is about 11 kPa and the friction angle 29.8 degrees.
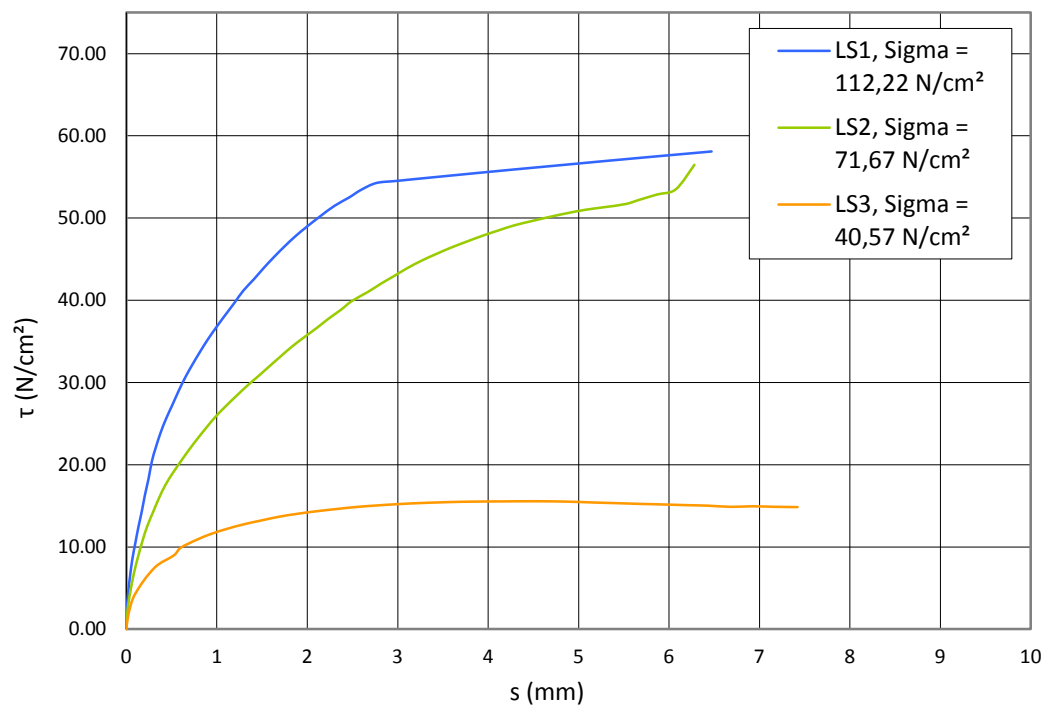

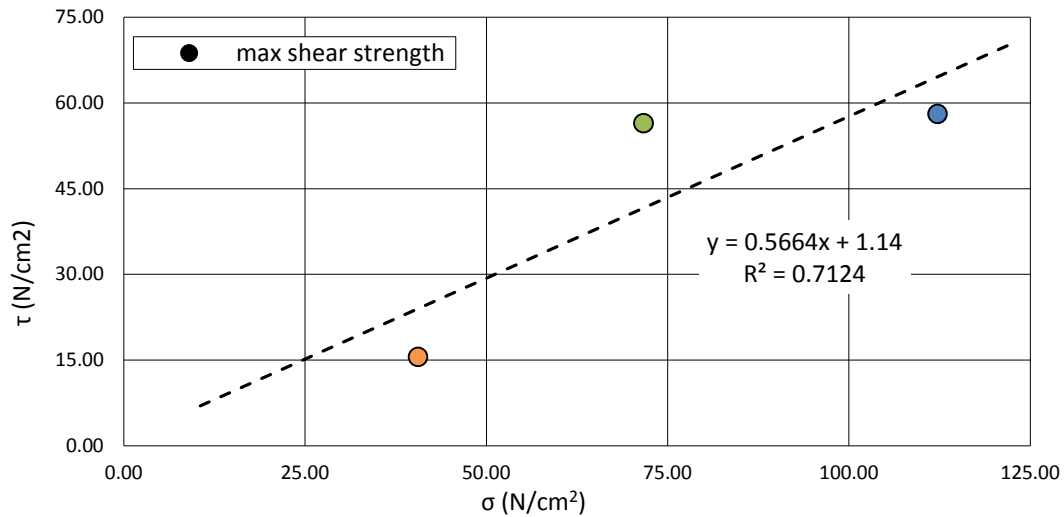*Figure 72. Direct shear tests results, s-τ*

Figure 73. Direct shear tests results, σ-τ graph

Results are in agreement with the values reported in literature for clay-shales in neighbouring areas (Ribacchi & Tommasi 1988; D'Ambra et al. 2004; Gibertoni 2007) and similar soils.

− *Oedometer (standard procedure)*

Results for the dry and wet tests are reported in semilogaritmic stress-void ratio diagrams, respectively in Figure 74 and Figure 75. Calculated Compression and Swelling index (C_c and C_s) are reported in Table 29. The Stiffness modulus, e.g. the gradient of the vertical stress-strain plot, was calculated for vertical stresses between 100 and 200 kPa. Its value is equal to 55.3 MPa for the dry test and decreases to 1.14 MPa in the wet one.
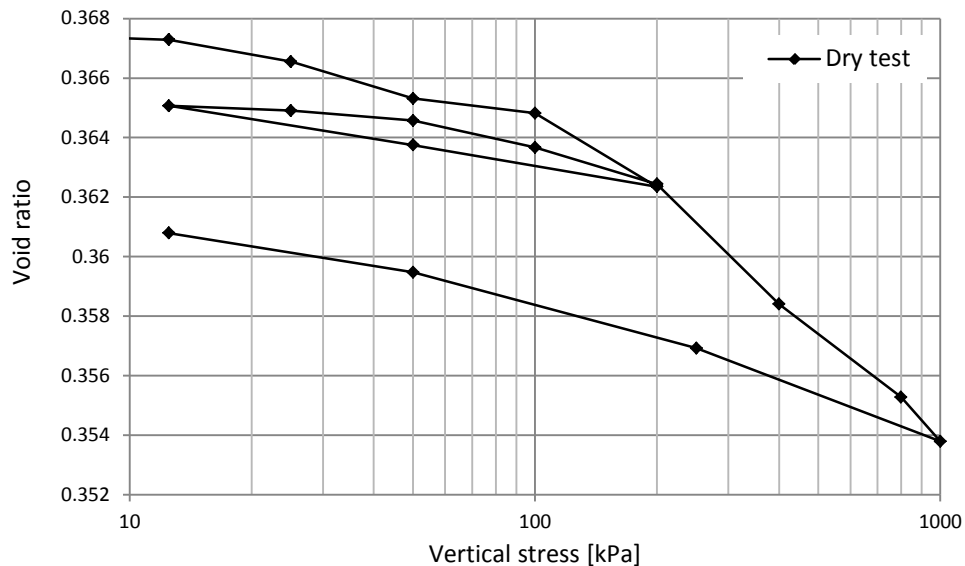

Figure 74. Dry oedometer test results
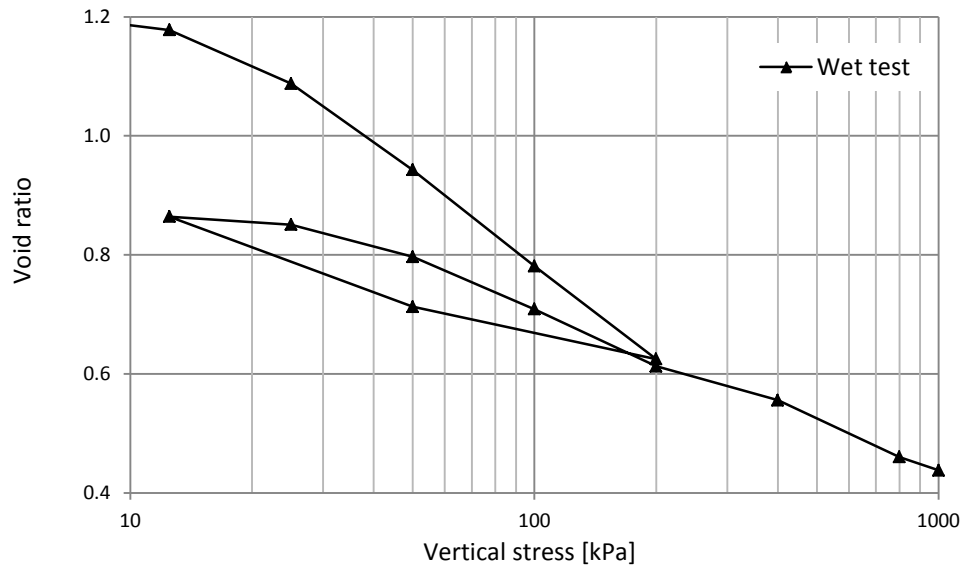
Figure 75. Wet oedometer test results

Table 29. Results of the double oedometer test

	Dry test	Wet test
Compression index C_c	0.0121	0.2576
Swelling index C_s	0.0037	0.1988
$E_{s\ 100\text{-}200\ kPa}$ (MPa)	55.29	1.14

− *Single oedometer collapse test*

Results of the collapse tests are reported in Figure 76 and Figure 77. Settlement versus time were plotted for the loading stage corresponding to 150 kPa, when the sample was inundated (Figure 76 and Figure 77), showing a swelling behaviour. In fact the samples showed an increase in vertical height due to the increase in the moisture content.
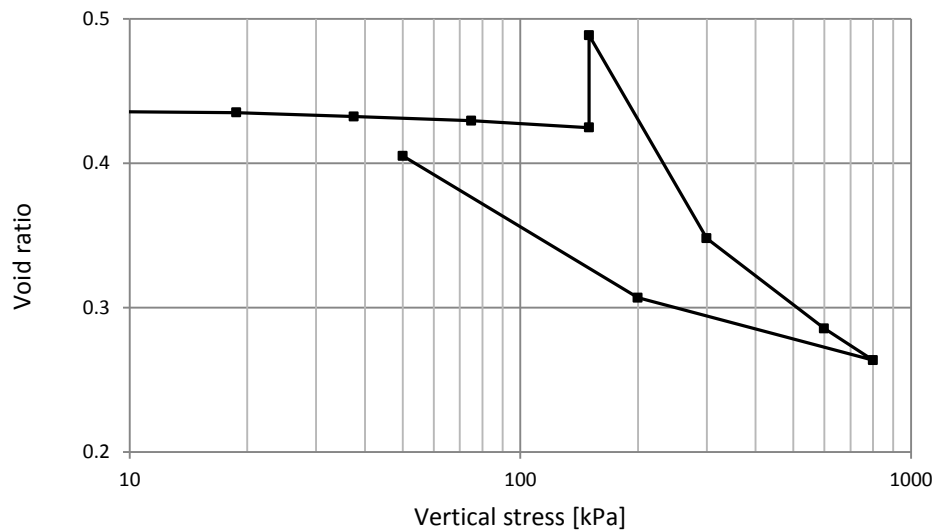
Figure 76. Oedometer collapse test 1
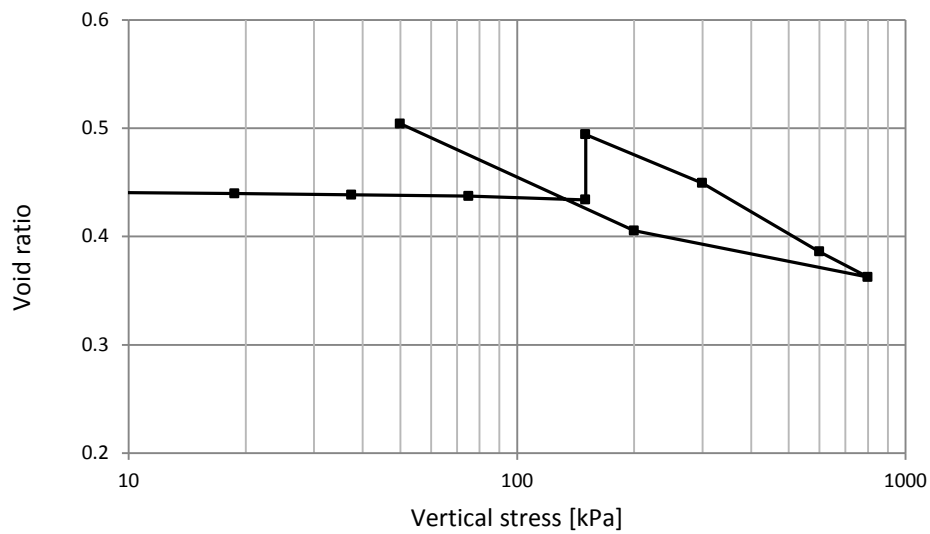
Figure 77. Oedometer collapse test 2

The time-swell curves usually consist in three regions, a minor initial swell attributable to the macrostructure, a major primary swell (steeper part of the curve) and a minor secondary swell, both associated to the microstructure (Rao et al. 2006). The Swell Potential (SP) is equal to 2.86% for the first test and to 3.12% for the second.
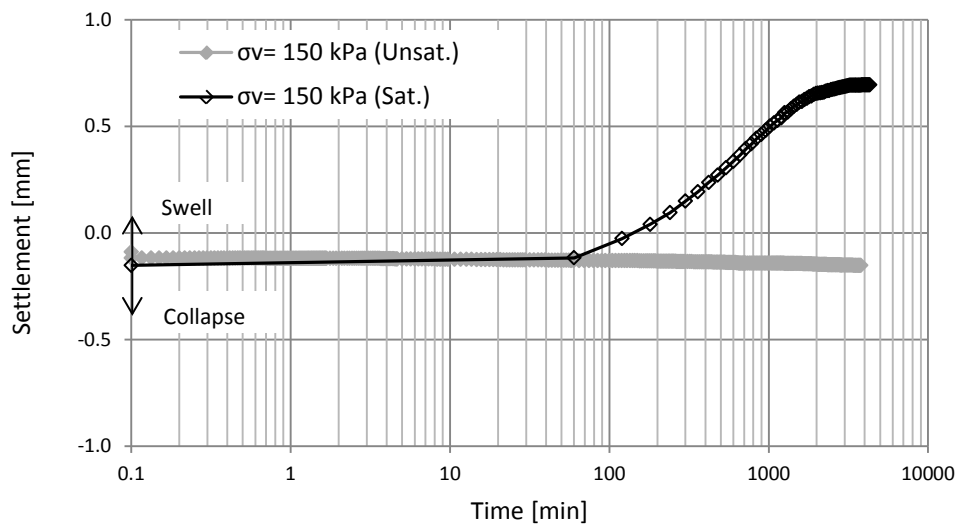
Figure 78. Settlement versus time in the 150 kPa loading step, test 1
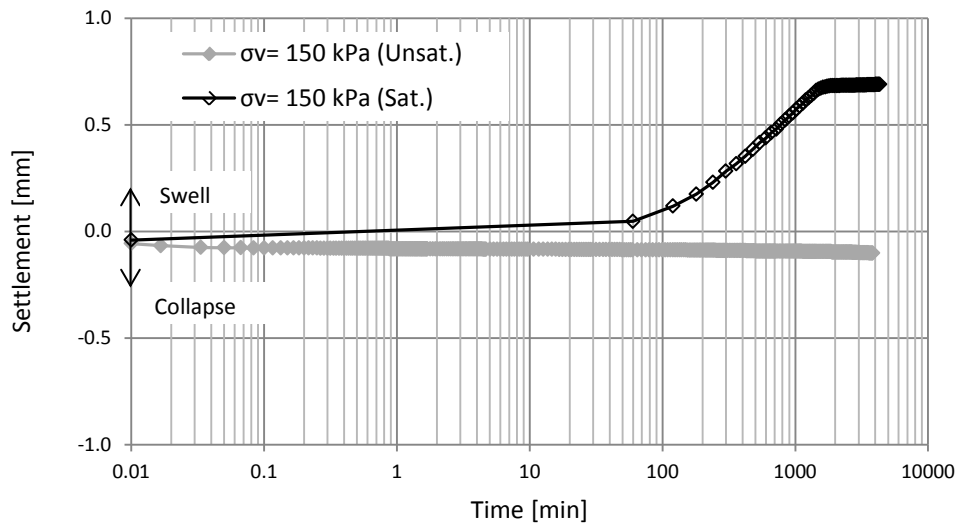
Figure 79. Settlement versus time in the 150 kPa loading step, test 2

− *In situ suction*

Results obtained using the chilled mirror technique, for the 3 clay-shale samples are reported in Figure 80, together with the values obtained for others reference materials, i.e. bentonite, illite and kaolinite (Baille 2014).

Results are reported in Figure 80. For the undisturbed sample (San Leo 2) a suction value of about 41.8 MPa was derived.

Table 30.Measured in-situ suction and average water content

Specimen	San Leo 1 (disturbed, shear test)	San Leo 2 (undisturbed)	San Leo 3 (disturbed, air dried)
Temperature (°C)	21.9	21.9	21.6
Suction (kPa)	69,407	41,833	4,035,798
Water content (%) average	4.58	5.52	0.84
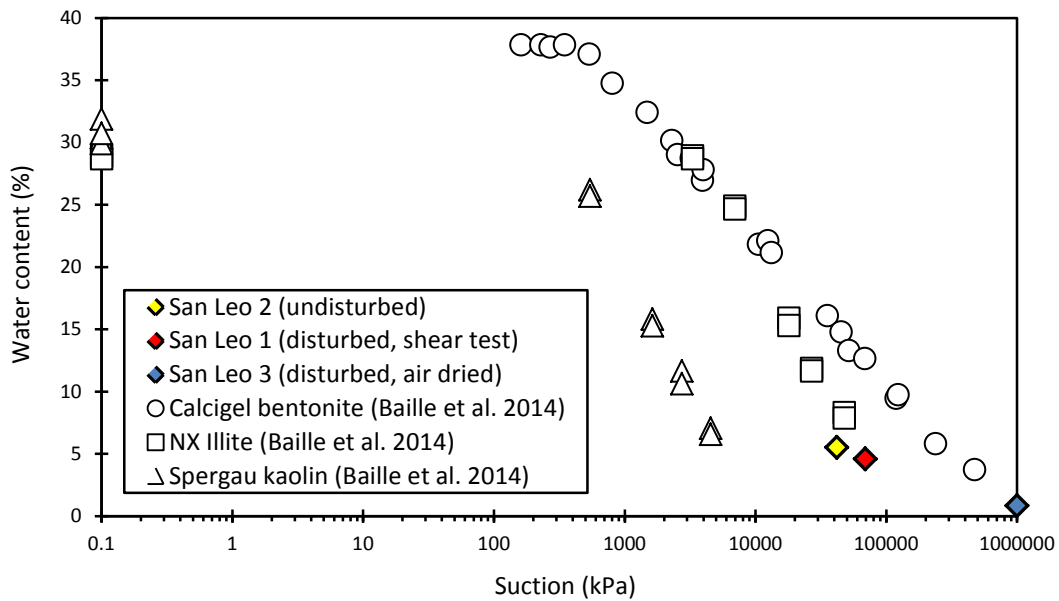
Figure 80. Suction measured for the San Leo samples, compared with measurements for bentonite, illite and kaolinite

- *Soil Water Characteristic Curve (SWCC): sample preparation and preliminary tests*

The mass-time saturation curve for the sample preparation is showed in Figure 81. Examples of preliminary results describing the mass specimen along time with a 5-10-5000 and 10000 kPa of applied suction are showed in Figure 82 and Figure 83.
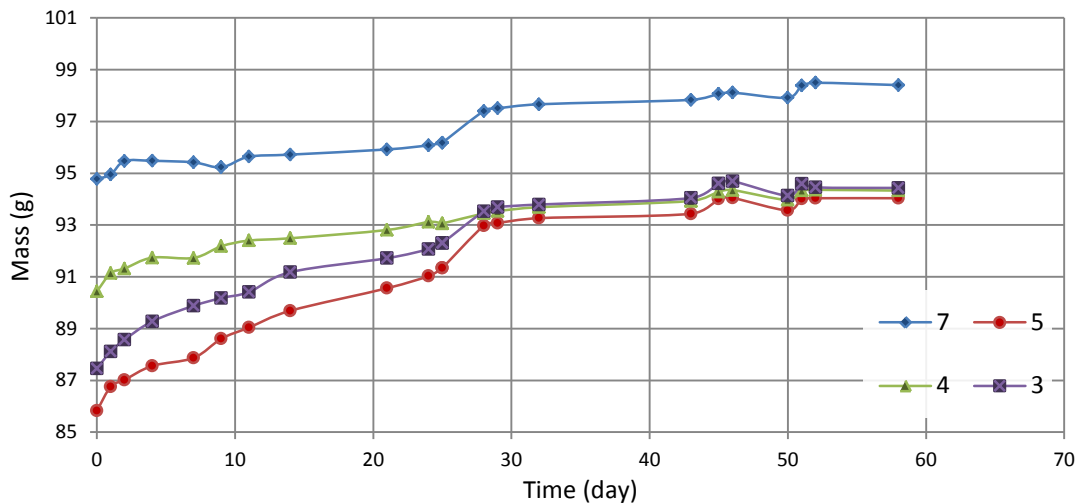
Figure 81. Mass-time curve for the specimen saturation
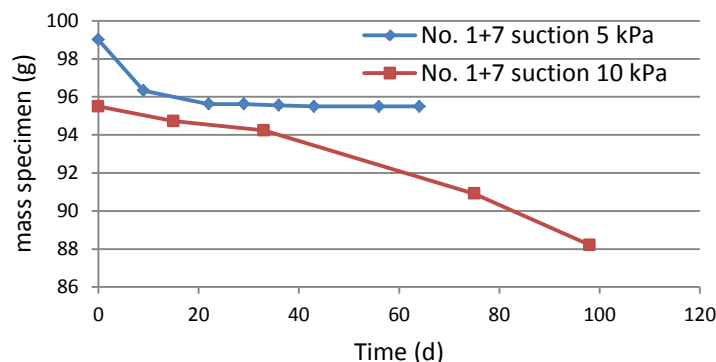
Figure 82. Mass specimen versus time for 5 and 10 kPa of suction
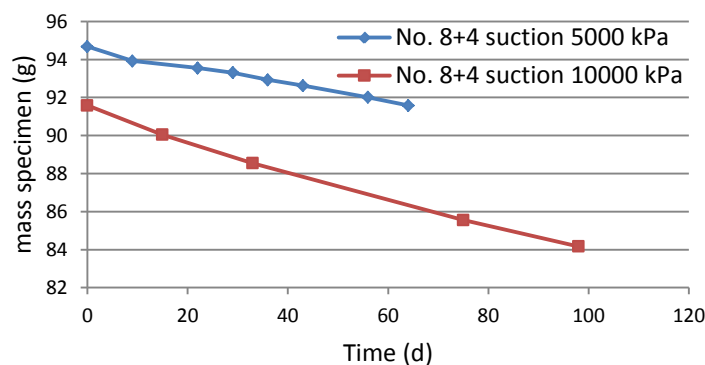
Figure 83. Mass specimen versus time for 5 and 10 kPa of suction

3.4   Rock mass

Rock mass behaviour can be anisotropic and variable in space. As anticipated, it is influenced by the intact rock properties and the discontinuities geometrical and mechanical parameters. Hence, even in the same rock formation, areas affected by a larger number of discontinuities, e.g. closely spaced, will probably show lower strength parameters if compared with less fractured sectors. A structural analysis of the rock mass has been performed (Chapter 2) in order to derive the characteristics of the discontinuities, e.g. orientation, spacing, persistence, mean trace length, roughness, aperture, infilling. Starting from the collected data cohesion and friction angles of the discontinuities were derived.

Moreover laboratory tests has been performed on boreholes sample to quantify the rock parameters to input in the numerical models. A review of the work previously done to characterize the rock mass strength can be found in D'Ambra et al. (2004) and in Ribacchi and Tommasi (1988).

3.4.1   Materials and methods

Laboratory tests were conducted in the Laboratory of Geoengineering and Natural Resources (LAGIRN) of the University of Bologna (Prof. P. Berry). In particular simple compression tests and Brazilian tests were conducted on borehole samples. Furthermore, thanks to the data collected during the geomechanical mapping in the field, discontinuities parameters were evaluated.

- *Compression test*

The compressive strength is widely used rock engineering parameters. The uniaxial compressive strength can be influenced by the water content, the porosity and the alteration degree of the sample. Experiments were conducted on cylindric samples, cutted to specified length. Uniaxial load was applied to 8 specimens, up to failure. The maximum stress that they can bear is defined as uniaxial compressive strength (σ_{ucs} or σ_c).

- *Brazilian test (indirect tensile strength)*

Tensile strength influences rock deformability and failure (Claesson & Bohloli 2002). Due to the difficulties encountered when performing a direct tensile test, this parameter is usually measured through indirect tests, where the tensile stress can be generated by compressive loading. Brazilian test was performed on 6 samples. The load was applied with a constant velocity of 0.2 kN/s.

- *Geomechanical characterization of discontinuities*

During the performed geomechanical surveys, orientation, spacing, roughness, aperture and infilling of the discontinuities were collected. The Joint Roughness Coefficient (JRC, Barton and Choubey 1977) and the Joint Compression Strength (JCS, Deere and Miller 1966) were also measured. Using the JRC and JCS values it was possible to estimate the values of cohesion and friction angle for each joint set by fitting the non-linear Barton Bandis strength envelope to the Mohr Coulomb envelope. For this purpose, the basal friction angle was assumed to be equal to 29 degrees, based on previous measurements. The fitting procedure was performed over a specific stress range based on the slope height (approximately 100 m) and the average unit weight of the material (26 kN/m3). Scale corrections were applied to the collected JRC.

3.4.2 Results

- *Compression test*

Results are reported in Table 31. Some pictures of the samples after the compression test are showed in Figure 84. The mean compression strength has a value of about 80 MPa. In D'Ambra et al. (2004) values of 92 MPa are indicated for intact rock, while specimens with closed joints showed a compression strength equal to 37 MPa.

In Ribacchi and Tommasi (1998) a distinction between the two geological units and dry and saturated conditions was made. For the *San Marino* formation compressive strength between 45 - 100 MPa for dry samples and 55 MPa for saturated samples was measured. The *Monte Fumaiolo* unit showed lower values, ranging between 25-50 MPa (dry samples) and 20-30 MPa (saturated samples). The measured apparent density is very similar to the one measured in the present work. Moreover D'Ambra et al. (2004) measured the specimens porosity, finding values between 3 and 11%.

*Table 31. Compression tests results. * along the discontinuity ** vertical fractures*

Sample	Diameter (mm)	Height (mm)	Mass (g)	Apparent density (Kg/m^3)	F max (N)	σ_c (MPa)
5B	83.10	82.00	1169.75	2630	458200	84.5

12	83.10	82.80	1182.49	2633	504500	93.0
13	82.70	80.30	1122.57	2603	433000	80.6
3	83.00	158.70	2264.10	2637	411200	76.0
7*	83.10	157.30	2211.29	2592	246000	45.4
8	83.20	158.10	2273.80	2645	408500	75.1
13A**	82.50	158.90	2229.66	2625	276500	51.7
18	83.10	159.90	2299.48	2651	404500	74.6
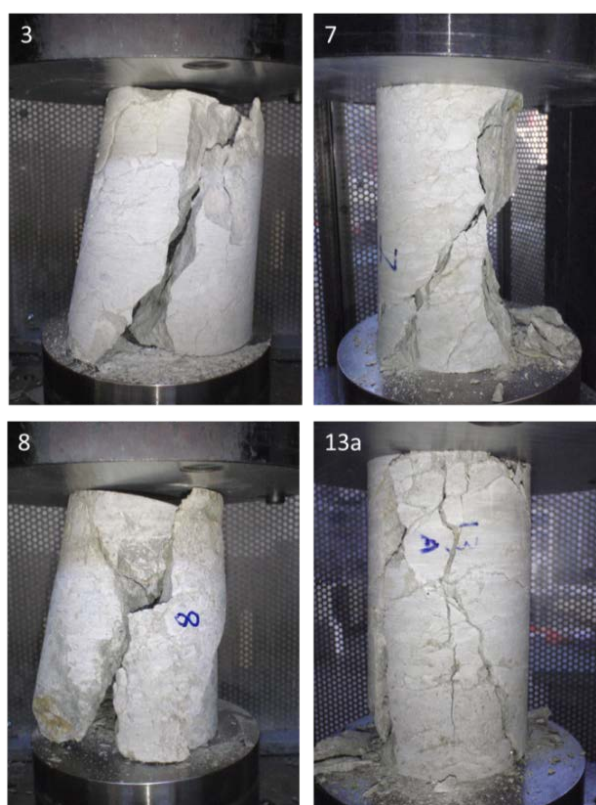
Figure 84. Specimens after the compression test

- *Brazilian test (indirect tensile strength)*

Results and pictures of the samples after the test are reported in Table 32 and Figure 85. The averaged tensile strength was evaluated in 3.5 MPa. Results are in agreement with previous laboratory tests reported in Ribacchi and Tommasi (1998) and slightly lower to the range of values (between 3 and 10 MPa) reported in D'Ambra et al. (2004). In saturated conditions the specimens tested by Ribacchi and Tommasi (1998) showed a lower tensile strength (0.5-1.5 MPa).

Table 32. Results of the Brazilian tests

Sample	Diameter (mm)	Height (mm)	Mass (g)	Apparent density (Kg/m3)	F max (kN)	σt (MPa)
6	82.5	40.5	563.95	2605	17.48	3.3
6A	82.3	39.6	556.05	2640	24.89	4.9
11A	82.7	39.5	555.38	2618	19.24	3.7
11B	82.8	38.7	541.78	2600	17.85	3.5

| 14 | 83.3 | 40.1 | 583.95 | 2672 | 18.68 | 3.6 |
| 10 | 82.2 | 40.6 | - | - | 10.24 | 2.0 |
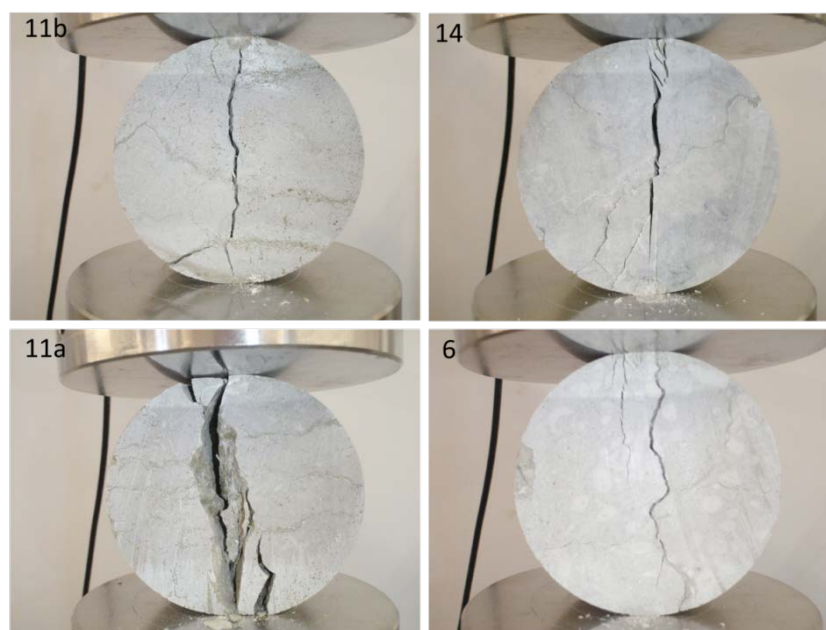
Figure 85. Specimen after the Brazilian test

- *Geomechanical characterization of discontinuities*

Cohesion and friction angle of the mapped joint sets are reported in Table 33, Table 34, Table 35, Table 36 and Table 37, subdivided for each of the areas individuated in the structural analysis. The friction angle varies between 33° and 35°, while the cohesion between 0.018 and 0.032 MPa.

Table 33. Cohesion and friction angle estimated on the base of JRC and JCS, 2006 landslide area

Set ID	JRC	JCS (MPa)	Cohesion (MPa)	Friction
TN1	8.6	40.3	0.029	34.7
TN3	9.0	38.3	0.03	34.7
TN4	10.0	39.7	0.031	34.9
TNV	7	26.3	0.026	33.5

Table 34. Cohesion and friction angle estimated on the base of JRC and JCS, North Western edge

Set ID	JRC	JCS (MPa)	Cohesion (MPa)	Friction
TN1	13	23.5	0.031	34.0
TN3	15	35	0.031	34.7
TN4	13	12	0.029	32.7

Table 35. Cohesion and friction angle estimated on the base of JRC and JCS, South cliff

Set ID	JRC	JCS (MPa)	Cohesion (MPa)	Friction
TS2	15	24.5	0.03	34.0

TS6	10	23.2	0.03	33.8
TS5	11	37.4	0.032	34.9
TSV	13	33.7	0.032	34.7

Table 36. Cohesion and friction angle estimated on the base of JRC and JCS, South Eastern edge –

survey 4

Set ID	JRC	JCS (MPa)	Cohesion (MPa)	Friction
TS1	9	38	0.030	34.6
TS2	12	35	0.032	34.8
TS3	13	46	0.032	35.3
TS5	7	37	0.026	34.1
TS6	10	47	0.031	35.2
TS7	6	52.5	0.024	34.3

Table 37. Cohesion and friction angle estimated on the base of JRC and JCS, South Eastern edge –

survey 5

Set ID	JRC	JCS (MPa)	Cohesion (MPa)	Friction
TS1	4	50	0.018	33.1
TS2	16	35	0.031	34.6
TS3	-	31	-	-
TS5	14	38	0.032	34.9
TS6	16	25	0.030	34.0
TS7	14	41	0.032	35.1

3.5 **Discussion**

Laboratory tests on slope materials samples and field data collection have been used to derive the main physical and mechanical characteristics of the clay-shale substratum and of the rock slab. A particular attention has been paid on the interaction between the clayey materials and water.

The tectonic processes and the landsliding phenomena which affected the geological units caused a marked heterogeneity of its properties (Ribacchi and Tommasi 1998). Thus a large number of test should be considered for a complete characterization of the clay-shale material. The characterization of the clay-shale is still ongoing, and preliminary results are shown. Anyway, the presented work, together with other data, can contribute to improve the knowledge about these materials and to examine the soil behaviour from various point of view, e.g. in the unsaturated soil framework.

Based on the grain size distribution, the Argille Varicolori substratum can be classified as a silty-clay, containing the 44% of clay (diameter<0.002 mm) and the 66% of silt (0.002mm<diameter<0.063). Atterberg tests allow to define an high degree of activity for the soil. The results are related to the composition of the same, mostly formed by Montmornillonite, Kaolinite and Illite (Ribacchi and Tommasi 1998). The presence of these minerals can explain also the swelling behaviour, measured and quantified in different oedometer test and in the preparation of the specimen for the SWCC. Swelling

and shrinkage related to wetting and drying cycles can promote the degradation of the mechanical properties of the material (Meisina et al. 2006; Picarelli 2000) and changes in the structure of the soil (Vogel et al. 2005). Moreover water infiltration in these almost impermeable soils is facilitated by cracking due to shrinkage. In fact, in the drought period, a well-developed network of shrinkage-induced cracks is clearly visible in the clayey substratum. Water infiltrations during rainy periods preceded by dry seasons can promote the triggering of shallow landslides (Meisina et al. 2006). In conclusion, the high plasticity and activity of the clayey soils control their strength properties, promoting slope instability.

The most significant properties of the rock mass were evaluated, both for rock specimens and for discontinuities. Results are in agreement with previous works. Scale factor and others influencing boundary conditions have to be considered when inserting these values in numerical models, anyway the present work contributes to the estimation of the rock mass strength parameters. Horizontal boreholes performed in the 60's and reported in D'Ambra et al. (2004) showed an intense degree of fracturing even at horizontal depths of 25 m from the cliff face. The same behaviour was observed in the inclined boreholes performed after the 2014 landslide. Based on geomechanical surveys and literature data a strong influence of the discontinuities properties on the rock mass behaviour can be inferred.

HYDROGEOLOGICAL CHARACTERIZATION

4.1   **Introduction**

As previously mentioned, several hypotheses were made on the factors influencing the lateral spreading of fractured brittle rock masses laying on more ductile terrains. The groundwater processes developing within the more permeable units (i.e., the jointed rock slab) have not been extensively investigated as eventual predisposing and/or triggering factors for the instability phenomena yet.

By focusing on the slabs from northern Apennines of Italy, they are normally characterized by intensively fractured rock masses. In several cases, as a result of this well-developed network of discontinuities within the rock mass, the secondary permeability can be much higher than the one characterizing the clay-shales. If the recharge area, represented by the top of these slabs, is large enough, they can act as reservoirs (Cervi et al. 2014), feeding perennial and/or ephemeral springs developing at the contact between the slab and the underlying units. The aquifer hosted in the slab can play a role in the developing of the slope instability mechanisms, i.e. locally increasing the pore-water pressure, influencing the stresses acting in the slab and in the underlying clay. Moreover, the springs developing at the contact aquifer-aquiclude, can promote the softening of the basal ductile terrains and subsequent accelerated erosion processes, as illustrated in Chapter 3. With time, this leads, together with earthflows, to the progressive undermining of the foot of the rock slab, causing rock falls in the overhanging cliffs. In Borgatti et al. (2015) the undermining of the slab was indicated as a predisposing factor for the onset of large-scale slope instability processes. Beside the work carried out by (Tazioli et al. 2012) on the Orvieto rock slab, in which the characterization was mainly focused on the hydrochemical and isotopic aspects of groundwater, the hydrogeological characteristics of these kinds of aquifers have not been fully investigated yet.

The San Leo case study can bring further insights for the understanding and the assessment of groundwater processes taking place in this geological context. A first simplified model of the slab was developed with the finite element code FEFLOW (Wasy). The rock matrix and the fractures were considered as a continuous medium, characterized by equivalent hydrodynamic properties, as suggested in the Equivalent Porous Media (EPM) approach (Bear 1972). Discontinuity characteristics (orientation, spacing and aperture) and major fault zones localization, gathered from geotechnical and TLS surveys and described in Chapter2, were then used to estimate the permeability tensor for different areas of the slab. This model was calibrated by approximating the piezometric surface with the discharge areas mapped on the field.

The model confirms the existence of an aquifer in the slab. The resultant piezometric surface was inserted in the stability analysis described in Chapter 5. Furthermore, with the aim of gathering more data to validate the model and to achieve a better understanding of the hydrogeological behaviour of

this medium, starting from 2014, in-continuous discharge and piezometric monitoring has been carried out and is still ongoing. Slug tests have been performed to infer the rock mass hydraulic conductivity. Maximum yields of the aquifer have been calculated to obtain data for further analyses, such as tracing injection.

4.2 Groundwater flow in fractured media

Water flow through fractured units is generally one of the most challenging issue for hydrogeologists (Neuman 2005). In fact, the spatial heterogeneity characterizing these media complicates the description of the flowing mechanisms.

Two kinds of permeability can be individuated: the primary permeability refers to the rock matrix, while the secondary one is developed because of the presence of discontinuities and includes all the groundwater flow along fractures and cavities. Where the latter occurs, it is generally the predominant type of permeability and the term related to the matrix can often be neglected. Furthermore faults and fractures may play an important role in groundwater recharge and flow, acting whether as permeable or impermeable barriers depending on the filling material. In fault-damaged zones (Figure 86) the overall permeability is influenced by the host-rock permeability and by the macro-scale fracture networks (Faulkner et al. 2010). Generally, in low porosity rocks, the latter is dominant (Balsamo et al. 2010).
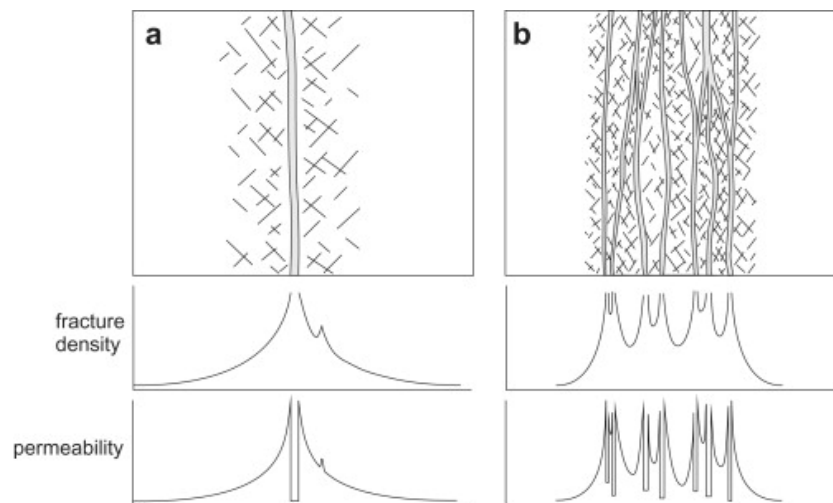

Figure 86. Examples of permeability related to fracture density in fault zones: (a) Single fault core and (b) multiple fault core (Faulkner et al. 2010)

Flow quantification in these media can be achieved by coupling discontinuities geometric data with pressure, flow or tracer tests (Neuman 2005). In fact, laboratory tests are generally not appropriate to characterize hydrological features of fractured rock, due to the scale influence and to the in situ stress and flow distribution, not easily replicable in a small sample. Time series analysis of hydrogeological data can be used to obtain information about the behaviour of the system. In the lasts decades statistic has been recognized as a powerful tool to examine groundwater systems, describing quantitatively the acting processes and detecting time series properties, e.g. the presence of trends and the cross-correlation between spring discharge and rainfall. A comprehensive review about time series analysis in

hydrogeology is reported by (Machiwal & Jha 2006). In addition, the analysis of spring hydrographs, showing the discharge temporal variation, and particularly the examination of the recession curve, has been widely used, e.g. to separate distinct flow components or estimate the storage capacity of the aquifer (Amit et al. 2004).

Considering a fractured rock mass, the permeability value mainly depends on the aperture of the discontinuities, on the spacing and on the interconnection between them. In such anisotropic media, the direction of the groundwater flow can be described using a permeability tensor, calculated on the basis of the discontinuities orientations (Kiraly 1969; Louis 1974; Scesi & Gattinoni 2009). Knowing these input data, the groundwater flow can be modelled using several approaches. Theory, background and reviews of fractured aquifers modelling can be found in Berkowitz (2002) and Neuman (2005).

Generally, hydrogeological models can be classified in lumped parameter and distributed models (Kovács & Sauter 2007). The lumped parameter models are also known as black or grey-box, where the colour represents the level of knowledge (completely unknown or partially known) of the system (Hao et al. 2006). Global transfer functions are here used to describe the flow and transport processes (Bodin et al. 2012). Time-series analysis methods (Rimmer & Salingar 2006; Bailly-Comte et al. 2008) or multi-reservoir systems (Geyer et al. 2008; Fleury et al. 2009) can be used. These approaches are generally well-suited to relate the response of the aquifer with a succession of input events, but they cannot handle spatial variability. Different approaches are suitable to simulate the groundwater flow in a fractured media using distributed models. The Equivalent Porous Media (EPM) approach (Bear 1972; Louis 1974) allows to consider rock matrix and fractures as a continuous medium, characterized by equivalent hydrodynamic properties over a volume that is sufficiently large to be considered statistically representative (Representative Volume Element or REV; Long et al. 1982; Kanit et al. 2003). Otherwise, a Discrete Fracture Network (DFN) (Long et al. 1982; Schwartz et al. 1983; Shapiro & Andersson 1985; Wang et al. 2001) explicitly represents the discontinuity characteristics, i.e. position, spacing, persistence and connectivity while the matrix medium is assumed to have negligible permeability. Hybrid models combine elements from both the approaches allowing to simulate the hydraulic relationships between matrix and the fracture network (Andersson 1987; Cacas 1990; Renz et al. 2009). In all the cases the data description can be deterministic or stochastic.

The balance between the complexity degree of the model and the available calibration data has been recognized as a critical issue by several authors (Wagener et al. 2001; Simmons et al. 2011; Bodin et al. 2012): an oversimplification may lead to the loss of important processes, while a very complex model requires a lot of effort in collecting and producing input data. Moreover, this effort does not always correspond to an equal improving in the quality of the results, being thus not strictly necessary to describe the main investigated mechanisms. DFN and Hybrid models are expensive in term of required parameters: a careful gathering of the geometric and hydrodynamic properties of distinct fractures is at the base of the model set-up and so they are used only in small test sites or at very detailed scale.

The EPM approach is recognized to be sufficiently accurate when large domains have to be modelled (Mun & Uchrin 2004), i.e. when the REV volume is exceeded. This approach has been successfully used by several authors for simulating groundwater flow in hard rock aquifers (Pankow et al. 1986; Gburek et al. 1999; Rayne et al. 2001; Dafny et al. 2010).

4.3   **Materials and methods**

Field and TLS surveys, monitoring data, in-situ tests and numerical simulations has been used to investigate the behaviour of the aquifer hosted in the slab. A first estimation of the equivalent hydraulic conductivity of the fractured slab was reached using the discontinuities parameters measured both in the field and using TLS-derived data (Chapter 2), through the calculations of the hydraulic conductivity tensors. Furthermore the observation and analysis of the rock mass permitted to hypothesise a control by the main structural lineaments, e.g. faults, on the groundwater flow. A first EPM numerical model was developed and calibrated based on the available data, e.g. the main fracture characteristics and the discharge areas. The results permit to confirm the presence of a groundwater flow inside the San Leo slab and to derive the mean equivalent hydraulic conductivity and storativity of the whole rock mass. Later on, an in-continuous discharge and piezometric monitoring system has been installed. The statistical analysis of the gathered data and the results of field tests permit to calculate some of the hydrogeological properties of the aquifer, as the hydraulic conductivity and the maximum yield.

4.3.1   Determination of the equivalent hydraulic conductivity

According to the EPM approach, the rock and the fractures can be considered as an equivalent medium. The rock mass permeability is mostly due to the water flow along discontinuities and can thus be evaluated from the discontinuities characteristics, e.g. aperture and spacing, applying the formula proposed by Snow (1969):

$$k_i = \frac{e_i^3 f_i g}{12 v}$$

Where:

k = hydraulic conductivity (m/s)

e = average discontinuity aperture (m)

g = gravity acceleration (m/s^2)

f = average frequency (1/m)

v = water kinematic viscosity at 20° (10^{-6}m^2/s)

To take into account also the discontinuities orientation, the hydraulic conductivity tensor was estimated, following the methodology described in Kiraly (1969) and in Scesi and Gattinoni (2009). It can be expressed as:

$$\bar{\bar{k}} = \sum_{i=1}^{m} [(e_i^3 \, g f_i)/12v] A_i$$

Where:

$\overline{\overline{k}}$ = hydraulic conductivity tensor (m/s)

$A_i = (\overline{\overline{I}} - \overline{n} \otimes \overline{n})$ = orientation tensor

$\overline{\overline{I}}$ = identity matrix

$\overline{n}$ = normal vector to the discontinuity plane

With the aim to classify areas with a similar hydrogeological behaviour, the slab was subdivided in sectors, based on structural data and field evidence; for each sector a hydraulic conductivity tensor was calculated, based on the data gathered in the area. In addition, this analysis permitted the more permeable areas to be individuated and the eventual control exerted by the structural features of the slab on the groundwater flow pattern to be highlighted.

In particular, firstly the discontinuities mapped with geomechanical field surveys and the ones derived from the TLS point cloud of the same area were compared to identify the main joint sets. Some of the joint sets derived from the TLS analysis were grouped together, due to their similar hydrogeological characteristics, to avoid the introduction of an unnecessary degree of complexity in the model.

Aperture and frequency data were calculated from the geomechanical field surveys, while joint set orientation was derived from the TLS structural characterization.

Then, the normal vector of each joint sets was calculated from the values of dip and dip direction of the joint set. Expressing the dip (α) and dip direction (β) in radians:

$$n_x = \begin{cases} -sen\alpha sen\beta & if\ \beta < \pi \\ sen\alpha sen(2\pi - \beta) & if\ \beta > \pi \end{cases}$$

$$n_y = \begin{cases} -sen\alpha cos\beta & if\ \beta < \pi \\ sen\alpha cos(2\pi - \beta) & if\ \beta > \pi \end{cases}$$

$$n_y = -cos\alpha$$

The orientation tensor derived for the different joint sets were then multiplied for the hydraulic conductivity of each set and summed to obtain the hydraulic conductivity tensor. The eigenvalues (K_1, K_2, K_3) and eigenvectors of the obtained matrix represent the three main hydraulic conductivities and their orientation in space. The equivalent hydraulic conductivity of the rock mass can be estimated as:

$$k_{eq} = (k_1 k_2 k_3)^{1/3}$$

Applying the following formulas to the eigenvectors (x_i, y_i, z_i) was possible to calculate the plunge ($\propto$) and strike (β) of the pole of the main planes:

$$\propto_i = arcsen|z_i|$$

$$\beta = tan^{-1} \left| \frac{x_i}{y_i} \right|$$

Corrections has to be applied to the β value, depending from the sign of the eigenvector terms (x_i, y_i and z_i, *Table* 37)

Table 38. Values to add to β (Zi is assumed ≥0, when it results < 0 the same corrections can be used, inverting the sign of each term of the eigenvectors)

x_i	y_i	correction
≥0	≥0	+180°
≥0	<0	+270°
<0	<0	-
<0	≥0	+90°

The resulting conductivities principal directions, described by the eigenvectors, are turned against the global Cartesian coordinate system by a rigid body rotation (Figure 87), which can be described by a rotation matrix. This matrix describes three successive rotation, performed in a specific sequence. It is formed by the directional cosines of the rotation angles, called Eulerian angles (ϕ, θ, ψ).
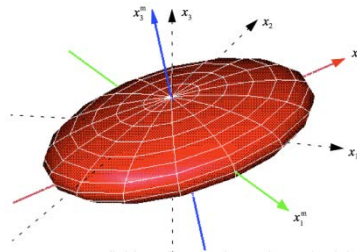

Figure 87. 3D anisotropic conductivity as defined in FEFLOW reference manual

The choice of rotation angles is arbitrary, as long as successive rotations are performed on different axes. The Feflow software uses a ZX'Z'' convention ($x_3 ξ' x_3^m$, as defined in Figure 88) following the Goldstein et al. (2001) definition:

- firstly the initial system is rotated by an angle Φ counter clockwise about the x_3 axis. The resultant system is defined as ξηζ, where $ζ = x_3$;

- then the axes are rotated by an angle θ counter clockwise around the ξ axes (line of nodes) and the resulting intermediate system is named ξ'η'ζ', where ξ'= ξ;

- finally the ξ'η'ζ' system is rotated counter clockwise by an angle ψ about the ζ' axis. The resulting coordinate system is $x_1^m x_2^m x_3^m$.

The angle Φ can thus be described as the angle between the x_1 axes and the intersection of the plane containing the x_1 and x_2 axes with the plane containing the x_1^m and the x_2^m axes, usually named "line of nodes". The angle θ is comprised between the axis x_3 and the x_3^m, while the angle ϕ is defined as the angle between the line of nodes and the x_1^m axes. Figure 88 illustrates the stages of the transformation.
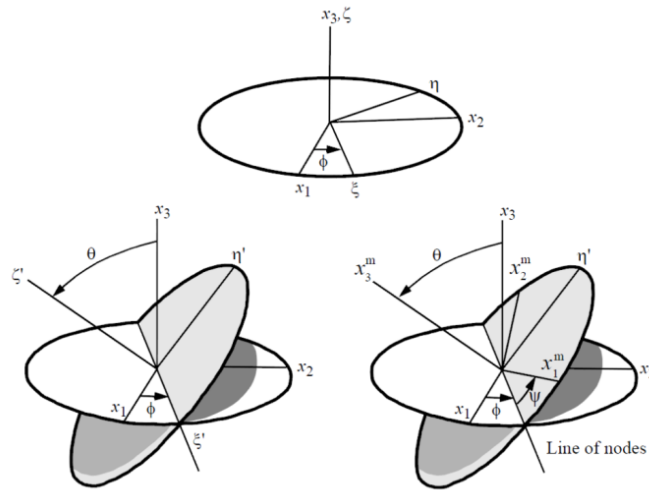
Figure 88. The rotations defining the Eulerian angles (FEFLOW Reference Manual)

The complete rotation matrix can be obtained as the triple product of the separate rotations:

$$A = \begin{bmatrix} a_{11} & a_{12} & a_{13} \\ a_{21} & a_{22} & a_{23} \\ a_{31} & a_{32} & a_{33} \end{bmatrix} = \begin{bmatrix} cos\psi cos\varphi - cos\theta sen\varphi sen\psi & cos\psi sen\varphi + cos\theta cos\varphi sen\psi & sen\psi sen\theta \\ -sen\psi cos\varphi - cos\theta sen\varphi cos\psi & -sen\psi sen\varphi + cos\theta cos\varphi cos\psi & cos\psi sen\theta \\ sen\theta sen\varphi & -sen\theta cos\varphi & cos\theta \end{bmatrix}$$

The Eulerian angles can be calculated using the function atan2, by applying the following relation:

$$\theta = ATAN2(\sqrt{a_{13}^2 + a_{23}^2}, a_{33})$$

$$\psi = ATAN2(a_{31}, a_{32})$$

$$\varphi = ATAN2(a_{13}, -a_{23})$$

or by inserting the principal directions in a 3D environment code and measuring directly the angles. In particular, the atan2 (or the atan2d, which express the results in degrees) function returns the four-quadrant inverse tangent (tan^{-1}) of the arguments, which must be real. In contrast to the classical arctangent function, atan2 is not subject to the indeterminacy between the first and the third quadrant. For each positive constant value a:

$$atan2(a\,sin(\alpha), a\,cos(\alpha)) = \alpha \qquad with\ \alpha \in [0, 2\pi)$$

The Eulerian angles of each calculated hydraulic conductivity tensor were used to characterise the different areas. Furthermore, an average equivalent hydraulic conductivity was estimated and inserted, as a starting value, in the numerical model.

4.3.2 Numerical model

In order to estimate the groundwater level inside the slab and the hydrogeological properties (permeability and storativity) of the rock mass, a numerical simulation has been set-up. Several data were collected: the topography of the area, the rainfall distribution, the springs localization and the discontinuity sets crossing the rock mass. This dataset permits to build a hydrogeological model of the rock slab, using an Equivalent Porous Medium (EPM) approach. Due to the large-scale test-site and to the lack of further parameters which can help in the calibration step (in-continuous spring discharges and groundwater levels data inside the slab), the EPM approach was selected. The hydrogeological

simulation was performed by using the 3D finite-element code Feflow (Diersch 2005). Firstly, the hydrogeological model was used to estimate the mean groundwater surface inside the slab. Then the effective daily rainfall (corrected with Penman-Monteith formula, modified by Allen et. al, 1998 and land cover data) from 1st October 2013 to 27th February 2014 (Figure 90) was inserted in the model, to simulate the fluctuation of the piezometric surface before the 2014 landslide.

4.3.2.1   Model geometry

The geometry was built using topographic and structural data. The first ones derived from the work carried out by the Marche Region in 1998. An aerophotogrammetic survey allowed to obtain the 1m*1m DTM of the area. The domain is about 0.329 km^2 and 100 m high. The structural data originate from several geognostic and geological surveys. More in detail, five boreholes were drilled in 1972 and 2001 near the borders of the slab, and three of them entirely crossed the calcarenites from the top up to the substratum (fig. 3b). The 1:2000 scale geological survey carried out by Badioli (2012) was used to map the contact between the slab and the clay-shales along the border of the cliffs. These data allowed to interpolate the contact surface over the whole area. Due to its lower permeability if compared with the fractured rock slab, the clay-shale substratum was assumed as impermeable and so it has not been considered in the model geometry. The 3D grid mesh is composed of 14,412 nodes and 14,296 prismatic elements and is refined in the steepest areas. Only one layer was used in the analysis.

4.3.2.2   System recharge

The rainfall and temperature data were collected by the San Marino raingauge, located 9 km north-eastward of San Leo, at an elevation of 670 m a.s.l. Data cover a period of 10 years (2001-2011). Mean annual effective rainfall has been estimated by using the Thornthwaite-Mather evapotranspiration formula.

For the period from October 2013, i.e. the begin of the hydrological year, to the day of the rock fall (27th February 2014), the effective daily rainfall has been estimated using the Penman-Monteith formula (modified by Allen et al. 1998) and the land cover database of the Emilia-Romagna Region (RER, http://geoportale.regione.emilia-romagna.it/it/catalogo/dati-cartografici/pianificazione-e-catasto/uso-del-suolo).
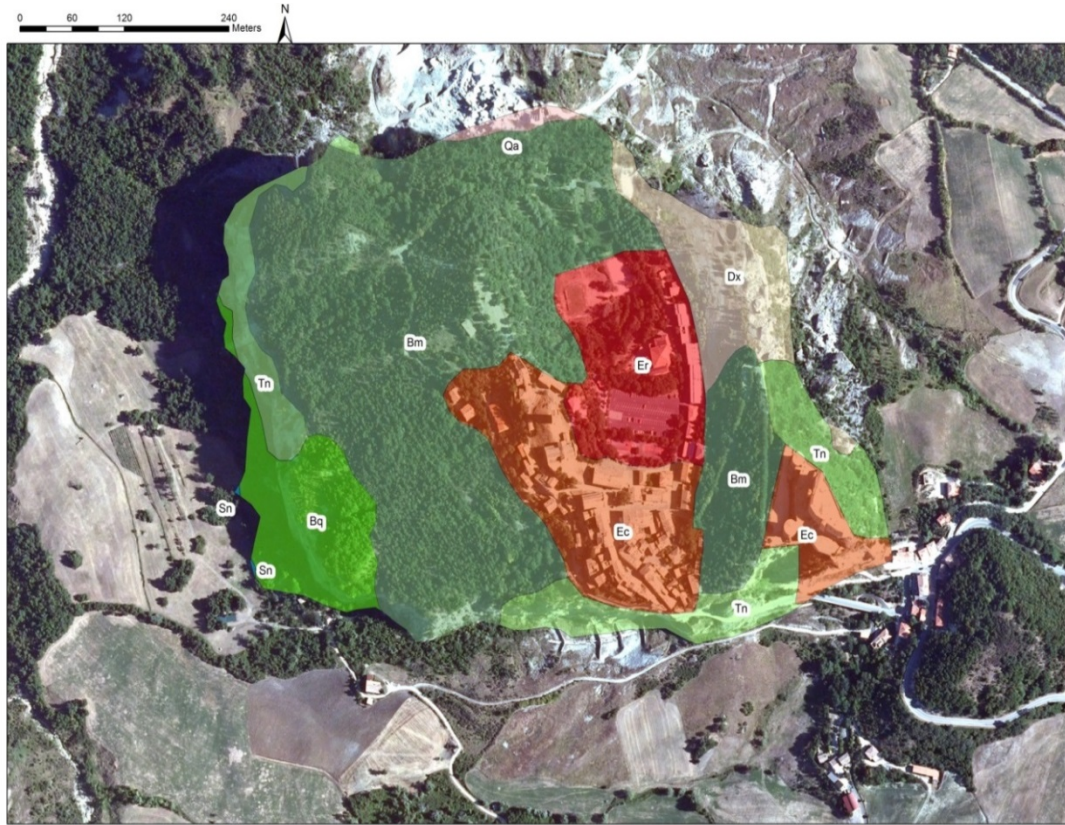
Figure 89. Land cover classification: Ec= continuous urban fabric, Er= discontinuous urban fabric, Qa= mineral extraction site, Sn= non irrigated arable land, Bq= Broad leaved forest, Bm= mixed forest, Dx= sparsely vegetated area, Tn= shrub and/or herbaceous vegetation

The weather data were collected by the Pennabilli raingauge (11 km South-Westward of San Leo, 627m a.s.l.). In particular the following parameters were taken from the ARPA website (Agenzia Regionale Per la Protezione Ambientale, www.arpa.emr.it):

- daily rainfall (mm/d);
- mean daily temperature (°C);
- minimum daily temperature (°C);
- maximum daily temperature (°C);
- mean wind velocity at 10 m above the ground (m/s);
- solar radiation (MJ/dm^2).

The mean wind velocity at 2 m above the ground, requested in the Penman-Monteith formula, was interpolated from the available data following the logarithmic relation reported in Greppi (2005).

Only the humidity data that were not available for the Pennabilli raingauge were collected from the Cusercoli weather station (about 30 km NW from San Leo, 330 m a.s.l.). The land use and cover classes derived from the RER database were used to estimate the evaporation or evapotranspiration coefficients following the Allen et al. (1998) and Papini et al. (2008) recommendations.

The cumulative total rainfall amount for the recharge period between October 2013 and February 2014 was approximately 20% higher compared with the mean one detected in the same period of the years between 2002 and 2013.

System recharge was simulated by applying the mean daily effective rainfall over a period of 30 years until the steady state was reached, as suggested by Vincenzi et al. (2010). To simulate the water surface change preceding the 2014 rock fall the effective daily rainfall from October 2013 to the 27th of February 2014 (Figure 90) was inserted in the model after the calibration phase, using the transient simulation mode.
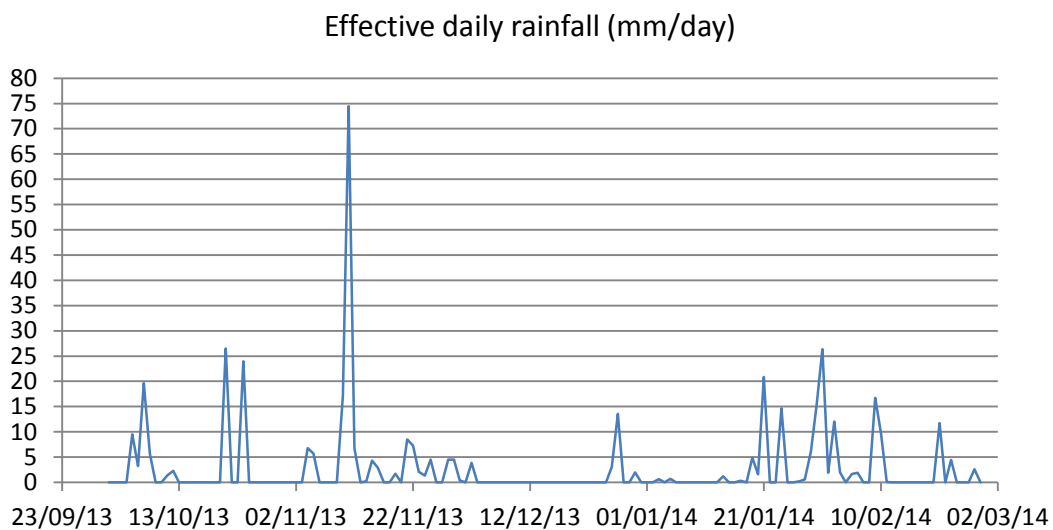

Figure 90. Effective daily rainfall in the period antecedent the 2014 rock fall (1st October 2013 -27th February 2014)

4.3.2.3   Models parameters and calibration

Applying the relationship proposed by Kiraly (1969) and Louis (1974) the initial values of the equivalent hydraulic conductivity was derived from the geomechanical surveys results. At this stage of the work only the mean equivalent hydraulic conductivity value was inserted in the model, not considering the direction of the flow, i.e. the orientation of the hydraulic conductivity tensor. Only a first approximation of the conductivity tensor was attempted, assigning a greater value (double than the others) in the z-direction. This permits to take into account the results of the TLS analysis, showing a main vertical orientation of the discontinuities. The initial storativity was assumed similar to the values reported in the literature for similar calcarenitic slabs in northern Apennines (about 2%; Cervi et al. 2015). A Dirichlet boundary condition (1st type, Hydraulic Head in Feflow) was assigned to the external perimeter of the slab. This specifies a hydraulic head at each node. This condition was constrained with the seepage face option, which implies that the hydraulic head at the node is considered equal to its elevation. The Feflow software permits to set a maximum or minimum flow rate for the nodes on which the previous boundary condition was applied. To avoid any inflow at the boundary (the external perimeter) a maximum value of 0 m[3]/d was chosen (inflow is considered positive).

A survey was conducted during the low-flow period (end of June 2013). It allowed to map several perennial springs outflowing mainly at the contact between the slab and the underlying clay-shales (Figure 92).

Figure 91. One of the main springs outflowing at the contact between the clay/shales and the rock slab
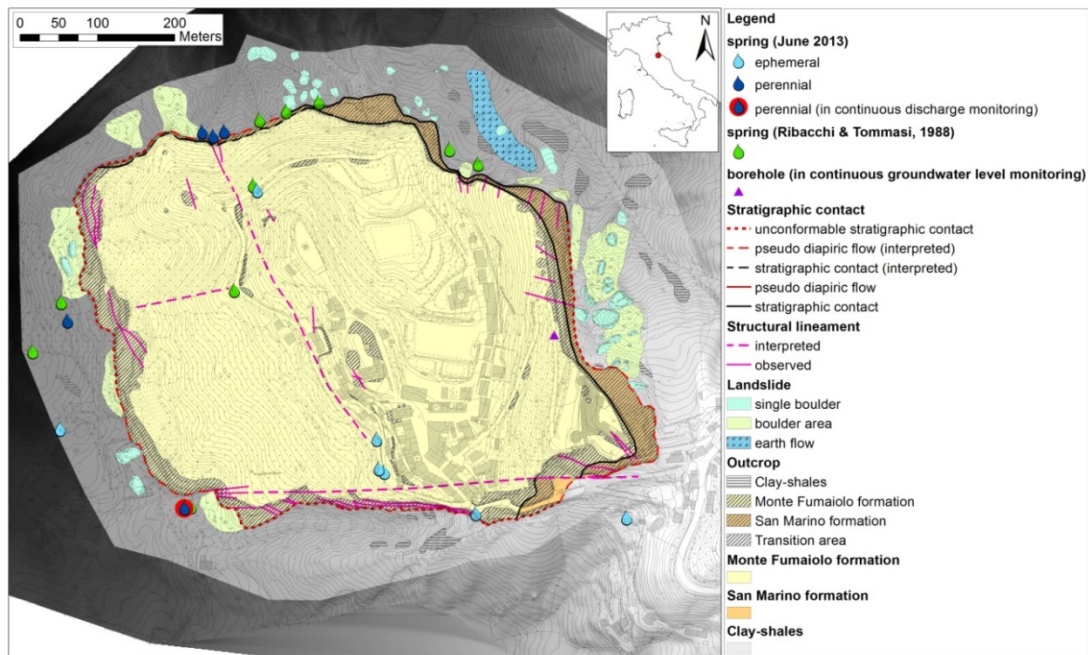

Figure 92.Geological, structural and hydrogeological elements of the San Leo slab.

Hydraulic conductivity and permeability were calibrated by approximating the piezometric surface with the discharge areas mapped on the field and validated by using the springs previously mapped by Ribacchi & Tommasi (1988). Model has been considered as calibrated when springs location exactly match the piezometric surface.

4.3.3   Monitoring data

Starting from 2014 in-continuous discharge and piezometric monitoring has been carried out and is still ongoing. The hydrogeological features of the San Leo slab were analysed by means of spring-discharge analysis, piezometric monitoring data and slug tests. The maximum spring yield and the depletion coefficient of the different systems contributing to the spring discharge were calculated applying the exponential model proposed by Maillet (1905). Hydraulic conductivity values were estimated analysing the slug tests drawdown curves with the Bouwer and Rice solution (1976). Time-series analyses such as Autocorrelation and Cross-correlation between discharge rate, piezometric data and rainfall datasets were used to better understand the groundwater behaviour within the rock slab and to estimate its response to rainfall regime.

4.3.3.1   Spring discharge analysis

One of the three perennial spring, located in the South-Western side of the slab (Figure 92), has been monitored since the end of April 2014, with a specific gauge equipped with an electric transducer (Figure 93).

Figure 93. Discharge-gauge equipped with an electric transducer

The discharge gauge collected the inflowing water in a first deposition chamber, where the smallest particles can deposit, then flows in a second chamber, where the electric transducer measures continuously the water height. Finally, the water passes through a triangular channel section, known as V-notch weir. The discharge-gauge works according to the basic principle that the discharge is proportional to the water head above the bottom of the weir. Usually, V-notch weirs are preferred for low discharges because they allowing small changes in discharge to have a large change in depth, compared to rectangular weirs. The Thompson relation (Citrini & Noseda 1987) was applied to calculate the discharge values (Q) from the water head measurements (h_0).

$$Q = 1.42 h_0^{2/3}$$

The acquisition time was initially set at 1 day, from the 20th of April 2014 to the 19th of June 2014. In the subsequent period, from the 19th of June 2014 to the 23rd of December 2014, the time step was changed to 1h. Then data were acquired every 10 minutes, with the aim to register all the hydrogeological processes. The spring discharge recession curve was analysed to infer the depletion coefficient α, as defined by the exponential model proposed by Maillet (1905):

$$Q_t = Q_0 e^{-\alpha t}$$

where Qt is the discharge at time t, Q0 is the discharge at time t0 (beginning of the discharge period). Plotting the data in a semilogaritmic Q-t graph, the slope of the curve (α) is proportional to the hydraulic conductivity of the system, while the intercept represent the discharge at time t0.

In Apenninic springs, recession curves are usually composed of two parts, a steeper one (falling curve) followed by a gentler portion (depletion curve), fed by different portions of the aquifer (Cervi et al. 2014). By analysing separately the two parts, it is possible to derive the contribution to spring discharge of each portion of the aquifer (Celico 1988). The two sectors are characterized by different depletion coefficients (α1 and α2). Bousinessq (1904) proposed to fit the whole recession curve with the sum of two exponential part; successively several authors (Mero 1964; Forkasiewicz & Paloc 1967) generalized the Bousinessq formula using a sum of N components:

$$Q_t = \sum_{i=1}^{N} Q_{0_i} e^{-\alpha_i t} = Q_{0_1} e^{-\alpha_1 t} + Q_{0_2} e^{-\alpha_2 t} + \ldots + Q_{0_N} e^{-\alpha_N t}$$

Where Q_{0i} is the initial discharge of the its component at time t_0.

The Maillet exponential model was used to fit the data of the late discharge period, when only the depletion baseflow was supposed to be active. Results were used to remove the effect of this component in the first period and the procedure was repeated for the more permeable system.

The total volume stored in the aquifer at the beginning of the discharge period W_0 and the amount of water drained from the spring during the recession period ΔW (m³) were calculated following Amit (2002) and Civita (2005):

$$W_0 = \int_0^\infty Q_t \, dt = \sum_{i=1}^{N} \frac{Q_{0_i}}{\alpha_i}$$

$$\Delta W = \int_0^1 Q_t \, dt = \sum_{i=1}^{N} \frac{Q_{0_i}}{\alpha_i} (1 - e^{-\alpha_i t})$$

where the discharge values are expressed in m³/d.

4.3.3.2   *Piezometric data and slug tests*

As anticipated, after the landslide occurred on the 27th of February 2014 a borehole was drilled in the North-Eastern sector of the slab, in the vicinity of the crown area, reaching the depth of 111 m across the calcarenitic units (Figure 92). It has been equipped with an open-pipe piezometer, which is slotted for the entire length. Piezometric data have been acquired since the 31st of October 2014 with a time step set to 1 h. After the 23rd of December 2014 the time step was changed to 10 minutes, to allow the

correlation with the spring discharge data. A first comparison with the hourly rainfall data was carried out. The latter was obtained by applying an Inverse Distance algorithm on datasets from 4 raingauges, located around San Leo (San Marino, Maiano, Ponte Verucchio and Pennabilli, Figure 94).
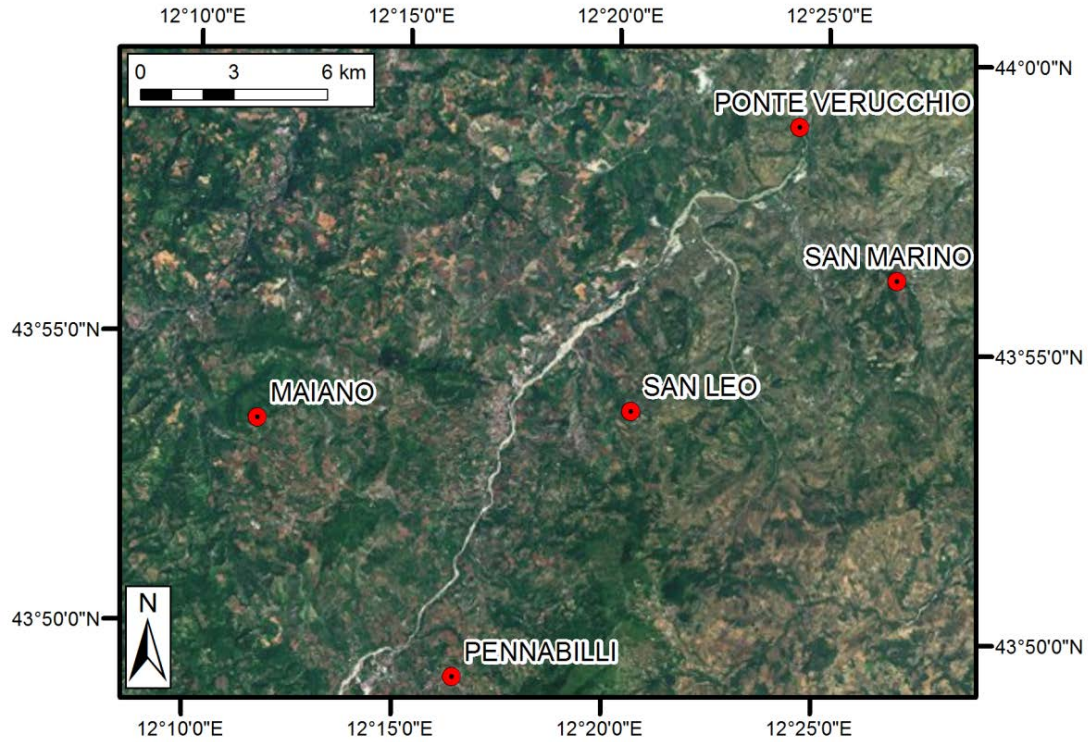

Figure 94. Location of the 4 raingauges, located around San Leo (San Marino, Maiano, Ponte Verucchio and Pennabilli) used for the IDW rainfall interpolation

Moreover, two slug tests were conducted in the piezometer. They consisted in the injection of 25 and 30 litres of water, respectively. Drawdown curves were acquired with a time-step of 5 seconds. The results were analysed with the AQTESOLV software (Duffield 2007), using the Bouwer and Rice (1976) and Hvorslev solution (1951), to determine the hydraulic conductivity of the fractured medium.

Both methods employ a quasi-steady-state model to empirically describe the water-level response in a unconfined aquifer due to the instantaneous water injection or withdrawal. When the resulting data exhibit curvature, Butler (Butler 1997) suggests the use of a normalized head range to overcome the resulting ambiguity and improve the line to curve fitting. Visual curve matching was thus preferred to the automatic matching option. In fact this method is retained more effective in fitting a specific range of data (Duffield 2007).

Table 39. Recommended normalized head ranges for straight line matching using the Hvroslev and Bouwer and Rice solutions, modified from (Butler 1997).

Solution Method	Recommended Normalized Head Range for Straight Line Match
Hvorslev (1951)	0.15 to 0.25
Bouwer-Rice (1976)	0.20 to 0.30

4.3.3.3   Time series analysis: auto and cross-correlation

Autocorrelation tests were conducted on the spring discharge and on the piezometric data. Daily and hourly data were used. The series is defined as autocorrelated if a value is affected by the past ones (Davis 2002), meaning a memory effect of the system. Moreover, cross-correlation test were conducted to infer the time lag between the rainfall and the response of the aquifer. Both piezometric and discharge data series were tested against the rainfall, i.e. the independent variable, after the removal of trends. The latter procedure is required as the time-series procedures are based on the assumption that the slope of the regression on time is zero, so that no tendency exists (Davis 2002). For the daily data the effective rainfall calculated using the Penman-Monteith equation (modified by Allen et. al 1998) was used. Unfortunately, not all the requested parameters were available with a lower time step. Hence, the hourly monitoring data were compared with the rainfall calculated by applying the Inverse Distance algorithm.

The time lag found analysing the cross-correlation between rainfall and the variation in the piezometric surface was used to estimate a mean hydraulic conductivity value for the non-saturated part of the rock mass.

4.4   **Results**

4.4.1   Determination of the equivalent hydraulic conductivity

Areas with different characteristics were individuated and an equivalent hydraulic conductivity (modulus and tensor) was estimated for each of them (Figure 95).
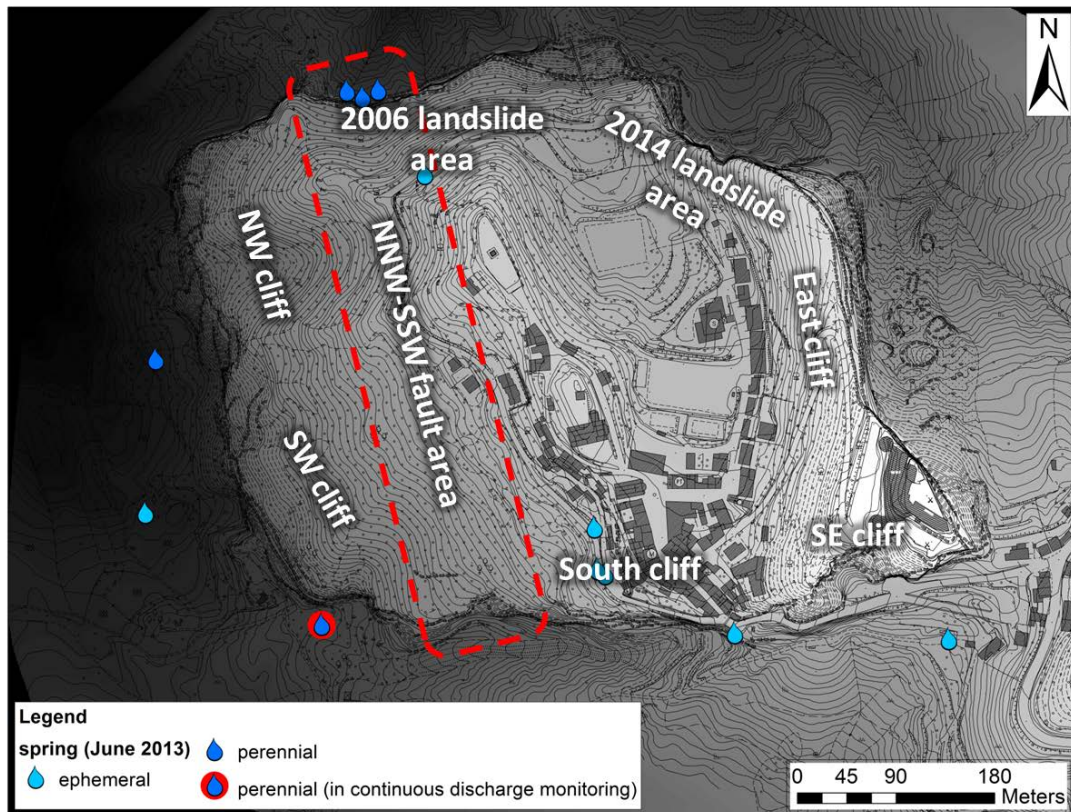
Figure 95. Areas individuated for the equivalent hydraulic conductivity determination

Data regarding the discontinuities detected during the field surveys and mapped on the TLS point clouds are showed and discussed in Chapter 2.

The bedding surfaces were not detected during the field surveys, in fact they didn't outcrop at the base of the slab, where the surveys were conducted. The bedding orientation was measured in each area by TLS fracture mapping and it was taken into consideration by assigning to it a low aperture value, e.g. 10^{-5} m.

 – South cliff

Hydrogeological parameters were estimated from geomechanical surveys data and TLS fracture mapping.

Results are shown in Table 40. The equivalent hydraulic conductivity was estimated in $4.73*10^{-6}$ m/s.

Table 40. Hydraulic conductivity tensor for the Southern cliff

Hydraulic conductivity tensor	(m/s)	Dip (°)	Dip direction (°)	k_{eq}
k1	$2.08*10^{-9}$	29	55	
k2	$2.25*10^{-4}$	55	199	$4.73*10^{-6}$
k3	$2.25*10^{-4}$	17	315	

 – SE edge

The two geomechanical surveys conducted in the area were used to estimate an equivalent hydraulic conductivity equal to $1.32*10^{-2}$ m/s. The higher value, if compared with the surrounding areas is due to the presence of a fault, detected during field surveys and also by Ribacchi and Tommasi (1988) and Borgatti et al. (2015). Thus the degree of fracturing in this sector is higher. Results are shown in Table 41.

Table 41. Hydraulic conductivity tensor for the South-Eastern edge

Hydraulic conductivity tensor	(m/s)	Dip (°)	Dip direction (°)	k_{eq}
k1	$9.03*10^{-3}$	19	0	
k2	$1.39*10^{-2}$	8	93	$1.32*10^{-2}$
k3	$1.83*10^{-2}$	70	204	

 – East cliff

It was not possible to conduct field surveys in this area, thus data from literature were used. In particular field surveys were conducted by a climber on the East cliff and on the North Eastern edge after the 2014 landslide (Enser srl 2014). The results were coupled with TLS fracture mapping and permitted to obtain the hydraulic conductivity tensor (Table 42). The equivalent conductivity was estimated in $3.6*10^{-2}$ m/s.

Table 42. Hydraulic conductivity tensor for the Eastern cliff

Hydraulic conductivity tensor	(m/s)	Dip (°)	Dip direction (°)	k_{eq}

k1	$1.01*10^{-2}$	13	102
k2	$6.30*10^{-2}$	50	207
k3	$7.32*10^{-2}$	37	2

($3.6*10^{-2}$ shown in the k_{eq} column spanning all three rows)

– 2014 landslide area

The same procedure was adopted for the 2014 landslide area. Results are shown in Table 43. The equivalent conductivity was estimated in $7.2*10^{-2}$ m/s.

Table 43. Hydraulic conductivity tensor for the 2014 landslide area

Hydraulic conductivity tensor	(m/s)	Dip (°)	Dip direction (°)	k_{eq}
k1	$5.35*10^{-2}$	16	172	
k2	$6.29*10^{-2}$	2	263	$7.2*10^{-2}$
k3	$1.10*10^{-1}$	73	358	

– 2006 landslide area

Geomechanical survey and TLS fracture mapping results permitted to obtain the hydraulic conductivity tensor in the 2006 landslide area (Table 44). The equivalent conductivity was estimated in $3.9*10^{-3}$ m/s.

Table 44. Hydraulic conductivity tensor for the 2006 landslide area

Hydraulic conductivity tensor	(m/s)	Dip (°)	Dip direction (°)	k_{eq}
k1	$3.59*10^{-4}$	21	108	
k2	$1.29*10^{-2}$	42	219	$3.9*10^{-3}$
k3	$1.33*10^{-2}$	41	359	

– NW edge

Geomechanical survey and analysis of the TLS point clouds were used. The field survey was conducted in a highly fractured area, probably influenced by the NNW-SSE fault, reported also by Ribacchi and Tommasi (1988) and Borgatti et al. (2015). Thus, the hydraulic conductivity of each joint set were diminished by an order of magnitude, to eliminate the fault effects, while the fault area was analysed separately. Results are presented in Table 45. The equivalent conductivity was estimated in $2.2*10^{-2}$ m/s.

Table 45. Hydraulic conductivity tensor for the North-Western edge

Hydraulic conductivity tensor	(m/s)	Dip (°)	Dip direction (°)	k_{eq}
k1	$3.59*10^{-4}$	24	7	
k2	$1.29*10^{-2}$	25	110	$2.2*10^{-2}$
k3	$1.33*10^{-2}$	54	239	

– SW edge

The south-western edge is characterized by a low degree of fracturing, thus the equivalent conductivity results in a very small value and the tensor is mainly influenced by the bedding orientation (Table 46). The equivalent conductivity was estimated in $3.2*10^{-13}$ m/s.

Table 46. Hydraulic conductivity tensor for the South-Western edge

Hydraulic conductivity tensor	(m/s)	Dip (°)	Dip direction (°)	k_{eq}
k1	$5.11*10^{-20}$	52	123	
k2	$8.01*10^{-10}$	31	342	$3.2*10^{-13}$
k3	$8.01*10^{-10}$	19	239	

− NNW-SSE Fault area

Data for the NNW-SSE fault area were calculated referring to the field surveys conducted in the NNW-SSE edge. The equivalent conductivity was estimated in $2.18*10^{-1}$ m/s. Results are repoted in Table 47.

Table 47. Hydraulic conductivity tensor for the NNW-SSE Fault area

Hydraulic conductivity tensor	(m/s)	Dip (°)	Dip direction (°)	k_{eq}
k1	$1.41*10^{-1}$	6	358	
k2	$2.12*10^{-1}$	28	92	$2.18*10^{-1}$
k3	$3.47*10^{-1}$	61	257	

4.4.2 Numerical model

The calibration was achieved using the equivalent permeability and storativity values indicated in Table 48. The resulting storativity values are slightly different than those expected in hard rock aquifers (storativity equal to 2%). Anyway, by investigating highly tectonized flysch rock masses from the northern Apennines, Ronchetti et al. (2008) found similar hydrogeological parameters values.

Table 48. Hydrogeological properties derived from the model calibration

Hydraulic conductivity	Kx	0.003x10-4 m/s
	Ky	0.003x10-4 m/s
	Kz	0.006x10-4 m/s
Storativity		0.1

The initial value of permeability, calculated using the relationships proposed by Kiraly (1969) and Louis (1974), ranged between 10^{-2} and 10^{-6} m/s. It must be considered that this initial value takes into account only the external and intensively disrupted part of the slab, while the simulation has been carried out by considering the whole slab. The hydraulic head on the contact with the clay-shale units reaches the maximum value of 48 m at the centre of the slab and decreases towards the borders (Figure 97).

The model results were compared with the water surface measurements obtained from the boreholes drilled in 1972 (S1, S2, S3 and S4) and in 2014 (BH SL1). The differences are shown in Table 49.

Table 49. Differences in water surface measured from boreholes and extracted from the FEFLOW model

borehole	Water level measured in the borehole	Water level from Feflow model
s1	467.7	470.7

s2	473.3	474.2
s3	507.7	502.4
s4	517.7	512.5
BH SL1	541.4	520.5

The results were further more validated by using the Ribacchi & Tommasi (1988) springs survey, not used in the calibration process. The discharge areas resulting from the model, i.e. the area in which the groundwater surface elevation results above the topography (from DTM) well agrees with the localization of the springs mapped around the San Leo slab in the 1988 survey, as shown in Figure 96.
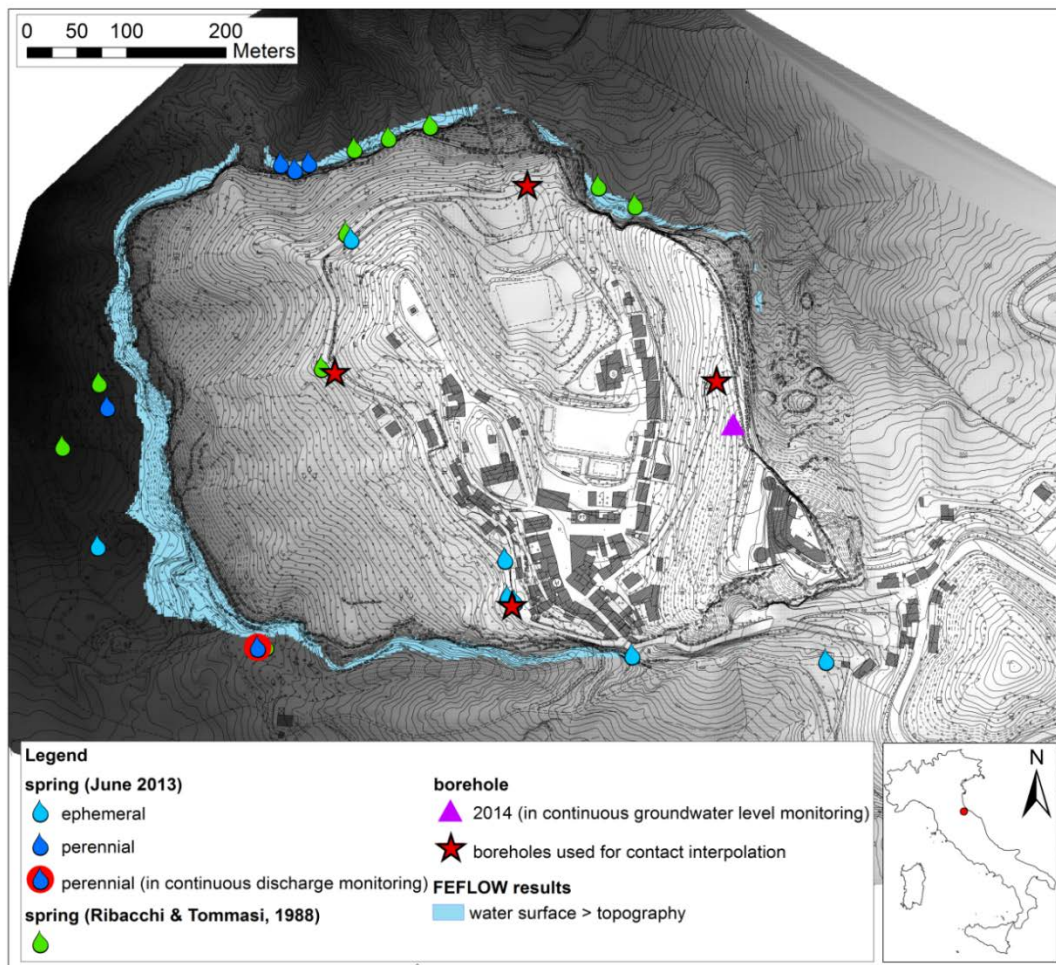
Figure 96. Model results: In blue, the discharge area resulting from the model. The blue and light blue drops show the springs localization used for the model calibration. The green drops refer to the springs mapped in a previous survey (1988) by Ribacchi & Tommasi. The red stars represent the position of the boreholes used for the contact surface interpolation, while the purple triangle is the localization of the monitored piezometer.

After the validation, the simulation of the water surface before the 2014 landslide showed a maximum rise of 4 m near the centre of the slab (Figure 98). The obtained piezometric surface variation was inserted in the numerical model (Chapter 6) to evaluate its influence in the triggering of the 2014 landslide.
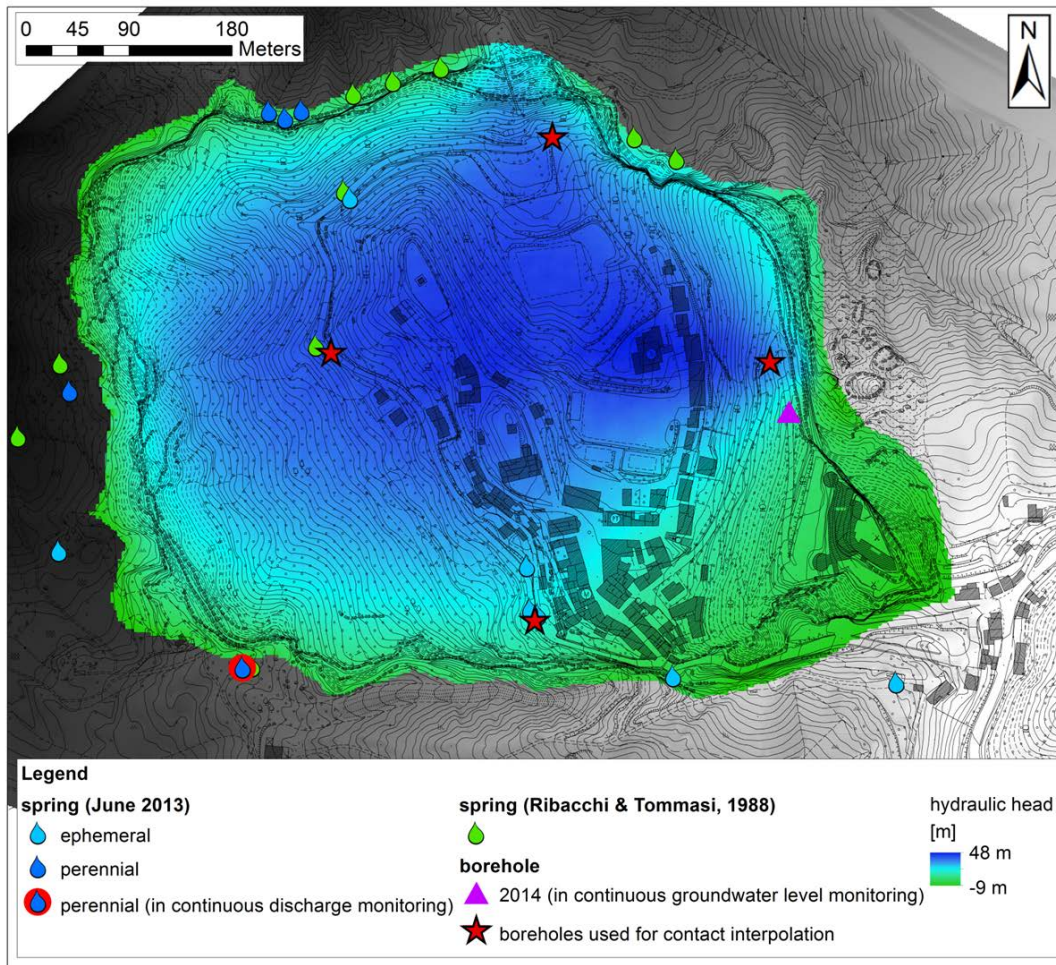
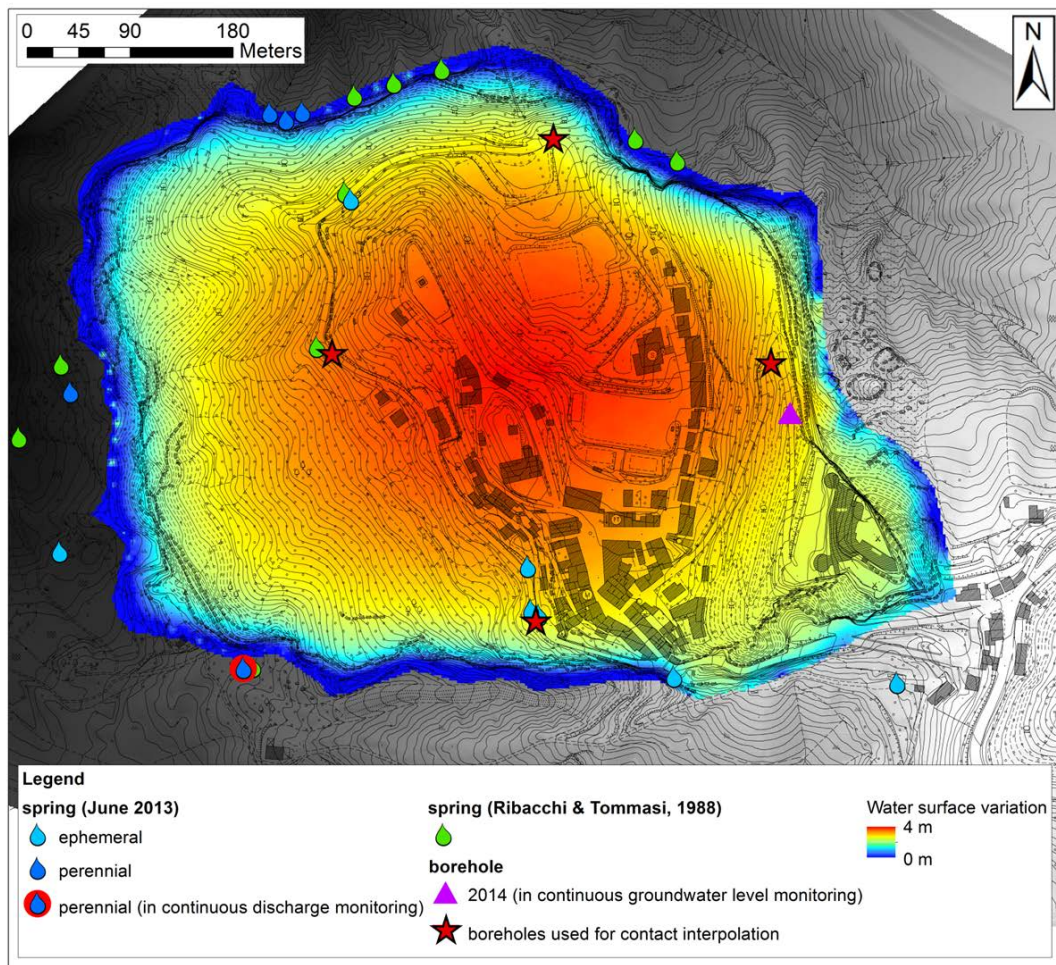*Figure 97. Model results: mean hydraulic head*

Figure 98. Model results: The variation between the mean water surface and the one calculated before the 2014 landslide. Positive values (in red) indicates an increase of the water surface

4.4.3   Monitoring data

4.4.3.1   Spring discharge analysis

Spring discharge curve is shown in Figure 99. The recession period ranges from the 12th of May 2014 to beginning of September 2014. The effective rainfall, calculated following the modified Penman-Monteith equation (modified by Allen et. al 1998) is reported on the same graph (in blue).
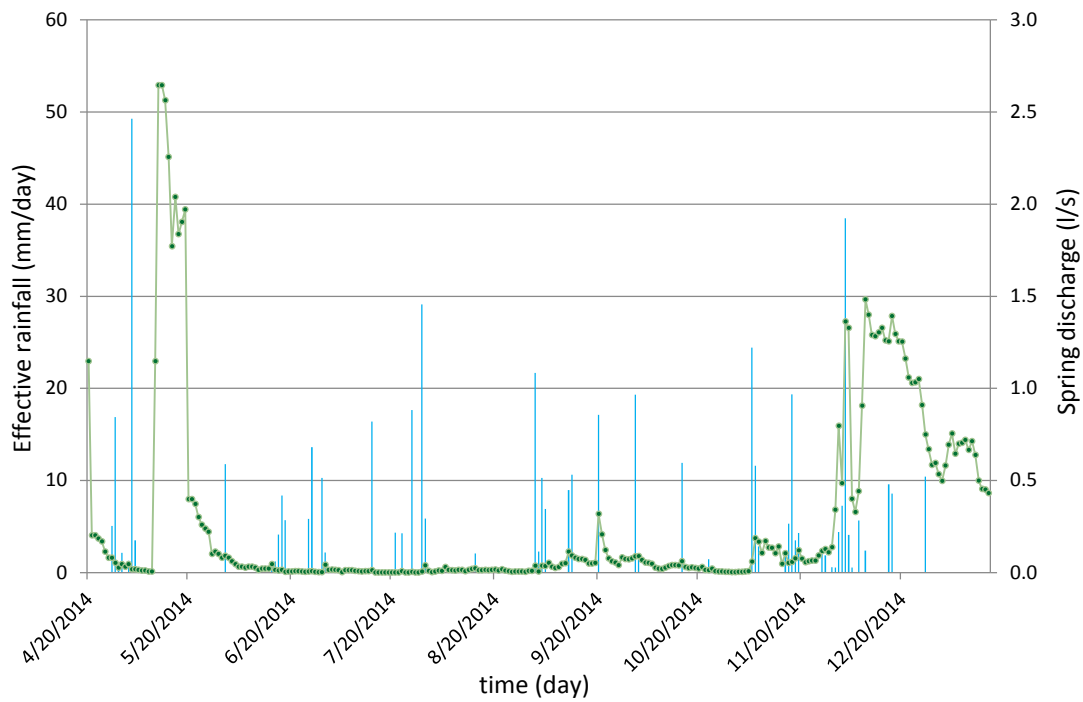
Figure 99. Spring discharge data from the 20th April 2014 to the 15th January 2015 (in green) compared with effective rainfall calculated for the same period

For the recession curve analysis only the period between the 12th of May 2014 and the 28th of July 2014 has been considered. This was due to the several recharge events disturbing the recession behaviour in August 2014. Plotting the recession curve on a semi logarithmic graph (Figure 101), two trends were found. This can be interpreted as the presence of two different portions within the aquifer. The first, acting from the 12th of May 2014 to the 22nd of July 2014, has a depletion coefficient ($\alpha1$) equal to 0.204, while the second one ($\alpha2$) is 0.065. The effects of the two portions in terms of discharge can be considered as superimposed, i.e. the second system is active since the beginning of the recession curve. For this reason, the values calculated for the first portion of the aquifer has to be corrected subtracting the contribution of the second system during the period between the 12th of May and the 22nd of July (Table 50). As pointed out by Celico (1988), the greater is α the higher is the hydraulic conductivity of the system. The first portion of the aquifer is represented by the more opened fractures and it released the infiltrated water more quickly. The second portion is characterized by less-opened discontinuities and so by lower permeability. The system has a maximum yield (W01) of about 1267 m^3. These volumes refer only to one of the main springs. In order to consider all the perennial springs individuated in the area, thus taking into account the whole aquifer they should probably be, at least, tripled.

Table 50. Results of the spring discharge analysis

First system – active from the 12th of May 2014 to the 22nd of July 2014	
Depletion coefficient α [1/d]	0.204
Initial discharge Q0 [m^3/s]	0.00249

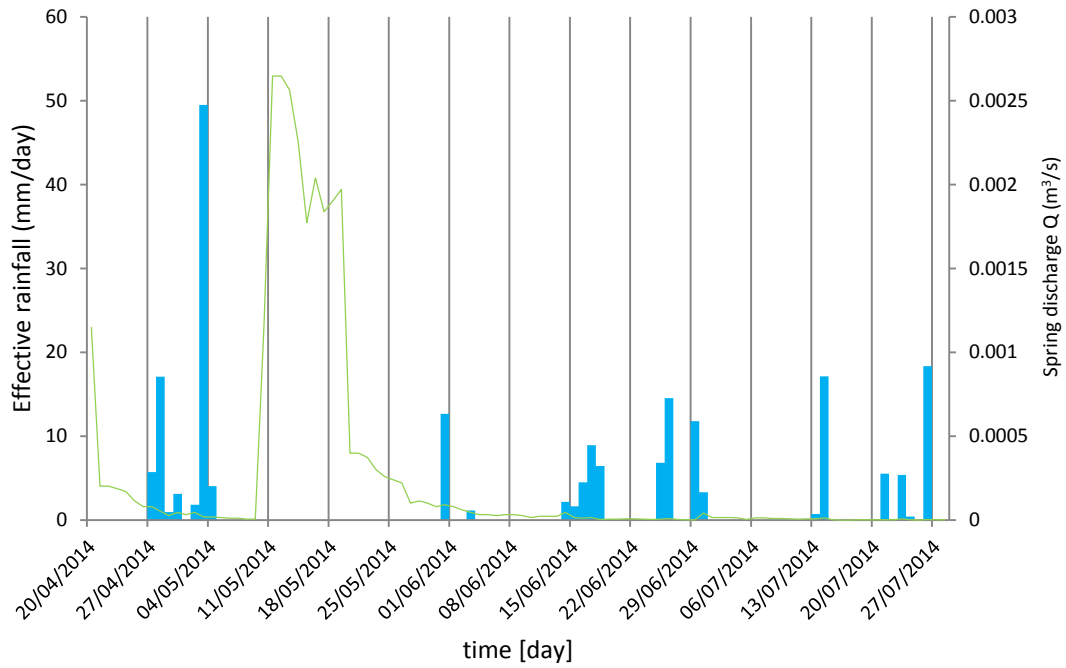|	
Active period [d]	23
Second system – active from the 12th of May 2014 to the 28th of July 2014	
Depletion coefficient α [1/d]	0.065
Initial discharge Q0 [m³/s]	0.00016
Active period [d]	78

Figure 100. Spring discharge data (in green) and effective rainfall (ETP calculated with the Penman-Monteith method, in blue) in the analysed depletion period (12th of May 2014 - 28th of July 2014).
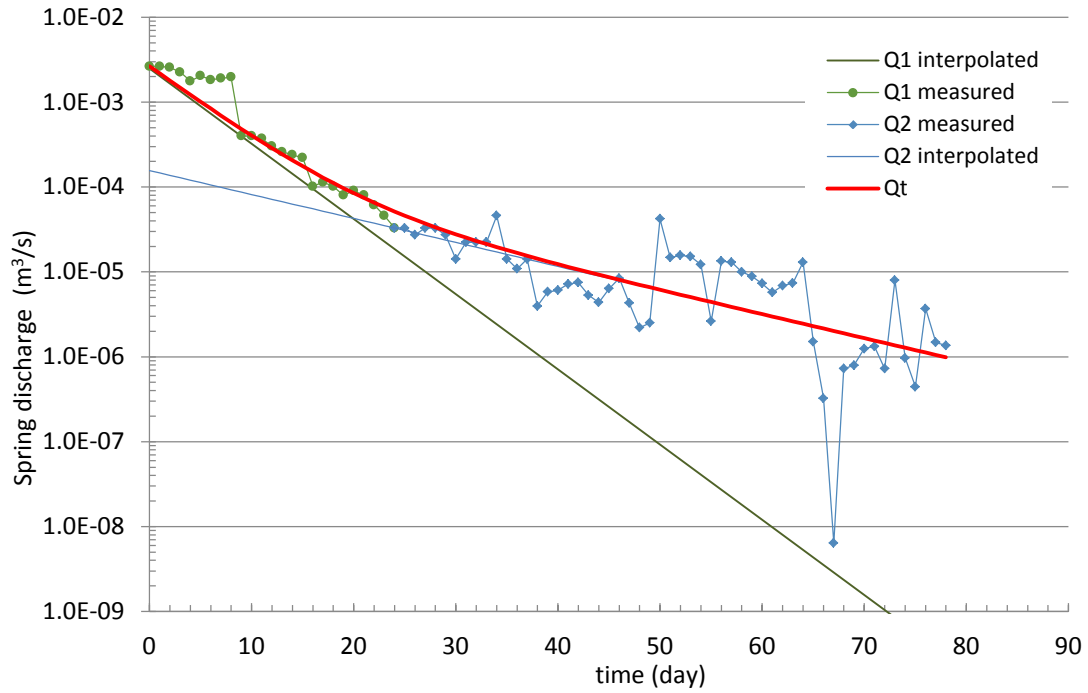
Figure 101. Semilogaritmic discharge-time graph of the recession curve. The red line represents the total discharge simulate using the Bousinessq generalized formula, thus as a sum of the discharge values of the two systems forming the aquifer (green and blue lines)

4.4.3.2   Piezometric data and slug tests

The water level in the slab was measured about 77.5 m below the ground (618 m a.s.l.). Despite the short acquisition period (from 31st October 2014 to 16th January 2015) the piezometric level seems to follow the rainfall regime. The maximum variation in this period was equal to 0.064 m.
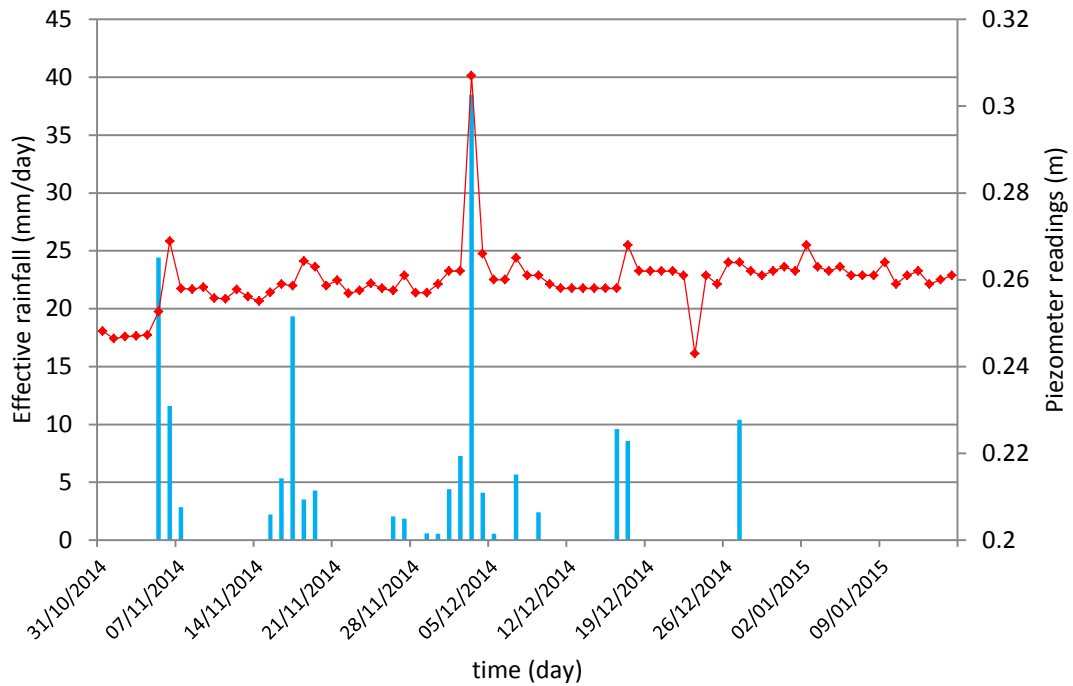
Figure 102. Piezometric data (in red) and effective rainfall (ETP calculated with the Penman-Monteith method, in blue)

The water level changing in the borehole, during the performed slug tests, is showed in Figure 103. The tests permitted to infer a mean value of hydraulic conductivity ranging from 5.0 to 5.3 *10^{-7}m/s (based on the Bouwer-Rice solution, Figure 104). An alternative solution, achieved fitting the data with the Hvroslev formula, is showed in Figure 105; results are quite similar.
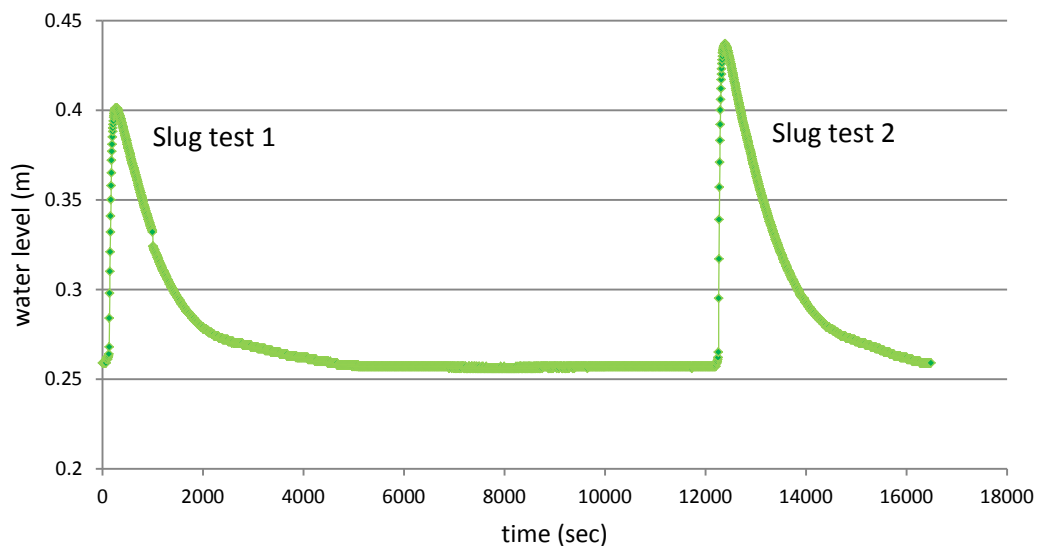

Figure 103. Water level changing in the borehole during the two slug tests

In both slug-tests, two parts of the decreasing curves were detected providing a further confirmation of the presence of two superimposed systems within the aquifer, as found from the discharge data. These

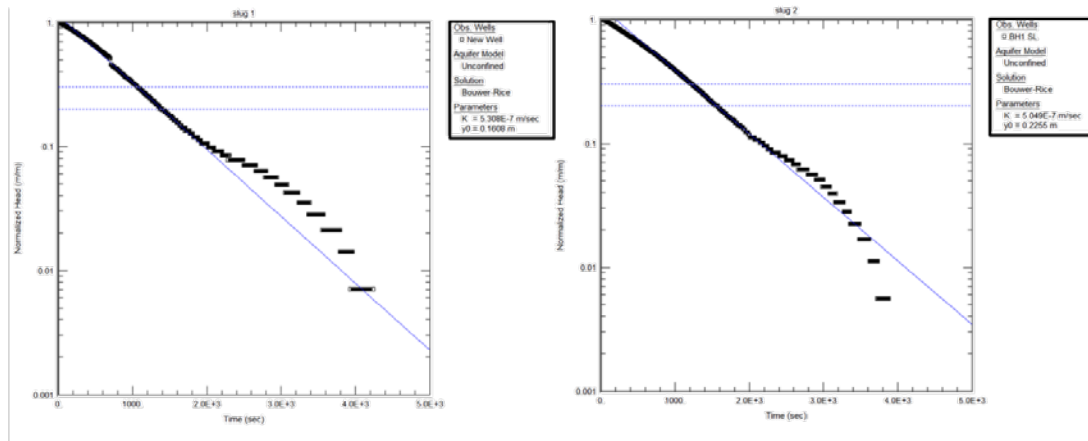permeability values are in agreement with the ones back-calculated with the hydrogeological modelling.

Figure 104. Slug tests data (slug 1 and 2) analysed with a visual fitting using the Bouwer-Rice solution
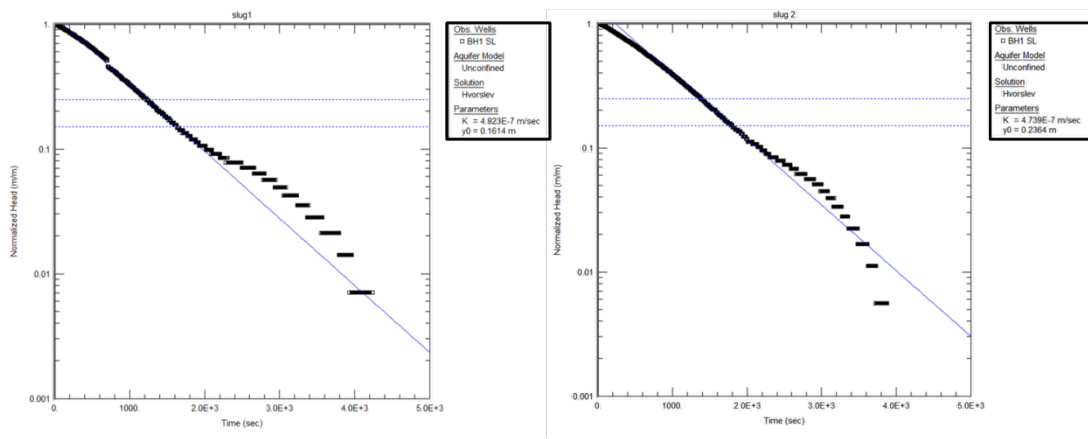

Figure 105. Slug tests data (slug 1 and 2) analysed with a visual fitting using the Hvroslev solution

4.4.3.3   Time-series analysis: auto and cross-correlation

Time series analysis should be performed on the whole hydrogeological year, which for the Apenninic springs usually starts at the beginning of October and ends at the lasts days of the successive September. Unfortunately daily spring discharge data cover a period ranging from the 20th of April to the 15th of January, while the hourly data were available only starting from the 19th of June.

The auto-correlation indices for daily data were plotted with the 95% confidence limits (Figure 106). The spring discharge autocorrelogram exceeds these confidence limits for 15 days.
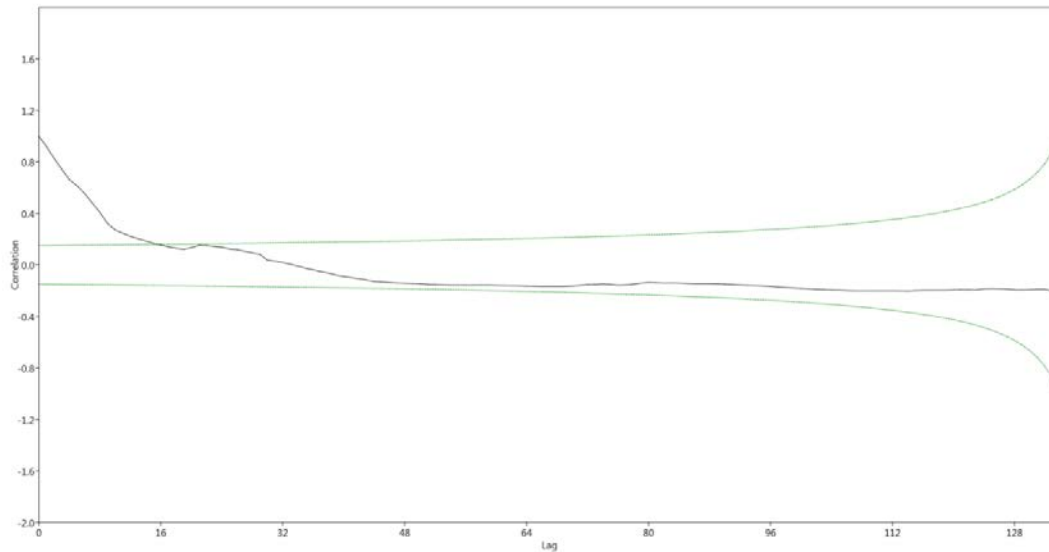
Figure 106. Autocorrelogram of the daily spring discharge data (in black) and 95% confidence limits (in green)

The same approach was used to test hourly spring discharge, in this case the autocorrelogram exceeds the confidence limits for approximately 477 h (19.9 h). Thus, the process of spring discharge is not independent and the current flow is influenced by the outflows up to about 15-20 preceding days. This result is explained with the memory effect due to the influence of the aquifer yield on the spring discharge rate (Civita 2005). The difference between the two can be ascribed to the difference in the investigated period, longer for the daily data, and to the time-step difference.
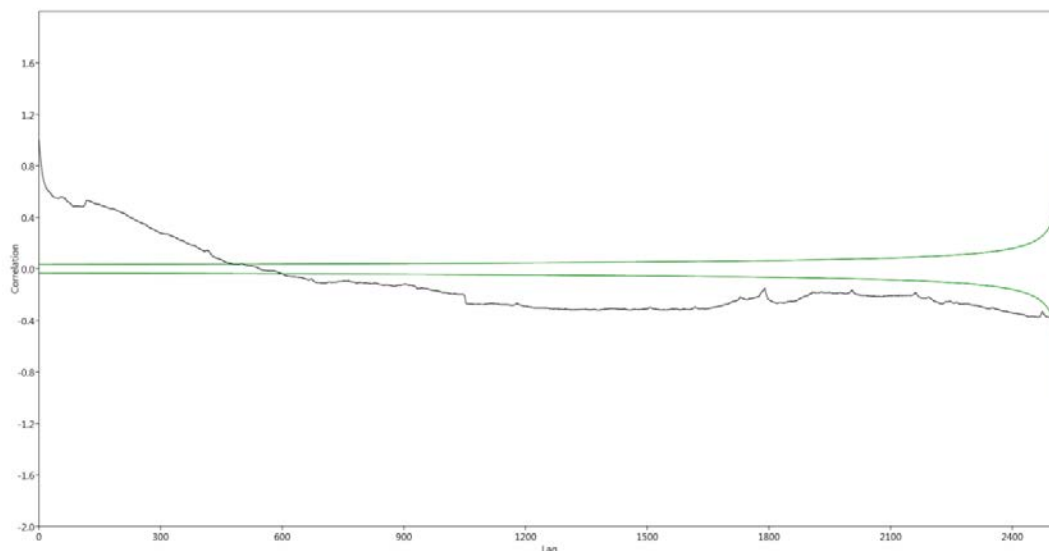

Figure 107. Autocorrelogram of the hourly spring discharge data (in black) and 95% confidence limits (in green)

Also the piezometric data show a time-dependent behaviour. In this case the available

time series were less extended and permitted only a preliminary evaluation. Analysing the daily data the autocorrelogram shows values out of the confidence limits after 1 day.
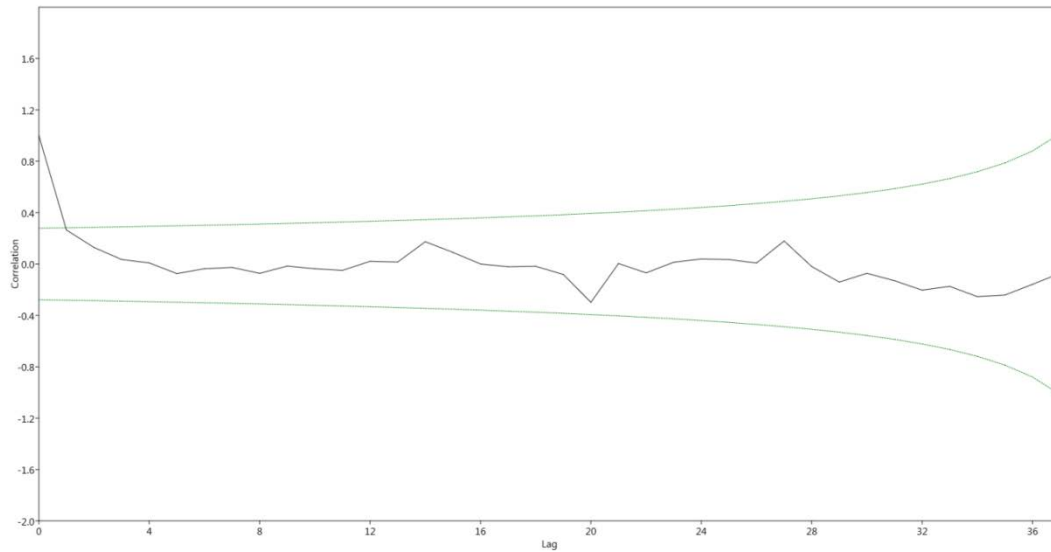

Figure 108. Autocorrelogram of the hourly spring discharge data (in black) and 95% confidence limits (in green)

Testing the hourly data was possible to obtain a more accurate estimation of the influencing period, which extends up to 27 h (1.12 days).

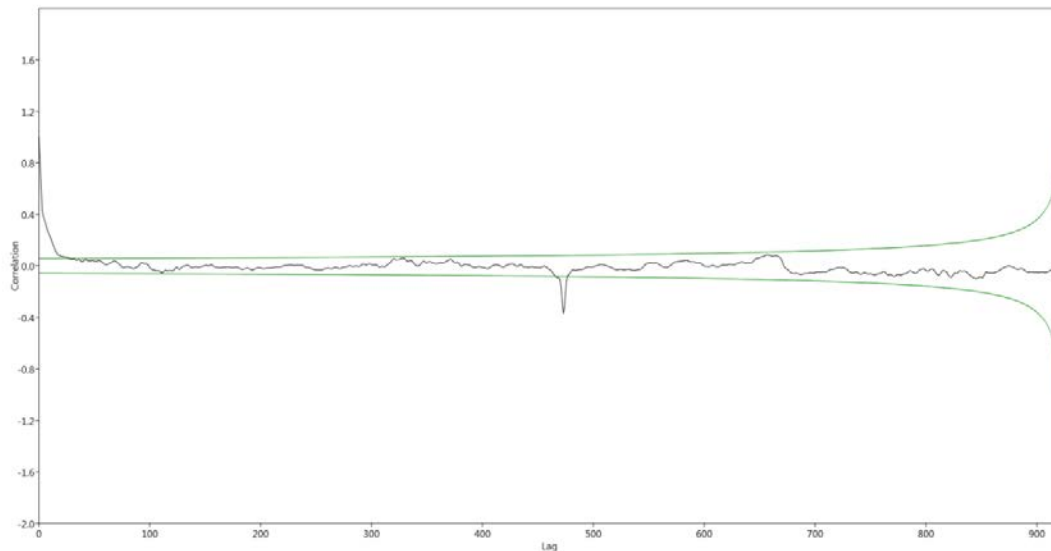*Figure 109. Autocorrelogram of the hourly spring discharge data (in black) and 95% confidence limits (in green)*

Cross-correlation between the PM effective rainfall and the daily spring discharge was tested (Figure 109). Results are shown together with the corresponding p-values. The p-value can be defined as the smallest level of significance at which the null hypothesis (H_0) is rejected. In other words it is the

probability that, assuming that H_0 is correct, the observed test results could be obtained by random chance (Davis 2002). If the p-value is lower than the specified α-level (usually 5%) the null hypothesis (H_0) should be rejected. P-values smaller than 0.05 are expected for 5% of lag times even for completely random (uncorrelated) data sets (Hammer et al. 2001). The analyses indicated two peaks. The first peak is equal to 8 days, while the second peak shows a time delay of about 14 days. Anyway the two peaks are not well defined and the correlation showed high values for all the period between them (from 8 to 16 days of time lag). Furthermore two minor peaks can be recognized after 28 and 34 days. In the same period the calculated p-value is low.
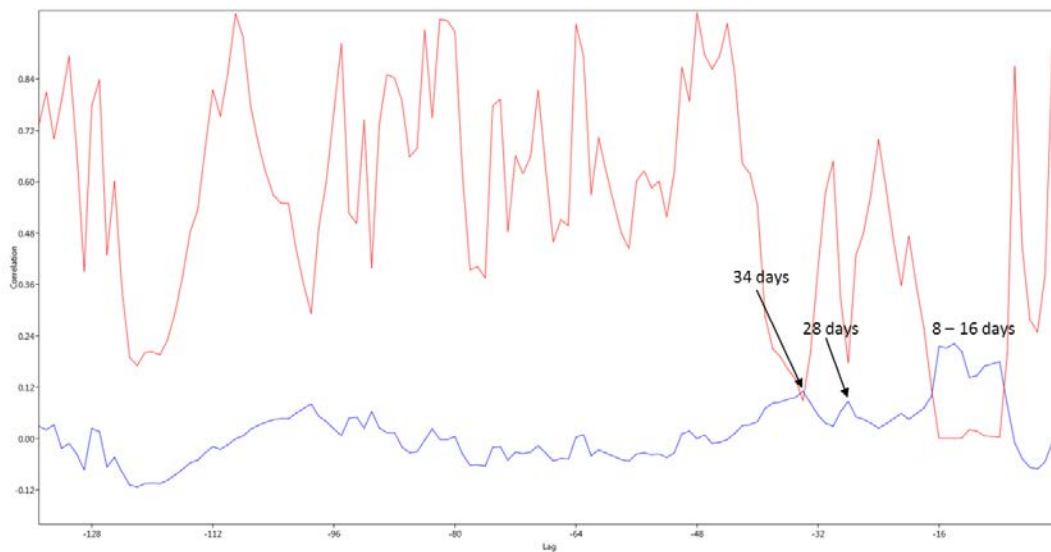
Figure 110. Cross-correlation between effective rainfall (ETP calculated with the Penman-Monteith method) and daily spring discharge data

The cross-correlation was tested also for the hourly data, results are shown in Figure 111. A first peak shows a 4 hours time-lag, probably related to the water flow coming from the area surrounding of the spring. Relatively high values of correlations can be observed between 123 and 191 hours (about 5 and 8 days), while other peaks fall in correspondence of 356 h, 387 h, 652 h and 677h (respectively 14.8 days, 16.1 days, 27.2 days and 28.2 days).
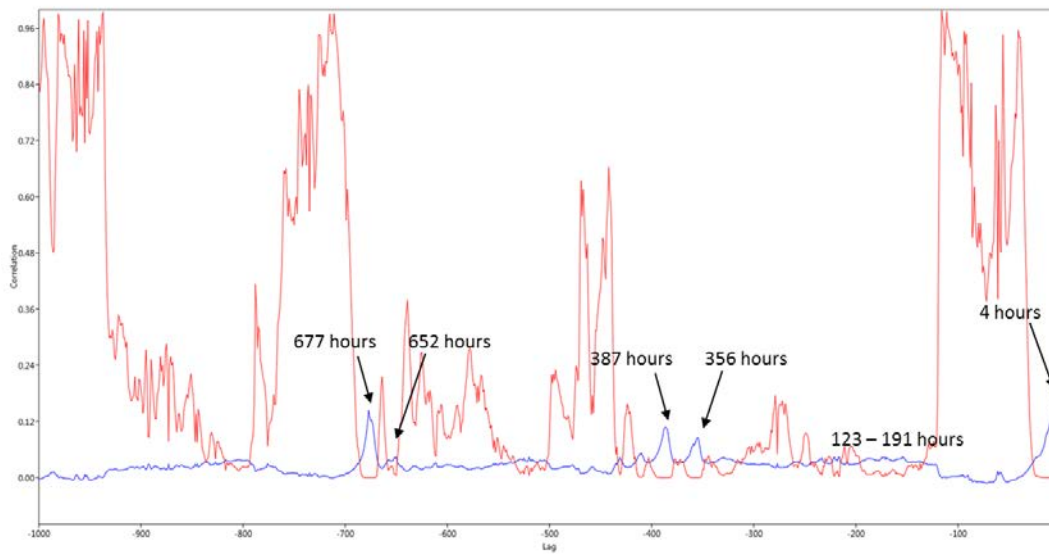
Figure 111. Cross-correlation between rainfall (calculated with the IDW method) and hourly spring discharge data.

In both cases the multiple peaks can be interpreted as the contribution of systems with different permeability or belonging to areas located at different distances from the spring. In particular, also observing the rainfall event registered the 3rd December 2014, the spring discharge showed several discharge peaks:

- the first between 0 and 1 day from the event, probably corresponding to the water fell in the spring neighbourhood;
- a second peak corresponding to a 6 days of time-lag;
- a third peak, 14 days after the main rainfall event, probably due to a minor rainfall event;

Between 6 and 17 days after the rainfall the spring discharge was particularly high (Figure 112). This is probably due to the contribution of several systems with different permeability, that can be identified as more or less opened discontinuities.
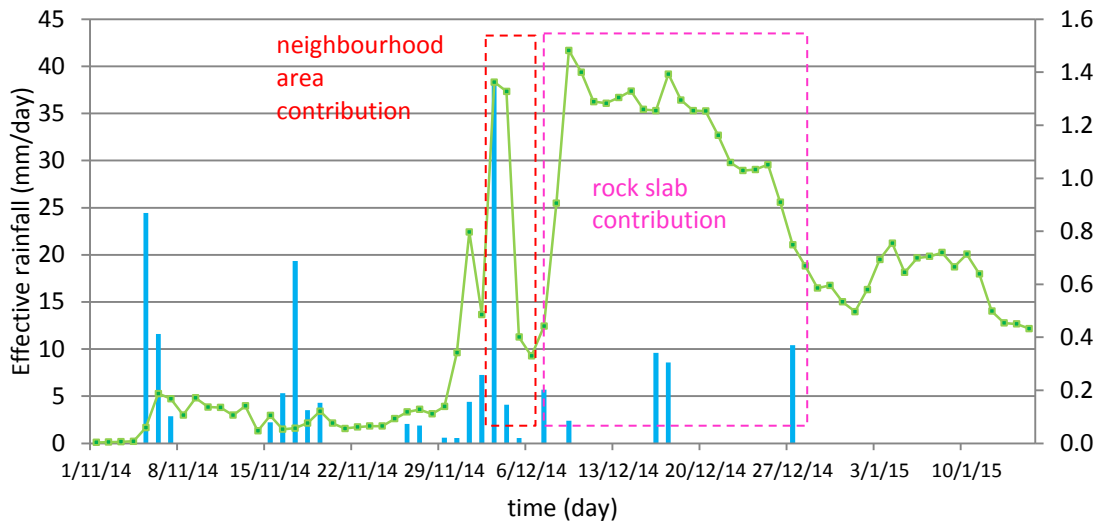
Figure 112. Spring discharge curve: rainfall event registered on the 3rd December 2014 and subsequent spring discharge rate variations

The same analyses were conducted to infer the correlation between the rainfall and the water surface level in the slab measured by the piezometer. The hourly data showed correlation peaks corresponding to 2h, 353h, 388h, 657h and 669 h (respectively 1, 14.7, 16.2, 27.3 and 27.8 days). Dividing the distance between the topographic surface and the groundwater level by the time lag, a first estimation of the mean hydraulic conductivity in the unsaturated zone was attempted.
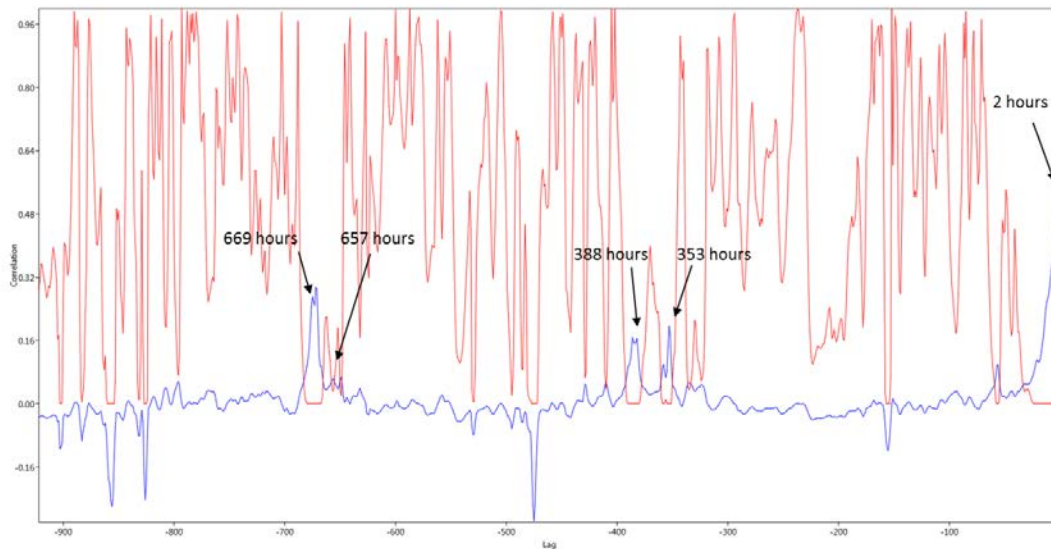
Figure 113. Cross-correlation between rainfall (calculated with the IDW method) and hourly piezometric data

The first time lag value (2h) was not considered because retained not significant. The others can be correlated with the hydraulic conductivity value reported in Table 51.

135

Table 51. Estimation of the hydraulic conductivity in the unsaturated rock mass, obtained dividing the distance between the topographic surface and the groundwater level by the recognized time lags

time lag (hours)	k (m/s) - unsaturated
353	$6.1*10^{-5}$
388	$5.5*10^{-5}$
657	$3.3*10^{-5}$
669	$3.2*10^{-5}$

Daily piezometric data were derived and tested for cross-correlation with the PM effective rainfall. Results are very similar to the ones obtained from hourly data tested with the total rainfall, showing peaks at 14, 16 and 28 days of time-lag.
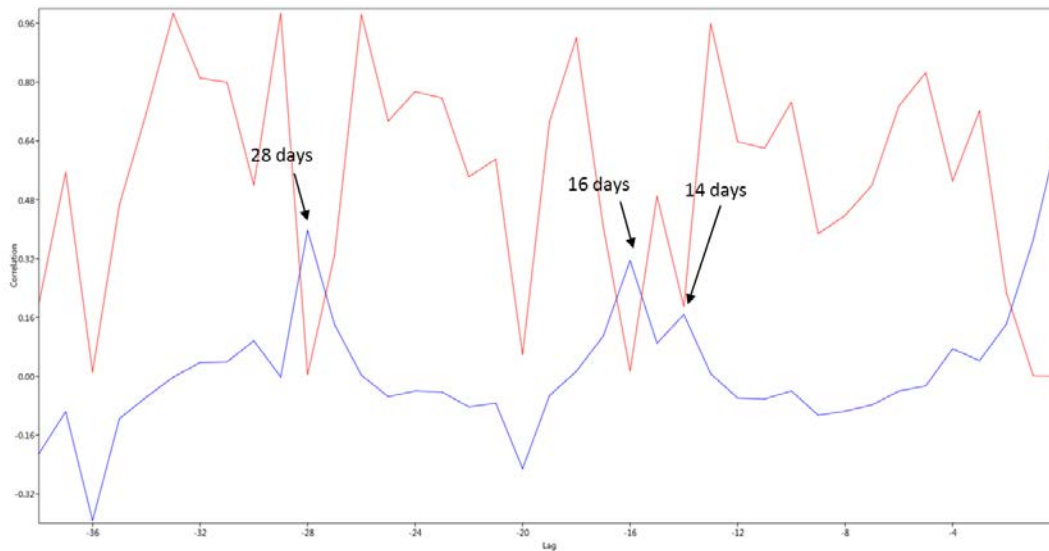
Figure 114. Cross-correlation between effective rainfall (ETP calculated with the Penman-Monteith method) and daily piezometric data

4.5   Discussion

The applied methodology permitted to reach a better knowledge on the groundwater flow in fractured rock slabs lying on a more impermeable substratum. Discontinuities characteristics, i.e. aperture, spacing and orientation, derived from field surveys and TLS data and illustrated in Chapter 2 permitted to infer an equivalent hydraulic conductivity value for each sectors of the slab. Along with that, rock mass areas characterized by variable degrees of fracturing or affected by different joint sets were identified. In particular, a main NNW-SSE highly fractured area that correspond to the fault detected by Tommasi and Ribacchi (1998) and Borgatti et al. (2015), was assumed. In the simulation, the rock slab was considered as a continuous medium (EPM approach). Results of the hydrogeological model suggested the presence of an aquifer inside the San Leo rock slab. The simulation represented a reasonable approximation of the general behaviour of the aquifer, allowing to calculate the mean

hydraulic head at the contact with the impermeable clay-shale units. Moreover the existence of the above mentioned piezometric surface justify the presence of softened clay-shales at the contact with the rock plateau.

The simulation performed for the period antecedent the 27th of February 2014 highlighted the slight groundwater level rise before the landslide event. More in detail, the maximum level in the centre of the slab was 4 meters higher than the mean one (calculated using the transient state for 30 years). The resulting groundwater level could be useful for the back-analysis of the event and to investigate the possible triggering factors. Based on the results of the hydrogeological model, starting from May 2014, one of the main springs has been monitored with a discharge-gauge equipped with an electric transducer. Total discharge from the slab will allow to further validate the 3D hydrogeological model.

The analyses of the monitoring data, coupled with the slug tests results, permitted to reach a better understanding of the hydrogeological behaviour of the San Leo rock slab. The groundwater flow is influenced by the rock mass discontinuities. Their frequencies and apertures control the hydraulic conductivity values in depth. Moreover, by processing the spring-discharge data and the slug tests results, the aquifer seems to be composed by two different systems: one with a larger hydraulic conductivity, probably including the more opened discontinuities, and a second with less opened ones. Statistic tests, e.g. autocorrelation and cross-correlation, confirmed the aforementioned results. In fact, the two peaks, individuated both in the spring discharge and in the piezometer data correlation with rainfall, can be interpreted as the contribution of systems with different permeability. Resulting values for the hydraulic conductivity are in agreement with the ones reported by Freeze & Cherry (1979).

Based on the reported results, an interpretation of the hydrogeological behaviour of the San Leo slab is given. As confirmed by the perennial springs location, the groundwater flow is controlled by the main structural elements, e.g. the main fault zones (Figure 95), which act as more permeable areas. The groundwater is mainly fed by the eastern area of the NNW-SSE fault, with a piezometric gradient lowering towards the west.

Moreover, a change in the hydraulic conductivity with depth can be suggested. That is due to lithostatic load inducing the closing of discontinuities in the deeper portion of the rock mass (Lee & Farmer, 1990). As a result, the upper and external parts of the slab are characterized by more-opened discontinuities and so by higher conductivity. The hydraulic conductivity resulting from the slug tests and the ones derived from the numerical model, which take into account the whole slab, are slightly lower than the those derived from in-situ geomechanical surveys. To bring forward the hydrogeological knowledge of San Leo, the hydraulic conductivity directions, calculated for each sector of the slab, can be inserted into the model allowing to consider in more detail the flow processes.

The hydrogeological monitoring is still ongoing: further piezometers will be installed and further investigations, including slug-tests and tracing injections, have been planned. The results will be fundamental for characterizing the groundwater flow within the fractured slab, and to better understand their relations with large slope instability phenomena affecting the site.

5.1   Introduction

In order to achieve a clear recognition of slope instability phenomena, it is necessary to understand the movement patterns and the eventual differential displacement occurring in the rocky slab. Monitoring activities, joined with geological, structural and geomorphological interpretation, are one of the fundamental step for risk management purposes.

Two monitoring systems were set up, during 2004, on the South-Eastern edge of the slab, in the proximity of the entrance road to the historical centre. Unfortunately data are lacking and some of the instruments are out of work. Data acquisition was interrupted in 2009. After the 2014 landslide the functioning of the pre-existent monitoring system was checked and new instruments were installed.

Often in similar geological contexts the monitoring system is missing or only poor data are available. The Permanent Scatterers (PS) analysis, due to its characteristics of precision, to the availability of quite long historical data set and wide area coverage can support the conventional in situ monitoring methods. The PSInSAR technique has proved to be applicable in different contexts to analyse ground displacements, from land subsidence to landslides.

Therefore the Permanent Scatterers (PS) data analysis has been tested, combining analysis on the PS velocity, on the direction of the movement and statistical consideration on the time series trend. Some preliminary results regarding the San Leo and Verucchio (RN, Italy) rock slabs are here presented.

5.2   Monitoring systems

2004-2009

Two monitoring systems (101 and 102) were installed, respectively in May and December 2004 on the Southern side of the slab, near to the entrance road. The localization of the instrument is reported in Figure 115 and in Figure 116. The monitoring systems worked irregularly until December 2009. Almost all the data acquired in this period showed a cyclic behaviour, probably related to seasonal variation. In some of the time-series displacements trends are recognizable, generally indicating the fractures opening. After the 2014 landslide, on the 26th and 27th March 2014, the systems named 101 and 102 were checked for proper functioning. The temperature sensor in the meteorological station, one inclinometer and one strain gauge located near to the town entrance are still operative, while all the others instruments of system 101 and 102 appeared to be out of work (Table 52).
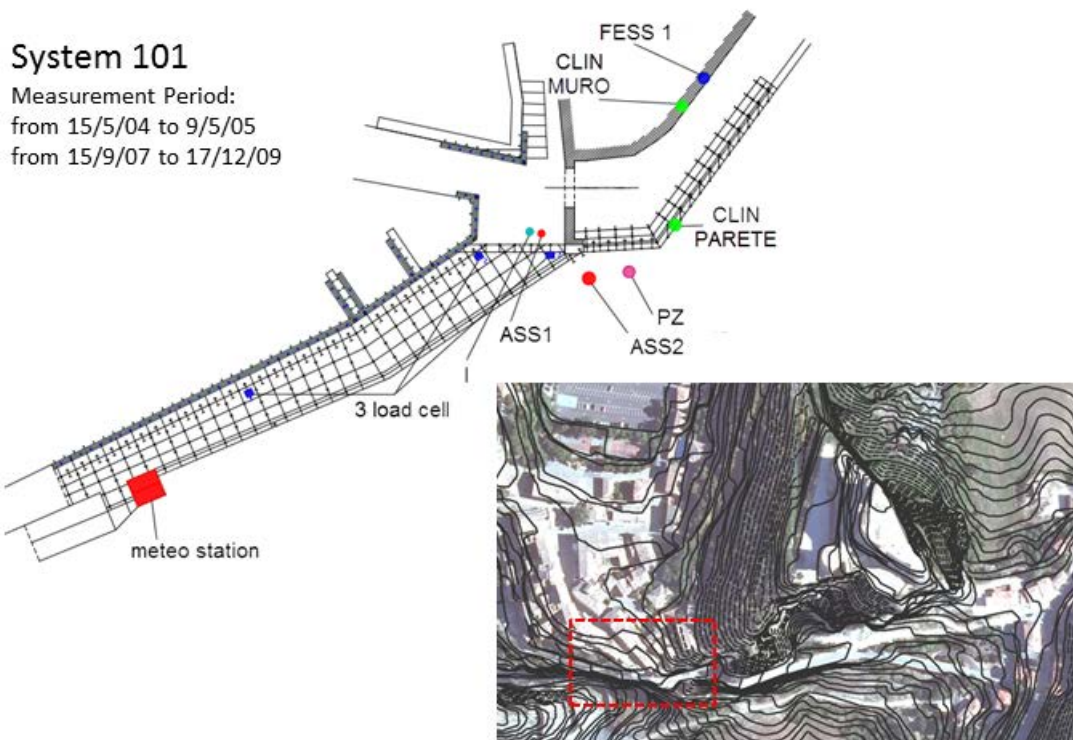
Figure 115. Localization of the monitoring instruments system belonging to the System 101

Table 52. Description of the monitoring system 101

| Instrument	Localization	Still functioning in 2014
meteorological station	Borgo Orsini road	Temperature yes relative humidity no
clinometer CLIN MURO	Town entrance	no
clinometer CLIN PARETE	Town entrance	no
extensimeter FESS1	Town entrance	no
inclinometer I	Town entrance	yes
strain gauge ASS1	Town entrance	yes
strain gauge ASS2	Toe of the slab	no
piezometer PZ	Toe of the slab	no
3 load cell	Borgo Orsini road	no

141
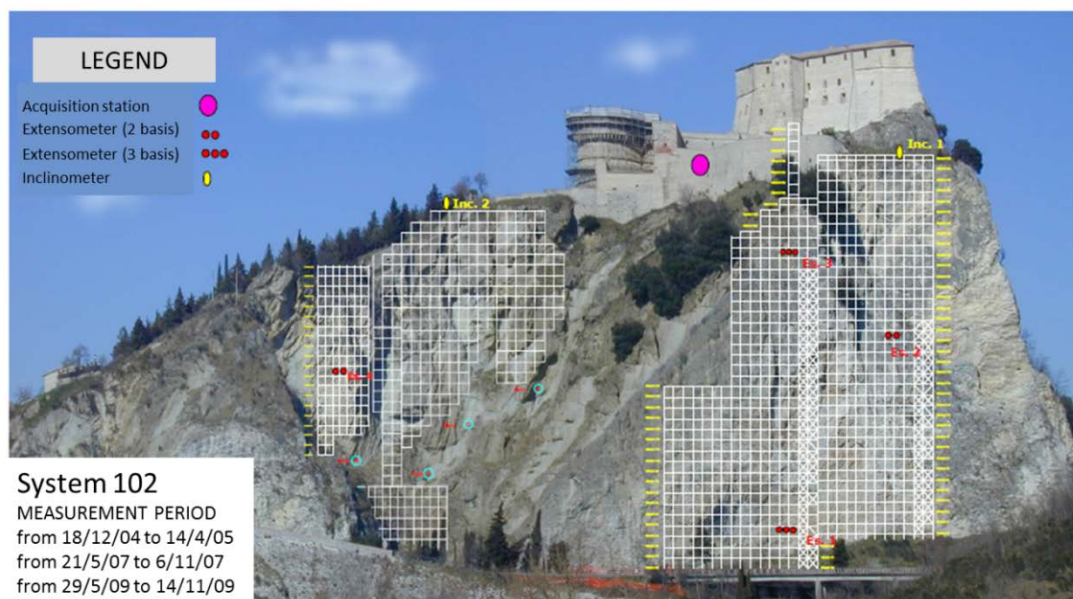
Figure 116. Localization of the monitoring instruments system belonging to the System 102

2014

The 17th March 2014, an integrated monitoring system was installed by Enser srl, on behalf of the Emilia Romagna Region RER (STB Romagna), in the North-Eastern side of the slab. A total of 13 wire crackmeters, 4 jointmeters, 2 borehole rod extensometers were used to monitor the main discontinuities as individuated during the field surveys. Data are automatically acquired by 3 control units (Figure 117). Starting from August 2014 the system was set to activate the civil protection emergency plan, if strain-rates larger than the fixed thresholds are measured. To date, displacements data are mainly related to daily and seasonal temperature changes (Borgatti et al. 2015).

In the same framework a manual monitoring of the fracture named K3.2 was initiated. Moreover 2 accelerometers were located in the same area. In fact minor crack propagations were recorded by a strong-motion seismic station managed by the National Institute of Geophysics and Volcanology (INGV) before the 2014 event.

A ground-based SAR, GBInSAR LiSAmobile (Ground-based Interferometric Synthetic Aperture Radar) was installed by the University of Florence (DST, Earth Science Department), for the in-continuous monitoring of the surface displacements in the cliff sector involved in the 2014 landslide. In the same project, financed by RER, multi-temporal TLS point clouds were acquired to individuate eventual small scale rock falls occurring on the same area, not detectable with the SAR technique. To date relatively small detachments have been registered, with a maximum volume of 94m[3]
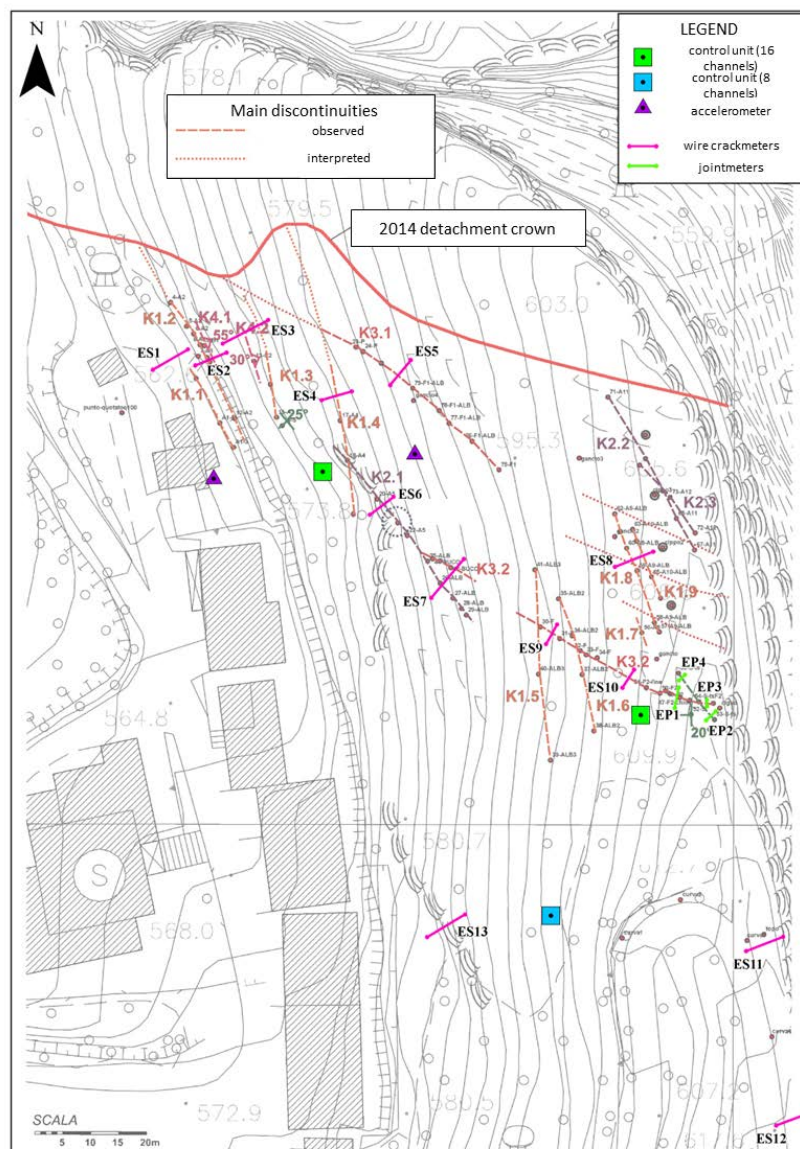
Figure 117. Localization of the monitoring system installed by Enser srl, on behalf of the Emilia Romagna Region RER (STB Romagna), in the North-Eastern side of the slab

(modified from Enser srl 2014)

5.3 **Interferometric data for movements recognition and characterization**

Radar satellite images provides an all-weather condition capability, despite their low spatial resolution and poor image quality, if compared with the optical sensors.

The use of two images taken at different times from the same position permit to detect displacements along the sensor Line-Of-Sight (LOS), allowing the monitoring of temporal evolution of surface deformations. In particular, the use of persistent scatterers, e.g. Permanent Scatterers (PS, Ferretti et al. 2001) and Small Baseline Subset (SBAS, Berardino et al. 2002) allows to extract useful information on long-term movements with a better accuracy with respect to optical techniques. The large spatial and temporal availability of satellite images determined the success of these techniques. The PS technique

provides displacements information on stable radar targets. PS analysis has been widely used in different fields, including land subsidence (Dehghani et al. 2013), landslides and tectonic motions (Colesanti et al. 2003; Meisina et al. 2007; Vilardo et al. 2010), infrastructures monitoring, post-seismic deformations (Zhang et al. 2011). Description and validation of the technique is reported in Ferretti et al. (2000; 2001) and in Colesanti et al. (2003). Referring to the Cruden and Varnes landslide velocity classification (1992), very slow (v<1.6 m/year) and extremely slow (v<16 mm/year) movements can be investigated using the PS techniques (MATTM 2009). In fact, excessive deformations between successive acquisitions can cause loss of radar coherence (Metternicht et al., 2005). The displacements to be registered must be less than half of the radar wavelength. Meisina et al. (2007) tested, in the Oltrepo Pavese (Northern Italy), the potential of the PS techniques for slow displacements recognition on stiffer slabs lying on a more ductile substratum. Example of the followed workflow is showed in Figure 118.
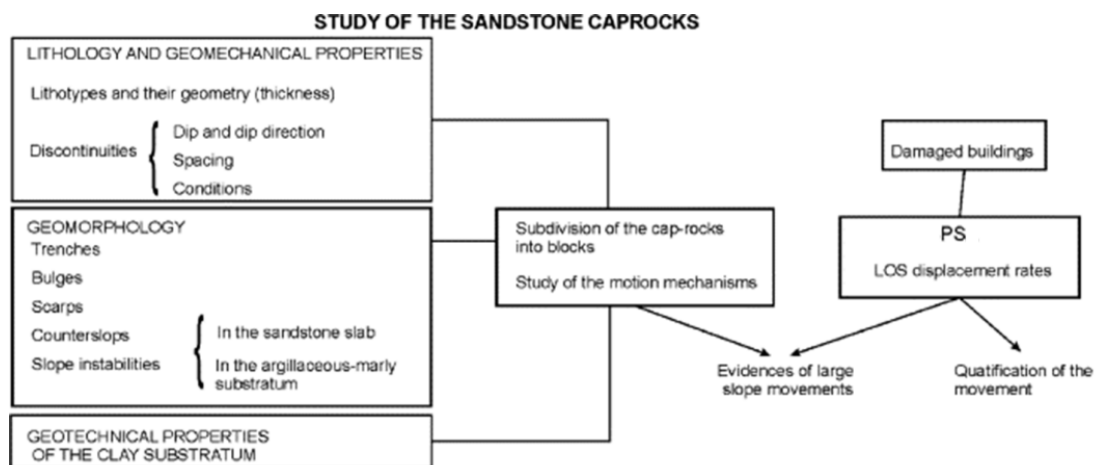

Figure 118. Example of workflow integrating lithological, geomechanical, geomorphological and geotechnical data with the PS techniques for the study of surface movements of sandstone slabs lying on a clayey substratum (modified from Meisina et al. 2007)

Some problems are to be considered when analysing the data, i.e. the displacements are detected only along the LOS, data are poor on slopes with a certain orientation due to the oblique angle of the radar beam and usually in natural highlands data density is low. Anyway, results of the interferometric analysis should be compared with ancillary data, such as geological and geomorphological maps, or displacements rate derived using other techniques to achieve a clear description of the occurring geomorphological processes.

5.4   **Materials and methods**

Different interferometric analysis techniques were integrated to enhance the knowledge of the instability phenomena acting on rocky slabs. The contribution of the radar interferometric analysis for the Valmarecchia area permits to provide information on the state of activity, on the direction and on the movement pattern of different types of slope instability phenomena. This information can be

integrated with geological, structural and geomorphological data to achieve a better comprehension of the phenomena.

The Permanent Scatterers analysis was performed using different dataset acquired in the frame of the PST-A (Piano Straordinario di Telerilevamento Ambientale/Extraordinary Plan of Environmental Remote Sensing) project: San Marino, Marecchia and Urbino datasets were collected between 1992 and 2000 and they are originated from the ERS images processing; Arezzo and Rimini datasets were collected between 2003 and 2008 and they are the results of the interferometric analysis of ENVISAT images. The images were processed by the companies T.R.E. S.r.l. and e-GEOS with the PS InSAR technique. The precision of the measurement is related to its coherence. PS with coherence inferior to 0.7 were not taken into account. The PS time series were analysed with a tool developed by T.R.E. (TRECustomerToolbar, Treuropa) and using a method for automated classification (Berti et al. 2013).

Moreover, the data of average velocity provided by the 2 geometries, ascending and descending, were combined to obtain the orientation of the velocity vector on the horizontal plane (EW) and vertical axis. Analysing the time series, it is possible to identify and map homogeneous areas with respect to the deformation processes. Differences in average velocity of deformation may be useful for the identification of areas with distinct evolution and for the discrimination of different deformation behaviour within the same landslide area, i.e., of rock blocks affected by differential subsidence due to deep-seated lateral spreading phenomena. The presented methodology was applied on the Valmarecchia rock slabs, namely San Marino, Perticara, Verucchio, Pennabilli and San Leo. Usually the PS are mostly located on man-made structures. The presence of inhabited areas on the top of these slabs permitted to have a good number of PS in the study area.

The most interesting results, obtained regarding the Verucchio slab, are described in the next chapter. Moreover a brief summary of the outcomes of the analyses conducted for the San Leo slab is reported. Findings regarding the San Leo slab were validated thanks to field surveys, focused on the identification and localization of damaged buildings in the citadel.

5.4.1 Time series analysis

In order to provide a general overview of the time series and to investigate the spatial distribution of different time series trends with respect to topographic and geologic features, the PS data were processed with PS Time software (Berti et al. 2013), which allowed the automated classification of the PS movement based on their time series trends. In particular, the datasets were subjected to a conditional sequence of statistical tests to classify each time series into one of the six pre-defined target trends: uncorrelated, linear, quadratic, bilinear, discontinuous with constant velocity and discontinuous with variable velocity. These trends describe different modes of ground deformation (Berti et al. 2013); uncorrelated time series represent random fluctuations of displacements around zero, and therefore PS with no significant movements during the observation period; linear trends indicate ground displacements with constant velocity and deformation phenomena acting over long time scales like creep, natural subsidence and slow and steady motion of so-called "dormant" landslides. Non-linear

trends, quadratic, bilinear and discontinuous, denote the displacement rate variation during the analysed period: velocity varies continuously in time for the PS with quadratic trends; for the PS characterized by a bilinear trend, the time series is segmented in two linear tracts of different velocity separated by a breakpoint in which the function is continuous; for the PS with a discontinuous trend, the time series is segmented in two linear tracts of similar or different velocity separated by a breakpoint in which the function is discontinuous.
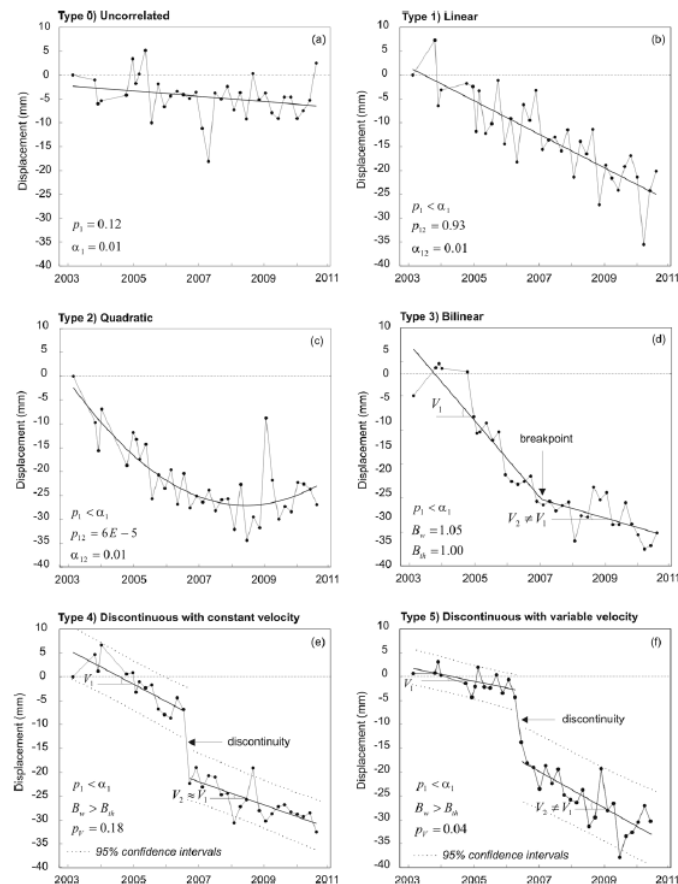

Figure 119. Examples of the trends identified by PS Time software (from Berti et al. 2013)

5.4.2   Displacements direction analysis

The possibility to combine the velocity of PS data processed in ascending and descending orbit improves the amount and quality of information obtainable on the analysed phenomena. The analysis procedures described in PST-A Guidelines (MATTM 2009) were followed. In areas where both acquisition geometries for the same satellite are available, velocity measurements along the two different LOS can be combined. It is almost never verified that a PS is considered as a target in both acquisition geometries, it is therefore necessary to proceed with a re-sampling of the ascending and descending datasets on a square grid mesh in order to make them comparable. The average velocity value of the Permanent Scatterers (PS) located inside each grid cell can be assigned to the cell centre. The velocity values recorded along the ascending and descending orbits are then geometrically combined to obtain the velocities along the vertical and E-W horizontal direction. Estimation of the N-S horizontal velocity of

deformation is not feasible, as one of the main limitations of the PS technique is the difficulty in recording horizontal movements along the North-South direction since the sensors operating orbits are oriented approximately along the meridians.

5.5 **Results**

5.5.1 Verucchio

Some promising results, reported in Spreafico et al. (2015) and regarding Verucchio site are here described. The town of Verucchio is located on a rock slab, in Valmarecchia area, about 20 km SW of Rimini, at an average altitude of about 300 meters a.s.l. The slab, formed by the so-called *San Marino* and *Monte Morello* geological units (limestones and sandstones) and crossed by several small faults or joints, lies on a clay-rich substratum. Finally it is worth to emphasize the presence of a vast overthrust on the East side of the slab having a roughly North-South direction, that testifies the movement of the plate on the older Ligurian units occurred in the past. ERS dataset, acquired between 1992 and 2000, was analysed to infer the behaviour of the rock slab. Three areas with different trends of movements were identified from the study of the PS data, even if an higher density dataset would be certainly useful for a better characterization of the phenomenon. The presence of an area located in the central part of the slab, showing higher velocities can be observed from the PS velocity map (Figure 120); in the Eastern sector of this area the landslide inventory map reports an active landslide, classified as rock fall or toppling. In this area damages to buildings were reported but the definition of the landslide type and evolution is not clear, since no in situ geotechnical instruments are available at present. Interferometric results can confirm the existence of an unstable area and suggest some features, i.e. the rate, the direction and the pattern of the movement; this can be the starting point on which further specific investigation and monitoring activities can be proposed.

Moreover, in the Western sector of the central area, where no landslides were previously mapped, some clusters of points with a mean velocity reaching values of -12 mm/year along the LOS in the descending geometry, are detectable; these points are located on the *San Marino* geological unit. The PS velocities suggest the presence of unstable areas, requiring specific investigations. The Northern area appears to be more stable, while in the South one velocity between 2 and 3 mm per year, along descending LOS, were registered.
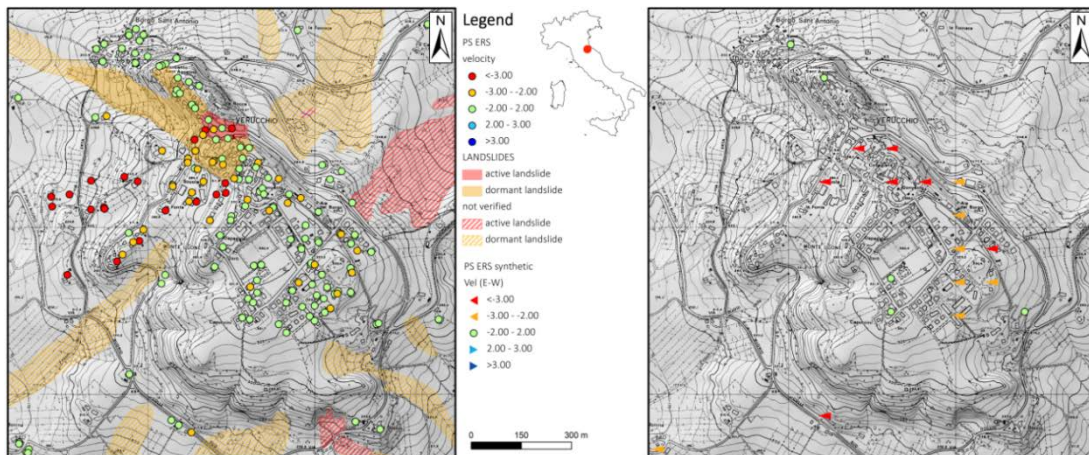
Figure 120. Velocity class along LOS of ERS PS (ascending and descending geometries) and direction of the movement on E-W axis

The synthetic PS obtained from Ascending and Descending geometries combination are fewer than the original points, because they can be obtained only in cells in which targets from the two geometries are present. By analysing PS trends, part of the slab is roughly characterized by E to W displacements. PS showed velocities reaching -4.0 mm per year; further investigations are required to better understand the main cause of the movement. The vertical displacements range between -1.5 and 0.7 mm per year, for the analysed period. Almost the same results were obtained with a slightly different procedure. Each descending geometry PS was joined with the closest ascending geometry PS using a 50 m maximum radius distance.
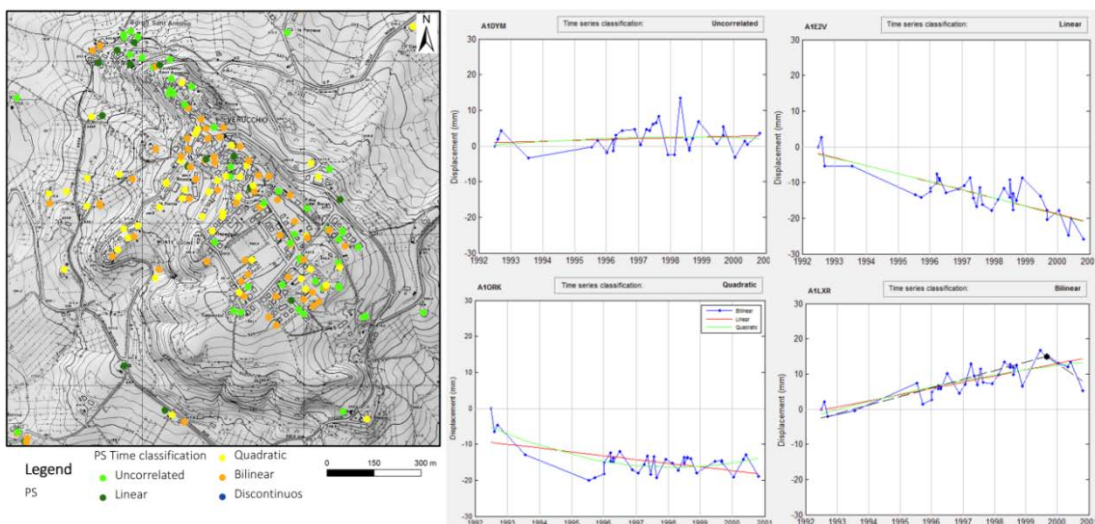

Figure 121. PS-Time classification and examples of the different movement patterns

Different types of movement patterns are identifiable analysing the LOS velocity. Uncorrelated and linear trends, probably indicating no movements and/or inactive landslides, are predominant in the North area, where, in fact, a dormant landslide is located. Quadratic and bilinear trends are prevalent in

the central part, in correspondence of the above mentioned mapped and newly detected landslides; a mix of quadratic, uncorrelated and bilinear trends characterize the South area (Figure 121).

5.5.2   San Leo

A PS analysis was conducted also on the San Leo slab, where more ancillary data and on site investigations are available. ERS and ENVISAT data, both in the Descending and Ascending geometries, were analysed. In the investigated area, the PS having the larger movement rate along LOS are located on the clay-shale substratum (Figure 122 and Figure 123).
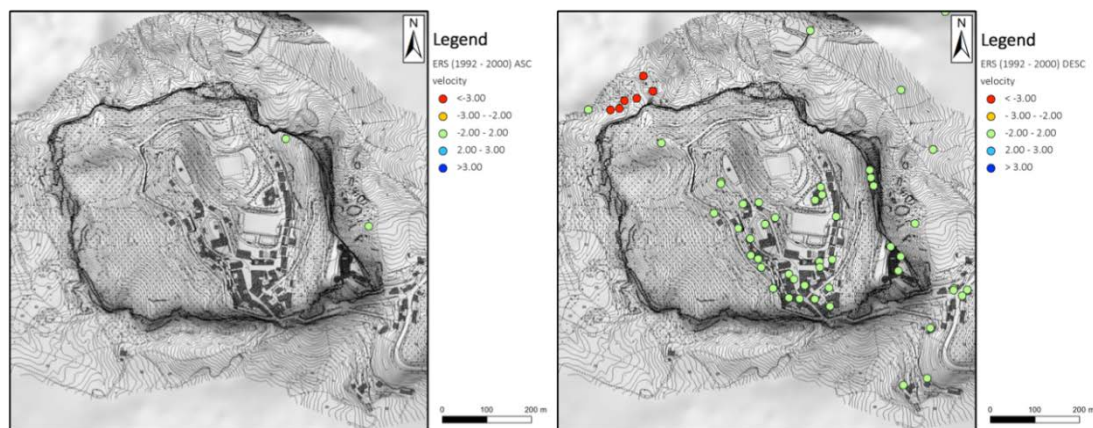
Figure 122. Velocity class along LOS of ERS PS (ascending and descending geometries)
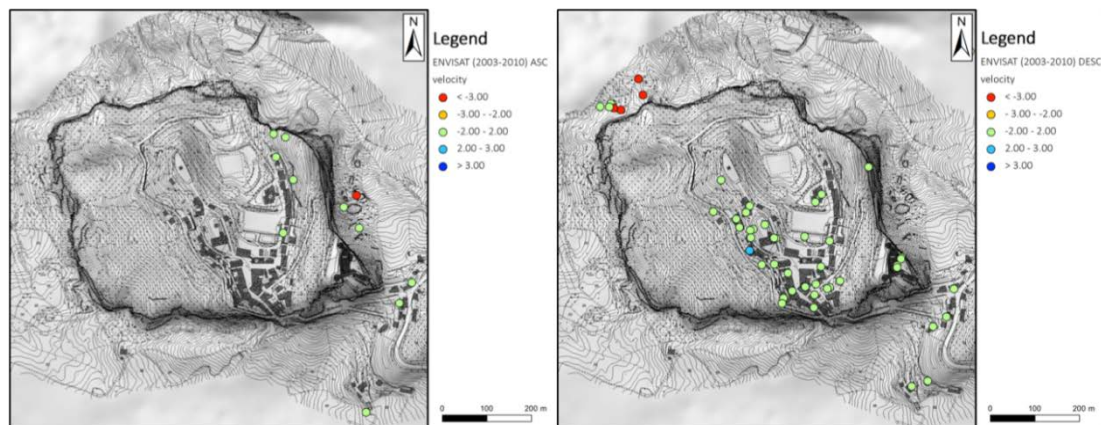
Figure 123. Velocity class along LOS of ENVISAT PS (ascending and descending geometries)

Probably the PS coincide with rock blocks, detached from the cliff of the slab. In fact their location correspond with the presence of the deposits of rock falls occurred in the past in the North-Western edge and in the Eastern cliff and described in Chapter 1. These blocks are now probably being transported by the underlying substratum. In particular the PS located near the North-Western edge of the slab showed displacements ranging from -4 and -9 mm/year during the period covered by the ERS data (1992-2000) and between -3 and -7 mm/year from 2003 to 2010. The movements are evident in the descending geometries, for both satellites. The movement patterns seemed to be mostly bilinear from 1992 to 2000 (Figure 124 and Figure 125).
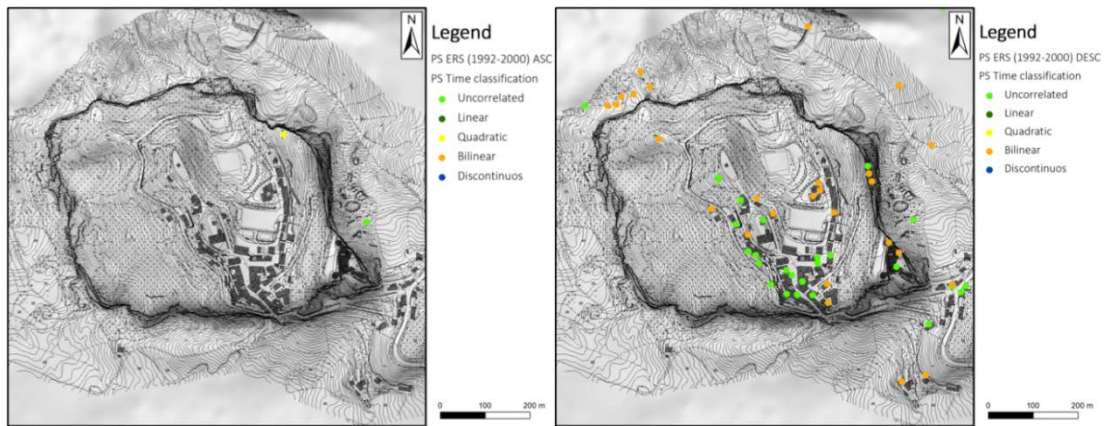
Figure 124. PS-Time classification of ERS PS (ascending and descending geometries)
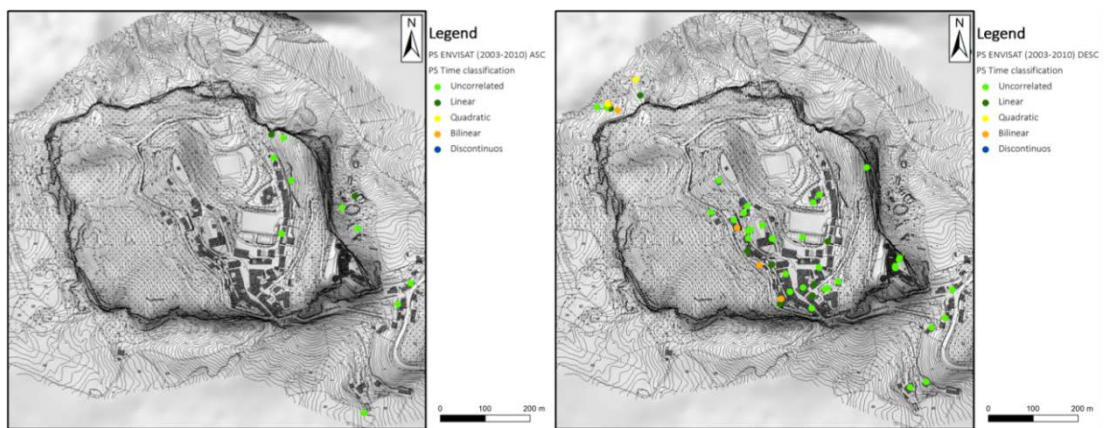
Figure 125. PS-Time classification of ENVISAT PS (ascending and descending geometries)

Analysing more in detail the time series, a lack of the data between 1993 and 1995 is evident (Figure 126) for the Marecchia dataset (1992-2000). The break point of the bilinear series for these PS mostly falls in this period.
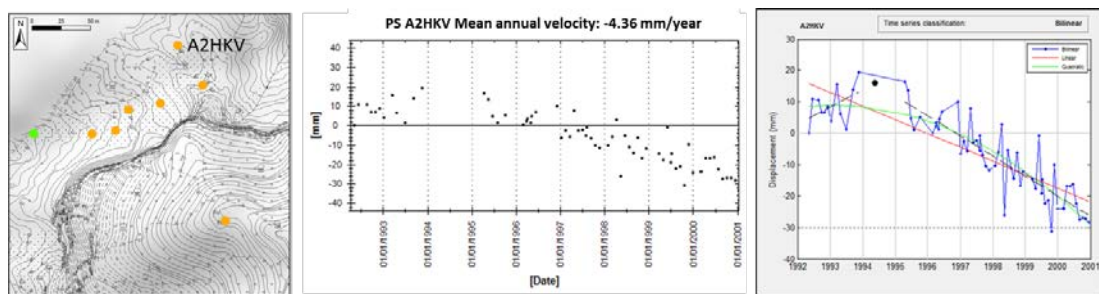
Figure 126. PS A2HKV: position and relative time series and time series classification of PS A2HKV. Colors are refereed to the legend reported in Figure 124

In the time series acquired by ENVISAT satellite linear, bilinear, quadratic and uncorrelated movements are registered. In the same areas landslide bodies and earth flows were detected by Borgatti et al. (2015) (Figure 127).
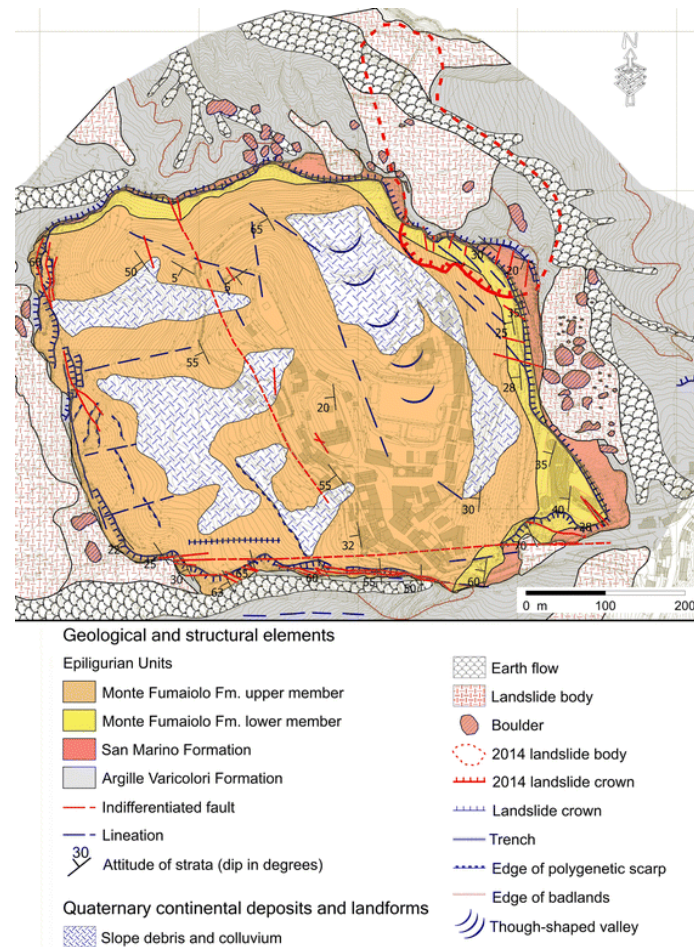
Figure 127. Geomorphologic map of San Leo rock slab, from Borgatti et al. (2015)

On the slab surface, the majority of the PS have an inferior velocity with respect to the accuracy of the measurement techniques (2 mm/year). Despite the small displacements didn't permit a clear definition of the phenomena, several areas with bilinear and uncorrelated movement patterns can be recognized in the ERS data. The North-Eastern zone of the town seems to be characterized by bilinear trend. In the same area small damages in buildings were recognized during the 2013 field survey (Figure 128 and Table 53). Examining the more recent ENVISAT data an uncorrelated behaviour is associated with the same area. Uncorrelated, linear and bilinear patterns are associated with the PS located in the town centre, while linear and bilinear behaviour seems to be predominant in the South-Western area of the urban area.

PS individuated in the ascendant and descendant geometries are located in different areas, thus the application of the displacements direction analysis did not have significant outcomes.
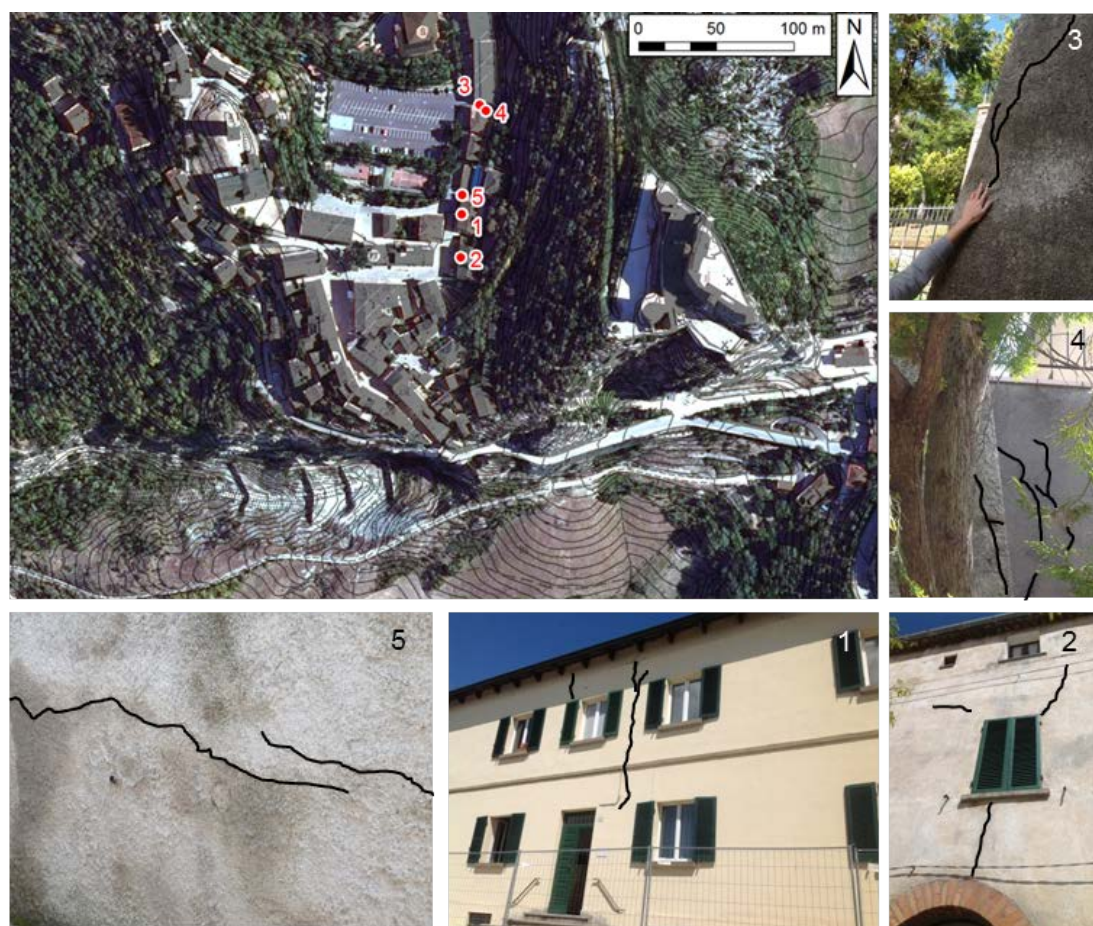
Figure 128. Small damages in buildings recognized during the 2013 field survey

Table 53. Fractures detected on buildings in the San Leo municipality. A= slightly damaged building

fracture ID	fracture orientation	type	Aperture (mm)	note
1	vertical	A	7	
2	vertical	A	5	3 fractures
3	vertical	A	10	
4	horizontal	A	5	
5	inclined	A	5	

5.6   Discussion

The preliminary PS analysis results need to be interpreted, validated and integrated with other techniques, but they show how the applied methodology can give an overview of the movements occurring in this particular context. These data are useful for the interpretation and the understanding of the phenomena, mostly when other monitoring data are not available or cover only limited periods. Regarding the San Leo slab, PS data showed the higher displacement rates of the clay-shale substratum, if compared with the ones affecting the rock slab. The displacements detected on the clayey substratum can be associated to the instability phenomena involving this geological unit. Shallow landslides, earth flows and earth slides were in fact mapped in the same areas. Displacements occurring at the border of

the slab, like rock-falls and toppling cannot be registered, due to the limitations related to the adopted techniques. In fact the velocities related to these kind of movements are out of the range which can be detected using the interferometric techniques. Indications deriving from interferometric analysis can give an overview of the type and of the movement rate, and are useful to choose where and how to continue or focus the investigation and monitoring activity. Another interesting issue can be the correlation between these results and the rainfall or the seismic records in a selected area, especially for points showing displacement rate variations during the analysed period. Interferometric techniques permit also to update landslide boundaries or to highlight unstable areas where no landslides were previously mapped, as in the Verucchio case. As anticipated a new monitoring system has been installed after the 2014 landslide. Since now, the stability analyses have not been calibrated with the measured displacement rates but in future, thanks to the availability of these new data, it will become probably possible to constrain the numerical modelling.

NUMERICAL MODELLING

Essentially all the models are wrong, but some are useful

(Box & Draper 1987)

6.1   Introduction

Numerical modelling has been applied by several Authors, with the aim to comprehend and verify landslide mechanisms, kinematics, and dynamics (Eberhardt et al. 2004; Hungr & McDougall 2009). Accurate investigations, the geological model of the area, the definition of the boundary conditions and the characterization of the material behaviour are fundamental to obtain a model representative of the acting phenomena. The main purpose of the numerical simulations is the contribution to the scientific understanding of the analysed phenomena and to the design of effective countermeasures. These pieces of information are essential for the comprehension of the phenomenon but not all of them have to be necessarily inserted in detail in the model, which, by definition, is a simplification of the reality. Critical considerations should be done regarding the factors which mostly influence the slope behaviour and therefore have to be considered in the modelling phase. Several Authors (Jing & Hudson 2002; Carter et al. 2000; Stead et al. 2001; Stead et al. 2006) described and discussed the applications of numerical methods for slope stability analysis. In Stead et al. (2006) an overview of the conventional and advanced methods is presented. Stability analysis are subdivided into three main categories, from the preliminary kinematics and limit equilibrium techniques to the continuum and discontinuum numerical modelling, to the most advanced hybrid methods (Figure 129). The Authors stressed that the choice of the stability analysis to be performed should be related with the complexity of the investigated mechanism. The use of advanced numerical codes should implicate the increase of the quality and quantity of the available data.

Regarding the San Leo area, investigations about the geological and structural settings, the slope materials characterization, the displacements pattern, and the hydrogeological behaviour have been performed. Based on the knowledge of these factors, some hypotheses were drawn to explain slope instability mechanisms developing in fractured fragile rocky slabs lying on a more ductile substratum. Kinematic analysis has been performed in the areas affected by the 2006 and 2014 landslides. Results are reported in Chapter 2. Anyway, simplified limit equilibrium techniques allow only a partially comprehension of the mechanisms related to lateral spreading and associated secondary slope instability phenomena, e.g. toppling and rock falls occurring at the edge of the slabs (Tommasi 1996; Benko 1997). The numerical modelling allowed these suggestions to be tested and to further deepen the knowledge about the analysed phenomena. The modelling phase involved several stages and the use of

continuum and discontinuum, 2D and 3D numerical codes. Each of them was used at different scales and with distinct focus (Figure 130 and Table 54).
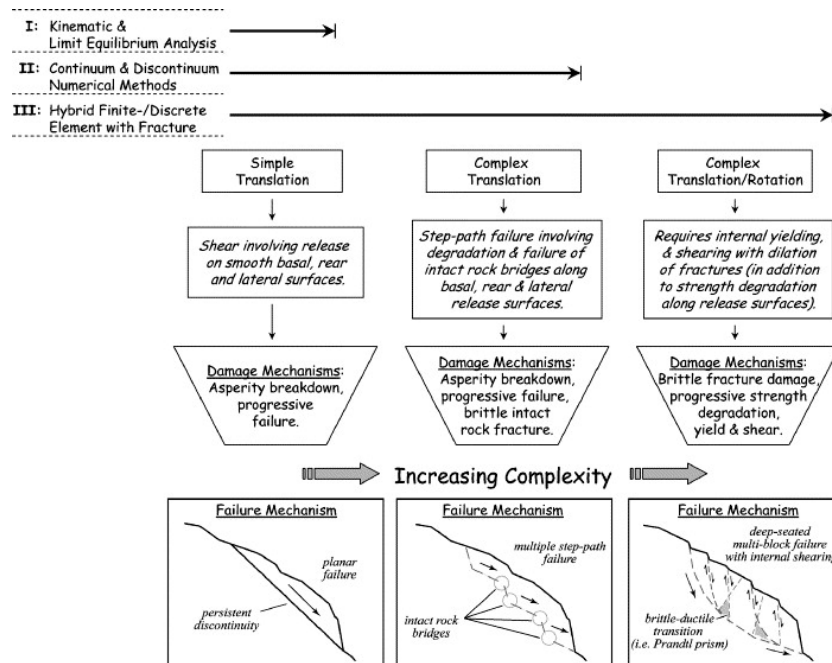

Figure 129. Flowchart illustrating three levels of landslide analysis and the modes of translational/rotational failure they apply to (from Stead et al. 2006).

A model of the whole slab, performed with the Flac3D (Itasca™ 2014) explicit continuum code, was built to achieve a comprehension of the general behaviour of the slab itself. The deformability contrast between the two units (the rock slab and the clay-shale substratum) and the subsequent stress development in the slab were investigated.

The secondary instability phenomena, strictly related to the lateral spreading evolution, can produce a high level of risk for the settlements located both at the top and at the toe of the slabs. The groundwater processes developing at the contact between the more permeable units, i.e. the jointed rock slab, and the relatively impermeable clay-rich units and the resulting undermining of the cliffs have been proposed as predisposing/triggering factor for these kind of instabilities. The behaviour of the clay-rich units has been discussed in Chapter 3: due to the interaction with water both chemical and physical alteration of the substratum were recognized in the field. The additional data acquired after the occurrence of the 2014 landslide provided the opportunity to deepen the understanding of these mechanisms. Back-analyses were conducted coupling Terrestrial Laser Scanning-derived data and Distinct Element Methods (DEMs). On the basis of the numerical simulations, the role of sub-vertical joints, striking almost parallel to the cliff orientation in the failure development was discussed. These analyses confirmed the importance of the erosion of the clay-shale substratum in promoting the rock slab instability.

The role of the softened clay layer and of the undermining at the base of the rock slab had been further investigated through a 2D back analysis of the 2014 landslide, using the finite element program Phase2 (Rocscience Inc. 2013). Other simulations were then performed, inserting the variation of the piezometric surface in the slab, derived from the hydrogeological model, and analysing the role of the water pressure on the pre-existing discontinuity recognized in the field survey. The use of a simplified Discrete Fracture Network (DFN) coupled with a Voronoi approach allowed to simulate fracture propagation trough pre-existing discontinuities and intact rock bridge breaking. As anticipated, at this stage of the research, reliable monitored displacements were not available, the models were mostly calibrated based on field surveys observations and by comparing them with the data from the TLS multi-temporal analysis.

Figure 130. Scales and areas considered in the FLAC3D (blue) 3DEC (red) and Phase2 (green) simulations.

Table 54. Characteristics of the performed simulations

Numerical code	Area	Continuum/ Discontinuum	2D/ 3D	Groundwater	Discontinuities	Fracture propagation	Excavation at the base of the cliff	Softened clay-shale layer
FLAC3D	Whole slab	C	3D	no	theoretical	no	no	no
3DEC	2014 landslide	D	3D	no	yes	no	yes	no
Phase2	2014 landslide	C	2D	yes	yes	yes	yes	yes

6.2 FLAC3D

The analyses performed with the Flac3D (Itasca[TM] 2014) explicit continuum code were focused on the comprehension of the general behaviour of the slab. Several simulations were carried out, starting with a simplified geometry and then inserting the actual topography of the area from the Digital Terrain Model (DTM). The deformability contrast between the two units, i.e. the rock slab and the clay-shale

substratum, and the subsequent stress development in the slab were investigated, with a particular focus on the formation of the actual topography of the slab. Among the others, Casagli (1994), D'Ambra et al. (2004) and Bozzano et al. (2008) modelled the stress development in similar contexts. Their findings indicates that the tensile stress developing in the slab is close to its tensile strength, allowing the formations of vertical discontinuities within the plateau. In a second phase the presence of blocks separated by vertical discontinuities in the rock mass was analysed. Similar block-type movements have been modelled by Benko (1997), who related the type of the external block failure, namely (a) vertical subsidence, (b) translational movement, (c) forward rotation and toppling and (d) backward rotation and sliding to the properties and to the depth of the weak layer. The influence of a softened clay layer, reported in laboratory and field tests, was also investigated. Finally, an attempt to relate these different behaviours with the stress history experienced by the rock mass was made.

6.2.1   Materials and methods

The investigated area included the whole slab and the surrounding clay-shale substratum. A simplified and a real geometries, extracted from the DTM of the area, were used in the modelling stages. The simplified geometry consisted in two superimposed blocks (Figure 131a), representing the clay-shale substratum and the slab. The surface of the block representing the clay-shales was supposed to be planar, i.e. the inclination of the substratum surface was not considered. Different heights were assumed for the edges of the slab, based on the dimensions measured directly on the DTM. The DTM geometry was derived from TLS point clouds and from the photogrammetric aerial surveys carried out by the Marche Region Authority in 1998 (Figure 131b). In both geometries a thickness of 900 m for the clayey unit was considered, to avoid problems at the boundary of the model. The contact between the two units was derived from the interpolation of boreholes data (Chapter 1). The 3D models were created thanks to the Rhinoceros SR4 (McNeel and Associates 2014) software. The Kubrix mesh generator (Itasca[TM] 2014c) allowed to create a suitable model for the Flac3D code.
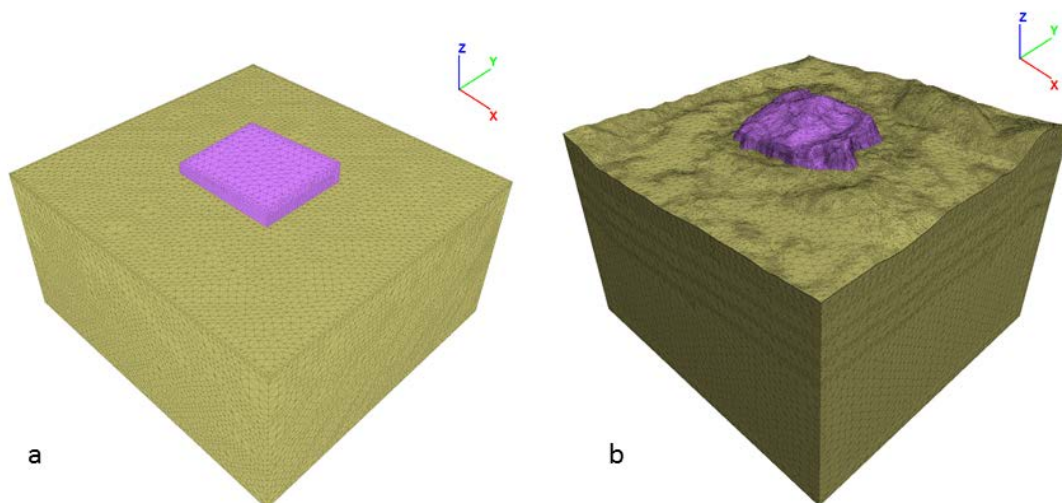
Figure 131. a) Simplified geometry and b) DTM geometry used in the simulations

Zero z-displacements boundary conditions were applied to the bottom and zero x- and y-displacements conditions were chosen respectively for the lateral side parallel to the y and x axis of the clay-shale layer. A Mohr Coulomb constitutive criterion was used for all the materials. Due to the their relative similar behaviour the *San Marino* and the *Monte Fumaiolo* units were supposed to have the same mechanical properties. The rock mass parameters were derived using RocLab (RocScience 2014), based on the structural characterization described in Chapter 2. A Geological Strength Index (GSI, Hoek 1994; Hoek et al. 1995; Hoek and Brown 1998) equal to 50, derived for the whole slab by geomechanical surveys, and an intact uniaxial compressive strength of 99 MPa (Di Giusto 2009) were used as a input to determine the Mohr-Coulomb parameters, reported in Table 55. The tensile strength was assumed equal to 1.25, based on the performed laboratory analysis and on the literature data.

Clay-shales parameters (Table 55) were derived from the performed laboratory tests and from literature (Casagli 1994; Froldi et al. 1994; Ribacchi & Tommasi 1988; Gibertoni 2007). Tensile strength was back analysed thanks to RocLab (Rocscience Inc. 2014b). Due to the thickness of the clay-shale layer, the Young's modulus was increased with depth, till reaching the maximum value reported in Bell (1981) for similar formations (35,000 MPa).

Table 55. Materials parameters used in the Flac3D simulations

Material	Young's modulus E (MPa)	Poisson's Ratio ν	Cohesion (MPa)	Friction angle (°)	Tensile strength (MPa)
Clay-shales	1000	0.3	0.02	20	0.024
Rock slab	8000	0.25	5.8	35	1.25

The last phases of the stress-strain history of the area, consisting in the differential erosion which affected the clay shales with respect to more resistant structural surface of the slab, were simulated through the gradual removal of three clay-shale layers, each with an average thickness of 20 m. Similar approaches have been used successfully by Bozzano et al. (2008) and D'Ambra (2004) to simulate the stress relief caused by the erosion in the softer layer. The same procedure was applied to the simplified (Figure 132) and to the DTM geometries.
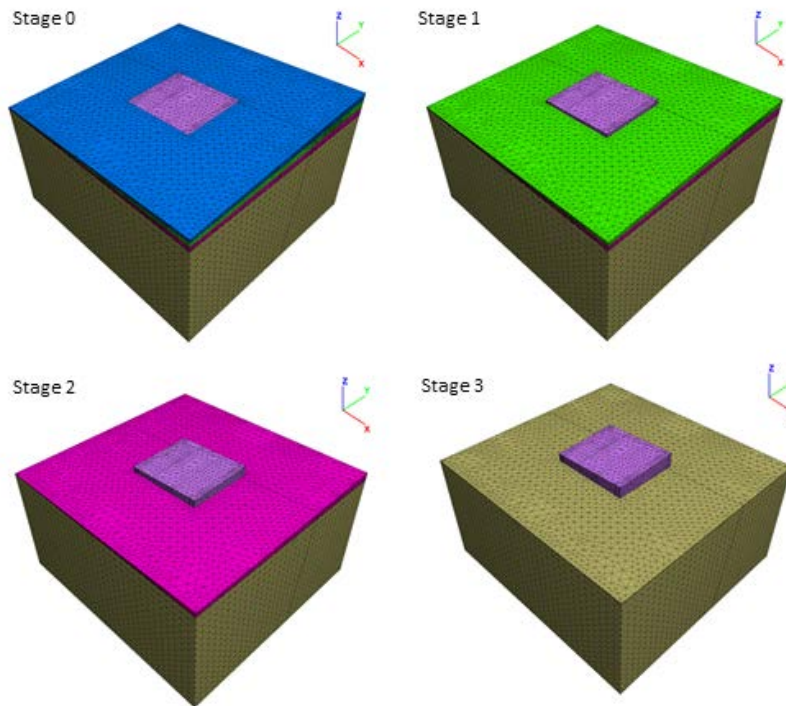
Figure 132. Stages of the model with the simplified geometry. The same stages were applied to the model derived from the DTM

In the successive simulations, 4 vertical discontinuities were inserted in the rock mass. The simulation was aimed to the theoretical analysis of the possible mechanisms controlling the relative displacements between blocks. Position and parameters assigned to the discontinuities (Figure 133) were not strictly based on field evidence.
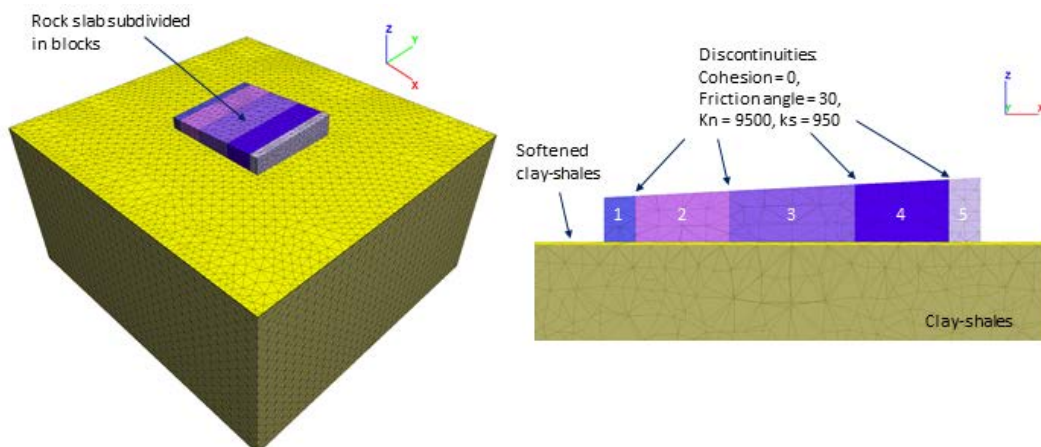
Figure 133. Position and parameters assigned to the discontinuities dividing the rock slab in blocks

Moreover blocks displacements and stresses developing with and without the insertion of a thin clay-shale layer of 5 m depth were investigated. The presence of this layer was pointed out during in-situ and laboratory tests performed after the 2006 landslide. The mechanical parameters of the layer were varied in order to analyse their influence on the results (Table 56). In the latter simulation, the influence

of the block detachments at the border of the slab was tested. The block-type landslides were simulated using a simplified approach, by the removing vertical slices of about 20 m thickness from the slab perimeter.

In this case an interface was inserted between the slab and the underlying clayey layer, to facilitate relative the movements between the two.

Table 56. Materials parameters assigned to the softened clay-shale layer in simulations 1 and 2

Simulation	Young's modulus E (MPa)	Poisson's Ratio ν	Cohesion (MPa)	Friction angle (°)	Tensile strength (MPa)
Softened clay-shales 1	1000	0.3	0.01	10	0.01
Softened clay-shales 2	1000	0.3	0.00	5	0.00
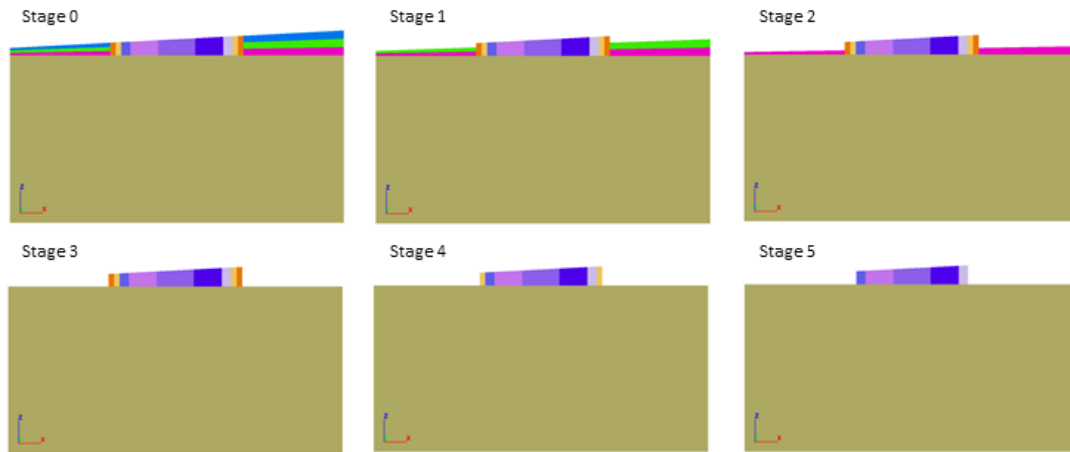
Figure 134. Stages of the model simulating the block-type landslides

The simulations workflow is summarized in Figure 135.

160
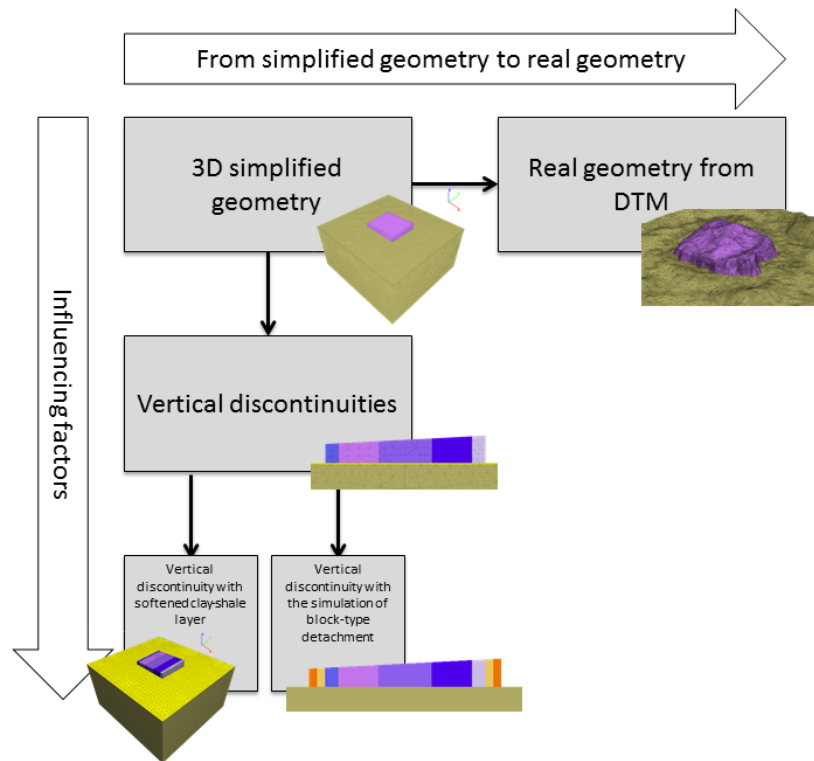
Figure 135. Flowchart showing geomechanical modelling methodology

6.2.2   Results

Results were extracted along sections, for visualization purposes. The EW section was retained to be representative of the general behaviour of the slab. The resulting stress distribution are reported in Figure 136. Both results extracted from the simplified-geometry and from the DTM models are showed. The stiffness contrast between the substratum and the slab generated horizontal stresses in the latter, which can lead to the development of extensional subvertical discontinuities.
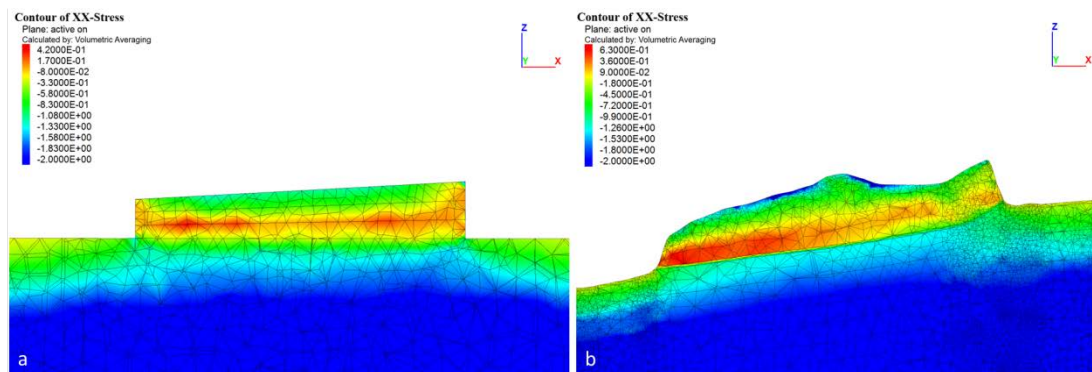
Figure 136. Resulting XX-stress contour in the slab for the simplified geometry (a) and for the DTM (b) simulations

The overburden of the slab causes the squeezing and extrusion of the clay-shales along its borders . The resulting displacements can be observed in Figure 137, representing a particular of the EW section

extracted from the DTM model. As expected also from the displacements behaviour detected with the PS analyses, the greater amount of the movement is concentrated in the clay-shale layer.
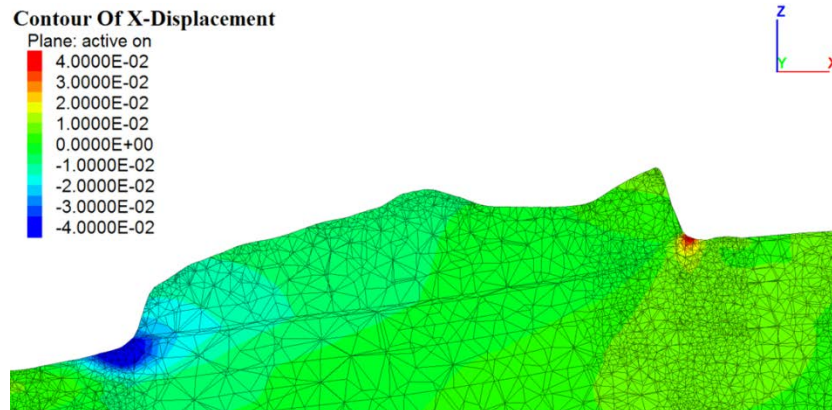
Figure 137. Particular of a EW section extracted from the DTM simulation: displacements in the x (EW) direction

Observing the vertical displacements in the model with the simplified geometry, the slab presents a central area showing negative displacements, in correspondence with the central SSE-NNW depression, named Valsanto, recognized in the field and by analysing the present-day topography (Figure 138). It is worthy to point out that the slab underwent a series of different geological processes in the course of its formation and in the following phases, during which the Epiligurian units were transported on the top of the Ligurian units up to the current position. The present model did not include a careful reconstruction of the geological history of the slab. Anyway, based on the performed simulations, the subsidence of the slab can be included between the factors which could have caused this central depression. Results are in accordance with Silberbauer et al. (1988). He suggested, performing physical modelling of a hard rock slab resting on a soft base, that the squeezing-out of the underlying material can induce the development of a syncline in the slab.
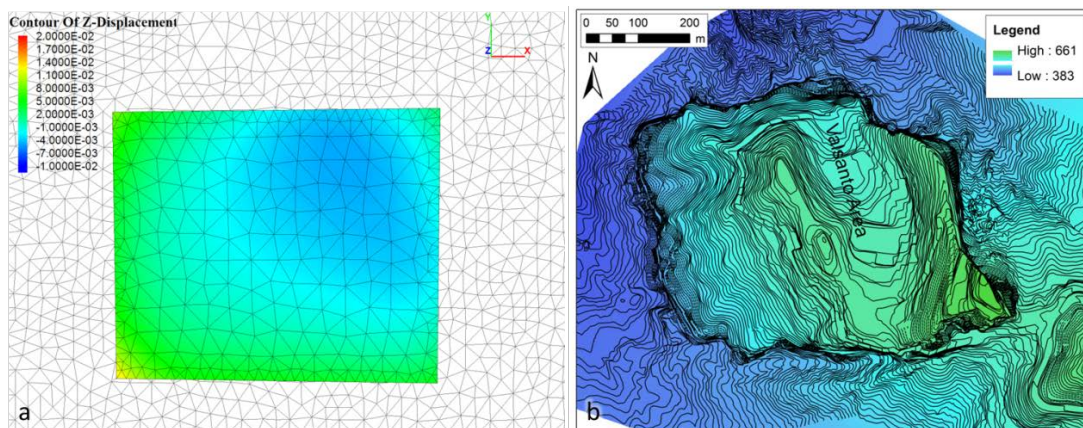
Figure 138. a)Top view of the simplified geometry model (clay-shales in white), showing a depression in the area corresponding to the depression in Valsanto area, recognizable in the present-day topography of the slab (b)

162

The introduction of the discontinuity slightly changed the stress distribution in the slab (Figure 139). Inserting the softened clay-shale layer with lowered parameters (simulations 1 and 2) the tensile stress in the slab increase, most of all in the external blocks, due to the greater contrast between the mechanical characteristics of the slab and of the substratum. Also the displacements increased due to the introducing of the softened layer. Results are presented in Figure 139.
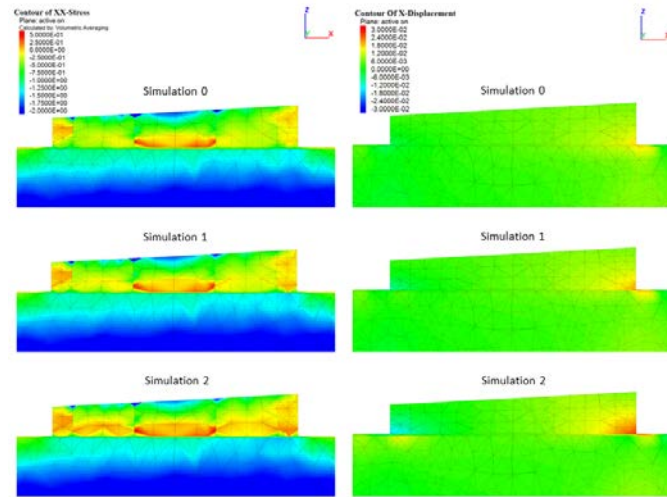
Figure 139. Results of the simulation performed with the insertion of vertical discontinuities and a softened clay-shale layer

The simulation of the stress release due to the detachments of vertical blocks from the edges of the slab highlights how the displacements in the remaining blocks of the slab depend also on the change in stress. The movements, mostly appearing as backward rotation and sliding in the stage 3, tended to assume a backward rotation and toppling tendency in stage 5. The results of this preliminary analysis is presented in Figure 140.
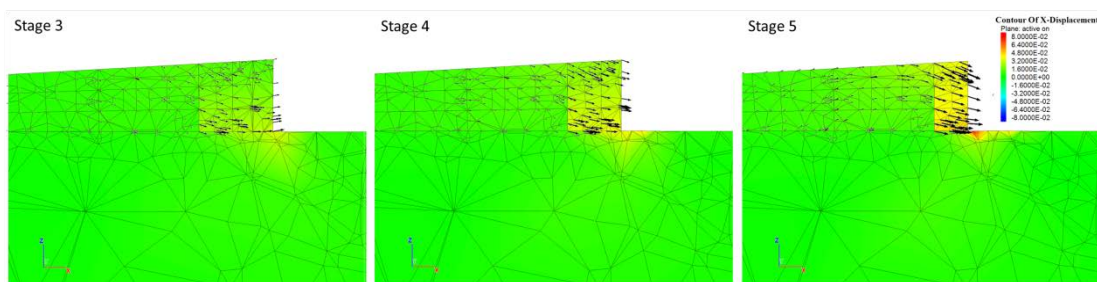
Figure 140. Influence of the simulated block failures at the edge of the slab

6.2.3   Discussion

The 3D simulations performed on the whole slab with the Flac3D code confirmed the results previously obtained by other Authors (Casagli 1994; D'Ambra et al. 2004). The stiffness contrast between the rocky slab and the underlying clay-shales induces horizontal stresses in the plateau, allowing the developing of subvertical discontinuities. The slab seems to have a sinking behaviour, with the lower areas of the

external blocks rotating outside from the centre. The formation of a depressed area in the central sector of the slab can be in part explained with the sinking of the same and the squeezing out of the softer substratum. The influence of the different factors in the kind of displacements developing in the latter have been analysed by Casagli (1994) and Benko (1997). More investigations are needed but, besides the dimension of the blocks, the mechanical properties and the thickness of the soft layer, also the stress-release pattern seems to affect the kind of movements developing at the edge of the plateau.

The larger displacements can be found in the clay-shale substratum, due to its lower strength properties with respect to the overlying rock mass. The presence of a softened clay-shale layer lead to the increase of the contrast between the two units and thus to a rise in the stress within in the slab and in the deriving displacements.

Suggestions for future works should include the insertion of the main structural lineaments individuated thanks to the structural analysis in the model derived from the DTM, in order to perform a more realistic study of the relative displacements between the blocks composing the San Leo slab.

6.3   **3DEC**

Terrestrial Laser Scanner (TLS) surveys and 3D Distinct Element Methods (DEMs) have been coupled to provide an improved understanding of the triggering mechanism of the 2014 landslide. Many Authors have demonstrated the use of TLS for describing the topography and the structural setting of rock cliffs (Sturzenegger & Stead 2009; Fekete & Diederichs 2013; Francioni et al. 2014). Distinct Element Methods have been widely used to simulate rock slope failure involving joint controlled displacements (Brideau et al. 2009; Kalenchuk et al. 2006; Brideau et al. 2011).

TLS-derived data, described in Chapter 2, and numerical modelling using Distinct Element Methods (DEMs) were combined in the back-analysis of the 2014 rock-slope failure. The pre-failure topography was inserted directly into the 3DEC models and a comparison between the pre- and post-failure surfaces was used to constrain the simulation results. Analysis of TLS point clouds provided the geometrical parameters of the joint systems (orientation, persistence, mean trace length) for input into the DEM models. The spacing between discontinuities was derived from the measurements of the dimension of the fallen blocks directly on the TLS point cloud. The 3DEC code (Itasca^{TM} 2014) was used for the rock slope stability simulations. Based on the results an interpretation of the landslide mechanism is proposed.

A flowchart summarizing the adopted workflow is illustrated in Figure 141.
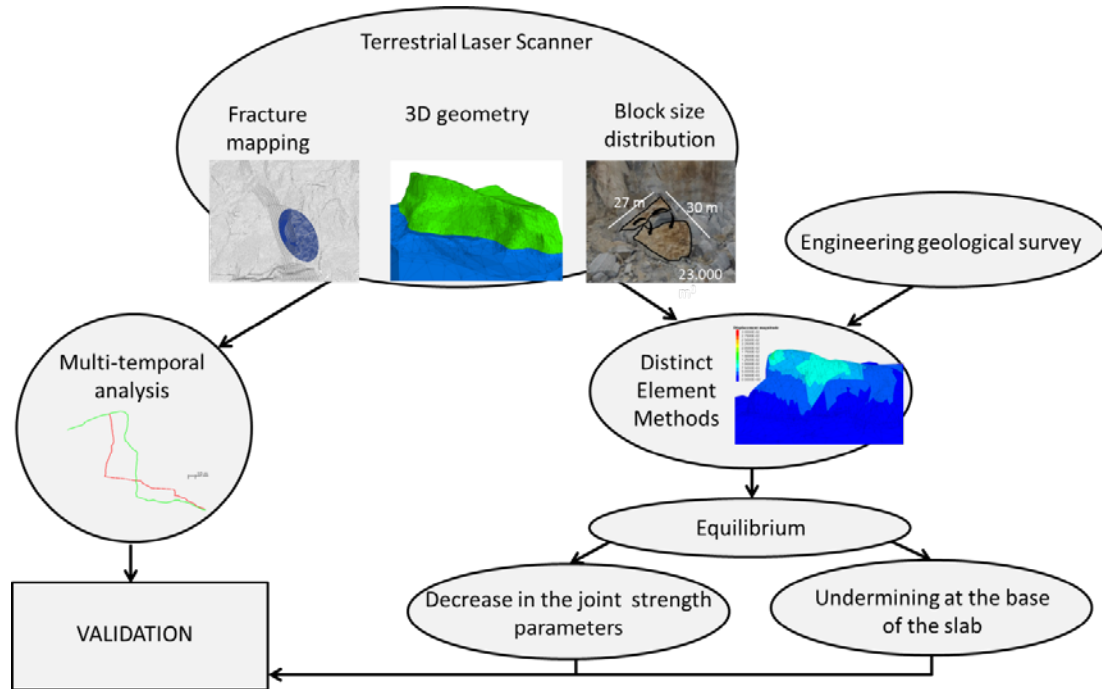
Figure 141. Flowchart showing engineering geological mapping and geomechanical modelling methodology

6.3.1   Materials and methods

In order to analyse the 2014 landslide, the three dimensional distinct element code 3DEC (Itasca[TM] 2014) was used. This software has been successfully applied to landslide modelling by several Authors as it allows representation of the full 3D geometry and the incorporation of discontinuities (Stead et al. 2006; Kalenchuk et al. 2006; Brideau et al. 2011; Firpo et al. 2011). An explicit time marching solution is used to simulate the response of discontinuous rock mass subjected to static or dynamic loading. Discontinuities are treated as boundary conditions between blocks, which can be considered either rigid or deformable. Different constitutive criteria can be used for blocks and for discontinuities. Large displacements along discontinuities are permitted in both the normal and shear direction. Moreover, excavation and backfill simulations can be easily performed using the "null" block procedure.

Based on field evidence, particular emphasis was given to the role of the recognized joint sets and of the undermining at the base of the slab.

Several assumptions were made:

- due to the geometrical complexity of the model, the blocks were considered to be rigid;
- the discontinuity systems were described using the mean spacing, the persistence and a constant orientation of the joint sets;
- groundwater was not accounted for.

The 3D pre-landslide point cloud was joined with the 1*1 DTM of the area derived from photogrammetric aerial surveys. This allowed the complete topography to be described, i.e. both the sub-vertical cliff faces and sub-horizontal top of the slab. The 3D model was firstly created using the

Delaunay triangulation in the CloudCompare (Girardeau-Montaut 2014) software. A resampling of the resolution at about 50 cm was used as an acceptable compromise between a precise description of the topography and a complexity that still permitted practical computer runtimes. The 3D model was imported into the Rhinoceros SR4 (McNeel & associates 2014) software to improve and correct the triangulated mesh. Finally the Kubrix mesh generator (Itasca[TM] 2014) allowed a suitable model for the 3DEC code to be created. The contact between the rock slab and the substratum was created directly in the 3DEC environment and was derived from the interpolation of the data collected in 5 boreholes which were drilled between 1972 and 2001.

The discontinuity orientations obtained from the TLS point clouds (Table 9) were grouped statistically into 3 main joint sets (SL1, SL3, and SL4), to be inserted in the model. Kinematic analysis, described in Chapter 2, highlights the possibility of toppling, planar sliding and wedge detachment for the same area. In the 3DEC software, persistence factor is defined as the probability that any given block lying in the joint path is cut by a discontinuity. On the basis of the field evidence, e.g. the clearly visible discontinuity surface (SL3.1), a persistence factor equal to 1 was assigned to joint set SL3, and 0.5 to the other two sets (SL1, SL4). The assumed spacing value in the numerical simulations depends on the scale of the analysis, i.e. the extent of the study area. In intensively fractured rock masses, the spacing between discontinuities can be very low. The input of these spacing values in the numerical simulations can sometimes represent a problem if the area affected by deformation is large in extent in comparison with the area represented in the point cloud. Moreover, the spacing obtained from slope face surveys may be not representative of the situation within the interior of the rock mass (Francioni et al. 2014). In the San Leo cliffs the surveyed spacing is low and the 3 joint sets were detected even at a small scale. The blocks in the deposit area have a larger dimension than expected in comparison to the joint spacing determined from the field survey. It is clear that not all the discontinuities have an active role in the failure process and that rock bridges both on the surface and between joints play a key role in slope failure. In order to consider only the fractures actively involved in the slope failure mechanism, the spacing was assumed on the basis of the average post-failure block dimensions, e.g. 48% of the blocks have an average side longer than 4 m and the 33% longer than 5 m. This is suggested to provide a more realistic representation of the failure mechanism. The relative spacing between joints was maintained, i.e. the spacing values obtained from the survey were multiplied by the same factor (approximately 10), not to modify the rock mass behaviour. A deterministic approach was used for the insertion of joints belonging to the system SL3, matching their position in the model with that surveyed in the field and visible in the TLS point cloud. Boundary and initial conditions were applied by prescribing zero displacement along the boundary of the model and a gravity load to the entire model. The density of the rigid blocks was assumed to be 26 kN/m^3 for the rock slab and 21 kN/m^3 for the blocks representing the clayey substratum (Ribacchi and Tommasi 1988). A Mohr-Coulomb constitutive criterion was assumed for the discontinuities. Cohesion and friction angle were derived from the results of the geomechanical survey performed in the neighbouring areas and are in the range of values reported in the published

literature (Barton, 1974; Hoek and Bray, 1981). The joint tensile strength was assumed equal to zero. The normal and shear stiffness were derived from the measured JRC and JCS parameters, applying the formulae reported in Barton and Choubey (1977). A mean spacing of 5 m and an average joint aperture equal to 1 mm were used, based on the results of the geomechanical and block dimensions surveys. The normal stress acting on a fracture was assumed to be in the order of 1 MPa. The initial values used in the simulations are reported in Table 57.

Table 57. Mechanical properties of discontinuities assumed in 3DEC analyses

Joint set ID	Cohesion [kPa]	Friction [°]	Kn [MPa/m]	Ks [MPa/m]
SL1	29	34.7	9500	950
SL3	30	34.7	9500	950
SL4	31	34.9	9500	950

3DEC models were first run to equilibrium; then, two different scenarios were simulated. In the first case, the joint parameters were modified lowering the cohesion of the discontinuities by one order of magnitude to account for the degradation of joint properties. In the second case, the observed undermining at the base of the rock cliff was simulated. The extent of the undermined area on the border of the slab was based on field surveys and analysis of photos and TLS point clouds taken before the 2014 landslide. The extent of the undermined area below the rock mass was estimated to be 20 m. The reliability of the simulation results was assessed by comparing them with the data from the TLS multi-temporal analysis. In particular, the difference between the pre- and post-failure point clouds, showing the extent of the area affected by slope instability phenomena, and the contours of the failure main scarp (Section 2.4.8) were used to constrain the 3DEC simulation results.

6.3.2   Results

The model results were evaluated by comparison with the data from the TLS multi-temporal analysis (Figure 142a). As stated above, the 3DEC model was initially run to equilibrium. Results of this phase are visible in Figure 142b, where the dotted white line indicates the extent of the detachment area derived from the multi-temporal analysis on the TLS point clouds. Displacements are mostly registered in the upper part of the slope, in an area similar to the one effectively involved in the 2014 failure. After the equilibrium state was reached, two further simulations were performed. The first simulation investigated the influence of a decrease in the joint cohesion. Results show only local movements in the upper part of the area affected by the landslide (Figure 142c). The maximum displacements are minimal and less than 1 mm. Comparing the results with the detachment area estimated from the TLS, it is clear that a decrease in the joint strength properties alone does not lead to a failure with features similar to the one occurred in February 2014. Displacements derived from this simulation appear to be more similar to localized rock falls and the rock mass volume is much lower than the one observed in the field. Thus, other predisposing and/or triggering factors need to be investigated. For this reason, a second simulation was performed, including the undermining at the base of the cliff. Results for different

calculations cycles are shown in Figure 142d, Figure 144 and Figure 145. The model did not reach equilibrium after the undermining. The area with the maximum displacements is very similar to that affected by failure. Examining the section in Figure 143, it appears that initially the upper part of the cliff is characterized by larger displacements when compared to the lower slope. The largest displacements are shown on the joint SL3.1. Along the nearest discontinuity belonging to the SL3 set, lower displacement rates are apparent. Due to the undermining, some blocks in the lower part of the rock mass detached from the cliff (Figure 144). Examining the results, it is clear that, in all the cases, the main displacements are related to the joint SL3.1. The position of the joint sets in 3DEC is defined assigning a point of origin. As can be seen in the sections, due to the large spacing of the SL3 discontinuity set (20 m) the definition of the point could plays an important role in the mechanism and also in the volume of the failure. To account for this, in the 3DEC simulations the position of joint SL3.1 was inserted deterministically.

It should be emphasised that the failure mechanism shown in the 3DEC model is slightly different from the one visible from the multi-temporal analysis (Figure 142a). It is in fact clear that the failure started along SL3.1, then propagated partly along other pre-existing discontinuities and partly through the intact rock mass. Due to the inability to simulate the formation of new factures in 3DEC, the numerical simulation also show displacements concentrated along the SL3 set in the lower slope area.
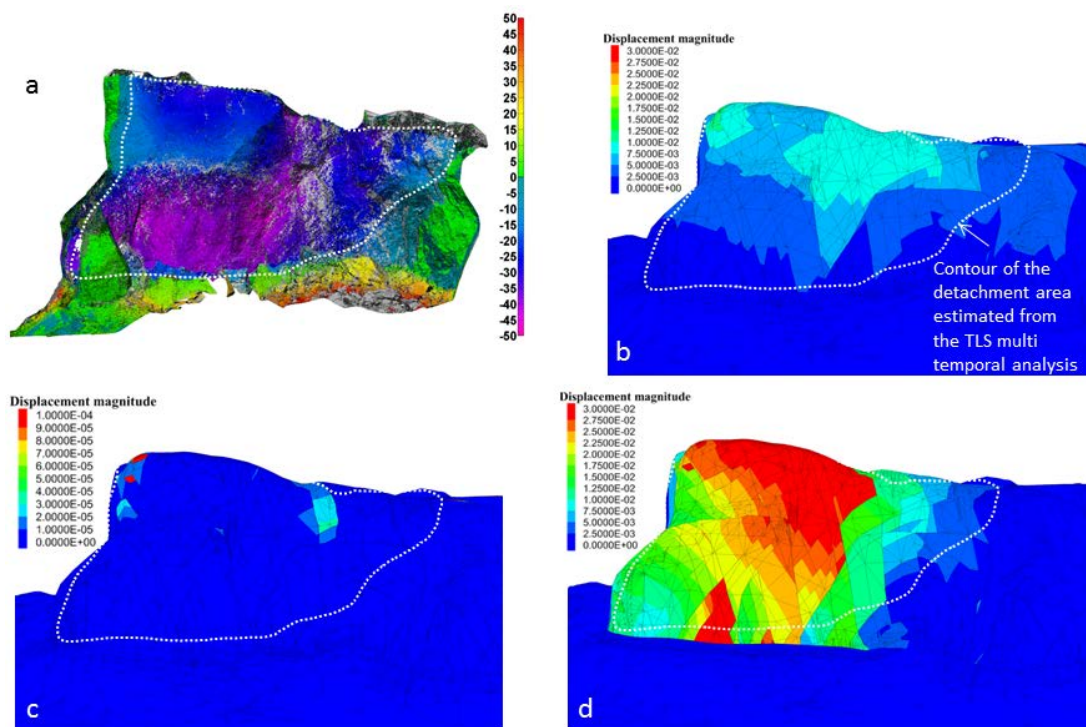
Figure 142. 3DEC results, comparing model simulations and multi-temporal TLS scans. a) The dotted white line indicates the contour of the detachment area derived from TLS point clouds. At the bottom of the slope the actual shape of the failure surface is covered from debris. The shape is reported on the

numerical model results for comparison. b) Results of the first phase of the 3DEC simulation in which the equilibrium was reached; c) results of the simulation performed by lowering the joint strength parameters; d) results of the simulation performed after simulating the undermined area (cycle 50,000). Displacement magnitude is expressed in metres.
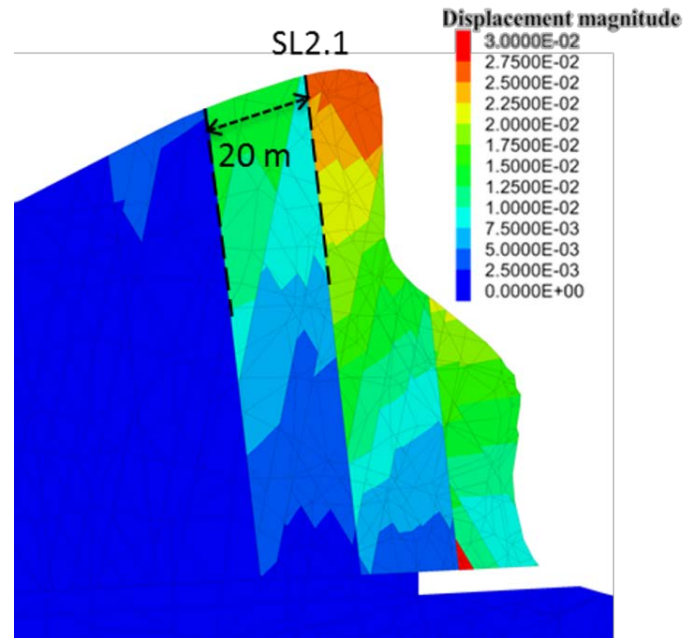
Figure 143. Displacements on a 2D section extracted from the 3DEC simulation (cycle 50,000) including the undermined area. Displacement magnitude is expressed in metres
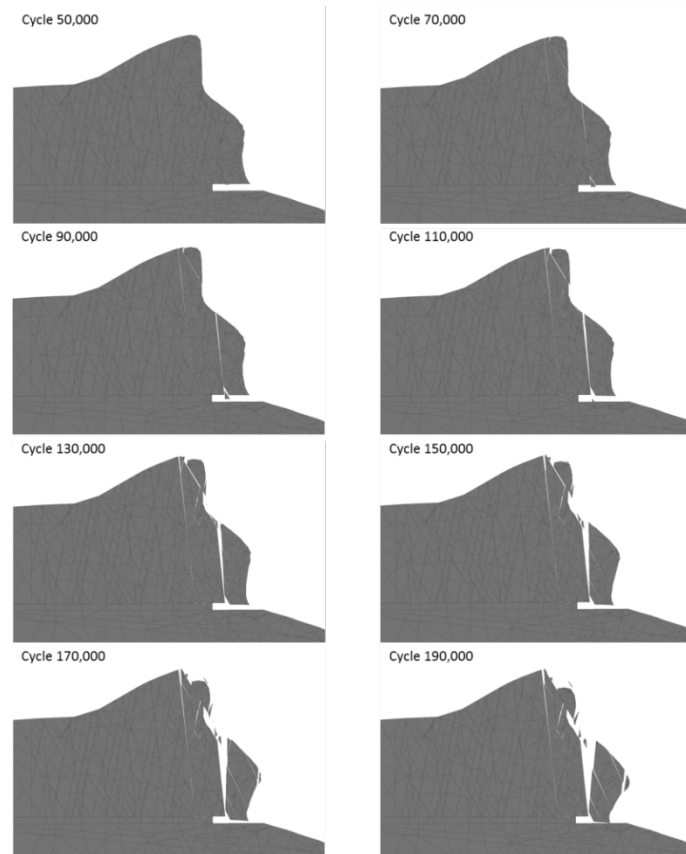
Figure 144. Evolution of the displacements on a 2D section extracted from the 3DEC simulation including the undermined area. Displacement magnitude is expressed in metres
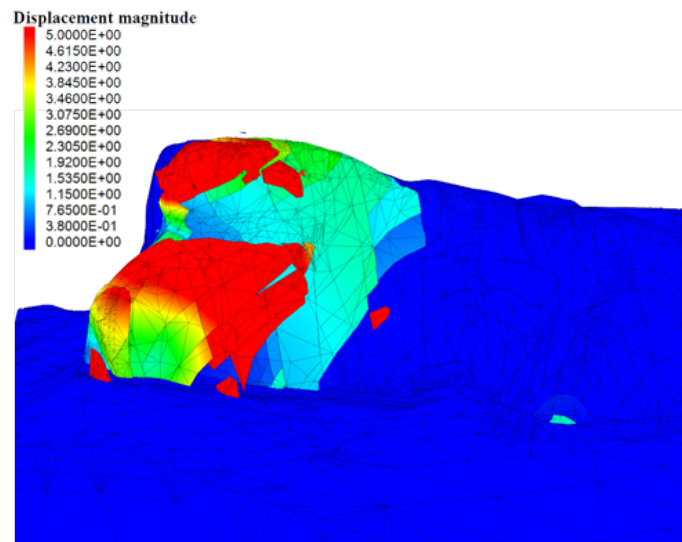
Figure 145. Results of the simulation performed after simulating the undermined area (cycle 140,000)

6.3.3   Discussion

The dataset provided by the TLS measurements allowed an improved understanding of the 2014 slope failure mechanism affecting the north-eastern side of the San Leo rock slab. A combination of the TLS

and traditional surveys allowed the estimation of the geometrical and mechanical properties required as input in the 3D Distinct Element Method simulations. Pre- and post-failure surfaces were derived and compared to estimate the detachment area. Measurements of the block sizes in the deposit area were used to infer an effective equivalent spacing for the three recognized joint sets. The Distinct Element model shows promising results and provides a further understanding of the roles of the discontinuities and of the undermining of the slab in slope failure mechanisms. Based on field evidence and on the results of the model simulations, joint set SL3 seems to be a critical factor in promoting slope instability. Consequently, a deterministic approach was used to input this joint set into the model, avoiding possible errors related to the use of random origin points. In addition, this joint set was characterized by a higher value of persistence. Based on kinematic analysis (Figure 38, section 2.5.1.1.2), this joint set was indicated as a potential plane along which sliding can occur. At the same time, from the photos taken before the 2014 failure and after field surveys, the presence of an undermined sector of the slope in the analysed area was clearly recognizable. Due to the almost-vertical orientation of SL3 joint set, and the undermining at the toe of the slope, the movement, even though having a sliding component, was probably developing as a secondary toppling mechanism, as described in (Evans 1981). The model results and the multi-temporal analysis suggest the following interpretation of the 2014 landslide:

- the cliff became unstable due to the progressive undermining of the rock slab;
- the movements started, or accelerated, along the pre-existing SL3.1 discontinuity, and probably propagated partly along other pre-existing discontinuities and partly through the intact rock mass, with the failure of intact rock bridges. In fact, the comparison between the measured P_{21} before and after the failure shows a small increase, indicating the creation of new fractures during the failure.

These hypotheses are in agreement with the landslide reconstruction proposed in Borgatti et al. (2015).

As stated before, discontinuities belonging to the SL3 joint set were mapped at the top of the slab. Not only joint SL3.1, but also the other joints having a similar orientation, located towards the inner part of the slab showed displacements in the simulations, indicating a progressive increase in their aperture. The slope failure may lead to the development of tension cracks and dilation of joints predisposing the slope to further instability of the same type.

Comparing the results of the simulations, the importance of the undermining of the rock slab in the 2014 landslide is evident. Without inserting the undermined area, the model-displacements are concentrated only in small areas in the upper part of the slope and a low rate of displacement is reached. In contrast, when the undermining is considered, almost the entire area affected by the landslide displays higher movement rates. It is important to note that in other parts of the slab, rock detachments (mostly wedge failures along at least two pre-existing joint sets), especially in the lower part of the cliff, were observed in the field in areas where no erosional features have developed yet, at least at the very border of the slab; as a matter of fact, they are always associated with the presence of a weathered clay-shale layer. The degradation of the clay-shale properties may act as predisposing

factor in the evolution of slope instability processes. More investigations are needed regarding this possible behaviour. Further studies are also required to evaluate the extent of undermining beneath the slab, which could only be estimated in the present work.

Due to the limitations of the performed simulations, i.e. the blocks were considered to be rigid and no new fractures could develop through intact rock, it was not possible to fully reproduce the landslide mechanisms. The dominant roles of joint set SL3 and undermining of the rock slab were however clearly demonstrated.

6.4 **Phase2**

A back analysis of the San Leo 2014 landslide is presented. The aim is to better describe the secondary instability phenomena developing at the edges of the plateau and to recognize the most influencing mechanisms. As anticipated, severe undermining of the rock slab, produced by the progressive removal of the clay-shale units, was noticed in the area prior to the failure (Figure 146b). To date, the erosion process was always associated with the shallow landslides occurring in the surrounding badlands. In this framework, countermeasures such as retaining walls founded on piles were taken in the most exposed areas to avoid further slope instabilities. The complex network of fractures and joints generates a rather high secondary permeability in the slab, with respect to the clay-shale substratum. As anticipated, the presence of several perennial springs, which are fed by the groundwater hosted in the slab, were recently recognized and monitored. Thus, the clay removal at the foot of the cliffs was linked also to spring sapping and piping phenomena occurring at the contact between the slab and the substratum. Moreover, as described in Chapter 3, during the investigations planned after the landslide occurred in 2006, a softened clay-shale layer was recognised (Gibertoni 2007). Field surveys conducted in 2014 in the same areas (Chapter 2), highlighted the presence of several rock detachments, especially at the base of the cliffs. In these areas only small-scale erosional features have developed to date. The phenomena mostly consist in wedge failures along at least 2 pre-existing joint-sets (Figure 146b). They are always associated with the presence of a softened clay-shale layer, along which the wedges can slide.

The softening of the clay-shale layer and/or the undermining of the slab could have caused the developing of toppling phenomena, as described by several Authors in similar contexts. More in detail, Goodman & Bray (1976) recognised different types of toppling phenomena, among which the secondary toppling. In this case, the failure is triggered by undercutting due, for example, to the weathering or the removal of the underlying materials. Evans (1981) focused his work on the secondary toppling, examining the possible failure mechanisms and describing the weathering pattern in claystones underlying sandstone cliffs. Since both removal and softening have been detected in San Leo, the detachment can be here ascribed to this kind of secondary toppling phenomena. Tommasi (1996) investigated on the possible methods used to study slope stability in similar contexts, concluding that the toppling caused by the weathering of the underlying material can be correctly interpreted only using numerical methods (Finite Elements, Finite Difference and Distinct Element Methods).
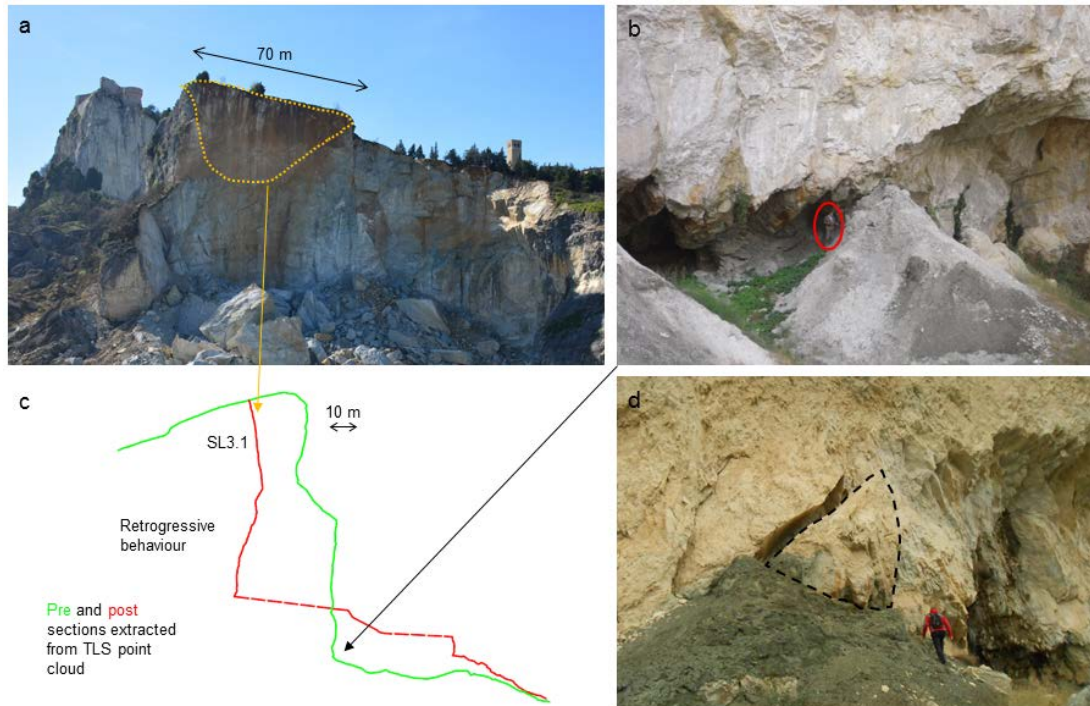
Figure 146. View of the landslide area: a) the dashed yellow line highlights the discontinuity named SL3.1; b) pre-failure photographs showing the undermining at the base of the cliff, in the red circle a person for scale (Photo courtesy STB Romagna); c) section 3 from TLS, in green the pre-failure surface and in red the post-failure surface and d)rock wedge detachments observed in the area of the 2006

The role of the softening and removal of the substratum was investigated more in detail, through a back analysis of the 2014 landslide, by using the Finite Element Methods (FEM) code Phase2.

6.4.1   Materials and methods

The San Leo 2014 back-analysis was aimed at investigating the failure mechanisms and the role of the different factors acting at the border of rock slabs affected by lateral spreading phenomena. As anticipated, two main possible predisposing causes were taken into account: 1) the softening of a relatively thin clay-shale layer down to 5 m depth, and 2) the undermining of the cliff due to the seeping-related erosion of the clay-shales. Simulations were conducted by using the 2D FEM code Phase2, for both cases. FEM code has been widely used to simulate slope failure. Styles et al. (2011) used the same code to back analyse the Joss Bay Chalk cliff failure: the development of a wave-cut notch at the base of the cliff was modelled thanks to the software capability to deal with excavation stages. Sturzenegger & Stead (2012) modelled the Palliser Rockslide stepped failure surface while Kaşmer et al. (2013) assessed the stability of natural slopes prone to toe erosion in Cappadocia (Turkey).

The software allowed the role played by the major discontinuity and by groundwater hosted in the slab to be examined as well. Fracture propagation through pre-existing discontinuities and intact rock bridges breaking were simulated using a simplified Discrete Fracture Network (DFN) coupled with a Voronoi approach.

173

6.4.1.1   Model geometry and parameters

A Mohr-Coulomb failure criterion was assumed for all the materials. In the simulations the discontinuous rock mass was treated as a continuous equivalent medium. Due to the purpose of the analysis and to the relative similarity of the two units composing the slab, the *Monte Fumaiolo* sandstone and the *San Marino* limestone were supposed to have the same mechanical properties. The rock parameters were calculated thanks to Roclab (Rocscience Inc. 2014b). In particular, an intact uniaxial compressive strength of 99 MPa was considered, based on field-test analysis carried out by means of the Schmidt hammer (Di Giusto 2009). A Geological Strength Index (GSI) equal to 50 was obtained from geomechanical surveys. The disturbance parameter D was varied between 0 and 0.7 to estimate respectively peak and residual properties. Since the simulations results are very sensitive to the tensile stress value, a sensitivity analysis was performed. Finally, a value of 1.25 MPa was selected. The latter falls between the minimum value resulting from the RocLab analysis and the maximum one based on the back analysis of the cohesion and friction angle values (6 MPa). Moreover the lab tests performed on borehole core showed values ranging between 2 and 4.9 MPa. Clay-shale parameters, reported in Table 58, were deducted from the performed laboratory tests and literature (Casagli 1994; Froldi et al. 1994; Ribacchi & Tommasi 1998; Gibertoni 2007). Tensile strength was back analysed using the Roclab software. A progressive increase of these parameters with depth was set in order to account for the data reported in Casagli (1994) and Froldi et al. (1994), who showed that the material becomes stiffer by increasing depth. Three main joint sets were mapped in the area (Table 9, section 2.5.1.1.2). A Mohr-Coulomb constitutive criterion was assigned to the pre-existing discontinuities. Cohesion and friction angle were derived from geomechanical survey. The joint tensile strength was back analysed using RocLab (Rocscience 2014). Applying the formula reported in Barton and Choubey (1977), the normal and shear stiffness were derived from the measured JRC and JCS parameters.

Table 58. Material parameters used in the numerical modelling

Material	Unit weight (MN/m^3)	Young's Modulus E (MPa)	Poisson's Ratio ν	Cohesion (MPA)	Cohesion (residual) (MPA)	Friction angle (°)	Friction angle (residual) (°)	Tensile strength (MPA)	Tensile strength (residual) (MPA)
Clay-shales	0.021	1500	0.3	0.040	0.032	28	19.6	0.048	0.045
Rock mass	0.024	17000	0.25	7.2	5.7	39.5	33.8	1.25	0.62

Table 59. Discontinuities and Voronoi parameters used in the numerical modelling

Discontinuity ID	Normal stiffness (MPa/m)	Shear stiffness (MPa/m)	Peak Cohesion (MPa)	Peak Friction Angle (°)	Tensile Strength (MPa)
SL1	9500	950	0.029	34.7	-
SL2	9500	950	0.030	34.7	-
SL3	9500	950	0.031	34.9	-
Voronoi	28000	11000	7.8	41	1.3

Pre- and post-failure geometries were obtained from the TLS surveys of the cliff. The section profiles

174

were extracted from the pre-landslide TLS point clouds and extended by using the DTM of the area, in order to minimize the numerical instability problems which can develop at the model boundaries. The final extension of the model is about 600 m (x direction) per 400 m (y direction). The models were discretized with a graded 6-noded triangle mesh, with a refined grid in the proximity of the edge of the plateau, i.e. the area affected by the failure. A zero y-displacement boundary condition was applied on the vertical sides of the model, while zero x and y-displacements were set for the bottom boundary. Initial conditions were applied by prescribing a gravity load to the entire model. The density of the rigid blocks was assumed to be 24 kN/m3 for the rock slab and 21 kN/m3 for the clayey substratum (Ribacchi and Tommasi 1988). Two sections were extracted and analysed: the first has been selected as the most overhanging one (section 17, Figure 147b), while the second one as it is representative of the pre-failure geometry of the cliff (section 3, Figure 148c).

In more detail, the section 17 was used to test the rock parameters, assuming that, prior to the failure, the factor of safety should have been larger than 1. The Shear Strength Reduction (SSR) tool permitted to individuate the limit of stability (Strength Reduction Factor, SRF) of the slope. In fact, the SSR approach gradually reduces the strength parameters of the materials, until failure is reached. A SRF lower than 1 means that the slope is not stable. The reliability of this methods was discussed by several authors (Hammah et al. 2005; Diederichs et al. 2007; Hammah et al. 2007). The resulting parameters (Table 58) were subsequently used to perform the simulations on the representative section (section 3).
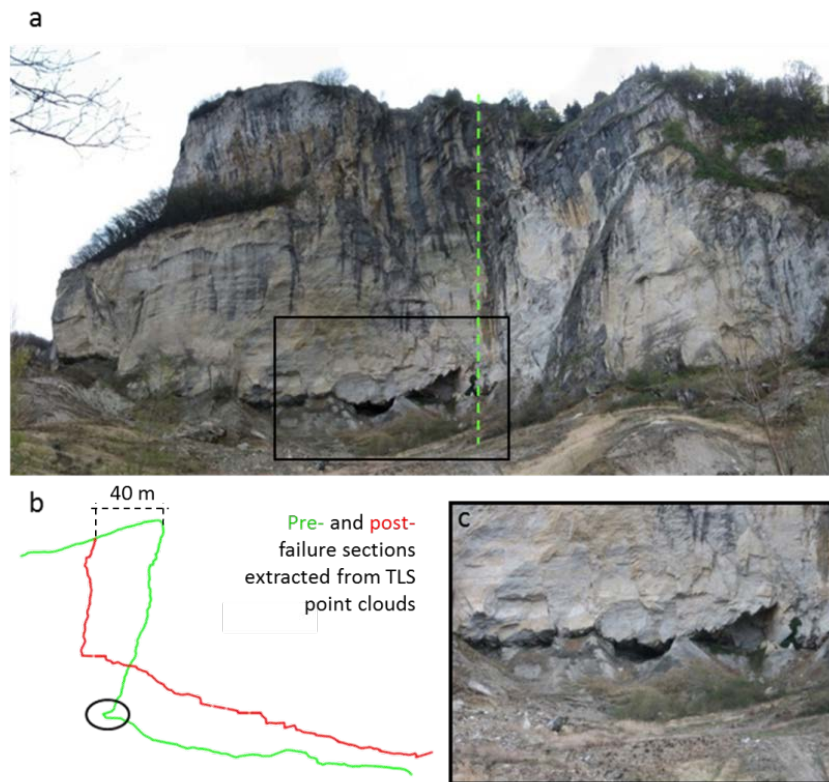
Figure 147. Undermining at the base of the cliff. Section 3 from TLS (b), in green the pre-failure surface with the undermined area highlighted in the black circle, and the post-failure surface shown in red. Photo of the area affected by the failure (pre-landslide): north-eastern cliff (a), and particular (c)

6.4.1.2 Simulations

The following simulations, described in Figure 148 and Figure 149, were performed on the section 3. For all the simulations, the first steps consisted in the gradual removal of 5 clay-shale layers. This approach was followed to simulate the recent evolution of the slope and the related stress history, i.e. the differential erosion (Figure 148, step 1 to 5) acting mostly on the softer clay-shale unit with respect to the rocky slab.
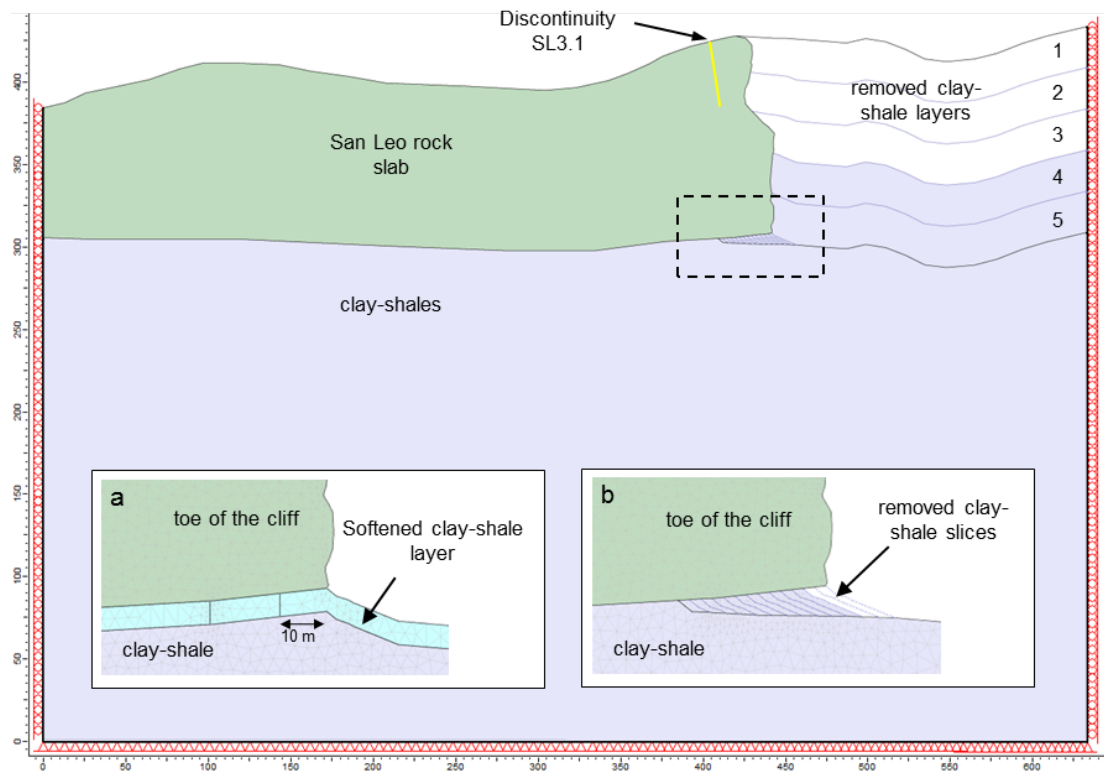
Figure 148. Geometry of the model and of the performed simulations: a) Softening of a thin Clay-Shale Layer of 5 m depth (SCSL) and b) Undermining of the Slab due to the seeping-related erosion of the clay-shales (US). The numbers from 1 to 5 indicate the first stages of the simulations, where the gradual removal of 5 clay-shale layers has been performed

Simulations results were compared with the information gathered by geomorphological surveys and TLS data. In particular the TLS post failure surface was used to validate the numerical results.

Figure 149. Scheme of the performed simulations

6.4.1.2.1   Softened Clay-Shale Layer (SCSL)

To simulate the clay-shale softening, the mechanical properties of a 5 m thick layer were decreased by a factor varying from 0.1 to 0.9. This means that the clay shale parameters, namely Young modulus, cohesion, friction angle and tensile strength, were decreased from 10 to 90% of their initial values, reported in Table 59. The extension of the softened area under the slab is unknown. By analysing claystone weathering pattern in similar context, Evans (1981) and Tommasi (1996) suggested that the softening degree can vary, increasing in the most external parts of the slab (Figure 150).
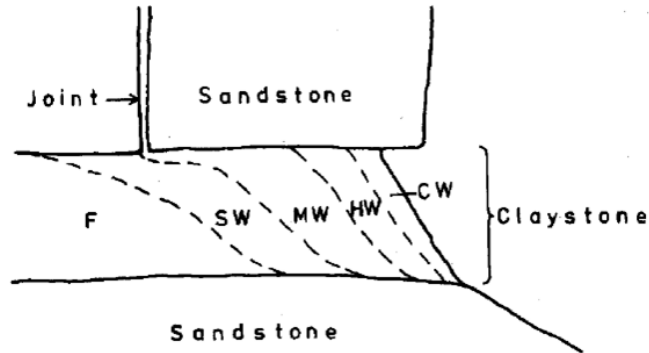
Figure 150. Possible weathering pattern in claystone beneath sandstone cliffs. F= fresh claystone, SW= slightly weathered, MW= moderately weathered, HW= highly weathered, CW= completely weathered (Evans 1981)

Due to the groundwater flow paths and referring to the illustrated weathering scheme, the softened clayey layer extension wa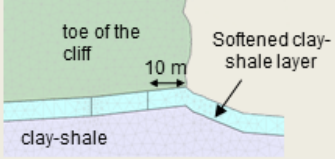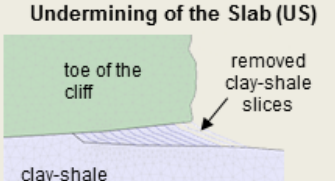s assumed to vary. In particular, simulations were performed with a layer extension of 10, 25 and 50 m, measured from the toe of the cliff and going inwards under the plateau. A latter simulation was performed with the same layer extended for the total length of the plateau. A first analysis was conducted to evaluate the failure mechanisms, with and without the insertion of the pre-existing discontinuity SL3.1. The position and the extension of the same were deducted from the TLS data. Then, several analyses were conducted, varying both the softening degree and the extent of the softened layer. The decreased parameters were then compared with the ones reported by Gibertoni (2007) and derived from laboratory tests. Additional analyses were performed on the simulation with an extension of the softened layer equal to 50 m, to quantify the influence of each decreased parameter.

6.4.1.2.2   Undermining of the Slab (US)

The modelling scheme is composed of several steps, which simulate the erosional processes driven by groundwater seepage (fig.3b). In particular, clay-shale slices of 2.5 m thickness were progressively removed starting from the toe of the cliff. The role of the pre-existing discontinuity SL3.1 was analysed through comparative simulations in which it was or it was not inserted. Then, a SSR approach was used, to calculate the SRF for each model step. A SSR Search Area option was adopted, to focus the research of the failure surface in a particular region of the model, i.e. the area located at the border of the slab. The results permitted to relate the degree of erosion with the stability factor of the slope.

The 3D hydrogeological model, carried out with the finite element code FEFLOW (Diersch 2005), showed a rising of the groundwater level of about 4 meters, prior to the 2014 landslide. To evaluate the influence of the groundwater on the stress conditions in the rock slab and the water pressure acting on the main discontinuity, simulations were performed inserting in the US model the rise of the piezometric line derived by the hydrogeological simulation and the water pressure on the discontinuity SL3.1. In particular, in the simulation of the water surface rise, the average piezometric line extracted from the hydrogeological model was inserted in the model from stage 6, i.e. after the initial phases representing the recent evolution of the slope (differential erosion). The model was run until the slope failure was detected. Then a new simulation was performed, stopping the clayey slices removal at the stage prior to the failure; in the following stage the excavation amount was maintained fixed and the groundwater surface was raised based on the FEFLOW simulation results. Regarding the simulation concerning the water pressure insertion, the slope was excavated since the stage prior to the failure, in the following stage the removal of a further clay-shale slice was substituted with the insertion of the water pressure in the discontinuity SL3.1. This permits to evaluate if the rising of the groundwater level or the water pressure in the discontinuities could be considered as triggering factor of the failure.

6.4.1.2.3   *Implementation of Voronoi approach in the US simulation*

As previously anticipated and pointed out by Borgatti et al. (2015), the failure appeared to develop firstly along a pre-existent discontinuity and then to propagate partly through the intact rock mass, with the failure of intact rock bridges, and partly along other pre-existing discontinuities. The Voronoi tessellation was used to simulate fracture propagation. Applications of Voronoi approach in slope stability have been recently described by several Authors. Gao & Stead (2014) applied this approach to brittle fracture modelling at laboratory and field scale. Havaej et al. (2014) successfully simulated bi-planar failure mechanisms in footwall slopes, while Vivas Becerra (2014) carried out a fully coupled hydro-mechanical analysis on open pit rock slopes using the Voronoi method implemented in the 2D UDEC code. This tessellation randomly subdivides the space into non-overlapping convex polygons. The Phase2 code allows the creation of joint boundaries network, to simulate natural or induced joint patterns within the rock mass. Among them, the Voronoi joint network consists of joints that are defined by the bounding segments of the Voronoi polygons. The Voronoi logic allows the different blocks formed by the polygons to detach completely one another. This approach was implemented in the US model. In order to allow the breaking only through the Voronoi contacts, elastic properties were assigned to the material included within the Voronoi boundaries. The density of the joint network was chosen setting the mean length of the Voronoi polygon edge equal to 0.5 m. This permits to have a fine network without an excessive increase of the computational effort. With reference to Gao & Stead (2014), as fractures can only develop along the block contact, a smaller block size results in a lower influence on the simulated fracture developing pattern. Anyway, due to the strong increase in computational effort caused by the insertion of Voronoi polygon and by the consequent reduction of the mesh size, the latter were inserted only in the area close to edge of the plateau, where the failure

was expected to develop. In this simulation, also the pre-existing discontinuities mapped by means of TLS point cloud, i.e. three main discontinuity sets, were taken into account. As anticipated, analysing the dimensions of the block in the deposit area it was supposed that not all the fractures were actively involved in the slope failure mechanism. Therefore the spacing was assumed on the basis of the average post-failure block dimensions. Three joint networks, each representing one of the joint sets, were introduced in the model, using parallel deterministic networks. This simplified Discrete Fracture Network was implemented with the aim to evaluate the interaction between the pre-existent discontinuities and their propagation trough intact rock failure.
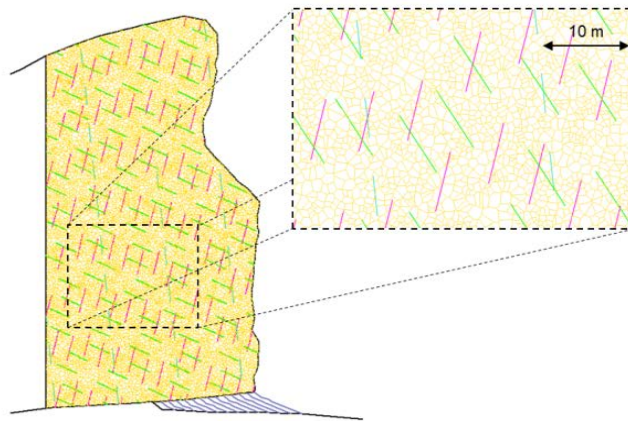
Figure 151. Geometry of the Voronoi network (in yellow) and of the simple DFN. In magenta, blue and green discontinuities belonging respectively to the set SL1, SL3 and SL4.

The strength properties of the rock mass utilized in the previous modelling were evaluated through the use of GSI. This index permit to estimate the equivalent rock mass properties, taking into account both the intact rock and the discontinuities. Thus, due to the explicit insertion of the main discontinuities in the model, the GSI of the rock mass was increased to 70, to avoid to double the effects of the discontinuities in lowering the rock mass parameters. The Voronoi rock mass contacts were characterized with the same cohesion, tensile strength and friction angle of the rock mass. The normal stiffness (k_n) was calculated based on the mean spacing between them, using the formula proposed by Alzo'ubi (2009). The shear stiffness (k_s) was then estimated using the K_n to K_s ratio reported in Christianson et al. (2006). In this way the overall Elastic and Shear modulus values of the rock mass were maintained. The same parameters used in the other simulations were assumed for the clay-shales. The use of the Voronoi logic is expected to provide a more realistic simulation, demonstrating the general trend of fracture initiation and propagation (Vivas Becerra 2014).

6.4.2   Results

In the firsts simulation phases, the step-by-step removal of the clay-shale layer promotes a unloading and a consequential swelling in the clay-shales. Moreover, in all the simulations, squeezing out and shear yielding were noticed in the clayey unit at the edge of the plateau. Both the RCSL and US simulations performed without the insertion of the discontinuity SL3.1 at the top of the slope, showed a

failure pattern dissimilar to the one occurred in 2014. The insertion of the discontinuity permitted to obtain a detachment surface very close to the one measured with the TLS. The comparison of the two is shown in Figure 154. The overall movement can be described as a forward rotation of the detached rock mass, thus the failure mechanism involving the cliff can be described as a toppling phenomenon.

6.4.2.1   Softened Clay-Shale Layer (SCSL)

Various degree of softening and different extension of the involved clay-shales layer were investigated. Analysing the maximum shear strain values and the yielded elements it is possible to recognize which combination of parameters was critical for the onset of slope instability. In Figure 152, the most relevant simulation results are showed: in the upper row the alteration degree was fixed to 80% of the initial values while the lateral extension of the softened layer was increased. The slope reached a critical state when the softened layer was expanded underneath all the slab. Simulations carried out by using a reduced extension of the softened layer (5, 10 and 50 m, respectively) did not reach the failure. Anyway, the lowering of the clay-shale properties appeared to trigger tensile failure in the upper area of the slope and the propagation of the discontinuity SL3.1 when the layer was extended for 50 m under the slab. In the simulations represented in the lower row (Figure 152) the extension of the layer (50 m) was fixed while its properties were gradually changed. The elements located near the failure surface seem to yield when the initial clay-shale properties were diminished by their 85%. The initiation of the discontinuity SL3.1 propagation is recognizable also with higher properties. The shape of the detachment surface was correctly reproduced by the model, showing the backward propagation in the lower sector of the scarp. Areas with higher tensile strain displaying a vertical shape were detected at top of the slab, about 100 m at the rear of the main cliff

The lowered values were compared with the ones derived from field and laboratory tests conducted after the 2006 landslide for the softened layer (Table 60). The cohesion values are very similar, while the friction angle obtained from the simulations appears to be very low in respect to the ones measured in the laboratory. Further analyses were conducted, assuming a 50 m extension of the softened layer and varying the parameters one by one. Results for the cohesion and friction angle variation are reported in Figure 153. For both the parameters the SRF=1 was reached diminishing their value by the 85%. As anticipated in Chapter 3 the several Authors (Calabresi & Scarpelli 1985; Rampello 1992), based on laboratory tests on clay-shales from Italy, suggested that the increase in the water content, acting on interparticle bonding, can produced a decrease in the cohesion.

Table 60. Comparison between the parameters of the softened clayey layer derived from laboratory tests (Gibertoni et al. 2007) and from numerical simulations

	Cohesion (kPA)	Cohesion (residual) (kPA)	Friction angle (°)	Friction angle (residual) (°)
Lab tests	9-10	0-5	17-26	10-16
Simulations (80%)	8	6.4	5.6	3.92

Simulations (90%)	6	4.8	4.2	2.94
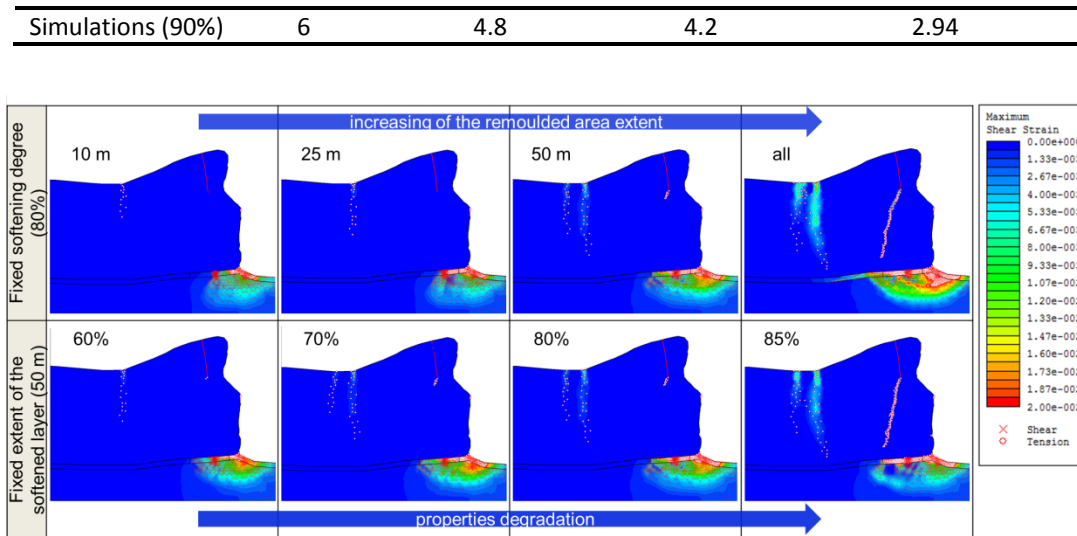
Figure 152. Results of the RCSL simulations. Upper row: fixed softening degree and increasing of the softened layer extent (from left to right); lower row: fixed softened layer extent and lowering of the mechanical properties of the layer (from left to right)
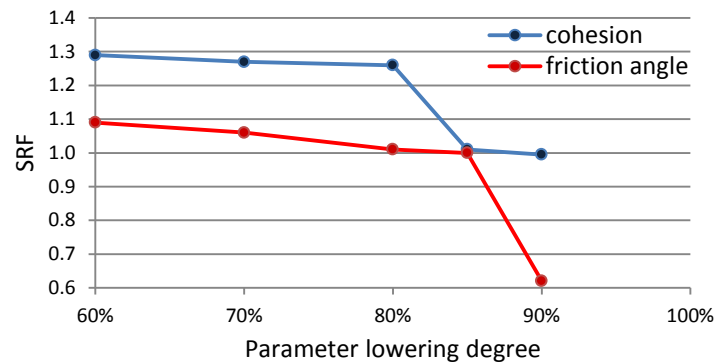
Figure 153. SRF-degree of lowering graph showing the results obtained with a fixed extension of the softened clayey layer and varying its strength parameters

6.4.2.2 Undermining of the Slab (US)

Also in the US simulations the strain propagation initiates from the lower tip of the discontinuity SL3.1 and propagates backwards (Figure 154). The SRF for each stage of the simulation were plotted against the meters of removed clay-shales, e.g. degree of undermining. The critical SRF= 1 is reached between 22.5 and 25 m of excavation (Figure 155). Tensile strain was recorded in the inner part of the slab, probably indicating the joint aperture.
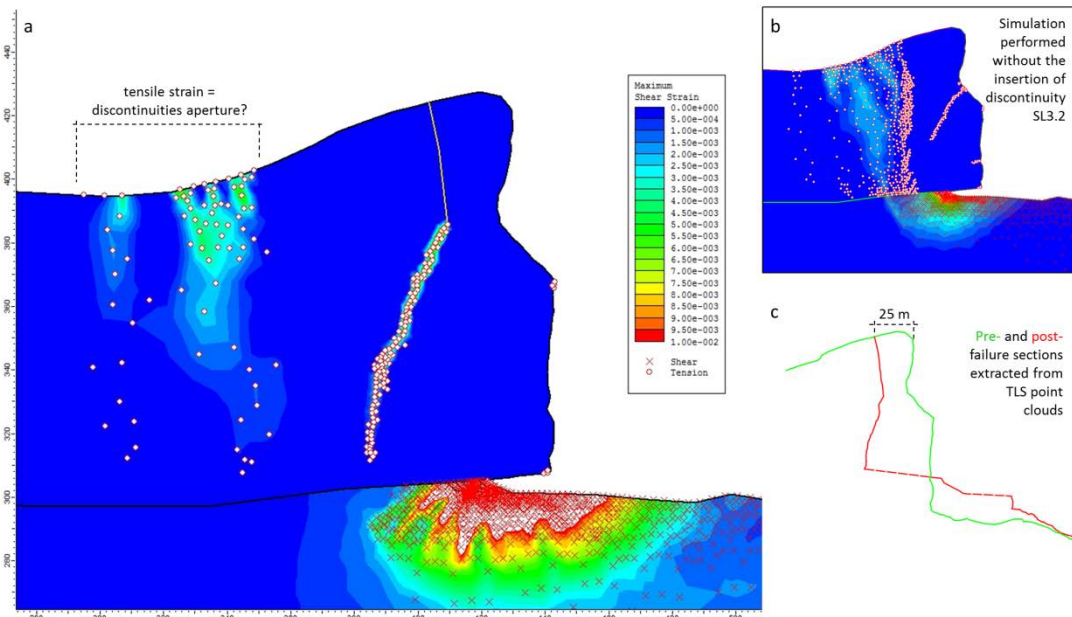
Figure 154. Results of the US simulations: a) Maximum shear strain measured at stage 14; b)US model results with no pre-existing discontinuities; c)Pre- and post-landslide sections extracted from TLS point clouds
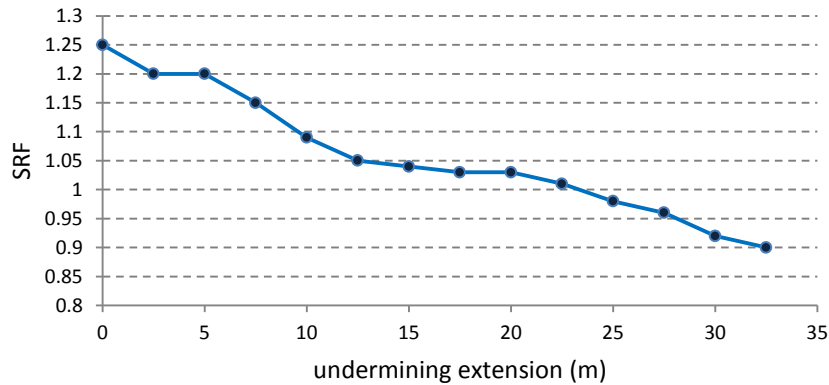
Figure 155. SRF for each stage of the simulation, plotted against the meters of removed clay-shales

The insertion of the piezometric line derived from the FEFLOW model in the US simulation led to the general worsening of the stability conditions of the slope. In particular in the model without the insertion of the piezometric line the failure developed at stage 15 (about 22.5 m of undermining), while taking into account the groundwater surface the failure developed at stage 10 (about 10 m of undermining). Thus, the groundwater level rising was simulated at the 11th stage. As shown in Figure 156a, the simulation stressed that this process alone was not sufficient to trigger the instability. Anyway, the water pressure acting on the main detachment discontinuity can be ascribed among the probable triggering factors. In fact, as illustrated in Figure 156b, the water pressure led to the failure at stage 10 (about 10 m of undermining). Is worth to mention that modelling only the rise in groundwater level do not allow the role of water flow in terms of weathering and erosion to be assessed. In fact, rising in

groundwater level might imply an increase of water seepage velocity and thus an enhancement of erosional and softening processes acting on the clay-shale layer. This phenomenon was not simulated in the model.
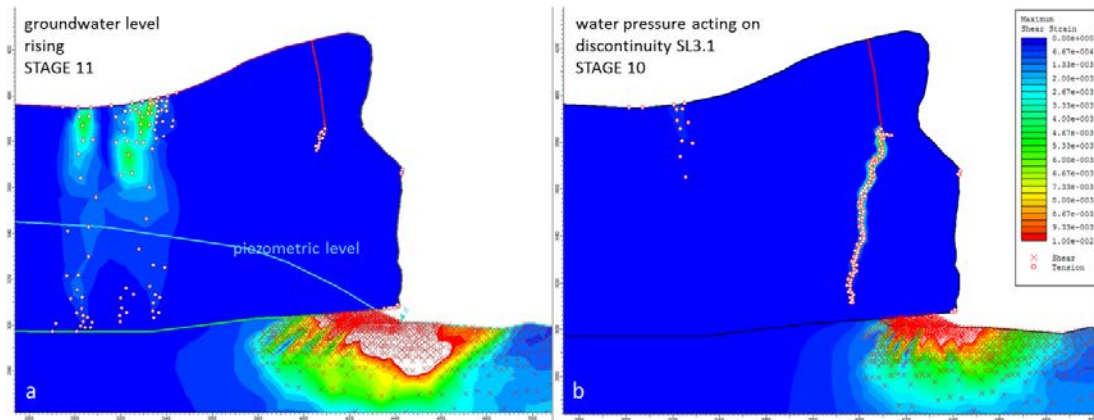
Figure 156. a) Effects of the groundwater level rising (about 4 m) at the 11[h] stage of the simulation; b) effects of the water pressure acting on discontinuity SL3.1 at the 10th stage of the simulation

6.4.2.3 Voronoi

The detachment surface follows the main joint in the upper area of the cliff. In the lower portion both the joints belonging to the simple DFN, e.g. the pre-existing joint sets, and the Voronoi joint network are involved in the failures. The resulting failure surface is representative of the actual failure surface (Figure 157).

Figure 157. Results of the Voronoi simulation, in red the joints yielded at the failure stage, in dark red the joints yielded at previous stages of the simulation. Non-yielded joints are represented with their original colour (green, magenta and blue), non-yielded Voronoi network is hidden for visualization purposes. The failure surface is highlighted in yellow

The Voronoi approach permitted to highlight the fracture propagation through intact rock mass and their interaction with the pre-existing ones and to fully reproduce the detachment mechanisms. The breaking of intact rock bridges can be detected also in areas not directly involved in the phenomena, probably due to boundary effects developing between the area with or without the Voronoi-network, or to the tensile stress developed in the inner part of the slab, visible also in the previous simulations.

6.4.3   Discussion

The work was focused on the long-term effects of groundwater hosted in the slab on the clay-shale unit and consequently on the stability of the rock cliffs. The 2D FEM code Phase2 allowed to correctly simulate the failure, confirming the possibility of a secondary toppling phenomenon acting at the edges of the plateau. The simulations take into account the effects of groundwater flow in the slab and at the contact with the underlying clay-shale layer by introducing (1) the lowering of the mechanical properties of a thin clayey layer underneath the cliff (illustrated by RCSL simulations) or (2) the removal of substratum slices to simulate the undermining of the slab (US simulations). Both these mechanisms have been observed in the field. In the simplified models they were threated separately but they are more probably acting together. In fact, the two effects are actually parts of the same process, i.e. while the shallower layer of clay-shale is progressively eroded the underlying portion is subjected to strength degradation. The undermining can be seen as the last stage of the softening phenomena. Anyway the role of the clay-shale substratum is fundamental in the initiation of the failures affecting the rock slab. Evans (1981) excluded the possibility of a relevant instability triggered by the material removal at the toe of the cliff, admitting that only minor failures (vertical column ranging from 0.5 to 1 m wide) are possible. The relevant difference between his work and the present one is the extension of the undercutting. In fact, areas investigated by Evans (1981) were characterized by maximum erosion depth in the order of 2 m. In the same work, the Author recognized that the size of the rock mass involved in the failure is determined by the extent of basal weathering and undercutting. In the San Leo case study, the undermining necessary for the onset of massive instability in the cliff is similar to the one observed in the field (i.e., about 20 m). Another predisposing factor is the presence of almost-vertical discontinuities at the top of the cliff. Without considering the vertical discontinuities, the actual failure mechanism cannot be reproduced. As shown by the simulations, the increase in the aperture of these discontinuities is favoured by the tensional stress developing in the upper part of the slab prior to the failure. In fact, the shape and the position of the tensile strain areas in the models well agree with the fractures mapped in the field before and after the failure. So, the failure itself lay the groundwork for the subsequent instability events. Tensile failure and subsequent growth of tension cracks at the top of the slope were shown to result from cliff undercutting also in Styles et al. (2011). In this case, probably due to the different mechanical properties of the investigated weak rock and to the absence of a well-developed discontinuity at the top of the cliff, the obtained failure mechanism was slightly different. It consists in a stress concentration developed from the notch and its subsequent upward migration. Also the failure surface shows a different geometry, without the backward propagation typical of the San Leo

2014 landslide. In the simulation performed without the insertion of the uppermost discontinuity, the failure surface geometry appears to be more similar to the ones described by Styles et. al. (2011).

The Voronoi approach was used to represent the fracture propagation in the intact rock mass, transforming a continuous medium in a combination of independent blocks. In this way it was possible to include some of the benefits of the discontinuum methods in a continuum code. The model successfully simulate the complex failure mechanisms, including both the opening of pre-existing fractures and the intact rock bridge fracturing. In the present work the Voronoi approach was used to confirm and integrate the results reached in the previous simulations. Gao and Stead (2014) and Havaeji et al. (2014) suggested that, for the Voronoi tessellation implemented in UDEC, a calibration of the block contact properties is required. The properties used in the performed simulations for the Voronoi joint network seem to reproduce correctly the failure mechanism, so no attempt was made in the calibration of the micro properties.

The achieved results well agree with the back analysis carried out on the same area using the DEM. Moreover, in the 2D simulations, thanks to the continuous numerical code capability, also the back-ward propagation of the detachment surface is reproduced.

6.5   Final considerations about modelling

The present study provides an enhanced knowledge of the slope instability phenomena related to lateral spreading affecting brittle rock masses laying on a softer substratum, which affect several rock plateaux in the northern Apennines of Italy.

The performed numerical modelling gave further insights in the understanding on the acting mechanisms at different scales and of the factors involved. An approach involving the use of different numerical codes is presented. The structural and geological considerations, based on the discontinuities mapping and on field surveys, the performed hydrogeological characterization, the piezometric surface behaviour, derived from the FEFLOW model and the obtained laboratory data were fundamental to create and constrain the performed numerical models.

At the slab scale the modelling results highlighted the influence of the contrast between the two units and of the stress-relief caused by the erosion of the clay-shales as driving factors for the developing of tensile stresses in the rock plateau. As hypothesized in Chapter 3, these phenomena are enhanced by the presence of a softened clay shale layer.

At the cliff scale, the modelling results permitted to relate the hydrogeological behaviour of the slab, investigated through monitoring data analysis and hydrogeological simulations, with the occurring processes, allowing an improved insight on collateral slope instabilities.

A multi-disciplinary approach involving Terrestrial Laser Scanning and 3D Distinct Element modelling is proposed in order to back-analyse the 2014 landslide. Moreover, an attempt was made to simulate the fracture propagation along pre-existing discontinuities and the breaking of intact rock bridge using the 2D Voronoi approach coupled with a simple DFN. The presence of secondary toppling mechanisms, developing at the edges of the fractured plateau was proven. The role of the predisposing and triggering

factors was investigated, highlighting the importance of the processes developing in the clay-shale layer in promoting the rock slab instability. The behaviour of the clay-rich substratum was shown to drive the instability in the area, both due to softening and erosion. In particular, the undermining of the slab, due to the water outflowing at the contact between the two units, was indicated as a predisposing factor. Furthermore the results emphasized the importance of the sub-vertical joints, striking almost parallel to the cliff orientation, in the failure development.

Similar processes can affect others slabs subjected to lateral spreading phenomena.

Some limitation of the present work can be recognized in the inability to fully model the evolution of the failure with time. Using hybrid finite/discrete element codes it is possible to simulate the development of new fractures in intact rock (Stead et al. 2006) and this analysis might be important in the simulation of San Leo slope instability processes. Due to the importance of the discontinuity networks, future developments should also include the application of an accurate DFN procedure, to allow a more realistic representation of the joint network (Elmo & Stead 2010). Input data for this DFN construction are already available through the TLS fracture mapping. Several authors (Elmo 2006; Sturzenegger et al. 2011) have shown how data achieved from terrestrial remote sensing techniques, including both photogrammetry and laser scanner, combined with traditional scanline surveys, can be used for the generation of a DFN, using a statistical approach. The use of these DFN models, combined with the deterministic definition of the main joints involved in the failure, i.e. the joint SL3.1, may lead to a more efficient approach for the discontinuities definition in the numerical models. Furthermore, to reach further insights on the clay-rich soil behaviour, coupled hydro-mechanical viscoplastic models should be performed. The model can be constrained with the displacements measured in the field, for example with the ones occurring in the clay-shales as a consequence of the undrained load of the detached rock mass, e.g. after the 2006 and the 2014 landslide.

CONCLUSIONS

Some Authors (Pasuto & Soldati 2013) recently pointed out the lack of detailed investigations on lateral spreading and related landslides, despite a quite large numbers of these slope processes have been recognized in all Europe. In this context, the present work represents an attempt to gather information and make hypotheses on the causes and on the evolution of these phenomena by means of an interdisciplinary approach. Such slope instability processes can become even more important due to the presence of historical towns and cultural heritage sites often located on the top of the affected plateaux.

Even if the movement rate of the overall slope processes is usually very low, the associated landslides occurring at the border of rock slabs can pose a severe risk to the inhabited centres located in their neighbourhood.

The study was focused on the San Leo rock slab, which represents an outstanding example of this type of landslides. In fact, the San Leo landslide which occurred on the 27th of February 2014 is only the latest of a number of similar events which affected San Leo and others noteworthy villages in the Valmarecchia region over historical time. Several studies were performed, at different scales, on the factors influencing these phenomena but, to date, none of adopted countermeasures seems to have been effective in controlling the phenomena (Borgatti et al. 2015).

The current research permitted to relate the aquifer behaviour of the rocky slab to slope instability processes. The whole process can be summarized as follows. The aquifer hosted in the fractured slab, due to its relatively higher secondary permeability in comparison to the lower clay-rich terrains leads to the development of perennial and ephemeral springs at the contact between the two units. Chemical and physical processes, mainly associated to the interaction of the clayey soil with groundwater, promote softening of the basal clay layer which, associated to piping erosion processes and shallow landsliding, lead to the removal of the clay-rich material at the toe of the slab. The cliff becomes progressively unstable due to undermining and undergoes large-scale landslides due to fall or topple. The resulting landslide deposits may cause an undrained loading on clay-rich terrains (both on bedrock and on loose landslide and slope deposits), which in turn leads to the reactivation or to the acceleration of slow-moving earth slides or flows. Moreover, the stress developing related to the rock failure may contribute to the formation or aperture of discontinuities within the rock slab.

In particular, in the present work:

- the existence of an aquifer and of groundwater flow within the slab was proven and analysed through hydrogeological modelling calibrated with monitoring data (piezometric level and spring discharge);
- the influence of groundwater flow on the clay-shales was investigated by means of specific laboratory tests;

- the subsequent slope instability processes and stress/strain development were back-analysed through continuum and discontinuum numerical models.

Others key aspects and contributions of the current research were:
- the characterization of the structural behaviour of the slab and the recognition of the main lineaments and faults, by means of field surveys and analysis of Terrestrial Laser Scanner (TLS) and Close Range Photogrammetry (CRP) data;
- the comparison of three different survey techniques, i.e. engineering geological surveys, TLS and CRP, in the framework of the structural analyses of the rock mass. The results highlight the main strength and limitations of each procedure and emphasise the importance of their integration. As a suggestion for future works, an indication of the scale at which the use of the different techniques is considered to be convenient was presented;
- the estimation of the effective mean joint spacing to be inserted in numerical models from a statistical analysis of the dimension of the fallen blocks, in order to consider only the fractures actively involved in the slope failure mechanism and to provide a more realistic representation of the failure. The blocks dimensions were mapped in the deposits by means of remote sensing techniques;
- the potential of the PS techniques to detect displacements on rock slabs overlying a softer substratum have been tested following an approach combining analysis on the PS velocity, on the direction of the movement and statistical considerations on the time series trend;
- numerical simulations have been performed coupling Terrestrial Laser Scanner (TLS) surveys and 3D Distinct Element Methods (DEMs) and 2D Finite Element codes;
- fracture propagation through pre-existing discontinuities and intact rock bridges breaking were simulated using a simplified Discrete Fracture Network (DFN) coupled with a Voronoi approach.

The results of this study have already been adopted by Regione Emilia-Romagna RER for the design of a new investigation campaign and a monitoring system, which will in turn provide data to improve the conceptual and numerical model of the slab. Further development should concentrate on the definition of the groundwater flow path within the slab and to the estimation of the seepage erosion rate it can produce in the underlying clayey units in space and time. The detection of the areas affected by an higher spring discharge rate and thus by a more accelerated undermining can help in the identification of the most hazard-prone regions. In fact, the results suggest that the future countermeasure works should be focused on the control of the seepage erosion directly at the source, e.g. acting on the groundwater flow discharge at the contact between the two hydrogeological units (e.g., with drainage tunnels). By considering the water seepage acting at the bottom of the slab as predisposing factor, a possible explanation of the limited effectiveness of the countermeasures adopted so far can be suggested. The adopted retaining walls and drainage trenches, located within the gullies at the foot of

the slope cannot avoid the physical erosion and the chemical weathering of the clay-shales located at the contact with the rock slab.

Regarding the hydrogeological model, the hydraulic conductivity tensors and moduli, describing the permeability values and direction for each area of the slab, can be inserted into the model, to account in more detail for the flow processes. Moreover the hydrogeological monitoring should be continued, allowing the knowledge of the hydrogeological processes in the San Leo rock slab to be brought forward. The clay-shales characterization should be deepened, focusing on the relation between the pore water and soil behaviour. The full characterization of the chemical alteration and of the physical weathering due to the groundwater seepage can improve the understanding of the time-scale related to the described processes. These can be achieved through the repetition of the laboratory tests described in Chapter 3 on the softened portion of the substratum, sampled at the contact with the slab, together with mineralogical and chemical analyses.

Recently RER planned the drilling of several deep-boreholes which will cross the whole slab down to the clay-shales substratum. On the basis of the results of this study, some of them will be equipped with piezometers and electric transducers which will serve to improve the overall hydrogeological dataset, complemented with tracing tests and further slug-tests. Load cells will also be installed in order to investigate the clay-shales behaviour at different depths. In addition to that, the collection of undisturbed clay-shales samples at the contact with the slab will allow the geotechnical characteristics of the clay-shales below the slab to be assessed

The in-continuous monitoring of the slab has just started using wire extensometers at the surface and in sub horizontal boreholes. The data collected can be used in future to further characterize the processes and to calibrate the numerical models. Even if the simulated collapses are mostly instantaneous, small displacements preceding the failure can be detected and accounted for in the simulations.

Moreover, as previously mentioned, the modelling can be improved by using an explicit modelling method, e.g. the code Elfen, to fully model the evolution of fractures with time and by inserting a complete DFN, created by using the data deriving from the performed discontinuity mapping, coupled with the deterministic insertion of the main structural lineaments.

The present work constituted the starting point for an enhanced comprehension of lateral spreading and related slope processes. A hydrogeological characterization of the rock mass was achieved. Finally, the aquifer behaviour of the slab was linked with the ongoing instability processes.

Acknowledgements

REFERENCES

Abellan, A., Jaboyedoff, M., Oppikofer, T. & Vilaplana, J.M., 2009. Detection of millimetric deformation using a terrestrial laser scanner : experiment and application to a rockfall event. *Natural Hazards and Earth System Sciences*, 9, pp.365–372.

Abellán, A., Vilaplana, J.M. & Martínez, J., 2006. Application of a long-range Terrestrial Laser Scanner to a detailed rockfall study at Vall de Núria (Eastern Pyrenees, Spain). *Engineering Geology*, 88(3-4), pp.136–148.

Agisoft, 2014. Agisoft Photoscan Pro. Available at: http://www.agisoft.com/.

Agliardi, F., Crosta, G. & Zanchi, A., 2001. Structural constraints on deep-seated slope deformation kinematics. *Engineering Geology*, 59, pp.83–102.

Agus, S.S. & Schanz, T., 2005. Swelling Pressures and Wetting-Drying Curves of a Highly Compacted Bentonite-Sand Mixture. *Springer Proceedings in Physics*, 93, pp.241–26.

Al-Badran, Y., 2011. *Volumetric Yielding Behavior of Unsaturated Fine-Grained Soils.* Ruhr-Universität Bochum.

Allen, R.G., Pereira, L.S., Raes, D. & Smith, M., 1998. *FAO Irrigation and Drainage Paper No. 56*, Rome.

Alzo'ubi, A.M., 2009. *The effect of tensile strength on the stability of rock slopes*. University of Alberta.

Amit, H., Lyakhowsky, V., Katz, A., Starinsky, A. & Burg, A., 2004. Interpretation of spring recession curves. *Groundwater*, 40(5), pp.543–551.

Andersson, J., 1987. A stochastic model of a fractured rock conditioned by measured information. *Water Resources Research*, 20(1), pp.79–88.

Antonellini, M., Cilona, A., Tondi, E., Zambrano, M. & Agosta, F., 2014. Fluid flow numerical experiments of faulted porous carbonates, Northwest Sicily (Italy). *Marine and Petroleum Geology*, 55, pp.186–201.

APAT, *267 San Marino*.

Arifin, Y. & Schanz, T., 2009. Osmotic suction of highly plastic clays. *Acta Geotechnica*, 4(8), pp.177–191.

Van Asch, T.W.J., Buma, J. & Van Beek, L.P.H., 1999. A view on some hydrological triggering systems in landslides. *Geomorphology*, 30, pp.25–32.

Assali, P., Grussenmeyer, P., Villemin, T., Pollet, N. & Viguier, F., 2014. Surveying and modeling of rock discontinuities by terrestrial laser scanning and photogrammetry: Semi-automatic approaches for linear outcrop inspection. *Journal of Structural Geology*, 66, pp.102–114.

ASTM-Standard-D2216, 2010. Standard Test Methods for Laboratory Determination of Water (Moisture) Content of Soil and Rock by Mass. In *Annual Book of ASTM Standards*. ASTM International.

ASTM-Standard-D422, 2002. Standard Test Method for Particle-Size Analysis of Soils. In *Annual Book of ASTM Standards*. ASTM International.

ASTM-Standard-D4318, 2010. Standard Test Methods for Liquid Limit, Plastic Limit, and Plasticity Index of Soils. In *Annual Book of ASTM Standards*. ASTM International.

ASTM-Standard-D854, 2014. Standard Test Methods for Specific Gravity of Soil Solids by Water Pycnometer. In *Annual Book of ASTM Standards*. ASTM International.

Atkinson, K.B., 1996. *Close Range Photogrammetry and Machine Vision*, Whittles Publishing.

Badioli, L., 2012. *Analisi strutturale della rocca di San Leo*. Università di Bologna.

Baille, W., 2014. *Hydro-Mechanical Behaviour of Clays - Significance of Mineralogy*. Ruhr-Universität Bochum.

Bailly-Comte, V., Jourde, H., Roesch, A., Pistre, S. & Batiot-Guilhe, C., 2008. Time series analyses for Karst/River interactions assessment: Case of the Coulazou river (southern France). *Journal of Hydrology*, 349(1-2), pp.98–114.

Balsamo, F., Storti, F., Salvini, F., Silva, A.T. & Lima, C.C., 2010. Structural and petrophysical evolution of extensional fault zones in low-porosity, poorly lithified sandstones of the Barreiras Formation, NE Brazil. *Journal of Structural Geology*, 32(11), pp.1806–1826.

Barton, N.R. & Choubey, V., 1977. The shear strength of rock joints in theory and practice. *Rock Mech.*, 10(1-2), pp.1–54.

Barton, N.R., Lien, R. & Lunde, J., 1974. Engineering classification of rock masses for the design of tunnel support. *Rock Mech.*, 6(4), pp.189–239.

Bear, J., 1972. *Dynamics of Fluids in Porous Media*, New York: Elsevier.

Bell, F.G., 1981. *Engineering Properties of Soils and Rocks*, Oxford: Butterworth-Heinemann Ltd.

Benedetti, G., Bernardi, M., Bonaga, G., Borgatti, L., Continelli, F., Ghirotti, M., Guerra, C., Landuzzi, A., Lucente, C.C. & Marchi, G., 2013. San Leo: Centuries of Coexistence with Landslides C. Margottini, P. Canuti, & K. Sassa, eds. *Landslide Science and Practice*, 6(IV), pp.529–537.

Benko, B., 1997. *Numerical modelling of complex slope deformations*. University of Saskatchewan.

Berardino, P., Fornaro, G., Lanari, R. & Sansosti, E., 2002. A new algorithm for monitoring localized deformation phenomena based on small baseline differential SAR interferograms. *IEEE International Geoscience and Remote Sensing Symposium*, 2(11), pp.2375–2383.

Berkowitz, B., 2002. Characterizing flow and transport in fractured geological media: A review. *Advances in Water Resources*, 25(8-12), pp.861–884.

Berti, M., Corsini, A., Franceschini, S. & Iannacone, J.P., 2013. Automated classification of Persistent Scatterers Interferometry time series. *Natural Hazards and Earth System Sciences*, 13, pp.1945–1958.

Besl, P.J. & McKay, N.D., 1992. Method for registration of 3-D shapes. In *Proc. SPIE*. pp. 586–606.

Bettelli, G., Bonazzi, U., Fazzini, P., Gasperi, G., Gelmini, R. & Panini, F., 1989. Nota illustrativa alla carta schematica dell'Appennino modenese e delle aree limitrofe. *Memorie della Società Geologica Italiana*, 39, pp.487–498.

Bettelli, G., Bonazzi, U., Fazzini, P. & Panini, F., 1989. Schema introduttivo alla geologia delle Epiliguridi dell'Appennino modenese e delle aree limitrofe. *Memorie della Società Geologica Italiana*, 39, pp.215–244.

Bilotta, E., Pellegrino, A. & Picarelli, L., 1985. *Geotechnical properties and slope stability in structurally complex clay soil*, A.G.I.

Biot, M.A., 1941. General theory of three-dimensional consolidation. *Journal of applied physics*, 12(2), pp.155–164.

Bisci, C., Dramis, F. & Sorriso-Valvo, M., 1996. Rock flow (sackung). In Dikau et al., eds. *Landslide recognition: Identification, Movement and Causes*. Chirchester: Wiley & Sons, pp. 150–160.

Bishop, A.W., 1959. The principle of effective stress. *Teknisk Ukeblad*, 39, pp.859–863.

Bistacchi, A., Ashley Griffith, W., Smith, S.A.F., di Toro, G., Jones, R. & Nielsen, S., 2011. Fault Roughness at Seismogenic Depths from LIDAR and Photogrammetric Analysis. *Pure and Applied Geophysics*, 168, pp.2345–2363.

Bitelli, G., Camassi, R., Gusella, L. & Mognol, A., 2004. Image change detection on urban area: the earthquake case. In O. Altan, ed. *XXth ISPRS Congress*. Istanbul, Turkey, pp. 692–697.

Bittelli, M., Valentino, R., Salvatorelli, F. & Rossi Pisa, P., 2012. Monitoring soil-water and displacement conditions leading to landslide occurrence in partially saturated clays. *Geomorphology*, 173-174, pp.161–173.

Bodin, J., Ackerer, P., Boisson, A., Bourbiaux, B., Bruel, D., Dreuzy, J.-R. De, Delay, F., Porel, G. & Pourpak, H., 2012. Predictive modelling of hydraulic head responses to dipole flow experiments in a fractured/karstified limestone aquifer: Insights from a comparison of five modelling approaches to real-field experiments. *Journal of Hydrology*, 454-455, pp.82–100.

Boehler, W. & Marbs, A., 2004. 3D Scanning and photogrammetry for heritage recording: a comparison. *Geoinformatics*, pp.291–298.

Borgatti, L., Guerra, C., Nesci, O., Romeo, R.W., Veneri, F., Landuzzi, a., Benedetti, G., Marchi, G. & Lucente, C.C., 2015. The 27 February 2014 San Leo landslide (northern Italy). *Landslides*, (July 2014). Available at: http://link.springer.com/10.1007/s10346-015-0559-4.

Boussinesq, J., 1904. Recherches théoriques sur l'écoulement des nappes d'eau infiltrées dans le sol et sur le débit des sources. *Journal de mathématiques pures et appliquées*, pp.5–78.

Bouwer, H. & Rice, R.C., 1976. A slug test for determining hydraulic conductivity of unconfined aquifers with completely or partially penetrating wells. *Water Resources Research*, 12(3), pp.423–428.

Box, G.E.P. & Draper, N.R., 1987. *Empirical Model-Building and Response Surfaces*, New York: John Wiley & Sons.

Bozzano, F., Bretschneider, A., Esposito, C., Martino, S., Prestininzi, A. & Scarascia Mugnozza, G., 2013. Lateral spreading processes in mountain ranges: Insights from an analogue modelling experiment. *Tectonophysics*, 605, pp.88–95.

Bozzano, F., Bretschneider, A. & Martino, S., 2008. Stress-strain history from the geological evolution of the Orvieto and Radicofani cliff slopes (Italy). *Landslides*, 5(March), pp.351–366.

Brideau, M. a., Yan, M. & Stead, D., 2009. The role of tectonic damage and brittle rock fracture in the development of large rock slope failures. *Geomorphology*, 103(1), pp.30–49.

Brideau, M.A., Sturzenegger, M., Stead, D., Jaboyedoff, M., Lawrence, M., Roberts, N.J., Ward, B.C., Millard, T.H. & Clague, J.J., 2011. Stability analysis of the 2007 Chehalis lake landslide based on long-range terrestrial photogrammetry and airborne LiDAR data. *Landslides*, 9(1), pp.75–91.

Butler, J.J.J., 1997. *The Design, Performance, and Analysis of Slug Tests*, CRC press.

Cacas, M.C., 1990. Modeling fracture flow with a stochastic discrete fracture network: calibration and validation. 2. The transport model. *Water Resources Research*, 26, pp.491–500.

Calabresi, G. & Scarpelli, G., 1985. Effects of swelling caused by unloading in overconsolidated calys. In *XI ICSMFE Conference*. San Francisco: AA Balkema, pp. 411–414.

Canuti, P., Casagli, N., Garzonio, C.A. & Vannocci, P., 1990. Lateral spreads and landslide hazards in the Northern Apennine: the example of Mt. Fumaiolo (Emilia Romagna) and Chiusi della Verna (Tuscany). *Proc. 6th Int. IAEG Congr., Rotterdam*, pp.1525–1533.

Carter, B.J., J, D., Ar, I. & Pa, W., 2000. Simulating fully 3D hydraulic fracturing. *Modeling in geomechanics*, 200, pp.525–557.

Casagli, N., 1994. Fenomeni di insatbilità in ammassi rocciosi sovrastanti un substrato deformabile: analisi di alcuni esempi nell'Appennino Settentrionale. *Geologica Romana*, 30, pp.607–618.

Cecere, V. & Lembo-Fazio, A., 1986. Condizioni di sollecitazioni indotte dalla presenza di una placca lapidea su un substrato deformabile. In *Proceedings 16th National Geotechnical Conference,(in Italian), Bologna*. pp. 14–16.

Celico, P., 1988. *Prospezioni idrogeologiche*, Liguori Editore Srl.

Cencetti, C., Conversini, P. & Tacconi, P., 2005. The Rock of Orvieto (Umbria , Central Italy). *Giornale Di Geologia*, 1, pp.103–112.

Cervi, F., Corsini, A., Doveri, M., Mussi, M., Ronchetti, F. & Tazioli, A., 2015. Characterizing the recharge of fractured aquifers: a case study in a flysch rock mass of the northern Apennines (Italy). *Engineering Geology for Society and Territory*, 3, pp.563–567.

Cervi, F., Marcaccio, M., Petronio, F. & Borgatti, L., 2014. Hydrogeological characterization of peculiar Apenninic springs. *Proceedings of the International Association of Hydrological Sciences*, 364(June), pp.333–338.

Chen, Y. & Medioni, G., 1991. Object modeling by registration of multiple range images. *Proceedings. 1991 IEEE International Conference on Robotics and Automation*, 3, pp.2724–2729.

Christianson, M.C., Board, M.P. & Rigby, D.B., 2006. UDEC Simulation of Triaxial Testing of Lithophysal Tuff. In *ARMA*. American Rock Mechanics Association.

Chrzanowski, A., 1993. *Rock Testing and Site Characterization*, Elsevier.

Citrini, D. & Noseda, G., 1987. *Idraulica* 2nd ed., Milano: Casa Editrice Ambrosiana.

Civita, M., 2005. *Idrogeologia applicata e ambientale*, Milano: Casa Editrice Ambrosiana.

Claesson, J. & Bohloli, B., 2002. Brazilian test: Stress field and tensile strength of anisotropic rocks using an analytical solution. *International Journal of Rock Mechanics and Mining Sciences*, 39, pp.991–1004.

Coleman, J.D., 1962. Stress/strain relations for partly saturated soil. *Géotechnique*, 12(4), pp.348–30.

Colesanti, C., Ferretti, A., Prati, C. & Rocca, F., 2003. Monitoring landslides and tectonic motions with the Permanent Scatterers Technique. *Engineering Geology*, 68, pp.3–14.

Conti, S., 1992. Caratteristiche geologico-strutturali delle placche epiliguri della coltre della Val Marecchia e loro riflessi sulla franosità. *Giornale Di Geologia*, 53(2), pp.47–65.

Conti, S. & Tosatti, G., 1996. Tectonic vs gravitational processes affecting ligurian and epiligurian units in the Marecchia Valley (Northern Apennines). *Estr. da: Memorie di scienze geologiche*, 48, pp.108–142.

Crosta, G.B. & Clague, J.J., 2006. Large landslides: Dating, triggering, modelling, and hazard assessment. *Engineering Geology*, 83, pp.1–3.

Cruden, D.M. & Varnes, D.J., 1996. Landslides investigation and mitigation. In A. K. Turner & R. L. Schuster, eds. *Landslide types and process*. National Academy Press, pp. 36–75.

Curtaz, M., Ferrero, A.M., Roncella, R., Segalini, A. & Umili, G., 2014. Terrestrial photogrammetry and numerical modelling for the stability analysis of rock slopes in high mountain areas: Aiguilles Marbrées case. *Rock Mechanics and Rock Engineering*, 47, pp.605–620.

Cvetkovic, V. & Frampton, A., 2010. Transport and retention from single to multiple fractures in crystalline rock at Aspo (Sweden): 2. Fracture network simulations and generic retention model. *Water Resources Research*, 46.

D'Ambra, S., Giglio, G. & Lembo-fazio, A., 2004. Arrangement and Stabilization of the San Leo cliff. In *International Symposium Interpraevent 2004 – Riva/Trient*. pp. 103–114.

Dafny, E., Burg, A. & Gvirtzman, H., 2010. Effects of Karst and geological structure on groundwater flow: The case of Yarqon-Taninim Aquifer, Israel. *Journal of Hydrology*, 389(3-4), pp.260–275.

Davis, G.H., Reynolds, S.J. & Kluth, C., 1996. *Structural geology of rocks and regions*, New York: Wiley & Sons.

Davis, J.C., 2002. *Statistics and data analysis in geology* 3rd ed., New York: John Wiley & Sons.

Deere, D.U. & Miller, R.P., 1966. *Engineering classification and index properties for intact rock.*

Dehghani, M., Valadan Zoej, M.J., Hooper, A., Hanssen, R.F., Entezam, I. & Saatchi, S., 2013. Hybrid conventional and Persistent Scatterer SAR interferometry for land subsidence monitoring in the Tehran Basin, Iran. *ISPRS Journal of Photogrammetry and Remote Sensing*, 79, pp.157–170.

Delmonaco, G., Margottini, C. & Spizzichino, D., 2009. Low impact interventions for the preservation of Cultural Heritage: the dying town of Civita di Bagnoregio (Central Italy) and the killer landslide. In *Protection of Historical Buildings, PROHITECH 09*. London: Taylor & Francis Group, pp. 1455–1459.

Derron, M.-H. & Jaboyedoff, M., 2010. LIDAR and DEM techniques for landslides monitoring and characterization. *Natural Hazards and Earth System Science*, 10(9), pp.1877–1879.

Dershowitz, W.S. & Einstein, H.H., 1988. Characterizing rock joint geometry with joint system models. *Rock Mechanics and Rock Engineering*, 21, pp.21–51.

Dershowitz, W.S., Lee, G., Geier, J., Foxford, T., LaPointe, P. & Thomas, A., 1998. FracMan Interactive Discrete Feature Analysis, Geometric Modeling and Exploratory Simulations User Documentation, Version 2. 6.

Devoto, S., 2013. *Cartografia, monitoraggio e modellizzazione di frane lungo la costa nord-occidentale dell'isola di Malta*. Università degli Studi di Modena e Reggio Emilia.

De Souza, M.K., Veronez, F.M., Tognoli, W., Da Silveira, J.L.G., Inociencio, L.C., Da Silva, R.M. & Modena, R.C.C., 2013. Terrestrial Laser Scanning: Application for Measuring of Structures Information in Geological Outcrops. *International Journal of Advanced Remote Sensing and GIS*, 2(1), pp.260–270.

Diederichs, M.S., Lato, M., Hammah, R. & Quinn, P., 2007. Shear strength reduction approach for slope stability analyses. In *Proceedings of the 1st Canada-US Rock Mechanics Symposium*. pp. 319–327.

Diersch, H.J.G., 2005. FEFLOW finite element subsurface flow and transport simulation system. *Reference manual.*

Di Giusto, M., 2009. Ispezione delle condizioni di stabilità del muro di contenimento del piazzale superiore del forte di San Leo (PU).

Dramis, F., 1985. Slope geomorphology. In *Italian Research on Physical Geography and Geomorphology: an overview*. Bologna: C.N.R.-Technoprint, pp. 5–11.

Dramis, F. & Sorriso-Valvo, M., 1994. Deep-seated gravitational slope deformations, related landslides and tectonics. *Engineering Geology*, 38, pp.231–243.

Duffield, G.M., 2007. AQTESOLV for Windows Version 4.5 User's Guide, HydroSOLVE. *Inc., Reston, VA*.

Eberhardt, E., Stead, D. & Coggan, J.S., 2004. Numerical analysis of initiation and progressive failure in natural rock slopes-the 1991 Randa rockslide. *International Journal of Rock Mechanics and Mining Sciences*, 41, pp.69–87.

Elmo, D., 2006. *Evaluation of a hybrid FEM/DEM approach for determination of rock mass strength using a combination of discontinuity mapping and fracture mechanics modelling, with particular emphasis on modelling of jointed pillars*. Unversity of Exeter.

Enser srl, 2006. *Interventi urgenti di difesa del suolo in località Fosso Campone*.

Enser srl, 2014. *Lavori di somma urgenza per il monitoraggio ed,approfondimento conoscitivo della nuova morfologia dei luoghi del versante nord della rupe di San Leo (RN) interessata da crollo*.

Evans, R.S., 1981. An analysis of secondary toppling rock failures—the stress redistribution method. *Quarterly Journal of Engineering Geology and Hydrogeology*, 14(2), pp.77–86.

Fardin, N., Feng, Q. & Stephansson, O., 2004. Application of a new in situ 3D laser scanner to study the scale effect on the rock joint surface roughness. *International Journal of Rock Mechanics and Mining Sciences*, 41(2), pp.329–335.

Faulkner, D.R., Jackson, C.A.L., Lunn, R.J., Schlische, R.W., Shipton, Z.K., Wibberley, C.A.J. & Withjack, M.O., 2010. A review of recent developments concerning the structure, mechanics and fluid flow properties of fault zones. *Journal of Structural Geology*, 32(11), pp.1557–1575.

Fekete, S. & Diederichs, M., 2013. Integration of three-dimensional laser scanning with discontinuum modelling for stability analysis of tunnels in blocky rockmasses. *International Journal of Rock Mechanics and Mining Sciences*, 57, pp.11–23.

Ferretti, A., Prati, C. & Rocca, F., 2000. Nonlinear subsidence rate estimation using permanent scatterers in differential SAR interferometry. *Geoscience and Remote Sensing, IEEE transactions on*, 38(5), pp.2202–2212.

Ferretti, A., Prati, C. & Rocca, F., 2001. Permanent scatterers in SAR interferometry. *IEEE Transactions on Geoscience and Remote Sensing*, 39(1), pp.8–20.

Firpo, G., Salvini, R., Francioni, M. & Ranjith, P.G., 2011. Use of Digital Terrestrial Photogrammetry in rocky slope stability analysis by Distinct Elements Numerical Methods. *International Journal of Rock Mechanics and Mining Sciences*, 48, pp.1045–1054.

Fleury, P., Ladouche, B., Conroux, Y., Jourde, H. & Dörfliger, N., 2009. Modelling the hydrologic functions of a karst aquifer under active water management – The Lez spring. *Journal of Hydrology*, 365(3-4), pp.235–243.

Forkasiewicz, J. & Paloc, H., 1967. Le régime de tarissement de la Foux de la Vis. *Etude preliminaire: Chronique d'Hydrogeologie, BRGM*, 3(10), pp.61–73.

Francioni, M., Salvini, R., Stead, D. & Litrico, S., 2014. A case study integrating remote sensing and distinct element analysis to quarry slope stability assessment in the Monte Altissimo area, Italy. *Engineering Geology*, 183, pp.290–302.

Fredlund, D.G. & Rahardjo, H., 1993. *Soil mechanics for unsaturated soils.*, John Wiley & Sons.

Freeze, R.A. & Cherry, J.A., 1979. *Groundwater*, Prentice-Hall, Englewood Cliffs, NJ.

Freudlund, D.G. & Morgenstern, N.R., 1977. Stress state variables for unsaturated soils. *Journal of the Geotechnical Engineering Division ASCE*, 103, pp.447–466.

Froldi, P., Mantovani, S., Lunardi, P. & Podesta, G., 1994. Argille Scagliose'complex in northern Italy: the geotechnical characterisation. In *Proceedings, International Association of Engineering Geology, 7th International Congress: Lisbon*. pp. 459–468.

Gao, F.Q. & Stead, D., 2014. The application of a modified Voronoi logic to brittle fracture modelling at the laboratory and field scale. *International Journal of Rock Mechanics and Mining Sciences*, 68, pp.1–14.

Gburek, W.J., Folmar, G.J. & Urban, J.B., 1999. Field data and ground water modeling in a layered fractured aquifer. *Ground Water*, 37(2), pp.175–184.

Geyer, T., Birk, S., Liedl, R. & Sauter, M., 2008. Quantification of temporal distribution of recharge in karst systems from spring hydrographs. *Journal of Hydrology*, 348(3-4), pp.452–463.

Gibertoni, F., 2007. *Analisi di una frana in località San Leo (PU)*. Università di Bologna.

Gigli, G., Frodella, W., Mugnai, F., Tapete, D., Cigna, F., Fanti, R., Intrieri, E. & Lombardi, L., 2012. Instability mechanisms affecting cultural heritage sites in the Maltese Archipelago. *Natural Hazards and Earth System Science*, 12, pp.1883–1903.

Girardeau-Montaut, D., 2014. CloudCompare. Available at: http://www.danielgm.net/cc/.

Golder Associates, 2009a. FracMan. Available at: http://www.fracman.golder.com.

Golder Associates, 2009b. FracMan.

Goldstein, H., Poole, C.P.J. & Safko, J.L., 2001. *Classical Mechanics* 3rd ed., Addison-Wesley.

Gonzalez de Vallejo, L., Ferrer, M. & de Freitas, M., 2011. *Geological Engineering*, London: Taylor & Francis Group.

Goodman, R.E. & Bray, J.W., 1976. Toppling of rock slopes. In *Rock Engineering for Foundations & Slopes*. ASCE, pp. 201–234.

Goudie, A.S. ed., 2004. *Encyclopedia of Geomorphology*, London: Routledge.

Grenon, M., Bruneau, G. & Kapinga Kalala, I., 2014. Quantifying the impact of small variations in fracture geometric characteristics on peak rock mass properties at a mining project using a coupled DFN-DEM approach. *Computers and Geotechnics*, 58, pp.47–55.

Greppi, M., 2005. *Idrologia*, Hoepli.

Hamdi, P., Stead, D. & Elmo, D., 2014. Damage characterization during laboratory strength testing: A 3D-finite-discrete element approach. *Computers and Geotechnics*, 60, pp.33–46.

Hammah, R.E., Yacoub, T.E., Corkum, B., Wibowo, F. & Curran, J.H., 2007. Analysis of blocky rock slopes with finite element shear strength reduction analysis. In *Proceedings of the 1st Canada-US Rock Mechanics Symposium*. pp. 329–334.

Hammah, R.E., Yacoub, T.E., Corkum, B.C. & Curran, J.H., 2005. The shear strength reduction method for the generalized Hoek-Brown criterion. In *Proceedings of the American Rock Mechanics Association*.

Hammer, Ø., Harper, D.A.T. & Ryan, P.D., 2001. PAST: Paleontological statistics software package for education and data analysis. *Palaeontologia Electronica*, 4(1).

Haneberg, W.C., 2007. Directional roughness profiles from three-dimensional photogrammetric or laser scanner point clouds. In E. Eberhardt, D. Stead, & T. Morrison, eds. *Rock Mechanics: Meeting Society's Challenges and Demands*. pp. 101–106.

Hao, Y., Yeh, T.-C.J., Gao, Z., Wang, Y. & Zhao, Y., 2006. A gray system model for studying the response to climatic change: The Liulin karst springs, China. *Journal of Hydrology*, 328(3-4), pp.668–676.

Hartley, L. & Joyce, S., 2013. Approaches and algorithms for groundwater flow modeling in support of site investigations and safety assessment of the Forsmark site, Sweden. *Journal of Hydrology*, 500, pp.200–216.

Havaej, M., Stead, D., Eberhardt, E. & Fisher, B.R., 2014. Characterization of bi-planar and ploughing failure mechanisms in footwall slopes using numerical modelling. *Engineering Geology*, 178, pp.109–120.

Humair, F., Pedrazzini, A., Epard, J.L., Froese, C.R. & Jaboyedoff, M., 2013. Structural characterization of turtle mountain anticline (alberta, canada) and impact on rock slope failure. *Tectonophysics*, 605, pp.133–148.

Hungr, O., Leroueil, S. & Picarelli, L., 2014. The Varnes classification of landslide types, an update. *Landslides*, 11(April 2013), pp.167–194.

Hungr, O. & McDougall, S., 2009. Two numerical models for landslide dynamic analysis. *Computers and Geosciences*, 35(5), pp.978–992.

Hvorslev, M.J., 1951. *Time lag and soil permeability in ground-water observations*.

Imiriland Project, 2004. *Guidelines on the use of numerical methods for the prediction of failure*,

Innovmetric Software, 2014. Polyworks. Available at: http://www.innovmetric.com/.

Inus Technology, 2012. RapidForm XOR. Available at: http://www.rapidform.com/.

ISO 14688, 2002. Geotechnical investigation and testing - Identification and classification of soil - Part 1: Identification and description, p.12.

ISRM International Society of Rock Mechanics, 1985. Suggested methods for determining point load strength. *International Journal of Rock Mechanics and Mining Sciences*, 22, pp.53–60.

ISRM International Society of Rock Mechanics, 1978. Suggested Methods for Quantitative Description of Discontinuties in Rock Masses. *International Journal of Rock Mechanics and Mining Sciences*, 15, pp.319–368.

Itasca^{TM}, 2014a. 3DEC. Available at: http://www.itascacg.com.

Itasca^{TM}, 2014b. Flac3D. Available at: http://www.itascacg.com.

Itasca^{TM}, 2014c. Kubrix. Available at: http://www.itascacg.com.

Jaboyedoff, M., Metzger, R., Oppikofer, T. & Derron, M., 2007. New insight techniques to analyze rock-slope relief using DEM and 3D-imaging cloud points : COLTOP-3D software. In E. Eberhardt, D. Stead, & T. Morrison, eds. *Rock Mechanics: Meeting Society's Challenges and Demands, Proceedings of the 1st Canada-US Rock Mechanics Symposium*. Taylor & Francis Group, pp. 61–68.

Jaboyedoff, M., Oppikofer, T., Abellán, A., Derron, M.-H., Loye, A., Metzger, R. & Pedrazzini, A., 2010. Use of LIDAR in landslide investigations: a review. *Natural Hazards*, 61(1), pp.5–28.

Jennings, J.E. & Knight, K., 1975. A guide to construction on or with materials exhibiting additional settlement due to collapse of grain structure. In *Proceedings Sixth Regional Conference for Africa on Soil Mechanics and Foundation Engineering*. pp. 99–105.

Jing, L., 2003. A review of techniques, advances and outstanding issues in numerical modelling for rock mechanics and rock engineering. *International Journal of Rock Mechanics and Mining Sciences*, 40(3), pp.283–353.

Jing, L. & Hudson, J. a., 2002. Numerical methods in rock mechanics. *International Journal of Rock Mechanics and Mining Sciences*, 39, pp.409–427.

Kalenchuk, K.S., Diederichs, M.S. & McKinnon, S., 2006. Characterizing block geometry in jointed rockmasses. *International Journal of Rock Mechanics and Mining Sciences*, 43(8), pp.1212–1225.

Kanit, T., Forest, S., Galliet, I., Mounoury, V. & Jeulin, D., 2003. Determination of the size of the representative volume element for random composites: Statistical and numerical approach. *International Journal of Solids and Structures*, 40, pp.3647–3679.

Kaşmer, Ö., Ulusay, R. & Geniş, M., 2013. Assessments on the stability of natural slopes prone to toe erosion, and man-made historical semi-underground openings carved in soft tuffs at Zelve Open-Air Museum (Cappadocia, Turkey). *Engineering Geology*, 158, pp.135–158.

Kemeny, J. & Post, R., 2003. Estimating three-dimensional rock discontinuity orientation from digital images of fracture traces. *Computers and Geosciences*, 29(1), pp.65–77.

Kemeny, J. & Turner, K., 2008. *Ground based LIDAR. Rock slope Mapping and assessment*.

Kiraly, L., 1969. Anisotropie et hétérogénéité de la perméabilité dans les calcaires fissurés. *Eclogae Geol. Helv.*, 562(2), pp.613–619.

Kligfield, R., 1979. The Northern Apennine as a collisional orogen. *American Journal of Sciences*, 279, pp.679–681.

Kovács, A. & Sauter, M., 2007. Modelling karst hydrodynamics. *Frontiers of Karst Research*, 13, p.107.

Kuhn, D. & Prüfer, S., 2014. Coastal cliff monitoring and analysis of mass wasting processes with the application of terrestrial laser scanning: A case study of Rügen, Germany. *Geomorphology*.

Lambe, T.W. & Whitman, R. V., 1969. *Soil mechanics*, John Wiley & Sons.

Laribi, A., Walstra, J., Ougrine, M., Seridi, A. & Dechemi, N., 2015. Use of digital photogrammetry for the study of unstable slopes in urban areas: Case study of the El Biar landslide, Algiers. *Engineering Geology*, 187, pp.73–83.

Lee, C.-H. & Farmer, I., 1993. *Fluid Flow in Discontinuous Rocks*, London: Chapman & Hall.

Lembo-Fazio, A., Ribacchi, R., Sciotti, M. & P., T., 1998. Problematiche di intervento su versanti naturali per la salvaguardia di abitati ed opere di ingegneria. Alcuni esempi in relazione a diversi tipi di dissesto. In *6° Ciclo di conferenze di Meccanica delle Rocce*.

Long, J.C.S., Remer, J.R., Wilson, C.R. & Witherspoon, P.A., 1982. Porous media equivalents for networks of discontinuous fractures. *Water Resour Res*, 18(3), pp.645–658.

Louis, C., 1974. Introduction a l'hydraulique des roches. In *BULL BRGM*. Paris: Paris Ed. BRGM., pp. 283–356.

Lu, N. & Godt, J., 2008. Infinite slope stability under steady unsaturated seepage conditions. *Water Resources Research*, 44(November), pp.1–13.

Machiwal, D. & Jha, M.K., 2006. Time series analysis of hydrologic data for water resources planning and management: a review. , pp.237–257.

Maillet, E., 1905. *Essais d'hydraulique souterraine et fluviale.*, Paris: A. Hermann.

Di Maio, C., Santoli, L. & Schiavone, P., 2004. Volume change behaviour of clays: The influence of mineral composition, pore fluid composition and stress state. *Mechanics of Materials*, 36, pp.435–451.

Di Maio, C., Vassallo, R. & Vallario, M., 2013. Plastic and viscous shear displacements of a deep and very slow landslide in stiff clay formation. *Engineering Geology*, 162, pp.53–66.

Malgot, J., 1977. Deap-seated gravitational slope deformations in neovolcanic mountain ranges of Slovakia. *Bull. IAEG*, 16, pp.106– 109.

Martinotti, G., Giordan, D., Giardino, M. & Ratto, S., 2011. Controlling factors for deep-seated gravitational slope deformation (DSGSD) in the Aosta Valley (NW Alps, Italy). *Geological Society, London, Special Publications*, 351, pp.113–131.

Matasci, B., Ravanel, L., Jaboyedoff, M. & Deline, P., 2012. Structural analysis and stability assessment of the West face of the Drus (3733m , Mont Blanc massif). *Geophysical Research Abstracts*, 14.

MATTM, M. dell'Ambiente e della T. del T. e del M., 2009. *Linee guida per l'analisi di dati interferometrici satellitari in aree soggette a dissesti idrogeologici, Direzione Generale per la Difesa del Suolo.*

Mauldon, M., 1998. Estimating Mean Fracture Trace Length and Density from Observations in Convex Windows. *Rock Mechanics and Rock Engineering*, 31, pp.201–216.

Mauldon, M., Dunne, W.M. & Jr, M.B.R., 2001. Circular scanlines and circular windows : new tools for characterizing the geometry of fracture traces. , 23, pp.247–258.

McColl, S.T., 2014. *Landslide Hazards, Risks and Disasters* T. Davies, ed., Oxford: Elsevier.

McNeel and Associates, 2014. Rhinoceros 4. Available at: http://www.rhino3d.com/download/rhino/4.0.

Meisina, C., Zucca, F., Conconi, F., Verri, F., Fossati, D., Ceriani, M. & Allievi, J., 2007. Use of Permanent Scatterers technique for large-scale mass movement investigation. *Quaternary International*, 171-172, pp.90–107.

Meisina, C., Zucca, F., Fossati, D., Ceriani, M. & Allievi, J., 2006. Ground deformation monitoring by using the Permanent Scatterers Technique: The example of the Oltrepo Pavese (Lombardia, Italy). *Engineering Geology*, 88, pp.240–259.

Mero, F., 1964. Application of the groundwater depletion curves in analyzing and forecasting spring discharges influenced by well fields. In *Publication no. 63 of the IASH, Symposium on Surface Waters*. pp. 107–117.

Molli, G., 2008. Northern Apennine Corsica orogenic system: an updated overview. *Geological Society of London Special Pubblications*, 298, pp.413–442.

Mora, P., Baldi, P., Casula, G., Fabris, M., Ghirotti, M., Mazzini, E. & Pesci, A., 2003. Global Positioning Systems and digital photogrammetry for the monitoring of mass movements: application to the Ca' di Malta landslide (northern Apennines, Italy). *Engineering Geology*, 68(1-2), pp.103–121.

Morgenstern, N.R., 1985. Geotechnical aspects of environmental control. In *XI ICSMFE Conference*. San Francisco: AA Balkema, pp. 155–185.

Mueller, R. & Loew, S., 2009. Predisposition and cause of the catastrophic landslides of August 2005 in brienz (Switzerland). *Swiss Journal of Geosciences*, 102, pp.331–344.

Mun, Y. & Uchrin, C.G., 2004. Development and application of a MODFLOW preprocessor using percolation theory for fractured media. *JAWRA Journal of the American Water Resources Association*, 40(1), pp.229–239.

Neuman, S.P., 2005. Trends, prospects and challenges in quantifying flow and transport through fractured rocks. *Hydrogeology Journal*, 13(1), pp.124–147.

Nuth, M. & Laloui, L., 2008. Effective stress concept in unsaturated soils: Clarification and validation of a unified framework. *International Journal for Numerical and Analytical Methods in Geomechanics*, 32, pp.771–801.

Oppikofer, T., Jaboyedoff, M., Blikra, L., Derron, M. & Metzger, R., 2009. Characterization and monitoring of the Aknes rockslide using terrestrial laser scanning. *Natural Hazards and Earth System Science*, 9, pp.1003–1019.

Palmstrøm, A., 1996. Characterizing rock masses by the RMi for use in practical rock engineering, part 2: Some practical applications of the rock mass index (RMi). *Tunnelling and Underground Space Technology*, 11(3), pp.287–303.

Pan, J.B., Lee, C.C., Lee, C.H., Yeh, H.F. & Lin, H.I., 2010. Application of fracture network model with crack permeability tensor on flow and transport in fractured rock. *Engineering Geology*, 116(1-2), pp.166–177.

Pankow, J.F., Johnson, R.L., Hewetson, J.P. & Cherry, J.A., 1986. An evaluation of contaminant migration patterns at two waste disposal sites on fractured porous media in terms of the equivalent porous medium (EPM) model. *Journal of Contaminant Hydrology*, 1(1-2), pp.65–76.

Papini, F., Corniello, A., Ducci, D. & Aquino, A., 2008. *Memorie Illustrative della Carta Idrogeologica del Parco Regionale dei Monti Picentini (Campania)*.

Pašek, J. & Pulinowa, M.Z., 1975. Mouvements de Gres Cretaces en Blocs dans les Monts Stolowe Gory (Pologne). *Bulletin of the International Association of Engineering Geology*, 14(5), pp.79–82.

Pasuto, A. & Soldati, M., 2013. *Lateral spreading*, Elsevier.

Pesci, A., Fabris, M., Conforti, D., Loddo, F., Baldi, P. & Anzidei, M., 2007. Integration of ground-based laser scanner and aerial digital photogrammetry for topographic modelling of Vesuvio volcano. *Journal of Volcanology and Geothermal Research*, 162, pp.123–138.

Picarelli, L., 2000. Mechanisms and Rates of Slope Movements in Fine Grained Soils. *GeoEng 2000*, pp.1618–1670.

Picarelli, L., Di Maio, C., Olivares, L. & Urciuoli, G., 2000. Properties and behaviour of tectonized clay shales in Italy. In Evangelista & Picarelli, eds. *The geotechnics of hard soils-soft rocks*. Rotterdam: Balkema, pp. 1211–1242.

Picarelli, L., Urciuoli, G., Mandolini, a. & Ramondini, M., 2006. Softening and instability of natural slopes in highly fissured plastic clay shales. *Natural Hazards and Earth System Sciences*, 6(1985), pp.529–539.

Poropat, G. V, 2009. Measurement of Surface Roughness of Rock Discontinuities. , 2009(May), pp.1–9.

Priest, S.D., 1993. *Discontinuity analysis for rock engineering.*, London: Chapman & Hall.

Prokop, a. & Panholzer, H., 2009. Assessing the capability of terrestrial laser scanning for monitoring slow moving landslides. *Natural Hazards and Earth System Science*, 9, pp.1921–1928.

Rampello, S., 1992. Some remarks on the mechanical behaviour of stiff clays: the example of Todi clay. In *Experimental Characterization and Modelling of Soils and Soft Rocks : A Workshop in Napoli*. Napoli: Università degli Studi di Napoli, pp. 131–190.

Rao, S., Thyagaraj, T. & Thomas, H., 2006. Swelling of compacted clay under osmotic gradients. *Geotechnique*, 56(10), pp.707–713.

Rauch, A.F., Martin, J.R., Brandon, T.L., Duncan, J.M., Filz, G.M., Kriz, R.D. & Mitchell, J.K., 1997. *EPOLLS : An Empirical Method for Predicting Surface Displacements Due to Liquefaction-Induced Lateral Spreading in Earthquakes*.

Ravanel, L. & Curtaz, M., 2011. *Terrestrial laser scanning (TLS) / Photogrammetry*.

Rayne, T.W., Bradbury, K.R. & Muldoon, M.A., 2001. Delineation of capture zones for municipal wells in fractured dolomite, Sturgeon Bay, Wisconsin, USA. *Hydrogeology Journal*, 9(5), pp.432–450.

Renz, A., Rühaak, W., Schätzl, P. & Diersch, H.J.G., 2009. Numerical modeling of geothermal use of mine water: Challenges and examples. *Mine Water and the Environment*, 28, pp.2–14.

Ribacchi, R. & Tommasi, P., 1988. Preservation and protection of the historical town of San Leo (Italy). In Marinos & Kuokis, eds. *IAEG Int. Symp. on Engineering Geology of Ancient Works Monuments and Historical Sites*. Atens: Balkema, pp. 55–64.

Ricci Lucchi, F., 1987. Semi-allochtonous sedimentation in the Apenninic thrust belt. *Sed.Geol.*, 50, pp.119–134.

Richards, L.A., 1941. A pressure-membrane extraction apparatus for soil solution. *Soil science*, 51(5), pp.377–386.

Ridley, A.M. & Wray, W.K., 1996. Suction measurement: a review of current theory and practices. In *Proceedings of the first international conference on unsaturated soils*. pp. 1293–1322.

Riegl, 2014. Riscan Pro 2.0.

Rimmer, A. & Salingar, Y., 2006. Modelling precipitation-streamflow processes in karst basin: The case of the Jordan River sources, Israel. *Journal of Hydrology*, 331(3-4), pp.524–542.

Rocscience Inc., 2014a. Dips. Available at: http://www.rocscience.com.

Rocscience Inc., 2013. Phase2. Available at: http://www.rocscience.com.

Rocscience Inc., 2014b. RocLab. Available at: http://www.rocscience.com.

Rohn, J., Resch, M., Schneider, H., Fernandez-Steeger, T.M. & Czurda, K., 2004. Large-scale lateral spreading and related mass movements in the Northern Calcareous Alps. *Bulletin of Engineering Geology and the Environment*, 63, pp.71–75.

Rohrbaugh, M.B.J., 2002. Estimating fracture trace intensity, density, and mean length using circular scan lines and windows. *AAPG Bulletin*, 86(12), pp.2089–2104.

Ronchetti, F., Borgatti, L., Cervi, F., Piccinini, L., Corsini, A., Emilia, R. & Ferrara, U., 2008. Modellazione numerica dei meccanismi di riattivazione di grandi frane per scivolamento di terra : l'esempio della frana di Tolara, Appennino settentrionale. *Giornale Di Geologia*, 8(2), pp.217–232.

SafeLand deliverable 4.1, 2010. *Review of techniques for landslide detection, fast characterization, rapid mapping and long-term monitoring*, Available at: http://www.safeland-fp7.eu.

Scesi, L. & Gattinoni, P., 2009. *Water Circulation in Rocks*, Springer Science & Business Media.

Schwartz, F.W., Smith, L. & Crowe, A.S., 1983. A stochastic analysis of macroscopic dispersion in fractured media. *Water Resources Research*, 19, pp.1253–1265.

Selroos, J.-O., Walker, D.D., Ström, A., Gylling, B. & Follin, S., 2002. Comparison of alternative modelling approaches for groundwater flow in fractured rock. *Journal of Hydrology*, 257, pp.174–188.

Shan, J. & Toth, C.K., 2008. *Topographic laser ranging and scanning: principles and processing.*, Boca Raton: CRC press.

Shapiro, A.M. & Andersson, J., 1985. Simulation of steady-state flow in three-dimensional fracture networks using the boundary-element method. *Advances in Water Resources*, 8, pp.106–110.

Shugar, D.H. & Clague, J.J., 2011. The sedimentology and geomorphology of rock avalanche deposits on glaciers. *Sedimentology*, 58(7), pp.1762–1783.

Silberbauer, J., Poisel, R. & Eppensteiner, W., 1988. Geomechanical model tests concerning the gliding apart of hard rock on soft ground. In *The engineering geology of ancient works, monuments and historical sites. Preservation and protection. Proceedings Vol. 1: engineering geology and the protection of historical sites and monuments*. AA Balkema, pp. 123–128.

Simmons, C.T., Centre, N., Sa, A., Hunt, R.J. & Survey, G., 2011. Updating the Debate on Model Complexity. , (8), pp.28–29.

Singhal, B.B.S. & Gupta, R.P., 2010. *Applied hydrogeology of fractured rocks: Second edition*, Dordrecht: Springer Netherlands.

Slama, C.C., Theurer, C. & Hendrikson, S.W., 1980. *Manual of Photogrammetry* American Society of Photogrammetry, ed.

Snow, D.T., 1969. Anisotropie permeability of fractured media. *Water Resources Research*, 5(6), pp.1273–1289.

Soldati, M., 2013. Deep-Seated Gravitational Slope Deformation. In P. T. Bobrowsky, ed. *Encyclopedia of Natural Hazards*. Springer Netherlands, pp. 151–155.

Soldati, M., 2004. Deep-seated gravitational slope deformation. In *Encyclopedia of Geomorphology*. London: Routledge, pp. 226–228.

Spreafico, M.C., Franci, F., Bitelli, G., Girelli, V.A., Landuzzi, A., Lucente, C.C. & Mandanici, E., 2015. Remote sensing techniques in a multidisciplinary approach for the preservation of cultural heritage sites from natural hazard: the case of Valmarecchia rock slabs (RN, Italy). In G. Lollino et al., eds. *Engineering Geology for Society and Territory - Volume 8*. Springer International Publishing, pp. 317–321.

Staub, I., Fredriksson, A. & Outters, N., 2002. *Strategy for a Rock Mechanics Site Descriptive Model. Development and testing of the theoretical approach.*, stockolm.

Stead, D., Eberhardt, E., Coggan, J. & Benko, B., 2001. Advanced numerical techniques in rock slope stability analysis - applications and limitations. In *LANDSLIDES – Causes , Impacts and Countermeasures*. pp. 615–624.

Stead, D., Eberhardt, E. & Coggan, J.S., 2006. Developments in the characterization of complex rock slope deformation and failure using numerical modelling techniques. *Engineering Geology*, 83, pp.217–235.

Stumpf, A., Malet, J.-P., Allemand, P., Pierrot-Deseilligny, M. & Skupinski, G., 2014. Ground-based multi-view photogrammetry for the monitoring of landslide deformation and erosion. *Geomorphology*, 231, pp.130–145.

Sturzenegger, M. & Stead, D., 2009. Close-range terrestrial digital photogrammetry and terrestrial laser scanning for discontinuity characterization on rock cuts. *Engineering Geology*, 106(3-4), pp.163–182.

Sturzenegger, M. & Stead, D., 2009. Quantifying discontinuity orientation and persistence on high mountain rock slopes and large landslides using terrestrial remote sensing techniques. , pp.267–287.

Sturzenegger, M. & Stead, D., 2012. The Palliser Rockslide, Canadian Rocky Mountains: Characterization and modeling of a stepped failure surface. *Geomorphology*, 138(1), pp.145–161.

Sturzenegger, M., Stead, D. & Elmo, D., 2011. Terrestrial remote sensing-based estimation of mean trace length, trace intensity and block size/shape. *Engineering Geology*, 119(3-4), pp.96–111.

Styles, T.D., Coggan, J.S. & Pine, R.J., 2011. Back analysis of the Joss Bay Chalk Cliff Failure using numerical modelling. *Engineering Geology*, 120(1-4), pp.81–90.

Svensson, U., 2001. A continuum representation of fracture networks . application to the Aspo Hard Rock laboratory. *Journal of Hydrology*, 250, pp.187–205.

Tapete, D., Casagli, N., Luzi, G., Fanti, R., Gigli, G. & Leva, D., 2013. Integrating radar and laser-based remote sensing techniques for monitoring structural deformation of archaeological monuments. *Journal of Archaeological Science*, 40, pp.176–189.

Tazioli, A., Conversini, P. & Peccerillo, A., 2012. Hydrogeological and geochemical characterisation of the Rock of Orvieto. *Environmental Earth Sciences*, 66, pp.55–65.

Terzaghi, D., 1965. Sources of Error in Joint Surveys. *Geotechnique*, 15(3), pp.287–304.

Teza, G., Galgaro, A., Zaltron, N. & Genevois, R., 2007. Terrestrial laser scanner to detect landslide displacement fields: a new approach. *International Journal of Remote Sensing*, 28, pp.3425–3446.

Tommasi, P., 1997. Analisi dei fattori che influenzano la resistenza dei giunti in rocce calcaree: un esempio di caratterizzazione per lo studio di una parete rocciosa. In *IV Convegno Nazionale dei Ricercatori Universitari*. pp. 549–565.

Tommasi, P., 1996. Stabilità di versanti naturali ed artificiali soggetti a fenomeni di ribaltamento. *Rivista Italiana di Geotecnica*, 4.

Treuropa, Customer Toolbar.

Umili, G., Ferrero, A. & Einstein, H.H., 2013. A new method for automatic discontinuity traces sampling on rock mass 3D model. *Computers and Geosciences*, 51, pp.182–192.

Vannucchi, P., Maltman, A., Clennel, M.. & Bettelli, G., 2003. On the nature of scaly fabric and scaly clay. *Journal of Structural Geology*, 25(5), pp.673–688.

Varnes, D.J., 1978. *Slope movements. Types and processes*, Washington: Schuster & Krizker.

Viero, A., 2011. *The analysis of the gravitational phenomena of the Cinque Torri group – Cortina d'Ampezzo (Bl)*. Università deli studi di Padova.

Viero, A., Teza, G., Massironi, M., Jaboyedoff, M. & Galgaro, A., 2010. Laser scanning-based recognition of rotational movements on a deep seated gravitational instability: The Cinque Torri case (North-Eastern Italian Alps). *Geomorphology*, 122(1-2), pp.191–204.

Vilardo, G., Isaia, R., Ventura, G., De Martino, P. & Terranova, C., 2010. InSAR Permanent Scatterer analysis reveals fault re-activation during inflation and deflation episodes at Campi Flegrei caldera. *Remote Sensing of Environment*, 114(10), pp.2373–2383.

Vincenzi, V., Piccinini, L., Gargini, A. & Sapigni, M., 2010. Parametric and numerical modelling tools to forecast hydrogeological impacts of a tunnel. *Aqua Mundi*, 1, pp.135–154.

Vivas Becerra, J., 2014. *Groundwater characterization and modelling in natural and open pit rock slopes*. Simon Fraser University.

Vlcko, J., 2004. Extremely slow slope movements influencing the stability of Spis Castle, UNESCO site. *Landslides*, 1, pp.67–71.

Vogel, H.J., Hoffmann, H. & Roth, K., 2005. Studies of crack dynamics in clay soil: I. Experimental methods, results, and morphological quantification. *Geoderma*, 125, pp.203–211.

Wagener, T., Boyle, D.P., Lees, M.J., Wheater, H.S. & Hoshin, V., 2001. A framework for development and application of hydrological models. , 5(September 2000), pp.13–26.

Wang, M., Kulatilake, P.H.S.W., Panda, B.B. & Rucker, M.L., 2001. Groundwater resources evaluation case study via discrete fracture flow modeling. *Engineering Geology*, 62, pp.267–291.

Westoby, M.J., Brasington, J., Glasser, N.F., Hambrey, M.J. & Reynolds, J.M., 2012. "Structure-from-Motion" photogrammetry: A low-cost, effective tool for geoscience applications. *Geomorphology*, 179, pp.300–314.

Wieczorek, G.F., 1996. *Landslide triggering mechanisms*, AK Turner and RL Schuster.

Wolf, P.R. & Dewitt, B.A., 2000. *Elements of photogrammetry with applications in GIS.*, Boston: McGraw Hill.

Wolter, A.E., 2014. *Characterisation of large catastrophic landslides using an integrated field, remote sensing and numerical modelling approach*. Simon Fraser University.

Zhang, L. & Einstein, H.., 2000. Estimating the intensity of rock discontinuities. *International Journal of Rock Mechanics and Mining Sciences*, 37(5), pp.819–837.

Zhang, L. & Einstein, H.H., 1998. Estimating the Mean Trace Length of Rock Discontinuities. *Rock Mechanics and Rock Engineering*, 31(4), pp.217–235.

Zhang, Y., Jiang, Z. & Cheng, X., 2011. Post-seismic deformation detection using permanent scatters technology for East Kunlun fault after 2001 Kokoxili earthquake. In *Proceedings - 2011 19th International Conference on Geoinformatics, Geoinformatics 2011*. pp. 2–5.

Zhang, Y., Stead, D. & Elmo, D., 2015. Characterization of strength and damage of hard rock pillars using a synthetic rock mass method. *Computers and Geotechnics*, 65, pp.56–72.

Zischinsky, U., 1969. Über Sackungen. *Rock Mechanics Felsmechanik Mecanique des Roches*, 1(1), pp.30–52.